Fast and Broadband Signal Integrity Analysis of Multiple Vias in Heterogeneous 3D IC and Die-Level Packaging by Using Generalized Foldy-Lax Scattering Method

Xin Chang

A dissertation

submitted in partial fulfillment of the

requirements for the degree of

Doctor of Philosophy

University of Washington

2015

Reading Committee:

John D. Sahr, Chair

Yaojiang Zhang

Feng Ling

Program Authorized to Offer Degree:

Electrical Engineering

University of Washington

Abstract

Fast and Broadband Signal Integrity Analysis of Multiple Vias in Heterogeneous 3D IC and Die-Level Packaging by Using Generalized Foldy-Lax Scattering Method

Xin Chang

Chair of the Supervisory Committee:
Professor John D. Sahr
Electrical Engineering

This dissertation proposal is concerned with the use of fast and broadband full-wave electromagnetic methods for modeling high speed interconnects (e.g, vertical vias and horizontal traces) and passive components (e.g, decoupling capacitors) for structures of PCB and packages, in 3D IC, Die-level packaging and SIW based devices, to effectively modeling the designs signal integrity (SI) and power integrity (PI) aspects. The main contributions finished in this thesis is to create a novel methodology, which hybridizes the Foldy-Lax multiple scattering equations based fast full wave method, method of moment (MoM) based 1D technology, modes decoupling based geometry decomposition and cavity modes expansions, to model and simulate the electromagnetic scattering effects for the irregular power/ground planes, multiple vias and traces, for fast and accurate analysis of link level simulation on multilayer electronic structures. For the

modeling details, the interior massively-coupled multiple vias problem is modeled most-analytically by using the Foldy-Lax multiple scattering equations. The dyadic Green's functions of the magnetic field are expressed in terms of waveguide modes in the vertical direction and vector cylindrical wave expansions or cavity modes expansions in the horizontal direction, combined with 2D MoM realized by 1D technology. For the incident field of the case of vias in the arbitrarily shaped antipad in finite large cavity/waveguide, the exciting and scattering field coefficients are calculated based on the transformation which converts surface integration of magnetic surface currents in antipad into 1D line integration of surface charges on the vias and on the ground plane. Geometry decomposition method is applied to model and integrate both the vertical and horizontal interconnects/traces in arbitrarily shaped power/ground planes. Moreover, a new form of multiple scattering equations is derived for solving coupling effects among mixed metallic/dielectric vias. The advantage of this kind of form has much better property for making inverse operation to obtain accurate results. All the proposed methods developed in this thesis have been verified by comparing the S parameters with the results from Ansoft's HFSS, for various via configurations and via array sizes in high density layout in benchmark simulations. It is shown that the hybrid method is accurate mostly within 5% difference from results of HFSS and is about tens to hundreds of times faster than running HFSS up to 100GHz.

TABLE OF CONTENTS

List of Figures v

List of Tables x

Chapter 1. Introduction 1

1.1 Research Background 1
1.2 Related Research Methodology and Literature 2
1.3 Previous Research on Foldy-Lax Multiple Scattering Equations for Vias Modeling 4
1.4 Tables and Figures New Contributions in This Thesis 6
1.5 Organization of the Dissertation 7

Chapter 2. New Approach of Making 1D MoM and Group T-matrix For Modeling Vias Sharing Same antipad 10

2.1 Summary 10
2.2 Introduction 10
2.3 Incident Fields from Magnetic Surface Currents Transformed to 1D Integral 12
2.4 Group T-Matrix 14
2.5 Solving Foldy-Lax Equations with Group T-Matrix 18
2.6 Combined Interior and Exterior Problem 20
2.6.1 The Combined Interior and Exterior Problem and Scattering Matrix for Single-Ended Case 20
2.6.2 References Generalized Mixed-Mode S-Parameters for $\boldsymbol{N}$ vias sharing same antipad 20
2.7 Numerical Results and Discussions 21
2.7.1 A. Case of Single Antipad with Two Vias (Fig. 2.4) and Comparison with Finite Difference Approach (FDM) 22
2.7.2 B. Cases of Differential Mode and Common Mode for Very Closely Spaced Vias 26
2.7.3 C. Case of Losses and Cross Talk of 5 Vias Sharing 1 Antipad 28
2.7.4 D. Modes Effects of Near Field Interactions for Closely Spaced Vias 31

2.7.5 E. Cases of Group T matrix for Vias Sharing an Antipad 34
2.8 Conclusions 42
Chapter 3. Modeling Vias with Arbitrarily Shaped Power/Ground Planes 43
3.1 Summary 43
3.2 Introduction 43
3.3 MoM Impedance Matrix $\boldsymbol{Z}$ for Finite Cavity Problem 44
3.4 Scattered Field from A Single Via and T-Matrix, Including Wall Reflections 47
3.5 Foldy-Lax Multiple Scattering Equations 50
3.6 Incident Field From the Source $\boldsymbol{aqj, inc}$, Including Reflection From The Wall 52
3.6.1 A. Single Via in An Antipad for Eccentric Case 52
3.6.2 B. Multiple Vias Sharing Same Antipad 53
3.7 Via Currents 54
3.8 Numerical Results and Discussions 55
3.8.1 A. 10 Vias Array for Each Via Going Through One Antipad Eccentrically (Single-Ended Signaling Case) in A Rectangular Cavity 55
3.8.2 B. 2 Vias Sharing Same Antipad (Differential Signaling Case) in A Square Cavity 57
3.8.3 C. 4 Vias Sharing Same Antipad in A L-Shaped Cavity 61
3.8.4 D. 36 Vias in A L-shaped Cavity Embedded with A SIW Structure 63
3.8.5 E. 5 X 10 Dense Vias Array for Each Via Going through One Antipad 64
3.8.6 F. 3 X 10 Dense Vias Array for Differential Singling Pairs 71
3.9 CPU Requirement and Discussions 78
3.10 Conclusions 81
Chapter 4. Modeling Traces in Power/Ground Planes with Vias for Link Level Simulation on Multilayer Electronic Structures 82
4.1 Summary 82
4.2 Introduction 82
4.3 Formulation of the Methodology 85
4.3.1 A. Mode Coupling between P/G Planes and Stripline at Via-Stripline Connection. 85

4.3.2 B. Boundary Value Problem Definition of P/G Planes with Vias Connecting with Stripline 86
4.3.3 C. 4-Ports Admittance Matrix $\boldsymbol{Ys}$ for Stripline 89
4.3.4 D. Admittance Matrix $\boldsymbol{YP/G}$ for P/G Planes with Vias 93
4.3.5 E. Model Recombination 95
4.3.6 F. Model for Multilayer Electronic Structures with Different Loads 96
4.4 Numerical Results and Discussions 96
4.4.1 A. 2 Common Vias Connected with 1 Trace in A Square Cavity for Higher Order Waveguide Modes Effects Investigation 97
4.4.2 B. 2 Eccentric Vias Connected with 1 Trace in A Square Cavity for Irregular Antipad Effects 100
4.4.3 C. 2 Common Vias Connected with 1 Trace in A L-Shaped Cavity for Irregular P/G Planes Effects 101
4.4.4 D. 48 Vias in A L-Shaped Cavity for Multiple Vias Scattering Effects 102
4.4.5 E. 3 Common Vias Connected with 2 Traces in 2 Layered L-Shaped Cavities for Multilayered Structures 105
4.4.6 F. 2 Pairs of Differential Signaling Connected with Coupled Traces in A Rectangular Cavity 106
4.5 Conclusions 109

Chapter 5. Extend Foldy-Lax Equation Method to Model Mixed Metal/Dielectric Cylinders in Parallel Plate Waveguide Structure 110

5.1 Introduction 110
5.2 T Matrix of Dielectric Cylinder in Parallel Plate Waveguide 110
5.2.1 TM case: 111
5.2.2 TE case 116
5.3 Foldy-Lax Equations for Multiple Scattering among Dielectric Cylinders in Parallel Plate Waveguide 118
5.4 Incident Field and Post Processing 122
5.5 Numerical Results and Summary 123

5.5.1 A. SIW structure with one signal via inside and without any dielectric cylinders. The first resonance happens at about 36GHz. 123
5.5.2 B. SIW structure with one signal via inside and 1 closely placed dielectric cylinder. The first resonance happens at about 37GHz. 125
5.5.3 C. SIW structure with one signal via inside and 3 closely placed dielectric cylinders. The first resonance happened at about 41GHz. 126
Bibliography 129
Appendix A 133
A.1 2D Method of Moment with 1D Discretization and Integration 133
A.1.1 Incident Electric Field and Surfaces Currents 133
A.1.2 Group T-Matrix 135
A.2 $\boldsymbol{\tau}$ Matrix and Foldy Lax Multiple Scattering Equations in the Presence of the Cavity Wall 137

LIST OF FIGURES

Figure 1.1. Via structure and its interior and exterior problems decomposition. 5
Figure 1.2. Cross-sections of C4 bumps on package (left) and via escape area on printed circuit board (right). [1]..... 8
Figure 1.3. Synthetic waveguides: putting vias connecting upper and lower metal plates of substrate (left) [2] and a monopulse antenna for 94+GHz (right) [3]. 9
Figure 2.1. N number of vias sharing the same antipad. 13
Figure 2.2. G groups of vias with each group of vias sharing the same antipad..... 15
Figure 2.3. N vias distributed in NA antipad with only antipad i excited. 18
Figure 2.4. Geometry under investigation for cases 1, 2 and 3. (a) (left) top view of 2 vias sharing one antipad, and (b) (right) cross-sectional view of 2 vias sharing one antipad. 22
Figure 2.5. Insertion loss (top) and return loss (bottom) of differential mode for case 1. 23
Figure 2.6. Insertion loss (top) and return loss (bottom) of differential mode for case 2. 24
Figure 2.7. Meshing mechanism of non-uniform cylindrical coordinate system (left) and rectangular coordinate system (right) applying to an oval antipad with 2 vias sharing the same antipad..... 25
Figure 2.8. Insertion loss (top) and return loss (bottom) of differential mode for case 3.26
Figure 2.9. Insertion loss (top) and return loss (bottom) of common mode for case 3.... 27
Figure 2.10. Case 4: top view of 5 vias sharing one antipad. 28
Figure 2.11. Insertion loss for 5 vias sharing one antipad for case 4. 29
Figure 2.12. Return loss for 5 vias sharing one antipad for case 4. 29
Figure 2.13. Near end cross talk among 5 vias sharing one antipad for case 4. 30
Figure 2.14. Far end cross talk among 5 vias sharing one antipad for case 4..... 31
Figure 2.15. Top view of 8 close vias layout for case 5. 32
Figure 2.16. Insertion loss comparisons of via 1 for case 5. 32
Figure 2.17. NEXT comparisons of via 1 and via 3 for case 5. 33
Figure 2.18. Insertion loss of differential mode for case 6. 34

Figure 2.19. Geometry under investigation for case 7: top view of 2 groups of vias with each 2 vias sharing one antipad. 35
Figure 2.20. Insertion loss of differential mode for one differential via pair for case 7… 36
Figure 2.21. Geometry under investigation for case 8: top view of 2 groups of vias with 5 vias sharing one antipad and 1 via in another antipad. 37
Figure 2.22. Insertion loss (top) and return loss (bottom) of single-ended mode for via 1 for case 8. 38
Figure 2.23. Geometry under investigation for case 9: top view of 4 groups of vias with each 5 vias sharing one antipad. 39
Figure 2.24. Insertion loss of single-ended mode for four center vias for case 9. 40
Figure 2.25. Return loss of single-ended mode for four center vias for case 9. 41
Figure 2.26. Near end cross talk of single-ended mode for four center vias for case 9.... 41
Figure 2.27. Far end cross talk of single-ended mode for four center vias for case 9. 42
Figure 3.1. Boundary integral equation method for the problem of finite cavity of irregular shape. The electric field in the z direction is governed by the 2D Helmholtz equation. Neumann boundary conditions are used for the cavity wall. 45
Figure 3.2 (b) Top view of N vias sharing the same antipad with arbitrarily shaped power/ground planes. 51
Figure 3.3. (Left) Top view of 10 eccentric vias layout for case A. (right) Zoom in for one eccentric via in anitpad. 56
Figure 3.4. Insertion loss comparisons of left corner bottom via and center bottom via for case A. 56
Figure 3.5. Return loss comparisons of left corner bottom via and center bottom via for case A 57
Figure 3.6. Top view of 2 vias sharing one antipad in a square cavity for case B. 58
Figure 3.7. Insertion/Return loss of differential mode for case B1. 59
Figure 3.8. Insertion/Return loss of common mode for case B1. 59
Figure 3.9. Insertion/Return loss of differential mode for case B2. 60
Figure 3.10. Insertion/Return loss of common mode for case B2. 60
Figure 3.11. Top view of 4 vias sharing one antipad in a L-shaped cavity for case C. 61

Figure 3.12. Insertion/Return loss of signal via 1 for case C. 62
Figure 3.13. NEXT between signal via 1, via 2 and via 3 for case C. 62
Figure 3.14. Top view of a L-shaped cavity embedded with a SIW structure. 63
Figure 3.15. Comparisons of insertion and return loss for signal via 1, NEXT and FEXT btween signal via 1 and 2. 64
Figure 3.16. Top view of 5x8 dense via array for case E. 65
Figure 3.17. Insertion loss for corner via for case E. 65
Figure 3.18. Return loss for corner via for case E. 66
Figure 3.19. NEXT for corner via for case E. 66
Figure 3.20. FEXT for corner via for case E. 67
Figure 3.21. Insertion loss for center via for case E. 67
Figure 3.22. Return loss for center via for case E. 68
Figure 3.23. NEXT for center via for case E. 68
Figure 3.24. FEXT for corner via for case E. 69
Figure 3.25. NEXT for center via for case E. 69
Figure 3.26. FEXT for corner via for case E. 70
Figure 3.27. Top view of 3x10 dense via array for case F. 71
Figure 3.28. Insertion loss of differential mode for corner pair for case F. 72
Figure 3.29. Return loss of differential mode for corner pair for case F. 72
Figure 3.30. Insertion loss of common mode for corner pair for case F. 73
Figure 3.31. Return loss of common mode for corner pair for case F. 73
Figure 3.32. Insertion loss of differential mode for center pair for case F. 74
Figure 3.33. Return loss of differential mode for center pair for case F. 74
Figure 3.34. Insertion loss of common mode for center pair for case F. 75
Figure 3.35. Return loss of common mode for center pair for case F. 75
Figure 3.36. NEXT differential mode for center/corner pairs for case F. 76
Figure 3.37. NEXT common mode for center/corner pairs for case F. 76
Figure 3.38. FEXT differential mode for center/corner pairs for case F. 77
Figure 3.39. FEXT common mode for center/corner pairs for case F. 77

Figure 4.1. Top and side view of two vias inside a parallel waveguide connected with a trace. 87
Figure 4.2. Geometry decomposition..... 88
Figure 4.3. Side view of a general stripline structure. 90
Figure 4.4. Three conductor transmission line problem and its equivalent circuit for 2 ports. 92
Figure 4.5. Top and side view of 2 vias connected with 1 trace in a square cavity..... 97
Figure 4.6. Y parameters for upper and upper ports comparisons for case A1. 98
Figure 4.7. Y parameters for upper and bottom ports comparisons for case A1. 98
Figure 4.8. Y parameters for upper and upper ports comparisons for case A2. 99
Figure 4.9. Y parameters for upper and upper ports comparisons for case A2. 99
Figure 4.10. Top view for eccentric via in case B. 100
Figure 4.11. S parameters comparisons for case B. 101
Figure 4.12. Top view for 2 vias connected with 1 trace in L shaped cavity for case C. 102
Figure 4.13. S parameters comparisons for case C. 103
Figure 4.14. Top view of a L-shaped cavity embedded with a SIW structure for case D. 103
Figure 4.15. S parameters comparisons for case D. 104
Figure 4.16. NEXT and FEXT between signal via 1 and 3 for case D. 104
Figure 4.17. 3D view for 2 layered L shape cavities with 3 vias and 2 traces for case E. 105
Figure 4.18. S parameters comparisons for case E. 106
Figure 4.19. Top view for 2 differential signaling pairs with coupled striplines for case F. 107
Figure 4.20. Differential mode S parameters comparisons for case F. 108
Figure 4.21. Common mode S parameters comparisons for case F. 108
Figure 5.1. Geometry for case A 123
Figure 5.2. Insertion loss comparisons between Foldy-Lax and HFSS for case A. 124
Figure 5.3. Return loss comparisons between Foldy-Lax and HFSS for case A. 124
Figure 5.4. Geometry for case B 125
Figure 5.5. Insertion loss comparisons between Foldy-Lax and HFSS for case B. 125
Figure 5.6. Return loss comparisons between Foldy-Lax and HFSS for case B. 126
Figure 5.7. Geometry for case C. 126

Figure 5.8. Insertion loss comparisons between Foldy-Lax and HFSS for case C..... 127
Figure 5.9. Return loss comparisons between Foldy-Lax and HFSS for case C. 127

LIST OF TABLES

Table 2.1. CPU Time per Frequency for The Simulation Case 1-3 On Ansoft HFSS and The Foldy-Lax Approach 24
Table 2.2. CPU Time per Frequency For The Simulation Case 7-9 On Ansoft HFSS and The Foldy-Lax Approach 35
Table 3.1. Case A: Foldy-Lax Approach 79
Table 3.2. Case A: HFSS v12 80
Table 3.3. Case C: Foldy-Lax Approach 80
Table 3.4. Case C: HFSS v12 80
Table 3.5. CPU Run Time at Frequency 5Ghz and 20ghz Comparisons For Case A-C .. 81
Table 3.6. CPU Run Time per Frequency Comparisons For Case E-F 81

ACKNOWLEDGEMENTS

I would like to express my deepest gratitude to my advisor, Prof. John D. Sahr, and my previous advisor, Prof. Leung Tsang, for their outstanding guidance, patience, caring and providing me with an excellent atmosphere for doing research. I would like to thank Dr. Yaojiang Zhang and Dr. Feng Ling, who kindly read this thesis carefully and made many valuable suggestions. I also would like to thank my manager Dr. Yaping Zhou in NVIDIA Corp., who guided and let me experience many practical issues beyond the textbooks, and patiently helped me to find out solutions. Thanks Prof. Vikram Jandhyala, Prof. Yasuo Kuga, Mr. Bryan Crockett and Ms. Brenda Larson for their kind hearted help. Special thanks goes to Prof. Gino Aisenberg who continuously encouraged me and pulled me up from haze during my toughest days. Thanks for all the persons who ever helped me.

DEDICATION

I dedicate my dissertation work and my love to my wife Dr. Chang Xue and my daughter Tian-Tian Xue. A special feeling of gratitude to my loving parents and my sister, for their raising and educating me and their words of encouragement.

Chapter 1. INTRODUCTION

1.1 RESEARCH BACKGROUND

For modern microelectronics, in order to integrate dissimilar technologies (digital, analog, RF circuits, etc) on different layers and to reduce problems such as signal propagation delay, thermal heating, power consumption and electromagnetic interference and compatibility (EMI/EMC) issues, vertical interconnects are widely used vehicles for 3D integration system. Today, with increasing multifunctional components combined in compact packages, these vertical vias are critical enablers for wafer, die and package stacking for which low-inductance, high-bandwidth vertical interconnects are needed for the design in multicore architectures in silicon. Technology scaling will soon enable high-performance processors with hundreds of cores integrated onto a single die, but the success of such systems could be limited by the corresponding massive interconnection networks. To consider the electrical behavior of the 3D interconnects, high density vertical vias are structures that have been difficult to model. Since the density of vias interconnections is dense (~10^5 – 10^8/cm^2), this presents tremendous design challenges on 3D integration and packaging requirements.

On the other hand, as demand for information bandwidth increases, information photonics are becoming more instrumental and photonic-based communication systems are playing a crucial role to overcome the inherently limited-speed barriers of electronics for millimeter-wave and terahertz application. As an emerging technology which can satisfy the demand of commercial communication systems of higher data rate links and smaller and lighter devices, SIW technology is a new platform for implementing all components with a high performance, low-cost and reliable technology for high-frequency electronics, and thus has attracted attention in recent years. These SIW waveguide-like structures are fabricated in planar form and are built by periodically arranged metallic via-holes and via-slots. Thus the structures take advantage of the well-known characteristics of conventional rectangular waveguides, namely, its high Q-factor, excellent crosstalk and electromagnetic interference immunity, high power capacity and low losses. A variety of devices have been realized based on SIW structures, including wireless network, automotive radars, imaging sensors and biomedical devices, which allow sophisticated packaging

and the integration of complex beam-forming networks and antennas on the same board. These highly integrated circuits result in challenges to modern electronic sub-system package modeling and optimization for real engineering solutions.

The high speed 3D integrated (3DI) system and SIW based structures are the key technologies to satisfy current and future high-frequency electronics and photonics. It is expected that high-density integration techniques, combined with a low-cost fabrication process, should be able to offer widespread solutions. High performance computing systems for 3DI in which the electrical I/O bandwidth and density have been the bottleneck at different packaging levels (PCB, package, interposer, 3D chip stack, etc).

Vias structures can cause serious concerns on signal integrity (SI), power integrity (PI) as well as electromagnetic interference (EMI). As a discontinuity, it can cause mismatch in a signal trace. Furthermore, a high-speed vertical current flowing on a via excites propagating parallel plate modes of a power/ground pair. As a result, strong cross-talk or voltage fluctuation may occur in adjacent signal vias or power distribution network (PDN). In addition, the propagating modes may excite the resonant modes of the power/ground pair and cause strong radiation from the edges. Therefore, simulation and modeling of vias in a plate pair are crucial for practical designs of high-speed PCBs or packages. Global optimization and detailed trade-off analysis require fast and accurate simulation tools of massively coupled vertical interconnects for both 3D heterogeneous high speed chip-package-board system and SIW based devices.

1.2 Related Research Methodology and Literature

The vias structures are essential elements for parallel–plate waveguide and are used extensively in high–speed electronic system. In order to efficiently model the coupling among vias and waveguide or cavity, classes of methods have been developed such as building up equivalent circuits model through hybrid field-circuit method [15, 26-29], semi-analytical full wave methods [14, 30, 31] and numerical full wave methods [32, 33].

For numerical full wave methods, electromagnetic field solvers can be used for simulations frequency response. These solvers are generally based on two kinds of numerical full wave methods: integral equation (IE) methods and partial differential equation (PDE) methods. The IE methods include method of moment (MoM) and partial element equivalent circuit (PEEC) method. The PDE methods include finite element method (FEM) and finite difference method (FDM).

These general purpose electromagnetic solvers can be used to make the simulations for simple interconnect system. However, as modern high-speed electronic systems often include hundreds or even thousands of off-chip interconnects to interface heterogeneous components, the task then is challenging for complicated structures. More accurate modeling requires full wave numerical methods, which induces large computational cost.

For the circuit model method in [15, 26-28], lumped elements circuit method is used to express equivalent RLGC network for via-trace transitions and parallel plate impedance for rectangular/circular cavity based on cavity model theory. All the RLGC parameters need to be pre studied or extracted analytically or numerically. For example for a lossless substrate and planes with perfect electric conductor (PEC), these RLGC parameters include C (capacitance) and inductance (L), they are via-plane capacitance, via self-inductance, plane-plane impedance and via-via mutual inductances and capacitances. If the substrate is with lossy material and the planes are good conductors instead of PEC, then the R (resistance) and G (conductance) parameters have to be also extracted and included. Generally speaking, there is no analytical solution for their extraction, hence the numerical methods are needed to extract the corresponding values. One of the drawback of the RLGC lumped model is that most of the calculation methods are based on the assumption of TEM mode, since the concept of RLGC is within the region of TEM mode. Then for high frequency modeling and simulation, the RLGC lumped model sometimes is not accurate, since higher order mode effects are necessary to be considered. Another drawback of the RLGC lumped model is that when the elements which need to be modeled are too many, for example, if there are 10^3 vias inside a PDN, then the number of RLGC units are huge, that can lead to cost a lot of computation resources. Some paper, for example in [29], RLGC parameters are extracted for irregular shape plane effects and they are investigated and incorporated into circuit model by applying boundary integral equations method. However, the circuit parameters are still extracted based on rigorous electromagnetic analysis, but not with TEM mode assumption any more.

For semi-analytical method, for example in [14, 30], a hybrid method is used for rigorous electromagnetic analysis of multiple scattering among vias and irregular shape cavity. It is worthwhile to note that the multiple scattering equations method used in [14, 30] are actually forms of generalized Foldy-Lax equations. In [31], a hybrid method is used to model the case of large number of vias. For full wave numerical methods, a combination of 2D integral equation method and 2D finite element method [32] is used to model vias and traces in arbitrarily shaped cavity

with multivias of arbitrary shapes and inhomogeneous media in substrate, up to 2GHz. However, all these investigations focus on common via case in which only one via goes through one circular antipad, or relative low frequency range (compared with 50GHz in this paper). The irregular shape antipads are common in practical PCB and packaging designs, e.g. cases of eccentric vias and multiple vias sharing one antipad. A differential vias structure in rectangular cavity is investigated for local vias region in [33] based on full wave method by using 3D rectangular Green's function. For other semi-analytical methods, Frequency-dependent cylinder layer (FDCL) method [24] is hard to exactly be modeled as Neumann boundary condition, hence failed to efficiently modeling the coupling between vias and cavity which has PMC walls. Contour integral method (CIM) [48] assumes that no higher order waveguide modes can be excited, which leads to inaccuracy when vias are closely placed and the thickness of the cavity is not electrically small compared with wavelength in high frequency range.

1.3 Previous Research on Foldy-Lax Multiple Scattering Equations for Vias Modeling

In our previous research, we used a mostly analytical technique of Foldy-Lax equations to compute the full wave solution of Maxwell equations that includes multiple scattering among cylindrical vias in both infinite large planar waveguides and finite circular cavity [4, 16].

The vias structure problem can be decomposed into exterior problem and interior problem [42], as shown in Fig. 1.1. The exterior problem is antenna problem and short circuit problem, the interior problem is problem of multiple vias scattering inside waveguide.

For interior problem, Foldy-Lax scattering equations was adopted to model multiple cylinders in planar waveguides [4]. The Foldy-Lax multiple scattering equations state that the final exciting field of certain cylinder is equal to the incident field plus the scattering fields from all the other cylinders. The Foldy-Lax equations were initially used to model multiple scattering by particles in volume scattering by discrete random media [50] and have been extensively used in microwave remote sensing [34]. It has been successfully adapted to model multiple scattering among vias in waveguide environment by using dyadic green's function, waveguide modal expansions [37] and cylindrical wave expansions [4].

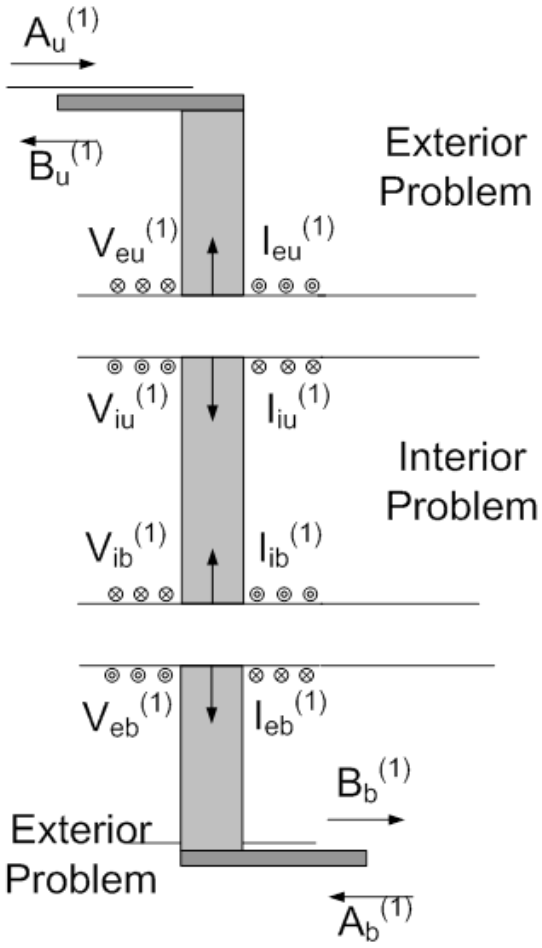

Figure 1.1. Via structure and its interior and exterior problems decomposition.

Based upon the magnetic Green's functions, this parallel waveguide structure is excited by using a voltage source at the port, which is equivalent to a magnetic current ring source at antipad. The surface currents on the cylinders are then calculated from the magnetic field.

The Foldy-Lax approach has been validated with measurements [5]. The efficiency comparisons with commercial software ANSYS HFSS were made for a BGA application [19]. It is worth noting that HFSS cannot handle vias size >256 in conventional computer. Foldy-Lax method take seconds per frequency point and provide accurate results.

The sparse-matrix canonical-grid (SMCG) method was invented based on wave translations and fast Fourier transforms to solve rough surface problems [34]. The pre-conditioned SMCG method was incorporated into Foldy Lax equations for problems with large number of vias [9].

The Foldy-Lax approach was extended to model the case of vias with irregular antipad [23] by using FDM to calculate the equivalent magnetic surface current, and the case of vias in substrate of layered dielectrics, and compared with HFSS. The fast all mode method (FAM) and numerical modified steepest descent path method (NMSP) were used to calculate the layered medium Green's function [11] and TSV structure [6]. The combination of these methods reduce the $O(N^2)$ memory and time requirement to O(rN logN). The layered medium Green's function reduces the number of unknowns by avoiding intensive discretization on reference planes and planar boundaries.

However, all above extensions are for infinite large waveguide. For finite large cavity, Foldy-Lax equations method was applied for a circular cavity in [35].

The exterior layer problem is solved by using the method of moments (MoM) with the layered media Green's functions [42]. The exterior layer and interior layer problems are combined to obtain the S-parameters of the trace and through-hole via. A fast approach for the layered-medium Green's functions using the numerical modified steepest descent path method is utilized [52]. The Green's functions require milliseconds to compute per point. Schemes for efficiently computing image contributions for the static portion of the mixed potential Green's function are also implemented to solve neighboring or self-RWG (basis function) interaction.

1.4 TABLES AND FIGURES NEW CONTRIBUTIONS IN THIS THESIS

In this dissertation, I continuously apply and extend this mostly analytical approach of Foldy-Lax multiple scattering equation method with recent major improvements, such as 1D technology, group T matrix and geometry decomposition method, to fast and efficiently model and solve physical/electromagnetics properties of a variety of complicated 3D structures, for current millimeter wave, submillimeter wave and terahertz wave application. The structures include chip-package-board system (figure 1.2) [1], and SIW based devices (figure 1.3) [2] [3]. These structures have massive coupled vertical interconnects with heterogeneous substrate. The physical/electromagnetics properties to be solved are network parameters, current and voltage distributions, field patterns, signal integrity, power integrity and electromagnetic emissions of sensitive electronic devices of the structures.

My contributions are:

1. Implement new approach of making 1D MoM and group T matrix for modeling structures with multiple vias sharing same antipad and different groups of vias in different antipad.

2. Propose and develop method to model multiple vias scattering in arbitrarily shaped cavity for vias sharing one antipad, by using 1D MoM and generalized Foldy-Lax equations method.

3. Propose and develop method to model structure of horizontal striplines connecting with vertical vias in irregular cavity by applying geometry decomposition method and generalized Foldy-Lax equations method.

4. Propose rigorous TE/TM modes coupling effects for multiple scattering among mixed PEC/dielectric cylinders in parallel plates waveguide, develop T matrix for dielectric cylinder and new form of Foldy-Lax equations using scattered field coefficients.

1.5 ORGANIZATION OF THE DISSERTATION

In chapter 2, the full-wave mostly-analytical approach, based on Foldy–Lax multiple scattering equations and modal expansions, is extended for modeling of vias sharing the same antipad in infinite large planar waveguide with boundary integral equation and group T matrix method. In order to accurately calculate all the effects of high order waveguide modes and azimuthal modes for complete signal integrity analysis of multiple closely spaced vias, we make use of transformation that converts the surface integration of magnetic surface currents into 1-dimensional line integration of surface charges on the vias and on the ground plane. We also use group T matrix to represent a group of vias to account for the scattering among different groups of vias, to accelerate the computation process. The new method has great accuracy and efficiency for modeling multiple closely spaced vertical vias.

In chapter 3, modeling method for multiple vias with irregular antipad in arbitrarily shaped 3D IC and packaging system is proposed, based on hybrid generalized Foldy-Lax equations method, boundary integral equation method and generalized T matrix. In modeling detail, the impedance matrix for finite cavity is first obtained, which includes the reflection features of the cavity boundaries. Then the scattered field from a single via and a generalized T matrix including the wall effects are derived. The Foldy-Lax multiple scattering equations are generalized to include the wall effects by using impedance matrix and the generalized T matrix. To obtain the incident field for the case of vias in the arbitrarily shaped antipad, the exciting and scattering field coefficients are calculated, based on the transformation which converts surface integration of

magnetic surface currents in antipad into 1D line integration of surface charges on the vias and on the ground plane, as discussed in chapter 2. The coupling among vertical vias are solved by applying Foldy-Lax multiple scattering equations.

In chapter 4, a novel hybridization of full wave method based on Foldy-Lax multiple scattering equations, 1D technology and modal decomposition are used to model the electromagnetic scattering effects for the irregular power/ground planes, multiple vias and striplines, for analysis of link level simulation on multilayer electronic structures. For the modeling details, instead of being analyzed separately, vias and irregular power/ground planes are treated as a whole which is solved by Foldy-Lax multiple scattering equations method, to obtain the coupling effects among vias and cavities. Then the modal effects of striplines can be decoupled and recombined with the modal solution of vias and cavities effects.

In chapter 5, T matrix for dielectric cylinders in infinite parallel plates waveguide is derived under consideration of TE/TM modes coupling effects. The new form of Foldy-Lax multiple scattering equations method which applies scattered field coefficients as unknowns are also derived and be further used to solve SIW structures and 3D IC signal/power integrity analysis. The results agree well with HFSS simulation benchmark results up to 50GHz.

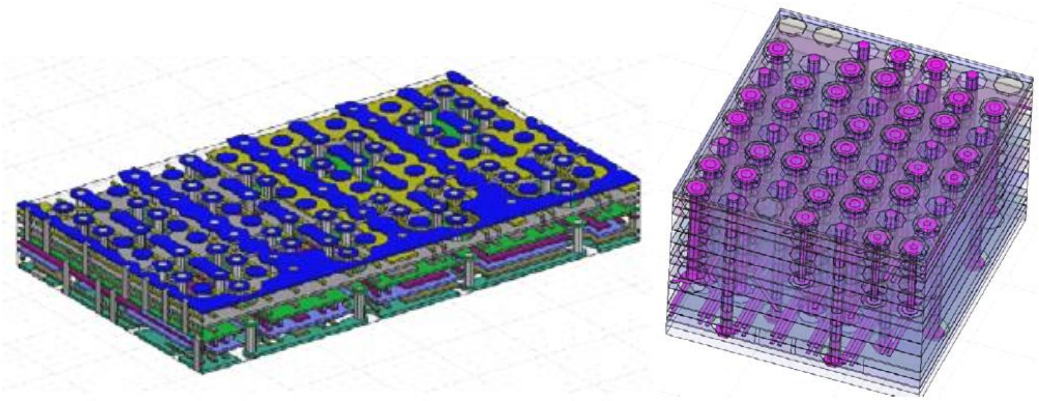

Figure 1.2. Cross-sections of C4 bumps on package (left) and via escape area on printed circuit board (right). [1]

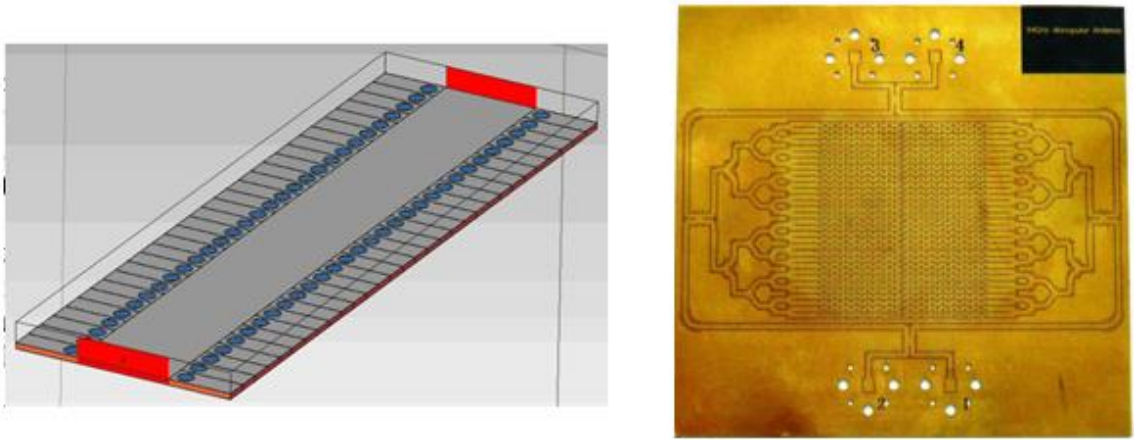

Figure 1.3. Synthetic waveguides: putting vias connecting upper and lower metal plates of substrate (left) [2] and a monopulse antenna for 94+GHz (right) [3].

For all chapters, numerical results and comparisons are made with HFSSv12 for various test scenarios. In all cases of illustrations, unless given special explanation, all single-ended S-parameters provided are referenced to 50 Ω, and all mixed-mode S-parameters are referenced to 100 Ω for differential mode and 25 Ω for common mode. The configurations of PC used in the simulations are: Intel(R) Core(TM)2 Duo E7300 2.66GHz processor, 3GB RAM and Windows Vista 32-bit operating system.

Chapter 2. NEW APPROACH OF MAKING 1D MOM AND GROUP T-MATRIX FOR MODELING VIAS SHARING SAME ANTIPAD

2.1 SUMMARY

This chapter considers multiple scattering among different groups of vias with each group of vias sharing one antipad in planar waveguide. A transformation is used that converts the 2D discretization and 2D surface integration of the product of Green's functions and magnetic surface currents into 1-dimensional discretization and 1D integration of surface charges on the vias and on the ground plane. This is used to calculate the incident fields onto the vias. Based on the incident fields, the Foldy-Lax equations can be solved to calculate the circuit parameters for the problem. We show that the results are superior to the previously used finite difference method. In addition, the group T matrix method is used to represent a group of vias to account for the scattering among different groups of vias. Results are illustrated for various cases of multiple vias up to 20 GHz. Results show the accuracy of the method even to very closely spaced vias when they are separated by merely 1 mil. Numerical results are in excellent agreements with ANSOFT HFSS.

2.2 INTRODUCTION

The switching noise of currents on the power/ground plane can interfere with other components and give rise to serious edge radiation. In order to significantly improve the performance of the signal transition, the structure of "differential via pair" is used, in current high-speed circuit designs. Similarly, the structures of multiple vias in one antipad can also be present. Due to its advantage and wide usage in current microelectronic system, an accurate, fast and efficient method of modeling scattering among multiple vias sharing one antipad is useful.

A number of classes of methods have been developed to model the crosstalk or coupling mechanism, such as methods developed in references [12] to [15]. Most of these models make simplifying assumptions such as assuming circularly shaped antipads, considering only the TEM mode and neglecting the axially-anisotropic modes etc. In the structure of multiple vias sharing the same anipad, vias can be placed very close to each other. Hence, the simplifying assumptions

are not valid for modeling the coupling among vias. Full wave numerical techniques such as finite element method (FEM) and finite difference time domain (FDTD) method require large computational time and memory overheads. To model multiple cylinders in planar waveguides, in my research, I have developed and have been using a mostly-analytic 3D full-wave approach, based on Foldy-Lax multiple scattering equations and cylindrical wave mode expansions [5, 11, 16-20]. The results were also validated using experimental data from hardware measurements [11] and ANSOFT HFSS [8].

In the initial work on the Foldy Lax approach, the antipad is assumed to be circular and the via is concentric with the antipad [16-19]. For the case of antipad of arbitrary shape, and arbitrary number of vias sharing the same antipad, we previously used the finite difference approach with nonuniform grids [11, 20] to calculate the magnetic surface currents on the antipad. After the magnetic surface currents are calculated, the incident fields on the vias are calculated by 2D surface integrations of the product of Green's functions and the magnetic surface currents.

The approach of finite difference of 2D antipad discretization [11, 20, 21] is inconvenient when there are two or more vias in the same antipad. The results also become inaccurate when the vias in the same antipad are close to each other. For such cases, one needs fine discretization of the finite difference grid, 2D interpolation of magnetic surface current and 2D surface integration of the product of Green's functions and magnetic surface currents. In this chapter, I made two improvements in the problem of groups of vias sharing the same antipad. The first improvement is that I show that the incident fields on the vias can be calculated by 1-dimensional line integrals of the product of surface charges on the vias and the Green's functions, that replaces the previous 2-dimensional surface integrations of the product of magnetic surface currents and Green's functions. This avoids the complication of 2D surface integration that needs to be accurate particularly for closely spaced vias. Furthermore, the surface charges on the line contours on the surfaces are derived readily by a 1-dimensional surface integral equation of the method of moments (MoM). Thus the previous 2D problems of 2D discretization and 2D integration were reduced to 1D discretization and 1D integrals. The second improvement is for the case of a group of vias sharing the same antipad, in which I use the Foldy-Lax equations to derive the group T-matrix to characterize the scattering by the group of vias. The group T matrix methodology follows that of reference [22] but is adapted to waveguide modes and cylindrical wave expansions in Foldy-Lax

method. This facilitates the calculations of multiple scattering of groups of vias belonging to different antipads.

I illustrate results for various numbers of vias sharing the same antipad. They show that the present approach is superior to the previous approach of finite difference solution of the antipad in terms of both accuracy and computational efficiency. They also show that results of this present approach are in good agreement with HFSS even for the case of closely spaced vias of as small as 1 mil in spacing between adjacent vias. The computational efficiency of the group T matrix is also shown. Besides comparing with HFSS, I also made independent checks by comparing the results with those based entirely on the 2D MoM approach [24]. Brief summary of 2DMoM for these problems are given in the Appendix A.1. The results are in good agreement with HFSS simulations.

2.3 Incident Fields from Magnetic Surface Currents Transformed to 1D Integral

Consider the problem of N number of vias sharing the same antipad (Fig. 2.1). In equivalence principle, the 2D magnetic currents $\bar{M}_s(\bar{\rho}')$ in the antipad are the excitations for the waveguide structure. Let the via line boundaries be $S_1, S_2, \ldots \ldots S_N$ and the ground plane line boundary be S_g. The "aperture" area is the antipad. Consider via q centered at $\overline{\rho_q}$. In the Foldy-Lax integral equations, the incident field coefficients $a_{ln}^{TM(q)}$ for via q are given by the 2D surface integral

$$a_{ln}^{TM(q)} = \frac{jk}{2d}\frac{(-1)^{n+l}}{k_{\rho l}^2} f_l \iint_A dx'dy' \, \bar{m}_{-n}\left(k_{\rho l}, k_{zl}, \bar{\rho}' - \overline{\rho_q}\right) \cdot \bar{M}_s(\bar{\rho}') \tag{2.1}$$

where A is the area of antipad, and the integration is a 2D surface integration over the antipad where $\bar{M}_s(\bar{\rho}')$ is nonzero.

In [4], the Green's function, $\bar{m}_{-n}\left(k_{\rho l}, k_{zl}, \bar{\rho}\right)$ is in terms of n^{th} order Hankel function with the argument that of waveguide mode $k_{\rho l}$

$$\bar{m}_{-n}\left(k_{\rho l}, k_{zl}, \bar{\rho}\right) = \left[\hat{\rho}\frac{jn}{\rho}H_{-n}^{(2)}\left(k_{\rho l}\rho\right) - \hat{\phi}k_{\rho l}H_{-n}^{(2)\prime}\left(k_{\rho l}\rho\right)\right] e^{jn\phi} \tag{2.2}$$

Other notations are as defined in reference [4]. For the case of arbitrary number of vias and arbitrary shape of vias and antipad, $\bar{M}_s(\bar{\rho}')$ is derived from solution of the Laplace equation. Let the voltage on the via i be V_i, $i = 1,2, \ldots N$ and the voltage on the ground plane be zero. Then the 2D Laplace equation in the antipad is $\nabla_t^2 \psi_L(x, y) = 0$, where ∇_t is the 2D Laplace operator. After

the Laplace equation is solved, then $\bar{M}_s(x,y) = \hat{z} \times \nabla_t \psi_L(x,y)$. In our previous work, we solved the 2D Laplace equation using finite difference method [23].

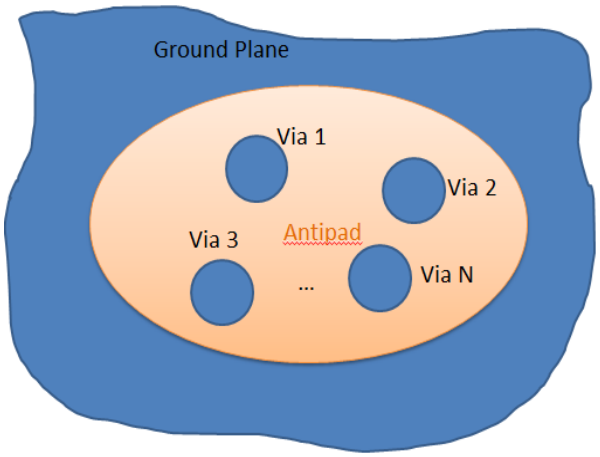

Figure 2.1. N number of vias sharing the same antipad.

Next the incident field is calculated by a 2D surface integral of $\bar{m}_{-n}\left(k_{\rho l}, k_{zl}, \bar{\rho}' - \overline{\rho_q}\right)\bar{M}_s(\bar{\rho}')$. The approach is computationally intensive; as the nonzero $\bar{M}_s(\bar{\rho}')$ region is irregular and the 2D surface integration is inconvenient when the vias are closely spaced as fine discretizations are required.

Let the n^{th} order Green's function be in terms of n^{th} order Hankel function

$$g_{ln}(\bar{\rho}) = H_n^{(2)}\left(k_{\rho l}\rho\right)e^{-jn\phi} \tag{2.3}$$

Then

$$\bar{m}_{-n}\left(k_{\rho l}, k_{zl}, \bar{\rho}' - \overline{\rho_q}\right) = -\hat{z} \times \nabla_t{}' g_{l(-n)}\left(\bar{\rho}' - \overline{\rho_q}\right) \tag{2.4}$$

The Foldy-Lax incident field coefficients become

$$a_{ln}^{TM(q)} = \frac{-jk}{2d}\frac{(-1)^{n+l}}{k_{\rho l}^2} f_l \iint_A dx'dy' \, \nabla_t{}' g_{l(-n)}\left(\bar{\rho}' - \overline{\rho_q}\right) \cdot \nabla_t{}' \psi_L(\bar{\rho}') \tag{2.5}$$

Using the 2D Green's theorem, I then have

$$a_{ln}^{TM(q)} = \frac{-jk}{2d}\frac{(-1)^{n+l}}{k_{\rho l}^2} f_l \left[-\iint_A dx'dy' \left[g_{l(-n)}\left(\bar{\rho}' - \overline{\rho_q}\right)\nabla_t'^2 \psi_L \right] \right.$$

$$\left. - \oint_S dl' g_{l(-n)}\left(\bar{\rho}' - \overline{\rho_q}\right)\hat{n}' \cdot \nabla_t{}' \psi_L \right] \tag{2.6}$$

where $\hat{n}'$ points into the antipad on the via and ground plane line boundaries, and $S = \sum_{i=1}^{N} S_i + S_g$ are the line boundaries of vias and the ground plane. Since $\nabla_t^2 \psi_L = 0$, we have

$$a_{ln}^{TM(q)} = \frac{jk}{2d} \frac{(-1)^{n+l}}{k_{\rho l}^2} f_l \left[\oint_S \; dl' g_{l(-n)}(\bar{\rho}' - \overline{\rho_q}) \hat{n}' \cdot \nabla_t' \psi_L \right] \tag{2.7}$$

Note that $-\varepsilon \hat{n} \cdot \nabla_t \psi_L = \sigma_s(\bar{\rho})$ is the surface charge density on the via and the ground plane. Thus

$$a_{ln}^{TM(q)} = -\frac{\eta j \omega}{2d} \frac{(-1)^{n+l}}{k_{\rho l}^2} f_l \oint_S \; dl' g_{l(-n)}(\bar{\rho}' - \overline{\rho_q}) \sigma_s(\bar{\rho}') \tag{2.8}$$

where $\eta = \frac{\mu}{\varepsilon}$ is the wave impedance. Equation (2.8) is the new result as the previous 2D integration in (1) becomes a 1D integration in (2.8). We note that $\sigma_s(\bar{\rho})$ obey the 1D surface (line) integral equation

$$\oint_S \; dl' g_L(\bar{\rho}, \bar{\rho}') \frac{\sigma_s(\bar{\rho}')}{\varepsilon} = \begin{cases} V_i & \bar{\rho} \; is \; on \; S_i \\ 0 & \bar{\rho} \; is \; on \; S_g \end{cases} \tag{2.9}$$

where g_L is Green's function for Laplace equation and is

$$g_L(\bar{\rho}, \bar{\rho}') = -\frac{1}{2\pi} ln \sqrt{(x - x')^2 + (y - y')^2} \tag{2.10}$$

Thus I have converted the incident wave problem to 1) first solve the surface charge on the via boundaries in the line integral equation of Laplace Green's function of equation (2.9) by using MoM. 2) Next the incident field coefficients in Foldy-Lax equations are obtained by line integrals of the product of surface charge and nth order Green's function of $g_{l(-n)}(\bar{\rho}' - \overline{\rho_q})$.

2.4 GROUP T-MATRIX

Next I introduce Group T matrix to accelerate the calculation of multiple scattering among different groups of vias. Each group of vias share the same antipad as shown in figure 2.2.

I can treat the group of vias as a single object and calculate the group T matrix. In structures such as in Fig. 2.2, often we are only interested in the final S parameters for certain vias or ports, and not the entire network. Then the other groups of vias can be treated as single objects with one object for each group of vias. Simplified network can be obtained and the speed of computation can be greatly improved.

Next I derive the group T matrix of multiple vias through Foldy-Lax equations. Let there be N_g vias in one antipad. Then these vias are of the same group. Let the group of N_g vias sharing

the antipad be centered at $\bar{\rho}_1, \bar{\rho}_2, \dots, \bar{\rho}_{N_g}$. The center of the antipad be at $\bar{O}_g$. Then for each via in this group, Foldy-Lax equations can be written as

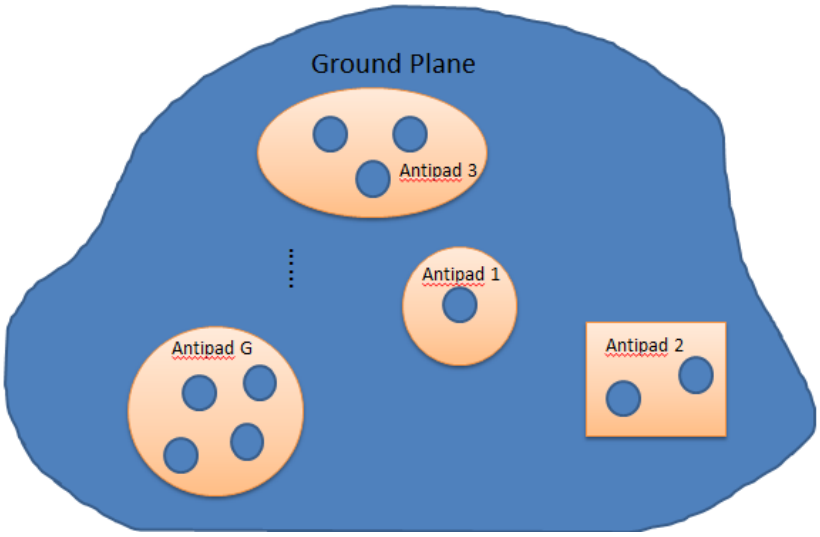

Figure 2.2. G groups of vias with each group of vias sharing the same antipad.

$$w_{ln}^{TM(q)} = a_{ln}^{TM(q)} + \sum_{\substack{p=1 \\ p\neq q}}^{N_g} \sum_{m=-\infty}^{\infty} H_{n-m}^{(2)}\left(k_{\rho l}\left|\overline{\rho_p} - \overline{\rho_q}\right|\right) e^{j(n-m)\emptyset_{\overline{\rho_p \rho_q}}} T_m^{(p)} w_{lm}^{TM(p)}$$

$$q = 1,2, \dots, N_g \tag{2.11}$$

where

$$T_m^{(p)} = -\frac{J_m(k_{\rho l} a)}{H_m^{(2)}(k_{\rho l} a)} \tag{2.12}$$

The scattered field coefficient is

$$a_{ln}^{sTM(q)} = T_n^{(q)} w_{ln}^{TM(q)} \tag{2.13}$$

Let the incident wave on the group from other antipads and from other sources, for the l^{th} mode, be

$$\bar{H}_{inc}(\bar{\rho}, z) = \sum_{n=-\infty}^{\infty} w_{ln}^{TM} Rg \bar{H}_n^{TM}\left(k_{\rho l}, k_{zl}, \bar{\rho} - \bar{O}_g, z \pm \frac{d}{2}\right) = Rg \bar{\psi}^t\left(\bar{\rho} - \bar{O}_g\right) \cdot \bar{w}^{TM} \tag{2.14}$$

where $\bar{\psi}^t(\bar{\rho})$ is the row matrix representing $\bar{H}_n^{TM}\left(k_{\rho l}, k_{zl}, \bar{\rho}, z \pm \frac{d}{2}\right)$, and $\bar{w}^{TM}$ is the column vector representing w_{ln}^{TM}.

Let the scattered wave from via p, centered at $\bar{\rho}_p$, in the group be $\bar{H}_s^{(p)}(\bar{\rho}, z)$

$$\bar{H}_s^{(p)}(\bar{\rho}, z) = \sum_{n=-\infty}^{\infty} a_{ln}^{sTM(p)} \bar{H}_n^{TM}\left(k_{\rho l}, k_{zl}, \bar{\rho} - \bar{\rho}_p, z \pm \frac{d}{2}\right) = \bar{\psi}^t\left(\bar{\rho} - \bar{\rho}_p\right) \cdot \bar{a}_s^{(p)} \tag{2.15}$$

Then, the total magnetic field is

$$\bar{H} = \bar{H}_{inc}(\bar{\rho}, z) + \sum_{p=1}^{N_g} \bar{H}_s^{(p)}(\bar{\rho}, z) = Rg\bar{\psi}^t\left(\bar{\rho} - \bar{O}_g\right) \cdot \bar{w}^{TM} + \sum_{p=1}^{N_g} \bar{\psi}^t\left(\bar{\rho} - \bar{\rho}_p\right) \cdot \bar{a}_s^{(p)} \tag{2.16}$$

where $\bar{\psi}^t\left(\bar{\rho} - \bar{\rho}_p\right)$ is the row vector matrix representing $\bar{H}_n^{TM}\left(k_{\rho l}, k_{zl}, \bar{\rho} - \bar{\rho}_p, z \pm \frac{d}{2}\right)$ and $\bar{a}_s^{(p)}$ is the column vector that represents $a_{ln}^{sTM(p)}$. Then the exciting field on via q is, summing scattered fields from the other vias except q,

$$\bar{H}_{ex}^{(q)}(\bar{\rho}, z) = Rg\bar{\psi}^t\left(\bar{\rho} - \bar{O}_g\right) \cdot \bar{w}^{TM} + \sum_{\substack{p=1 \\ p \neq q}}^{N_g} \bar{\psi}^t\left(\bar{\rho} - \bar{\rho}_p\right) \cdot \bar{a}_s^{(p)} \tag{2.17}$$

From the vector addition theorem

$$\bar{\psi}^t\left(\bar{\rho} - \bar{\rho}_p\right) = Rg\bar{\psi}^t\left(\bar{\rho} - \bar{\rho}_q\right) \cdot \bar{\bar{\alpha}}_{qp} \tag{2.18}$$

$$Rg\bar{\psi}^t\left(\bar{\rho} - \bar{\rho}_p\right) = Rg\bar{\psi}^t\left(\bar{\rho} - \bar{\rho}_q\right) \cdot \bar{\bar{\beta}}_{qp} \tag{2.19}$$

where $\bar{\bar{\alpha}}_{qp}$ and $\bar{\bar{\beta}}_{qp}$ are matrices with

$$\left[\bar{\bar{\alpha}}_{qp}\right]_{nm} = H_{n-m}^{(2)}\left(k_{\rho l}\left|\bar{\rho}_p - \bar{\rho}_q\right|\right) e^{j(n-m)\emptyset_{\overline{\rho_p \rho_q}}} \tag{2.20}$$

$$\left[\bar{\bar{\beta}}_{qp}\right]_{nm} = J_{n-m}^{(2)}\left(k_{\rho l}\left|\bar{\rho}_p - \bar{\rho}_q\right|\right) e^{j(n-m)\emptyset_{\overline{\rho_p \rho_q}}} \tag{2.21}$$

Then the exciting field in equation (2.17) becomes

$$\bar{H}_{ex}^{(q)}(\bar{\rho}, z) = Rg\bar{\psi}^t\left(\bar{\rho} - \bar{\rho}_q\right) \cdot \left[\bar{\bar{\beta}}_{qO_g} \cdot \bar{w}^{TM} + \sum_{\substack{p=1 \\ p \neq q}}^{N_g} \bar{\bar{\alpha}}_{qp} \cdot \bar{a}_s^{(p)}\right] \tag{2.22}$$

The scattered field from via q is, using the T matrix $\bar{\bar{T}}^{(q)}$

$$\bar{H}_s^{(q)}(\bar{\rho}, z) = \bar{\psi}^t\left(\bar{\rho} - \bar{\rho}_q\right)\bar{\bar{T}}^{(q)} \cdot \left[\bar{\bar{\beta}}_{qO_g} \cdot \bar{w}^{TM} + \sum_{\substack{p=1 \\ p \neq q}}^{N_g} \bar{\bar{\alpha}}_{qp} \cdot \bar{a}_s^{(p)}\right] \tag{2.23}$$

The Foldy Lax equation becomes, on equating (2.23) to (2.15),

$$\bar{a}_s^{(q)} = \bar{\bar{T}}^{(q)} \cdot \left[\bar{\bar{\beta}}_{qO_g} \cdot \bar{w}^{TM} + \sum_{\substack{p=1 \\ p \neq q}}^{N_g} \bar{\bar{\alpha}}_{qp} \cdot \bar{a}_s^{(p)} \right] \tag{2.24}$$

In matrix form, equation (2.24) becomes,

$$\begin{bmatrix} \bar{\bar{I}} & -\bar{\bar{T}}^{(1)} \cdot \bar{\bar{\alpha}}_{12} & \dots & -\bar{\bar{T}}^{(1)} \cdot \bar{\bar{\alpha}}_{1N_g} \\ -\bar{\bar{T}}^{(2)} \cdot \bar{\bar{\alpha}}_{21} & \bar{\bar{I}} & \dots & -\bar{\bar{T}}^{(2)} \cdot \bar{\bar{\alpha}}_{2N_g} \\ \dots & \dots & \dots & \dots \\ -\bar{\bar{T}}^{(N_g)} \cdot \bar{\bar{\alpha}}_{N_g1} & -\bar{\bar{T}}^{(N_g)} \cdot \bar{\bar{\alpha}}_{N_g2} & \dots & \bar{\bar{I}} \end{bmatrix} \begin{bmatrix} \bar{a}_s^{(1)} \\ \bar{a}_s^{(2)} \\ \dots \\ \bar{a}_s^{(N_g)} \end{bmatrix} = \begin{bmatrix} \bar{\bar{T}}^{(1)} \cdot \bar{\bar{\beta}}_{1O_g} \cdot \bar{w}^{TM} \\ \bar{\bar{T}}^{(2)} \cdot \bar{\bar{\beta}}_{2O_g} \cdot \bar{w}^{TM} \\ \dots \\ \bar{\bar{T}}^{(N_g)} \cdot \bar{\bar{\beta}}_{N_gO_g} \cdot \bar{w}^{TM} \end{bmatrix} \tag{2.25}$$

Let $\bar{\bar{Q}}$ be the inverse of the matrix of the left hand side of equation (2.25), and let it be decomposed as follows

$$\bar{\bar{Q}} = \begin{bmatrix} \bar{\bar{Q}}_{11} & \bar{\bar{Q}}_{12} & \dots & \bar{\bar{Q}}_{1N_g} \\ \bar{\bar{Q}}_{21} & \bar{\bar{Q}}_{22} & \dots & \bar{\bar{Q}}_{2N_g} \\ \dots & \dots & \dots & \dots \\ \bar{\bar{Q}}_{N_g1} & \bar{\bar{Q}}_{N_g2} & \dots & \bar{\bar{Q}}_{N_gN_g} \end{bmatrix} = \begin{bmatrix} \bar{\bar{I}} & -\bar{\bar{T}}^{(1)} \cdot \bar{\bar{\alpha}}_{12} & \dots & -\bar{\bar{T}}^{(1)} \cdot \bar{\bar{\alpha}}_{1N_g} \\ -\bar{\bar{T}}^{(2)} \cdot \bar{\bar{\alpha}}_{21} & \bar{\bar{I}} & \dots & -\bar{\bar{T}}^{(2)} \cdot \bar{\bar{\alpha}}_{2N_g} \\ \dots & \dots & \dots & \dots \\ -\bar{\bar{T}}^{(N_g)} \cdot \bar{\bar{\alpha}}_{N_g1} & -\bar{\bar{T}}^{(N_g)} \cdot \bar{\bar{\alpha}}_{N_g2} & \dots & \bar{\bar{I}} \end{bmatrix}^{-1} \tag{2.26}$$

Then

$$\bar{a}_s^{(q)} = \sum_{p=1}^{N_g} \bar{\bar{Q}}_{qp} \cdot \bar{\bar{T}}^{(p)} \cdot \bar{\bar{\beta}}_{pO_g} \cdot \bar{w}^{TM} \tag{2.27}$$

The total field, from equations (2.16) and (2.27), is

$$\bar{H}(\bar{\rho}, z) = Rg\bar{\psi}^t\left(\bar{\rho} - \bar{O}_g\right) \cdot \bar{w}^{TM} + \sum_{q=1}^{N_g} \bar{\psi}^t\left(\bar{\rho} - \bar{\rho}_q\right) \cdot \sum_{p=1}^{N_g} \bar{\bar{Q}}_{qp} \cdot \bar{\bar{T}}^{(p)} \cdot \bar{\bar{\beta}}_{pO_g} \cdot \bar{w}^{TM} \tag{2.28}$$

Using vector addition theorem

$$\bar{\psi}^t\left(\bar{\rho} - \bar{\rho}_q\right) = \bar{\psi}^t\left(\bar{\rho} - \bar{O}_g\right) \cdot \bar{\bar{\beta}}_{O_gq} \tag{2.29}$$

then the field in the group of N_g vias become

$$\bar{H}(\bar{\rho}, z) = Rg\bar{\psi}^t\left(\bar{\rho} - \bar{O}_g\right) \cdot \bar{w}^{TM} + \sum_{q=1}^{N_g} \bar{\psi}^t\left(\bar{\rho} - \bar{\rho}_q\right) \cdot \bar{\bar{\tau}}_{Ng} \cdot \bar{w}^{TM} \tag{3.30}$$

In equation (3.30), $\bar{\bar{\tau}}_{Ng}$ is the group T matrix of N_g vias, and is

$$\bar{\bar{\tau}}_{Ng} = \sum_{q=1}^{N_g}\sum_{p=1}^{N_g} \bar{\bar{\beta}}_{O_g q} \cdot \bar{\bar{Q}}_{qp} \cdot \bar{\bar{T}}^{(p)} \cdot \bar{\bar{\beta}}_{pO_g} \tag{3.31}$$

The solution of the problem consists of calculating the inverse in (2.26) to get $\bar{\bar{Q}}_{qp}$, and then use (2.31) to obtain group T matrix $\bar{\bar{\tau}}_{Ng}$.

2.5 Solving Foldy-Lax Equations with Group T-Matrix

Let there be N_A antipads. The antipads are labeled as $i = 1,2, \ldots N_A$ and their centers are at $O_1, O_2, \ldots \ldots O_{N_A}$. For each antipad, the vias are labeled as $q_i = 1,2, \ldots N_i$ vias. Thus the total number of vias is $N = \sum_{i=1}^{N_A} N_i$.

Let the magnetic current source be at antipad i, as shown in Fig. 2.3. The shadow antipad means that antipad is excited, while the other antipads, $j \neq i$, have idle vias. Then I use $\bar{\bar{\tau}}^{(j)}$ to represent the group T-matrix of the vias in antipad j. For the source antipad i, I do not use the $\bar{\bar{\tau}}$ matrix as the source arises from the space in between the vias at the antipad i.

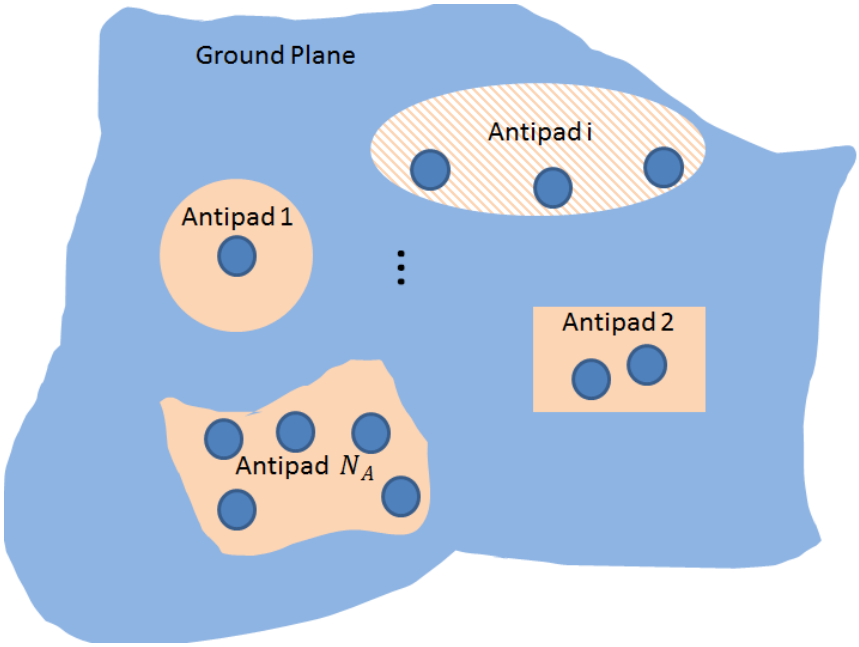

Figure 2.3. N vias distributed in N_A antipad with only antipad i excited.

For Foldy-Lax equation in such case, the exciting field coefficients at antipad j will then be at O_j and not at individual via. Thus I use $w_{ln}^{TM(O_j)}$. The incident filed coefficients are denoted as $a_{ln}^{TM(O_j)}$. Then in matrix notation, for the exciting field of via q_i in the source antipad i,

$$\bar{w}^{q_i} = \bar{a}^{q_i} + \sum_{p_i=1, p_i \neq q_i}^{N_i} \bar{\bar{\alpha}}_{q_i p_i} \bar{\bar{T}}^{(p_i)} \bar{w}^{p_i} + \sum_{j=1, j \neq i}^{N_A} \bar{\bar{\alpha}}_{q_i O_j} \bar{\bar{\tau}}^{(j)} \bar{w}^{O_j} \tag{2.32}$$

Then for the group of vias in antipad j

$$\bar{w}^{O_j} = \bar{a}^{O_j} + \sum_{p_i=1, p_i \neq q_i}^{N_i} \bar{\bar{\alpha}}_{O_j p_i} \bar{\bar{T}}^{(p_i)} \bar{w}^{p_i} + \sum_{j'=1, j' \neq j}^{N_A} \bar{\bar{\alpha}}_{O_j O_{j'}} \bar{\bar{\tau}}^{(j')} \bar{w}^{O_{j'}} \tag{2.33}$$

In equations (2.32) and (2.33), I can see there are a total of $(N_A - 1 + N_i) \times M$ equations, where $M = 2N_{max} + 1$, and N_{max} is the truncation number of the axially anisotropic modes.

After solving the exciting field coefficients, I next only post process the port parameters that we are interested in.

Hence I only need $J^{(q_i)}$, the surface current coefficients on the via in the source antipad. The relation between the surface current coefficients and the exciting field coefficients w_{ln}^{TM} is [4]

$$w_{ln}^{TM} = \frac{1}{B_{ln}^{TM}} J_{ln}^{TM} \tag{2.34}$$

where $B_{ln}^{TM} = \frac{2/(\eta \pi a)}{H_n^{(2)}(k_{\rho l} a)}$.

For the magnetic surface current source at $z' = \frac{d}{2}$, the surface current density on the via p is

$$\bar{J}_s^{TM(p)} = \sum_{m,l} J_{lm}^{TM(p)} \hat{z} \cos\left(k_{zl}\left(z + \frac{d}{2}\right)\right) e^{-jm\phi} \tag{2.35}$$

The currents are obtained by the integration

$$\bar{I}^{(p)} = \int_0^{2\pi} a d\,\phi \bar{J}_s^{TM(p)} \cdot \hat{z} \tag{2.36}$$

In the integration, only the zeroth harmonic of $m = 0$ contributes.

$$\bar{I}^{(p)} = 2\pi a \sum_l w_{l0}^{TM(p)} \frac{2/(\eta \pi a)}{H_m^{(2)}(k_{\rho l} a)} \cos\left(k_{zl}\left(z \pm \frac{d}{2}\right)\right) = 2\pi a \sum_l J_{l0}^{TM(p)} \cos\left(k_{zl}\left(z \pm \frac{d}{2}\right)\right) \tag{2.37}$$

where the $+$ sign corresponds to the magnetic current source at $\frac{d}{2}$ and the $-$ sign corresponds to the magnetic current source at $-\frac{d}{2}$. The Y parameters of single-ended case for N vias sharing same antipad can be obtained according to section 5 and 6 in [4]. One can also get S parameters for interior problem by transforming Y parameters.

2.6 COMBINED INTERIOR AND EXTERIOR PROBLEM

2.6.1 *The Combined Interior and Exterior Problem and Scattering Matrix for Single-Ended Case*

The exterior problem for N vias sharing same antipad is a transmission line with N conductors in which only TEM mode is excited. The TEM modal solution is computed by solving the same Laplace equation as (2.3). As stated in section 6 in [4], the exterior problem has magnetic current opposite to that of interior problem, but with the same voltage enforced and the same electric field in the aperture.

Following the same notations in [4], for single-ended case, a matrix equation is used to characterize the exterior structure as follows:

$$\begin{bmatrix}\bar{B}\\ \bar{I}\end{bmatrix} = \begin{bmatrix}\bar{\bar{\Gamma}}_{sc} & \bar{\bar{T}}_{ant}\\ \bar{\bar{I}}_{sc} & \bar{\bar{Y}}_{ant}\end{bmatrix}\begin{bmatrix}\bar{A}\\ \bar{V}\end{bmatrix} \tag{2.38}$$

where $\bar{B}$, $\bar{I}$, $\bar{A}$ and $\bar{V}$ are $N \times 1$ vectors, $\bar{\bar{\Gamma}}_{sc}$, $\bar{\bar{T}}_{ant}$, $\bar{\bar{I}}_{sc}$ and $\bar{\bar{Y}}_{ant}$ are $N \times N$ matrices. The surface current for the i^{th} via can be obtained by performing the line integral on the i^{th} via

$$I_i = -\oint_{S_i} dl \frac{1}{\eta}\hat{n}\cdot\nabla\psi \tag{2.39}$$

where η is wave impedance.

After solving both the exterior and interior problems, I relate the admittance matrix $\bar{\bar{Y}}$ found in the interior problem and the parameters of the exterior-problem, $\bar{\bar{\Gamma}}_{sc}$, $\bar{\bar{T}}_{ant}$, $\bar{\bar{I}}_{sc}$ and $\bar{\bar{Y}}_{ant}$. Then the $2N \times 2N$ scattering matrix is:

$$\bar{\bar{S}}_{single-eneded} = \begin{bmatrix}\bar{\bar{\Gamma}}_{sc}^{u} & \bar{\bar{0}}_N\\ \bar{\bar{0}}_N & \bar{\bar{\Gamma}}_{sc}^{b}\end{bmatrix} + \begin{bmatrix}-\bar{\bar{T}}_{ant}^{u} & \bar{\bar{0}}_N\\ \bar{\bar{0}}_N & \bar{\bar{T}}_{ant}^{b}\end{bmatrix} \times \begin{bmatrix}\bar{\bar{Y}}^{uu} + \bar{\bar{Y}}_{ant}^{u} & \bar{\bar{Y}}^{ub}\\ -\bar{\bar{Y}}^{bu} & -\bar{\bar{Y}}^{bb} - \bar{\bar{Y}}_{ant}^{b}\end{bmatrix}^{-1} \begin{bmatrix}\bar{\bar{I}}_{sc}^{u} & \bar{\bar{0}}_N\\ \bar{\bar{0}}_N & \bar{\bar{I}}_{sc}^{b}\end{bmatrix} \tag{2.40}$$

2.6.2 *References Generalized Mixed-Mode S-Parameters for $\boldsymbol{N}$ vias sharing same antipad*

Consider the general n-ports network. In order to get n-ports mixed-mode scattering matrices, the overall number of n-ports is split into two different sets: the mixed-mode port set composed by the even number of p-ports requiring the differential and common mode description,

and the one given by the remaining single-ended $(n-p)$ ports. One can transform the conventional single-ended scattering matrix to generalized mixed-mode scattering matrix by using

$$\bar{\bar{M}} = \frac{1}{\sqrt{2}}\begin{bmatrix} 1 & -1 & 0 & 0 \\ 0 & 0 & 1 & -1 \\ 1 & 1 & 0 & 0 \\ 0 & 0 & 1 & 1 \end{bmatrix} \tag{2.41}$$

$$\bar{\bar{S}}_{mixed\_mode} = \bar{\bar{M}}\bar{\bar{S}}_{single-ended}\bar{\bar{M}}^{-1} \tag{2.42}$$

2.7 Numerical Results and Discussions

The Foldy-Lax multiple scattering equation method is a mostly analytical method based on modal expansion of the scattering of cylindrical waves. The truncation of the numbers of modes and the truncation of the number of harmonics are large enough to guarantee good accuracy. On the other hand, it is advisable not to overestimate these truncations indices as it leads to an unnecessary increase in the computational cost of the method. The convergence studies and the rules of choosing the truncation were discussed in references [8] and [14].

I first illustrate the case of a single antipad with multiple vias, in order to verify the accuracy and efficiency of the proposed method. I compare the results with the previous Foldy-Lax finite difference method with non-uniform grid (Foldy-Lax/nuFDM2D). I then discuss the high order modes effects for three cases. Next I illustrate results when the group T matrix is incorporated. I illustrate the cases of multiple antipads with multiple vias in each antipad by applying Foldy-Lax/GT/MoM1D and the group T matrix (GT) for the group of vias sharing the same antipad. By MoM 1D, I refer to the results of reducing to 1D discretization of MoM solution of Laplace equation and 1D integration of the product of the charge and the Green's functions.

For discussion of modes effects, the indices l and n stand for the mode order for waveguide modes and azimuthal modes for vertical vias respectively. L_{max} and N_{max} are the truncation mode order numbers of l and n respectively. For excitation in the antipad, only TEM or TM_{z00} mode is considered, hence only TM_z modes are excited in the waveguide. Then the modes can be classified as

TEM or TM_{z00} mode, with $l = n = 0$, it is propagating and isotropic.

TM_{zn0} modes, with $l = 0$ and $n \neq 0$, they are propagating and anisotropic.

TM_{z0l} modes, with $l > 0$ and $n = 0$, they are nonpropagating and isotropic.

TM_{znl} modes, with $l > 0$ and $n \neq 0$, they are nonpropagating and anisotropic.

In the setup of HFSS, the boundary condition is set as radiation boundary. In order to keep enough distance between the port and boundary (at least one wavelength of the lowest interested frequency point), we set the plane size at $1\ inch \times 1\ inch$.

I calculate the single-ended case first and then transform the conventional S parameters into mixed-mode form using (2.41) and (2.42).

2.7.1 *A. Case of Single Antipad with Two Vias (Fig. 2.4) and Comparison with Finite Difference Approach (FDM)*

I first compare the present method with the previous method that uses finite difference. In using finite difference, the method is fast if non uniform grid is used. I label this as Foldy-Lax/nuFDM2D. On the other hand, when the vias are closely spaced, fine uniform grids need to be used. I label this approach as Foldy-Lax/FDM2D. It then has the accuracy with significant increase of CPU as shown later.

Fig. 2.4(a) and (b) show the top view and the cross-sectional view of structure about 2 vias sharing one antipad which is called differential vias. In the specifications, h stands for waveguide thickness, t stands for the plane thickness and ε_r is the relative dielectric constant. The antipad shape is oval. The pitch between the two centers of the vias varies from $80\ mil$ to $31\ mil$, or the closest spacing between the two vias varies from $50\ mil$ to only $1\ mil$.

The average CPU times per frequency for simulation of single-ended S parameters by using the method of Foldy-Lax/MoM1D, Foldy-Lax/nuFDM2D, Foldy-Lax/FDM2D and HFSS for cases 1 to 4 are compared in Table 2.1.

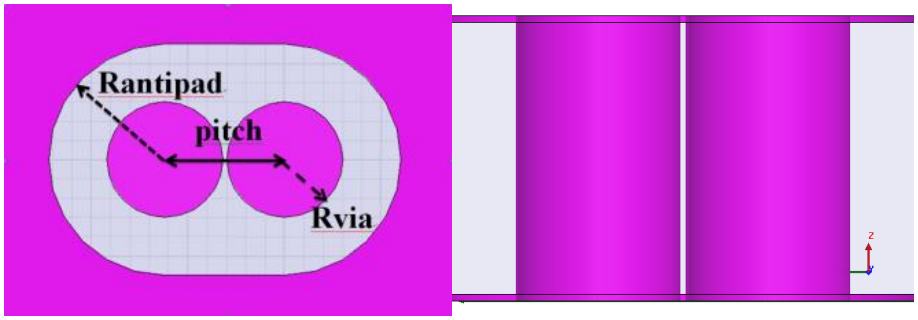

Figure 2.4. Geometry under investigation for cases 1, 2 and 3. (a) (left) top view of 2 vias sharing one antipad, and (b) (right) cross-sectional view of 2 vias sharing one antipad.

Specifications for case 1 are: $\varepsilon_r = 4.4$, $R_{via} = 15\,mil$, $R_{antipad} = 30\,mil$, $pitch = 80\,mil$, $h = 50\,mil$, $t = 1.3\,mil$.

In this case, the pitch between the two centers of the vias is quite far apart at 80 mil, so that the closest spacing between the two vias is 50 mil. Fig. 2.5 shows the comparisons of the three methods of both insertion loss and return loss for differential mode. There are greater losses in general at high frequencies because of radiation losses. Good agreements are found for the three methods. We can see that for differential signaling, since the signal propagating along the vias are equal and opposite, the radiated EMI is reduced. The insertion loss is less than 3dB even up to 20 GHz.

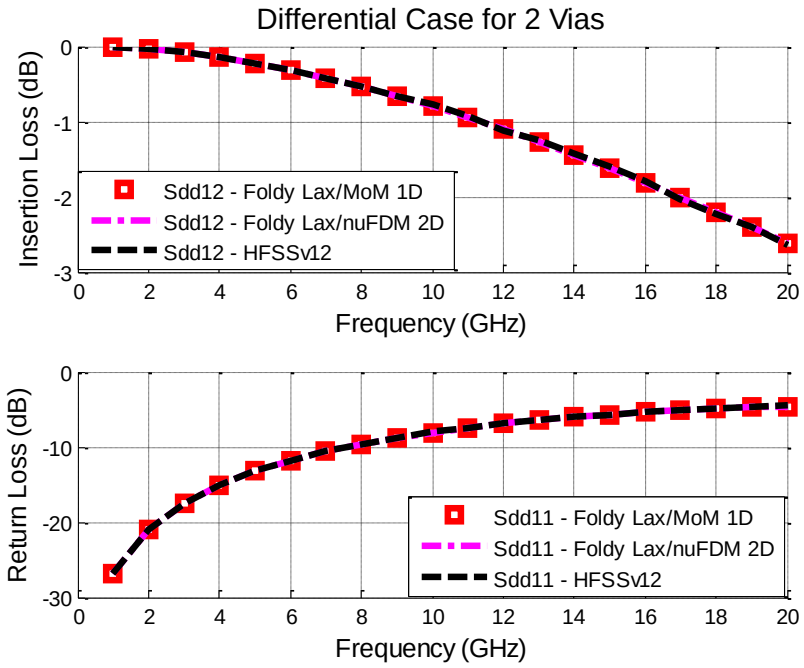

Figure 2.5. Insertion loss (top) and return loss (bottom) of differential mode for case 1.

This comparison shows that the method of Foldy Lax/MoM1D is slightly faster than Foldy-Lax/nuFDM2D for this case of via separation. However, if the two vias are much closer, Foldy-Lax/nuFDM2D is not accurate and finer uniform gridding for FDM need to be used. These are illustrated in cases 2 to 4.

Specifications for case 2 are: $\varepsilon_r = 4.4$, $R_{via} = 15\,mil$, $R_{antipad} = 30\,mil$, $pitch = 50\,mil$, $h = 50\,mil$, $t = 1.3\,mil$.

In this case, the pitch between the two centers of the vias is 50 mil so that the closest spacing between the two vias is 20 mil. Fig. 6 shows both insertion loss and return loss for differential mode.

Table 2.1. CPU Time per Frequency for The Simulation Case 1-3 On Ansoft HFSS and The Foldy-Lax Approach

Case No./vias No.	CPU Run Time per Frequency			
	Ansoft HFSS version 12	Foldy-Lax/MoM1D	Foldy-Lax/nuFDM2D	Foldy-Lax/FDM2D
1/2	19.4 s	0.18 s	0.25 s	-
2/2	21.2 s	0.30 s	0.43 s	131 s
3/2	24.7 s	0.35 s	-	246 s
4/5	100.3 s	5.36 s	-	375 s

Fig. 2.6 shows that the results of Foldy-Lax/nuFDM 2D are different from the results of all the other three methods which agree well with each other. This is due to the application of non-uniform meshing mechanism built in cylindrical coordinates. The non-uniform meshing mechanism is shown in the left figure in Fig. 2.7, in which we consider an example of an oval antipad with a differential via pair going through it.

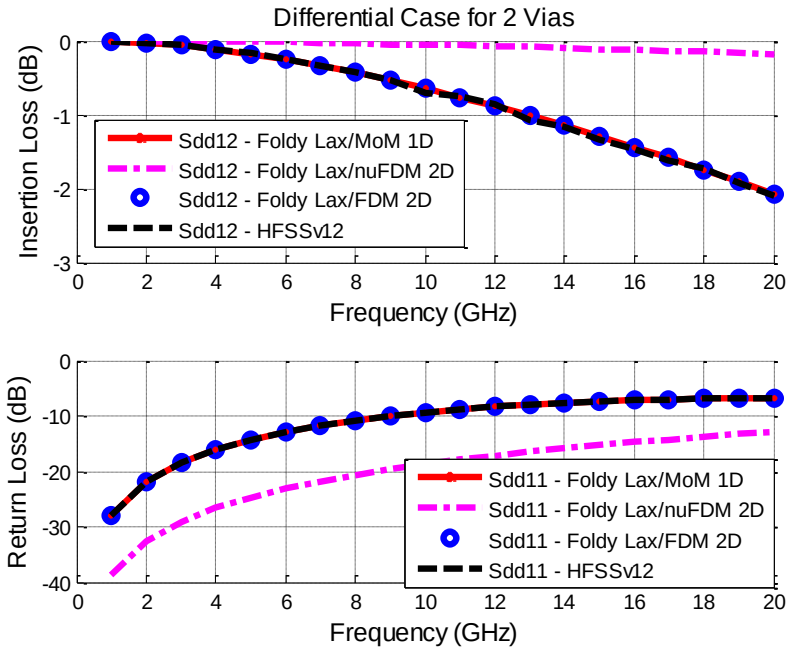

Figure 2.6. Insertion loss (top) and return loss (bottom) of differential mode for case 2

We can see that for this non-uniform grid, as the aperture size becomes large or irregular for the shared antipad, the artificial boundaries created by the meshing element edges will be impractical for describing the domain of the object [23]. This is caused by the adopted fixed cylindrical coordinate system.

In order to improve accuracy of FDM, we then apply Foldy-Lax/FDM2D method in which very fine and uniform discretization of grid and 2D interpolation of magnetic surface currents are used to obtain the incident wave. The meshing mechanism is shown in the right figure in Fig. 2.7. The uniform meshing can exactly describe the whole domain of the object, but with significant increases in CPU as shown in Table 2.1. I used 10000 uniform meshes for case 2.

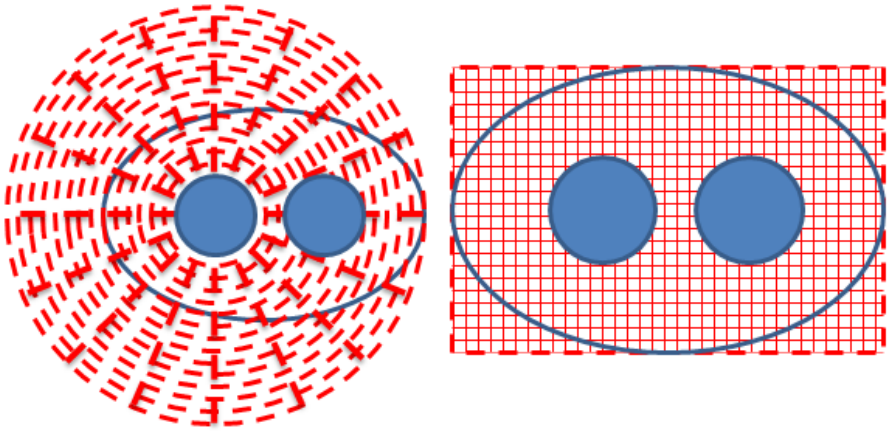

Figure 2.7. Meshing mechanism of non-uniform cylindrical coordinate system (left) and rectangular coordinate system (right) applying to an oval antipad with 2 vias sharing the same antipad.

Because the Foldy-Lax method is a mostly analytical method based on modal expansion, the number of unknowns is small and matrix inversion is used to solve the system of matrix equations. However, the number of unknowns does not depend merely on the number of vias especially when the vias are very close to each other. In such a case, the number of unknowns in the Foldy-Lax equations depends also on the modes truncation number and the truncation of azimuthal harmonics.

For example, in table 2.1, consider the case when the number of vias increases from 2 to 5, and the antipad structure has changed. For Foldy-Lax/1D MoM, the total number of unknowns increases from 270 for case 3 to 675 for case 4 in Foldy-Lax equation part and 150 for case 3 to 400 for case 4 in 1D MoM part. Because the total number of unknowns for Foldy-Lax/1D MoM

is much less than HFSS, the CPU of Foldy-Lax/1D MoM is much less than HFSS. For Foldy-Lax/FDM2D, in order to obtain accurate results, 10000 uniform meshes are used to calculate surface magnetic current and incident field for case 3. Because most CPU are used to calculate 2D surface integrals, the CPU of Foldy-Lax/FDM2D does not change significantly though the vias number increases from 2 for case 3 to 5 for case 4. This shows that Foldy-Lax/1D MoM is more convenient and efficient than Foldy-Lax/FDM2D.

For the case of large number of vias, we previously have used fast matrix solvers that can be applied to more general dense matrices such as matrices that result from Foldy-Lax equations. These include the SMCG method [9] and the multilevel UV method [25].

The CPU run time per frequency of the method of Foldy-Lax/MoM 1D is just 0.3 second. This comparison shows that the method of Foldy Lax/MoM1D is accurate and greatly improves the computational speed.

In the rest of cases, I only show comparisons of simulation results generated by this improved method of Foldy Lax/MoM1D and HFSS.

2.7.2 *B. Cases of Differential Mode and Common Mode for Very Closely Spaced Vias*

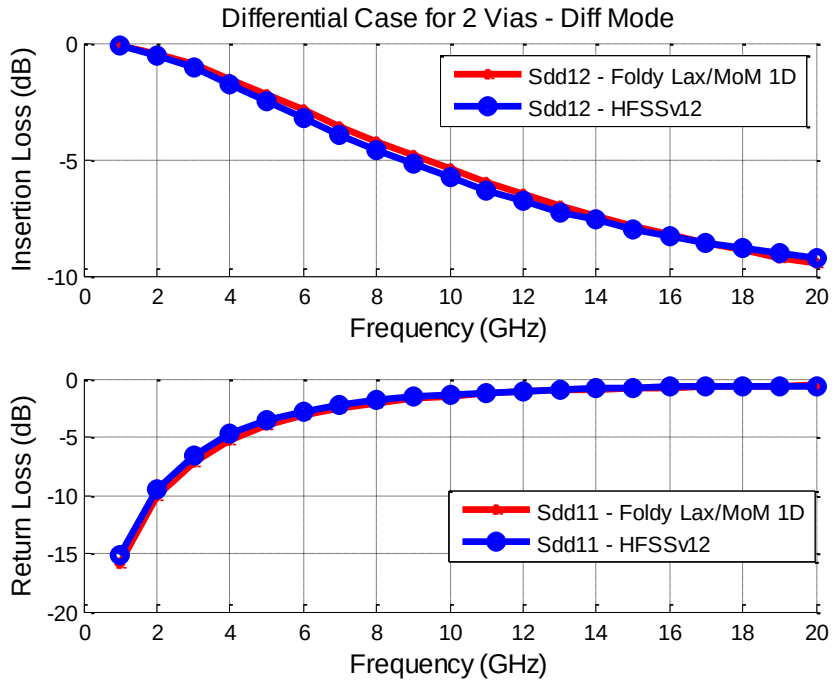

Figure 2.8. Insertion loss (top) and return loss (bottom) of differential mode for case 3.

I next compare differential mode and common mode for very closely spaced vias. The specifications for case 3 are: $\varepsilon_r = 4.4$, $R_{via} = 15\,mil$, $R_{antipad} = 30\,mil$, $pitch = 31\,mil$, $h = 50\,mil$, $t = 1.3\,mil$.

Note that the closest spacing between the 2 vias is merely 1 mil. In order to calculate the strong coupling between the two vias, we truncate the waveguide mode up to $l_{max} = 8$ and azimuthal harmonics up to $N_{max} = 7$.

Fig. 2.8 and 2.9 show the insertion loss and return loss for both differential mode and common mode. Good agreements are obtained between the simulation results and HFSS for differential mode. For common mode, the simulation results of HFSS fluctuate at high frequencies. This is due to the fact that common mode waves radiate along the waveguide. I used HFSS version 12 and we set in HFSS the cross sectional plane size of the computation region as 10000 mil by 10000 mil. If I increase the distance of the radiation boundary of HFSS, then results of HFSS improve, but with much higher CPU resources. On the other hand, the results given by Foldy-Lax/MoM1D method are stable.

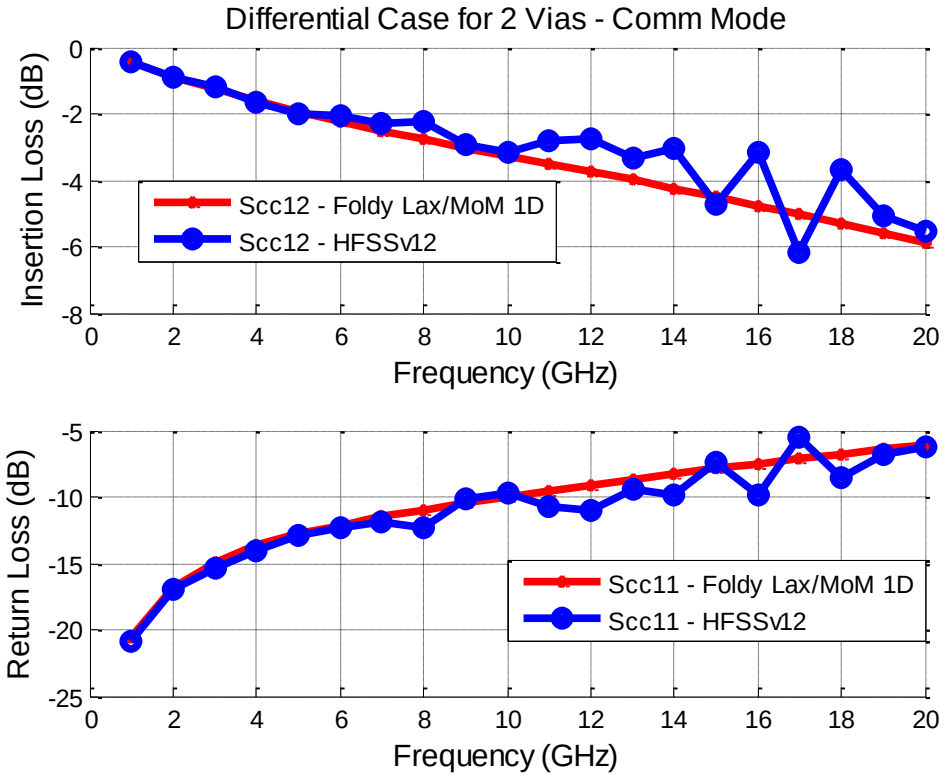

Figure 2.9. Insertion loss (top) and return loss (bottom) of common mode for case 3.

I also note that the insertion loss of the differential mode has more loss than the common mode for frequency above 3.5GHz. This is due to the port impedance mismatching (as we treat all mixed-mode S-parameters referenced to 100 Ω for differential mode and 25 Ω for common mode). It does not mean that the electrical performance for common mode is better than the differential mode.

2.7.3 *C. Case of Losses and Cross Talk of 5 Vias Sharing 1 Antipad*

Case 4 Fig. 2.10 shows a top view of symmetric structure about 5 vias sharing one antipad. The specifications are: $\varepsilon_r = 4$, $R_{via} = 7\,mil$, $R_{antipad} = 30\,mil$, $pitch1 = 15\,mil$, $pitch2 = 20\,mil$, $h = 40\,mil$, $t = 1\,mil$. The orders of the vias in figure 11 are via 1 (center), via 2 (above), via 3 (right), via 4 (below) and via 5 (left).

In this case, four side signal vias are placed around one center signal. I calculate the couplings among the five vias and study the electrical performance of each via.

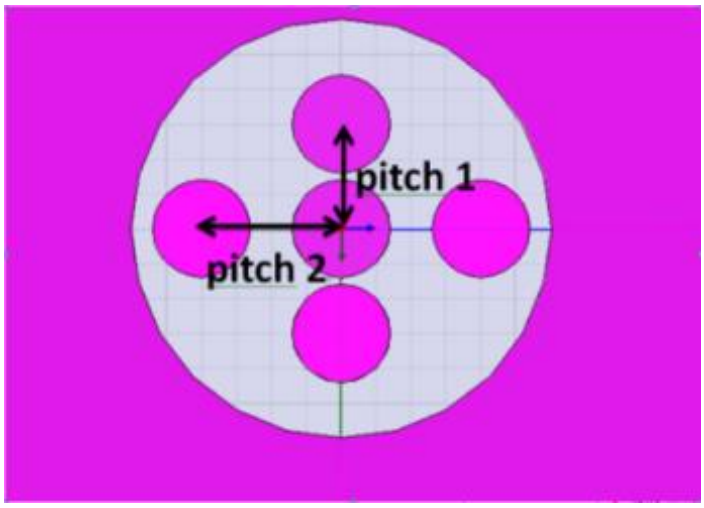

Figure 2.10. Case 4: top view of 5 vias sharing one antipad.

Fig. 2.11-2.14 show the S parameters of these 5 vias, respectively for insertion loss, return loss, near end cross talk (NEXT) and far end cross talk (FEXT), all for single-ended case. Good agreements are obtained with simulation results of HFSS.

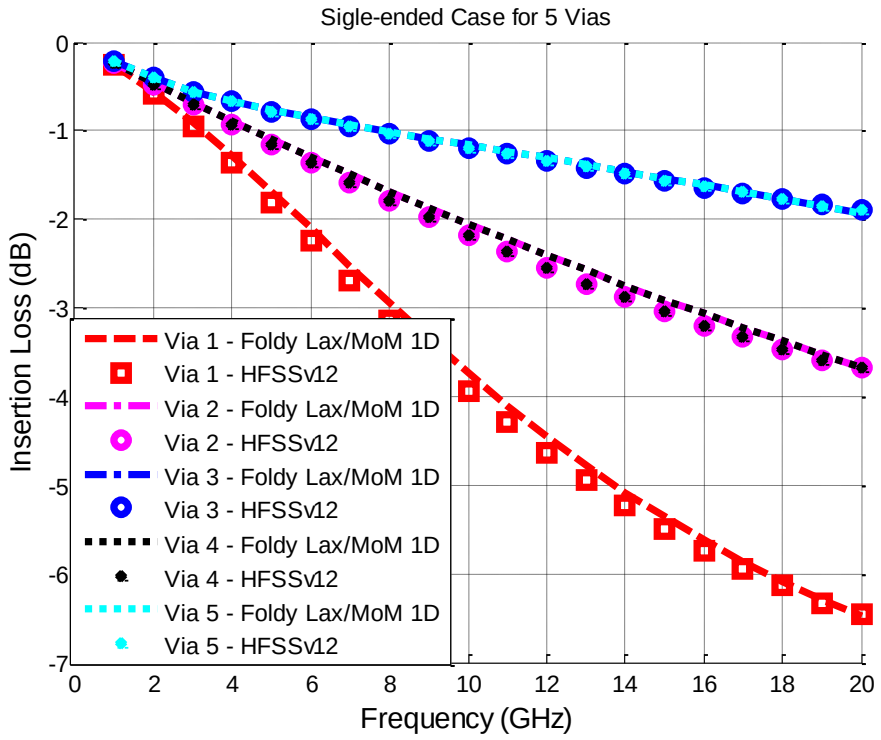

Figure 2.11. Insertion loss for 5 vias sharing one antipad for case 4.

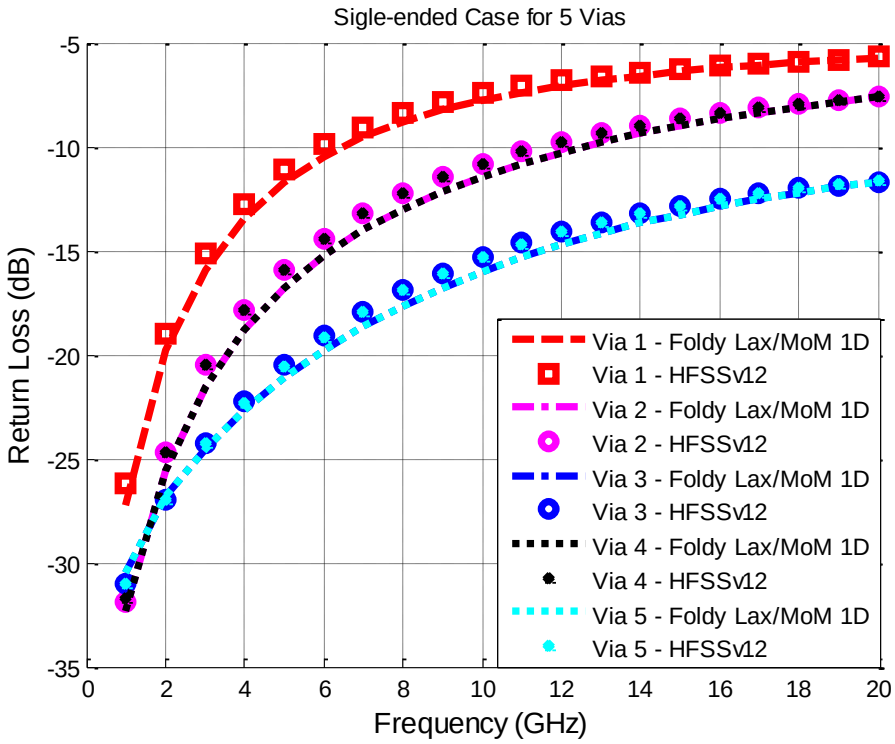

Figure 2.12. Return loss for 5 vias sharing one antipad for case 4.

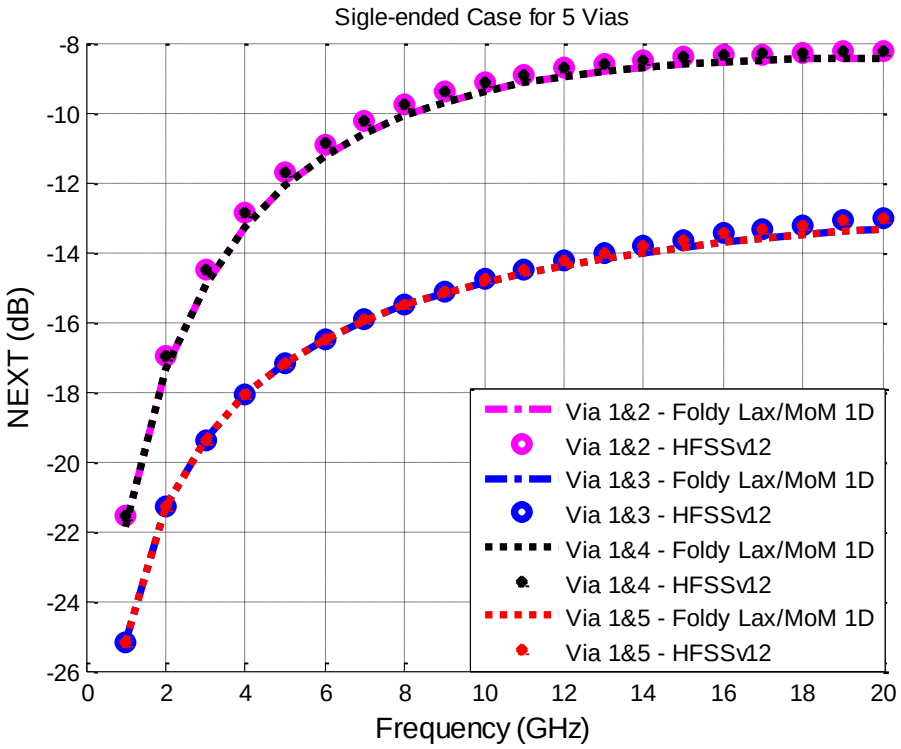

Figure 2.13. Near end cross talk among 5 vias sharing one antipad for case 4.

Fig. 2.11 and 2.12 show the insertion loss and return loss for the 5 vias. The figures show that the two horizontal side signal vias have good electrical performance for insertion loss, while the center via has the worst one. This is because the two horizontal side signal vias are the ones which are the closest to ground plane. Thus they can find current return path better than the other 3 vias. But via 1 is surrounded by four idle signal vias and is furthest from the ground plane. Thus, the electrical performance is worse than the other vias.

Fig. 2.13 and 2.14 show the cross talk among signal via 1 and other idle signal vias when via 1 is excited with unit sinusoidal voltage. Due to the coupling between via 1 and via 2 is the same as coupling between via 1 and via 4, and coupling between via 1 and via 3 is the same as coupling between via 1 and via 5. For NEXT, which is capacitance dominated, coupling between via 1 and via 2 is stronger than the coupling between via 1 and via 3 (5dB difference at 20GHz), due to the smaller impedance. But for FEXT, which is inductively dominated, there is an interesting phenomenon for frequency larger than about 7.5GHz. The coupling between via 1 and via 2 is less than the coupling between via 1 and via 3, due to the smaller current loop area or smaller input impedance. In Fig. 14, there is about 1dB difference between MoM/Foldy-Lax method and HFSS

at 20GHz for coupling between via 1 and via 3 (also via 1 and via 5). However, note that the magnitude of the cross talk is below -22dB. Thus, the 1dB difference for such small magnitudes is negligible.

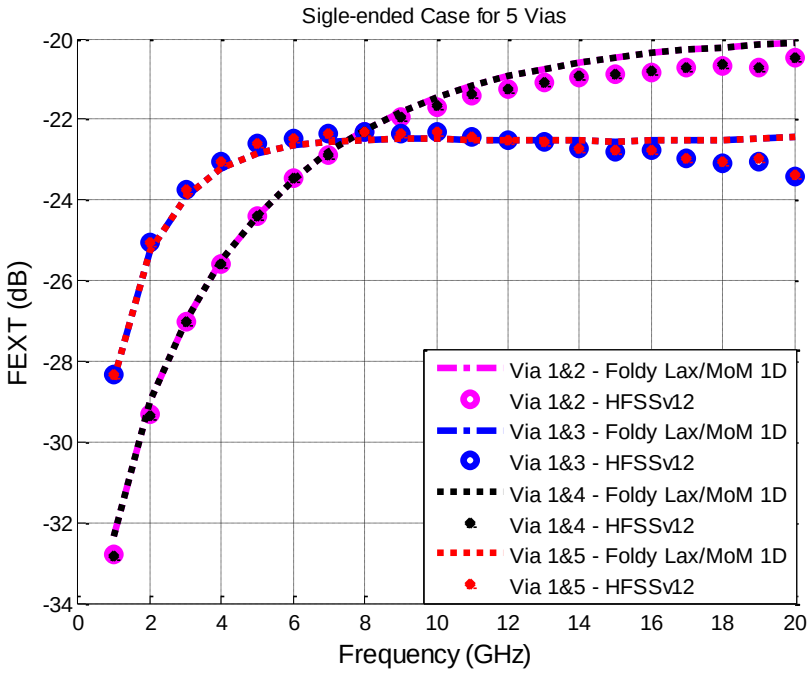

Figure 2.14. Far end cross talk among 5 vias sharing one antipad for case 4.

2.7.4 *D. Modes Effects of Near Field Interactions for Closely Spaced Vias*

Case 5 Eight close vias for each via going through one antipad. Figure 2.15 shows top view of structure about 8 close vias geometry with 6 signal vias and 2 ground vias. Each signal via goes through one antiapd. The specifications are: $\varepsilon_r = 4.4$, $R_{via} = 7\ mil$, $R_{antipad} = 15\ mil$, $tan\delta = 0.02$, $pitch = 31\ mil$, $h = 50\ mil$, $t = 1.3\ mil$. The 6 signal vias locate at $(-6,10)\ mil$, $(-6,60)\ mil$, $(12,35)\ mil$, $(12,130)\ mil$, $(35,-10)\ mil$ and $(51,73) mil$; the 2 ground vias are at $(12,85)\ mil$ and $(51,25)\ mil$.

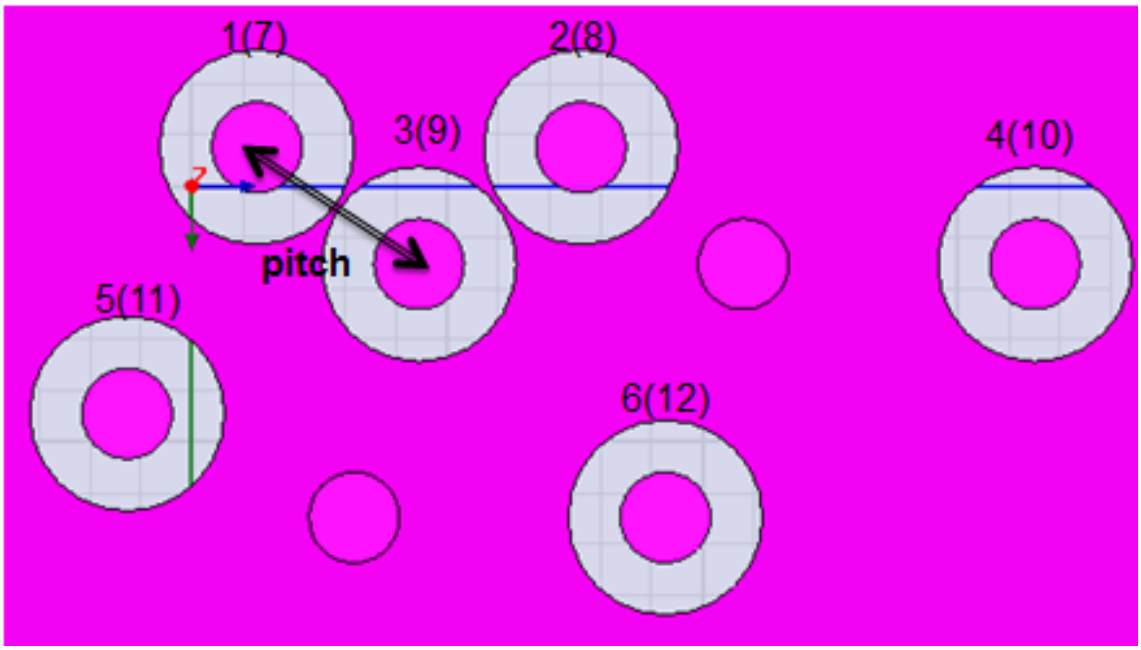

Figure 2.15. Top view of 8 close vias layout for case 5.

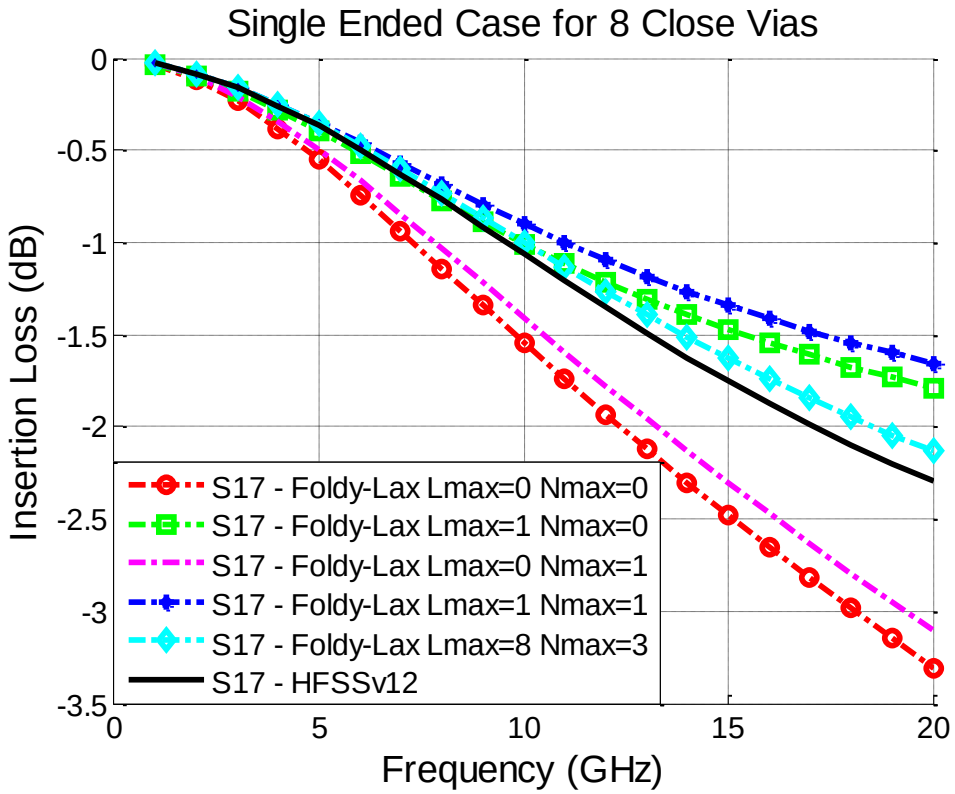

Figure 2.16. Insertion loss comparisons of via 1 for case 5.

Note that the remaining of the antipads for via 1 and via 3 is just 1 mil. From figure 2.16 and 2.17, for insertion loss and NEXT, the high order nonpropagating isotropic mode are very important to the accuracy of the model. The insertion loss is more sensitive than the NEXT is for the effect of high order nonpropagating anisotropic modes.

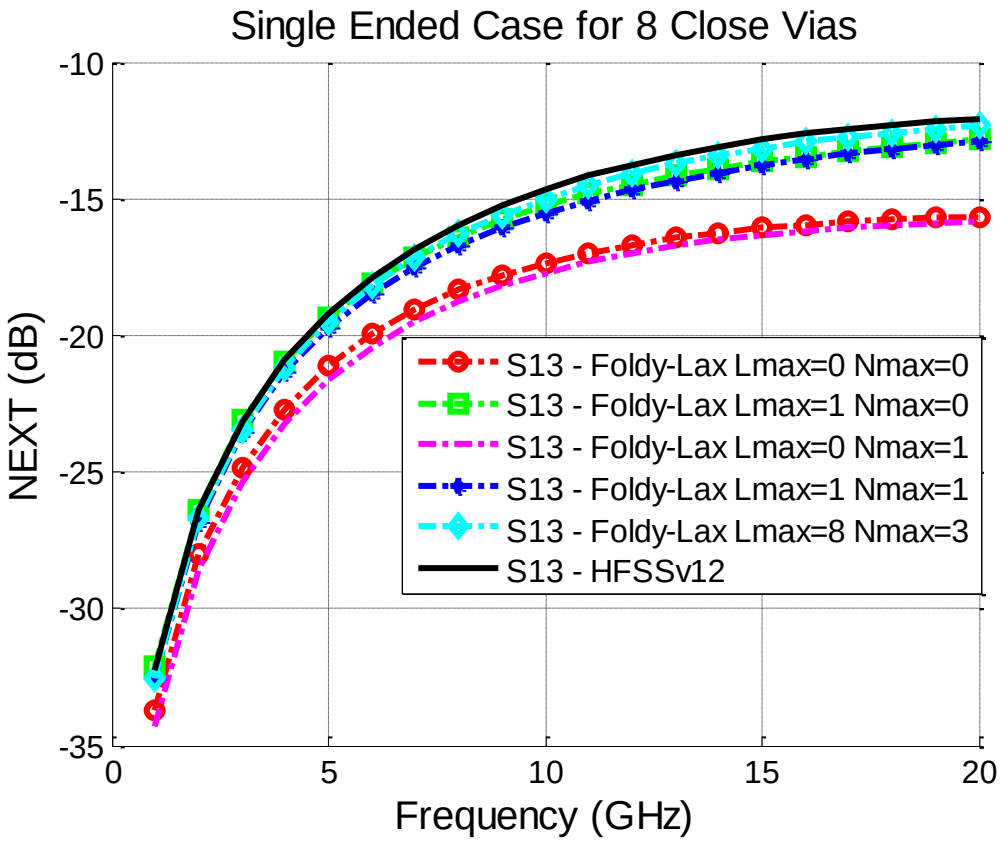

Figure 2.17. NEXT comparisons of via 1 and via 3 for case 5.

Case 6 Close Vias Sharing Same Antipad (Differential Case). Top view of structure for this case is same as shown in Figure 2.4. The specifications are: $\varepsilon_r = 4.4$, $R_{via} = 15\ mil$, $R_{antipad} = 30\ mil$, $pitch = 31\ mil$, $h = 50\ mil$, $t = 1.3\ mil$.

I only test the case with closest spacing between the 2 vias, in which the spacing is merely $1\ mil$. In order to correctly calculate the strong coupling between the 2 vias, I truncate the $L_{max} = 8$ and $N_{max} = 7$.

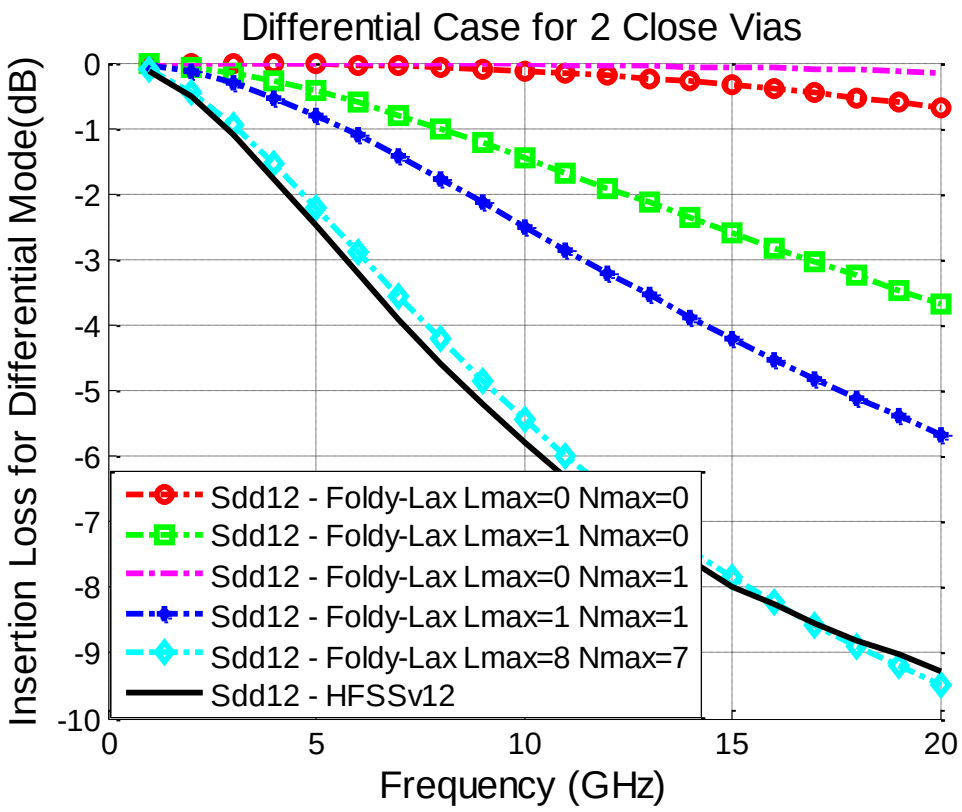

Figure 2.18. Insertion loss of differential mode for case 6.

For the 2 close vias sharing the same antipad, from the comparisons shown in figure 2.18, it is clear to observe that high order modes strongly contribute to the insertion loss for the case of multiple vias sharing same antipad. This is because firstly the two vias are so close that the nonpropagating modes scattered from one via to another via are still strong, and secondly the final actual current distribution on each via is not uniform around the vertical cylinder. These two reasons lead to the necessity of including the high order modes effects for differential signaling.

2.7.5 *E. Cases of Group T matrix for Vias Sharing an Antipad*

To study the performance of the method of Group T matrix (GT), I use cases 7, 8 and 9 to solve for the structures of different groups of vias distributed in different antipads, with each group of vias sharing the same antipad. I compare the method of Foldy-Lax/GT/MoM1D with the method of Foldy Lax/MoM 1D. The average CPU run times per frequency for the simulation of single-ended S parameters by using the method of Foldy-Lax scattering equations and HFSS for case 7-9 are shown in Table 2.2.

Table 2.2. CPU Time per Frequency For The Simulation Case 7-9 On Ansoft HFSS and The Foldy-Lax Approach

Case No./vias No.	CPU Run Time per Frequency		
	Ansoft HFSS version 12	Foldy-Lax/MoM 1D	Foldy-Lax/GT/MoM 1D
7/4	75.2 s	1.10 s	1.07 s
8/6	126.4 s	5.41 s	5.23 s
9/20	368.7 s	14.45 s	6.75 s

Case 7 Fig. 2.19 shows a top view of symmetric structure about 2 vias sharing one antipad. The specifications are: $\varepsilon_r = 4.4$, $R_{via} = 15\ mil$, $R_{antipad} = 30\ mil$, $pitch1 = 31\ mil$, $pitch2 = 80\ mil$, $h = 50\ mil$, $t = 1.3\ mil$.

For this case, 4 vias are distributed in 2 antipads. Due to the symmetric geometry, I only calculate the differential signaling parameters of the left pair. I then treat the right pair of vias as one object, and then the 4 vias are treated as 3 objects.

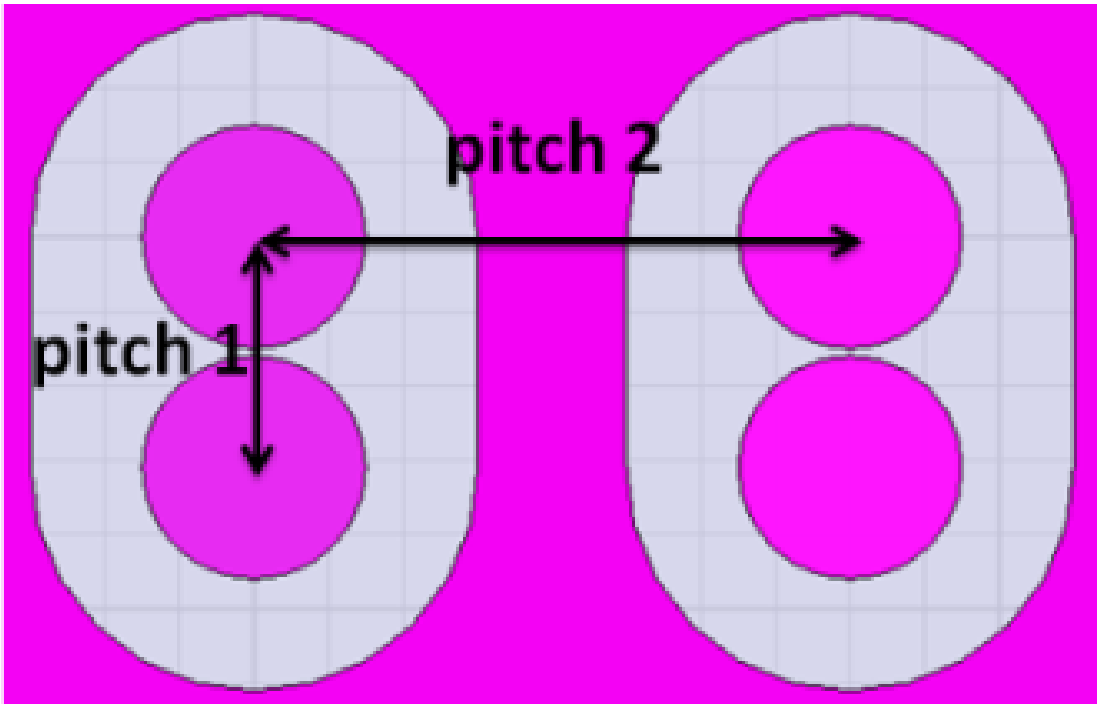

Figure 2.19. Geometry under investigation for case 7: top view of 2 groups of vias with each 2 vias sharing one antipad.

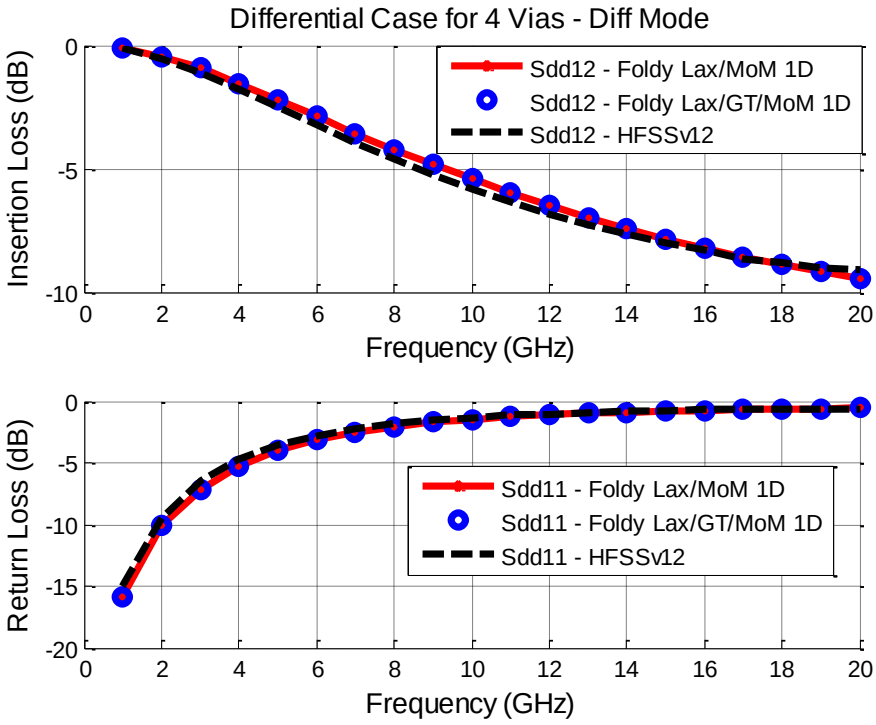

Figure 2.20. Insertion loss of differential mode for one differential via pair for case 7.

Fig. 2.20 shows both insertion loss and return loss for the differential mode case of one of the differential via pair. Good agreements are obtained with simulation results of HFSS. The result shows the electrical performance for this differential pair is good as the results are not much affected by the other pair which is only 80 mil away. This shows differential signaling is not sensitive to SSO noise and is tolerant of its multiple "local ground" moving around. For this case, the method of Foldy-Lax/GT/MoM1D is not much faster than the method of Foldy-Lax/MoM1D, because it needs one more time of Foldy Lax scattering equation to obtain the group T matrix of each group of vias. Thus the CPU is nearly the same as that of method of Foldy-Lax/MoM1D. Nevertheless, the results validate the group T matrix method.

Case 8 Fig. 2.21 shows the top view of an asymmetrical structure about 5 vias sharing one antipad and 1 via in another antipad. The specifications are: $\varepsilon_r = 4$, $R_{via} = 7\,mil$, $R_{antipad1} = 30\,mil$, $R_{antipad2} = 15\,mil$, $pitch1 = 15\,mil$, $pitch2 = 20\,mil$, $pitch3 = 50\,mil$, $h = 40\,mil$, $t = 1\,mil$. The orders of the vias in figure 2.21 are: in the right antipad, via 1 (center), via 2 (above), via 3 (right), via 4 (below) and via 5 (left); in the left antipad, via 6.

In this case, I treat all the 5 vias in one antipad as one object. Then there are 2 objects in the structure. I use Foldy-Lax scattering equation to obtain the group T matrix for the 5 vias sharing one antipad, and then apply Foldy-Lax scattering equation method again to solve for the multiple scattering between the 2 objects.

Fig. 2.22 shows both insertion loss and return loss for single-ended mode of via 1. Good agreements are obtained with simulation results of HFSS. The simulation results of case 5 and 6 show that the method of Fold-Lax/GT/MoM1D is accurate. Thus, I only show comparisons between method of Foldy-Lax/GT/MoM1D and HFSS in the next case.

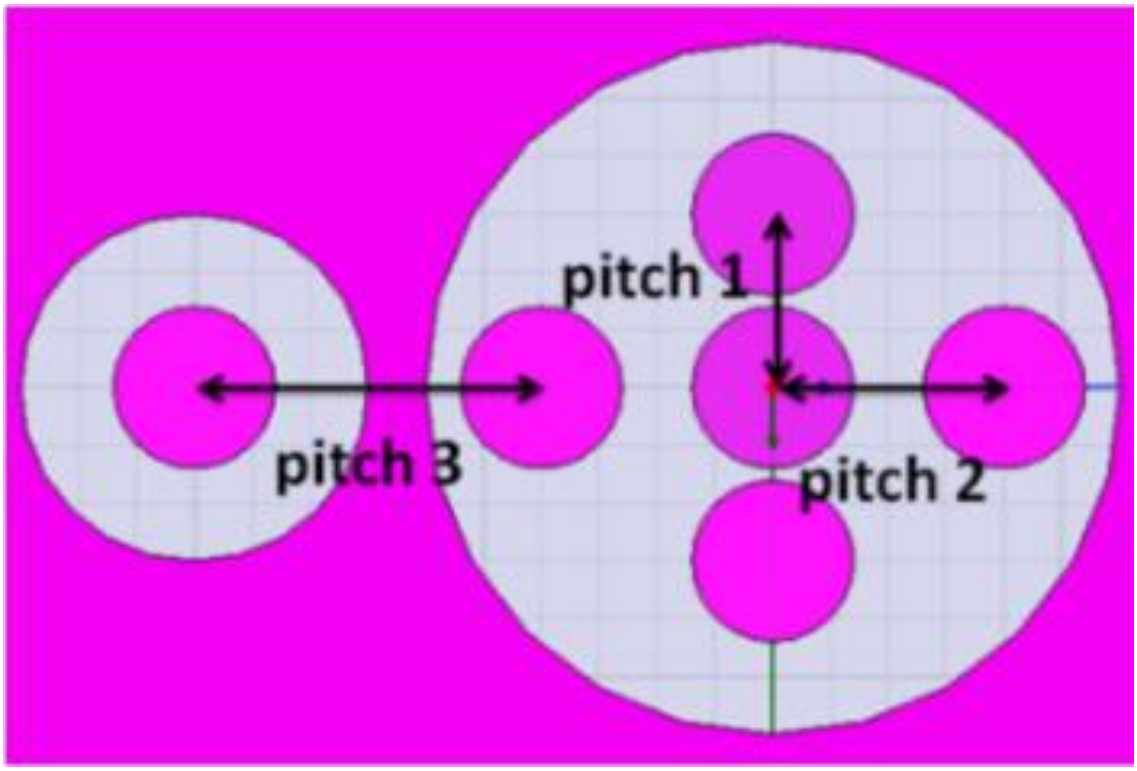

Figure 2.21. Geometry under investigation for case 8: top view of 2 groups of vias with 5 vias sharing one antipad and 1 via in another antipad.

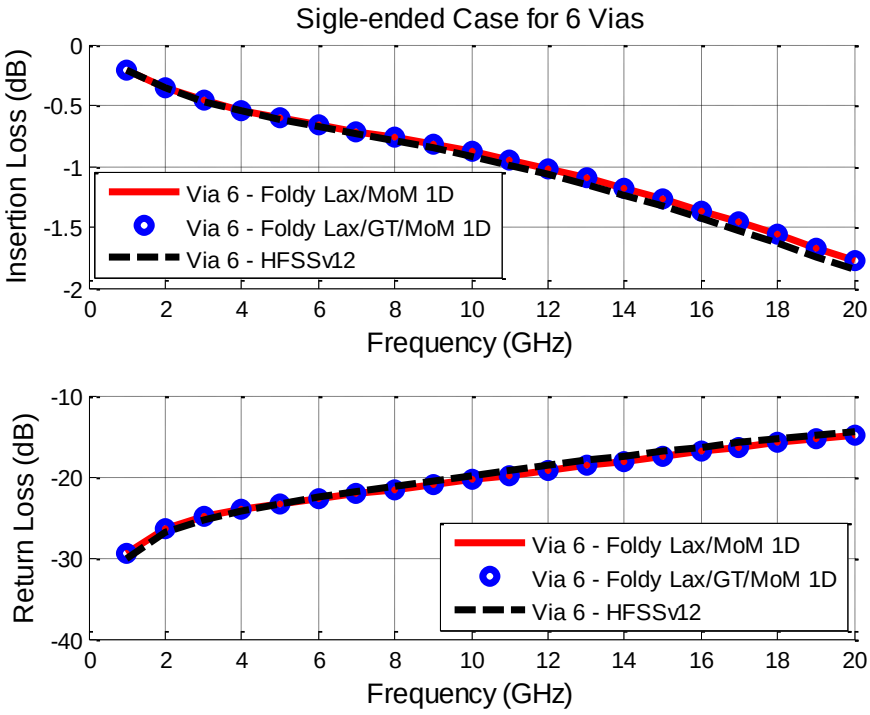

Figure 2.22. Insertion loss (top) and return loss (bottom) of single-ended mode for via 1 for case 8.

Case 9 Fig. 2.23 shows the top view of a symmetric structure about each 5 vias sharing one antipad. The specifications are: $\varepsilon_r = 4$, $R_{via} = 7\ mil$, $R_{antipad1} = 30\ mil$, $R_{antipad2} = 15\ mil$, $pitch1 = 15\ mil$, $pitch2 = 20\ mil$, $pitch3 = 80\ mil$,$h = 40\ mil$, $t = 1\ mil$. The orders of the vias in figure 13 that we are interested in are: in the left above antipad, via 1 (center), via 2 (above), via 3 (right), via 4 (below), via 5 (left), via 6 (right above antipad center), via 11 (left below antipad center) and via 16 (right below antipad center).

In this case, I treat each 5 vias in one antipad as one object. If we are only interested in the vias in one antipad, there are a total of 8 objects in the structure. Hence the problem of multiple scattering among 20 vias becomes a problem of multiple scattering among only 8 objects.

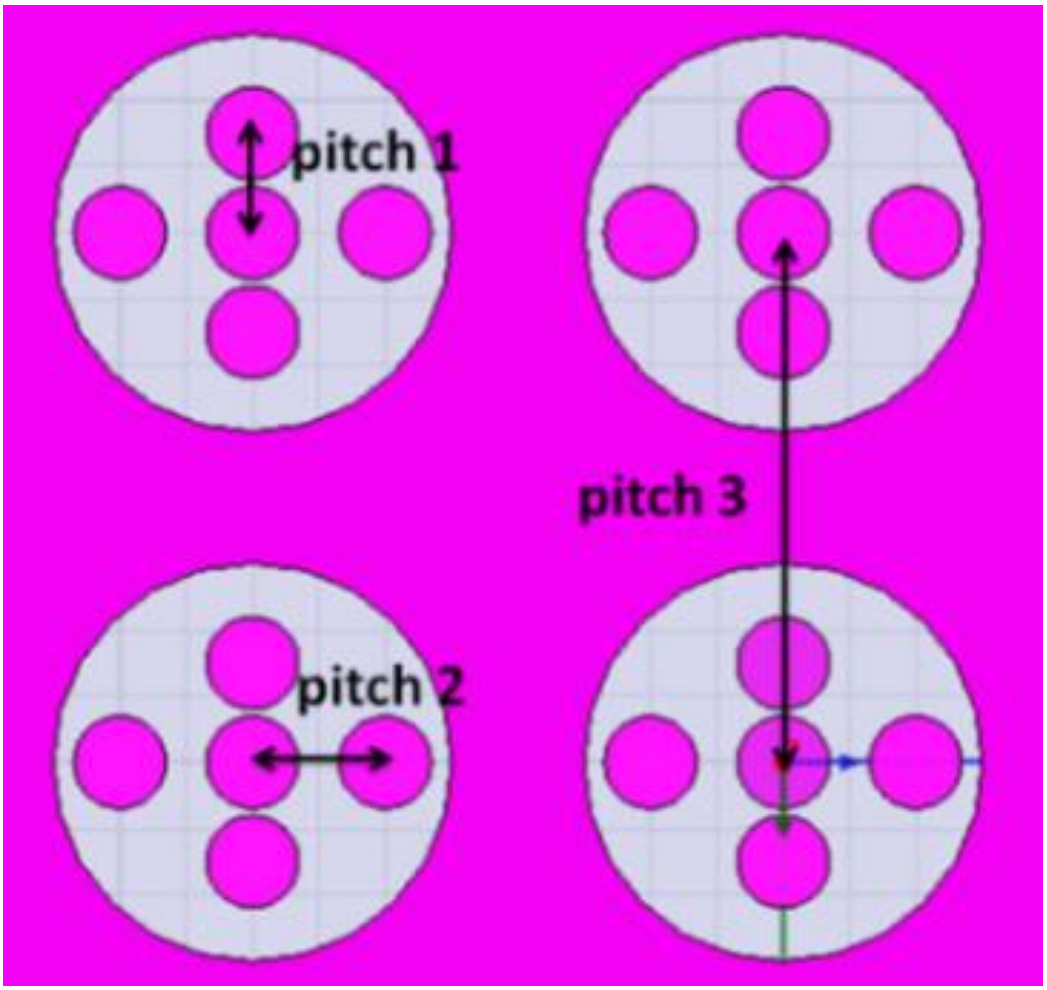

Figure 2.23. Geometry under investigation for case 9: top view of 4 groups of vias with each 5 vias sharing one antipad.

Fig. 2.24 and 2.25 respectively show the insertion loss and the return loss for single-ended mode of all the centered vias in each antipad. The figures show that, the centered via in each antipad has nearly the same insertion loss and return loss, due to the same local symmetric structure of 4 surrounding vias. The crosstalk among these 4 centered vias, whether near end cross talk or far end cross talk, are weak due to the same reason. Note that for the crosstalk between via 1 and via 11, there is about 7dB difference between the results and HFSS. The maximum difference of 7dB happens at 20GHz. However, the disagreement starts to happen below the magnitude of -38dB which is just 0.0125. Thus, the 7dB difference can be negligible. Also, in the HFSS simulation, the maximum magnitude of ΔS calculated is 0.0143 after 6 iterations. The accuracy of the simulation results of HFSS are comparable.

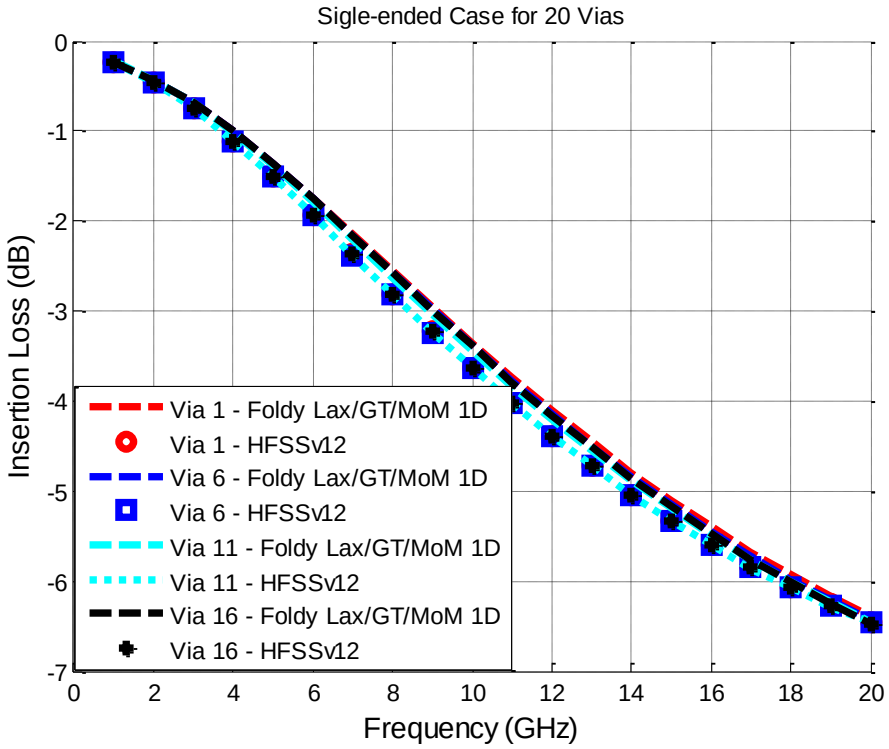

Figure 2.24. Insertion loss of single-ended mode for four center vias for case 9.

Fig. 2.26 and 2.27 show respectively the near end and far end crosstalk among vias sharing one antipad. The figures show that all the near end crosstalk among the 5 vias sharing the same antipad preserve the same performances as in Fig. 2.13. However, the far end crosstalk between via 1 and via 5 is impacted due to the effects from other antipads.

The use of Group T matrix is not an approximation. It makes use of the fact that one object can be composed of many or several other objects. Thus the T matrix of a group can be derived from the T matrices of objects in the group. For the group of vias in the source antipad, the vias cannot be treated as a single object because the excitation arises from sources among the vias.

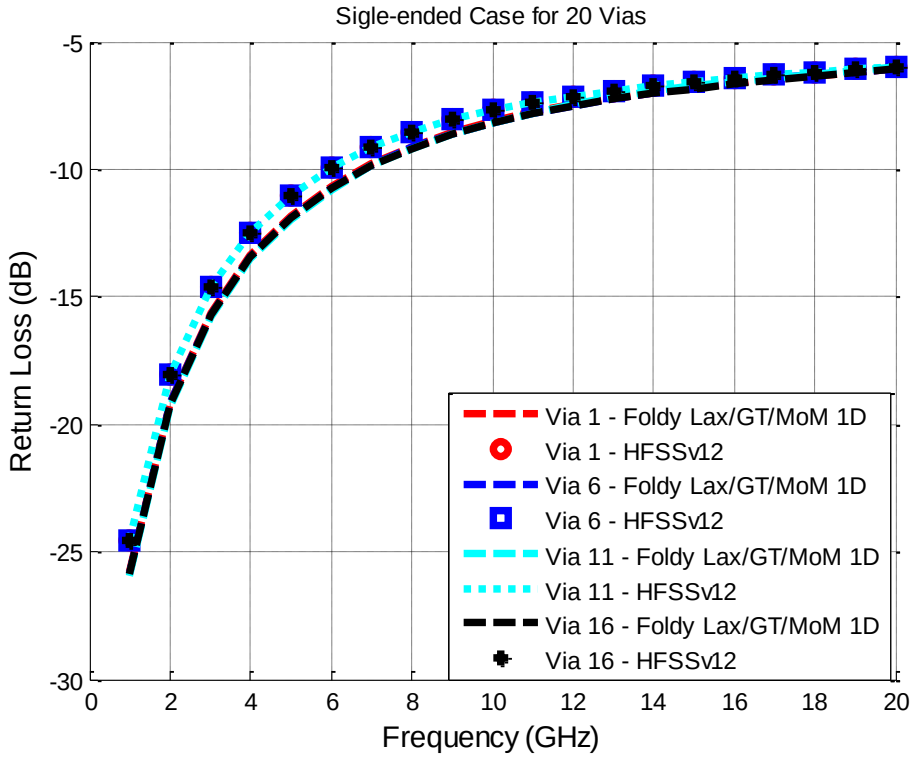

Figure 2.25. Return loss of single-ended mode for four center vias for case 9.

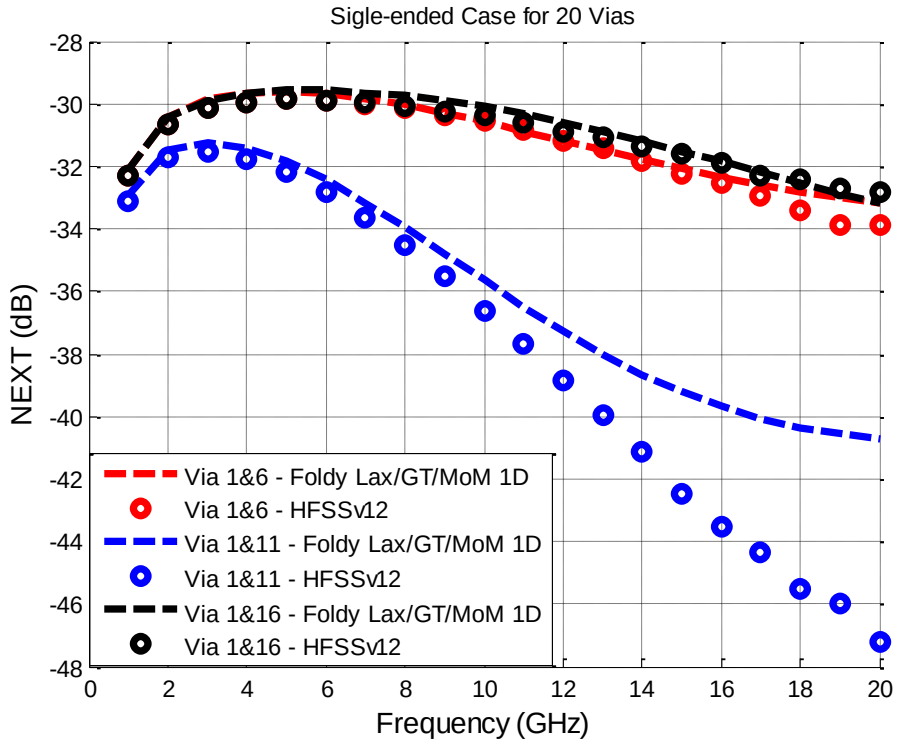

Figure 2.26. Near end cross talk of single-ended mode for four center vias for case 9.

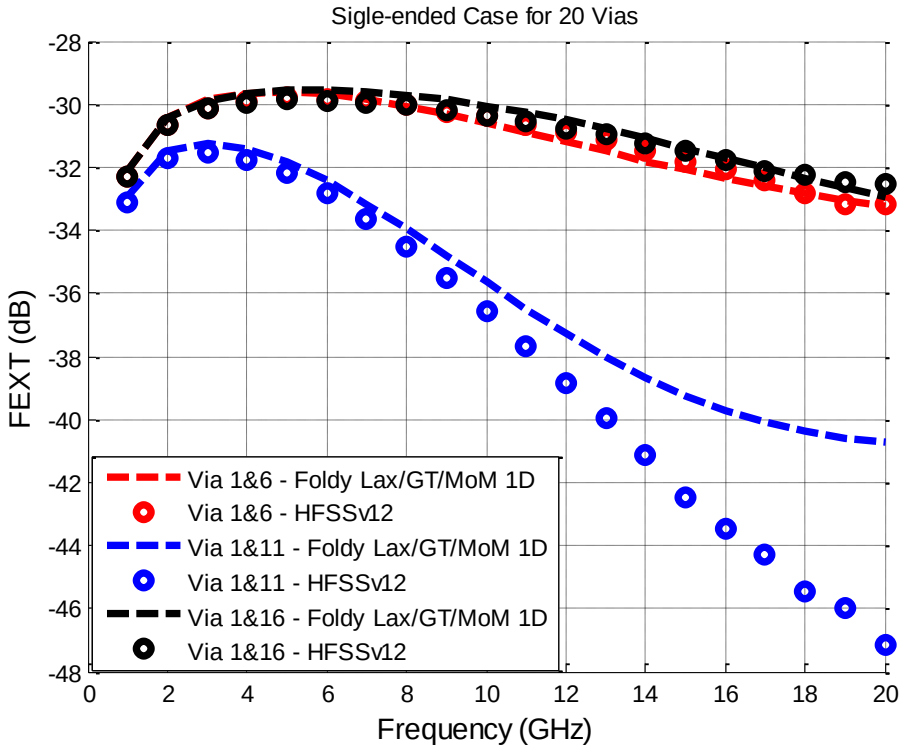

Figure 2.27. Far end cross talk of single-ended mode for four center vias for case 9.

2.8 CONCLUSIONS

For the problem of vias sharing one antipad in planar waveguide, the finite difference method, which was previously used to calculate magnetic surface current with non-uniform grid, are restricted in accuracy and efficiency. By converting the surface integration of magnetic surface currents into 1-dimensional line integration of surface charges, and applying group T matrix to speed up the calculation of multiple scattering among different groups of vias, one can accurately make simulations of complicated designs with multiple vias sharing antipad. The two improvements in this paper enable early design, optimization and practical modeling of PCBs or packaged systems.

Chapter 3. MODELING VIAS WITH ARBITRARILY SHAPED POWER/GROUND PLANES

3.1 SUMMARY

In this chapter, I model multiple vias with irregular antipad in arbitrarily shaped 3D IC and packaging system based on generalized Foldy-Lax equations method, boundary integral equation method and generalized T matrix. I first obtain the impedance matrix for finite cavity, which includes the reflection features of the cavity boundaries. Then the scattered field from a single via and a generalized T matrix including the wall effects are derived. The Foldy-Lax multiple scattering equations are generalized to include the wall effects by using impedance matrix and the generalized T matrix. To obtain the incident field for the case of vias in the arbitrarily shaped antipad, I calculate the exciting and scattering field coefficients based on the transformation which converts surface integration of magnetic surface currents in antipad into 1D line integration of surface charges on the vias and on the ground plane. The coupling among vertical vias are solved by applying Foldy-Lax multiple scattering equations. The scattering matrix of coupling among vias is calculated to make corresponding signal/power integrity analysis. Numerical results for the method are in good agreement with a commercial full wave numerical tool up to 50 GHz.

3.2 INTRODUCTION

In chapter 2, I discussed the modeling method for multiple vias scattering in infinite large waveguide. In this chapter, I model multiple vias with irregular antipad in arbitrarily shaped 3D IC and packaging system based on generalized Foldy-Lax equations method, boundary integral equation method and generalized T matrix.

The three-dimensional integrated circuit (3D IC) in electronics is a chip in which two or more layers of active electronic components are integrated both vertically and horizontally into a single circuit. With the increasing of the clock rate, complex interconnects system result in that timings now are interconnects driven. Also, with the increase of high density 3D integrations, via size is decreasing while the number of vias is increasing, which leads to strong interactions among vias

for high speed circuit usage. Higher order modes effects and wave harmonics effects have to be considered for accurate modeling and practical design.

The results of this present approach are shown to be in good agreement with HFSS even for the case of closely spaced vias of as small as 1 mil in spacing between adjacent vias. In the Appendix A.2, I use a simplified derivation, based on operator formalism of the T matrix in the presence of cavity wall, i.e. the τ matrix. I then derive the Foldy Lax multiple scattering equations using the τ matrices of the vias.

The main contributions of this chapter are as follows.

1) Unlike reference [30] which uses the single via T in the absence of the cavity wall, the T-matrix of the via in the presence of the cavity wall, τ, is derived in this thesis. Then the generalized Foldy-Lax equations are derived based on this τ matrix.

2) The combination of generalized Foldy-Lax equations method and boundary integral equations method are used to solve eccentric vias structures and multiple vias sharing same antipad structures in arbitrarily shaped cavity. The proposed method is fast and can be used for broadband simulations.

3) The TM modes excitations for irregular shaped antipad in the presence of arbitrary cavity shapes are derived. Convergence of results are also shown for closely spaced vias.

3.3 MoM Impedance Matrix $\overline{\overline{\boldsymbol{Z}}}$ for Finite Cavity Problem

In this section, I briefly describe the boundary integral equation method for the problem of finite cavity of irregular shape. The walls of the cavity will be treated as perfect magnetic conductors and will cause reflections. In the multiple scattering using Foldy-Lax equations, we treat the TM modes with

$$k_{zl} = \frac{l\pi}{d}; k_{\rho l}^2 = k^2 - k_{zl}^2 \tag{3.1}$$

where $l = 0,1,2\ldots..,$ d is the separation between the two plates, and k is the wavenumber. Consider an irregular shape cavity as shown in figure 3.1. Different from [30], since $kd \ll 1$, where the modes with $l \geq 1$ are evanescent and will not propagate to the wall and have little reflection from the boundary walls. To treat the finite boundary effect, we consider only the $l = 0$ mode so that $k_{zl} = 0$. Higher order waveguide modes $l \geq 1$ are evanescent and decay within short distance of the order of the thickness of the waveguide. Unless the vias are placed within such

short distance from the cavity walls, the reflections of these waveguides form the cavity walls are negligible. I assume that distances of vias from the walls are more than 50 mils which are the thicknesses of the waveguide used in the simulations.

Extensions of the formalism to $l \geq 1$ do not present conceptual difficulty and can be done if needed. The modes with $l \geq 1$ follow the same treatment as that of infinite ground plane. They contribute to the near field interactions among the vias and between the antipad source and the vias. Such effects are included in this chatper. On the other hand, the $l = 0$ mode solutions are modified by including the wall effects. For TM_0 mode, the electric field only has the E_z component to represent the interactions. The "z" subscript will be suppressed. For the $l = 0$ mode, $k_{zl} = 0$ and $k_{\rho l} = k$. Since there is no variation withz, we use only the 2-dimensional ∇_t operator and the two dimensional position vector $\bar{\rho}$. I next define the MoM impedance matrix $\bar{\bar{Z}}$ and the inverse $\bar{\bar{Z}}^{-1}$.

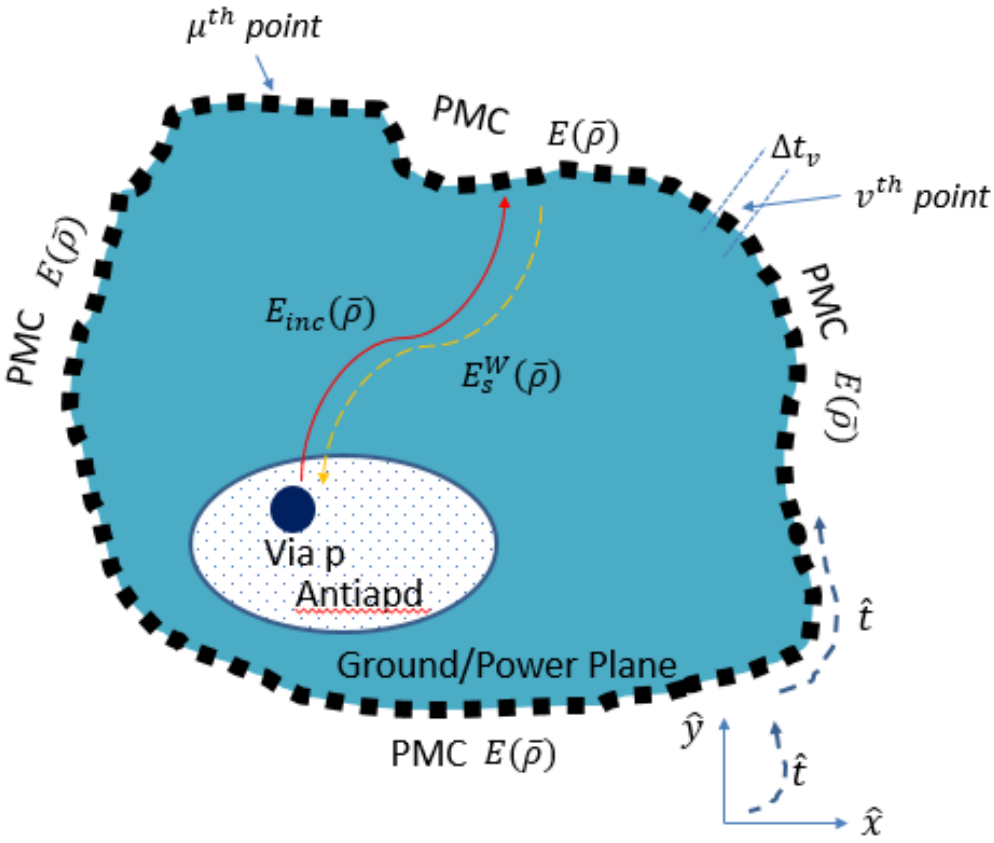

Figure 3.1. Boundary integral equation method for the problem of finite cavity of irregular shape. The electric field in the z direction is governed by the 2D Helmholtz equation. Neumann boundary conditions are used for the cavity wall.

Consider an incident electric field $E_{inc}(\bar{\rho})$ incident on the boundary wall. I use perfect magnetic wall boundary condition, so that the normal derivative of the electric field is equal to zero. Let $E(\bar{\rho})$ be the electric field on the boundary. I use the t coordinate to describe the line contour of the boundary. I assume the boundary is that of magnetic wall. In the MoM formulation, 1-dimensional discretization of the boundary wall is used. Let there be N_t segments. I use pulse basis functions and point matching for the t_v coordinates with $v = 1,2\ldots N_t$ and the length of segment v is Δt_v.

I use the 2D scalar Helmholtz equation for the z component of the electric field. The electric field satisfies Neumann boundary conditions on the cavity wall. By using boundary integral equations method and MoM, I obtain the impedance matrix. I use 1D discretization, pulse basis functions and point matching. The MoM 1D discretization formulated matrix equations are given below.

$$\sum_{v=1}^{N_t} Z_{\mu v}\, E\big(\bar{\rho}(t_v)\big) = E_{inc}\left(\bar{\rho}\big(t_\mu\big)\right), \mu = 1,2\ldots N_t \tag{3.2}$$

where $\bar{\rho}\big(t_\mu\big)$ is the position of the μ^{th} point on the boundary. The impedance matrix $\bar{\bar{Z}}$ is of dimension $N_t \times N_t$. The impedance matrix elements are

$$Z_{\mu v} = \begin{cases} [\hat{n}' \cdot \nabla_t{}' g(\bar{\rho}, \bar{\rho}')\Delta t_v]_{\bar{\rho}=\bar{\rho}(t_\mu), \bar{\rho}'=\bar{\rho}(t_v)} & \mu \neq v \\ \frac{1}{2} & \mu = v \end{cases} \tag{3.3}$$

for $\mu, v = 1,2\ldots N_t$, and $g(\bar{\rho}) = \frac{1}{4j} H_0^{(2)}(k\rho)$. In matrix notations,

$$\bar{E}^M = \bar{\bar{Z}}^{-1} \bar{E}^M_{inc} \tag{3.4}$$

where $\bar{E}^M_{inc}$ and $\bar{E}^M$ are $N_t \times 1$ column vectors and $\bar{\bar{Z}}^{-1}$ are the inverse of the impedance matrix. The "M" supercript denotes MoM discretization so that the dimension of the column is N_t. It is used to distinguish harmonic discretization later on. Thus, with $[\bar{E}^M_{inc}]_\mu = E_{inc}\left(\bar{\rho}\big(t_\mu\big)\right)$, $[\bar{E}^M]_\mu = E\left(\bar{\rho}\big(t_\mu\big)\right)$.

Using the discretized surface field, the scattered field from the wall $E_s^W(\bar{\rho})$ is

$$E_s^W(\bar{\rho}) = -\sum_{v=1}^{N_t} [\hat{n}' \cdot \nabla_t{}' g(\bar{\rho} - \bar{\rho}')\Delta t_v]_{\bar{\rho}'=\bar{\rho}(t_v)} \big(\bar{\bar{Z}}^{-1} \bar{E}^M_{inc}\big)_v \tag{3.5}$$

3.4 SCATTERED FIELD FROM A SINGLE VIA AND T-MATRIX, INCLUDING WALL REFLECTIONS

In this section, I reformulate the Foldy-Lax equations for solving the multiple scattering among cylinders with the presence of the cavity walls. As stated in section 3.3, only the longitudinal components of exciting and scattering electric field $E^{e}_{z(l,n)}$ and $E^{s}_{z(l,n)}$ are considered.

The difference of scattering from a via for finite cavity is the additional reflection from the wall. In this section, we derive the reflection and also derive the T matrix of the via including this reflection. The derivation is parallel to that of the circular ground plane case in [35] but using the MoM inverse impedance matrix to include the arbitrary shape boundary effect.

Consider the q^{th} via centered at $\bar{\rho}_q$, and consider outgoing m^{th} wave harmonic from via q. In general, we include harmonics of $m = 0, \pm 1, \ldots\ldots \pm M$. Harmonics of $m \neq 0$ give rise to anisotropic effects. The outgoing cylindrical wave of the m^{th} harmonic of the electric field is

$$E_m(\bar{\rho} - \bar{\rho}_q) = kH_m^{(2)}\left(k\left|\bar{\rho} - \bar{\rho}_q\right|\right)e^{-jm\phi_{\bar{\rho}\bar{\rho}_q}} \tag{3.6}$$

Let $\bar{E}^{qM}$ be of dimension $N_t \times 1$, so that

$$\left[\bar{E}_m^{qM}\right]_\mu = E_m\left(\bar{\rho}(t_\mu) - \bar{\rho}_q\right), \mu = 1,2 \ldots N_t \tag{3.7}$$

The electric field is incident on the wall, and the scattered field from the wall is, using the inverse MoM impedance matrix

$$E_s^{Wqm}(\bar{\rho}) = -\sum_{v=1}^{N_t}[\hat{n}' \cdot \nabla_t{}' g(\bar{\rho} - \bar{\rho}')\Delta t_v]_{\bar{\rho}'=\bar{\rho}(t_v)}\left(\bar{\bar{Z}}^{-1}\bar{E}_m^{qM}\right)_v \tag{3.8}$$

Next I use vector addition theorem to expand $E_s(\bar{\rho})$ about via q. In the addition theorem as I followed notations in reference [36], with wave functions $\bar{E}(\bar{\rho})$ where the column vector $\bar{\psi}$ stands for harmonics $m = 0, \pm 1, \ldots\ldots \pm M$. It is of dimension $2M + 1$

$$[\bar{E}(\bar{\rho})]_m = E_m(\bar{\rho}); m = 0, \pm 1, \ldots\ldots \pm M \tag{3.9}$$

Then the field on via p can be expressed as

$$\bar{E}^t\left(\bar{\rho} - \bar{\rho}_p\right) = Rg\bar{E}^t\left(\bar{\rho} - \bar{\rho}_q\right) \cdot \bar{\bar{\alpha}}_{qp}^{+} \tag{3.10}$$

where superscript t stands for transpose giving a row vector, Rg stands for regular, with Bessel functions being used.

In the above equation, $\bar{\bar{\alpha}}_{qp}^{+}$ matrix is the translation matrix for cylindrical waves and is of dimension $(2M + 1) \times (2M + 1)$

$$\left[\bar{\bar{\alpha}}_{qp}^{+}\right]_{nm} = H_{n-m}^{(2)}\left(k\left|\overline{\rho_p} - \overline{\rho_q}\right|\right)e^{j(n-m)\emptyset_{\overline{\rho_p\rho_q}}} \tag{3.11}$$

I use "+" to distinguish from

$$\left[\bar{\bar{\alpha}}_{qp}^{-}\right]_{nm} = H_{n-m}^{(2)}\left(k\left|\overline{\rho_p} - \overline{\rho_q}\right|\right)e^{j(-n+m)\emptyset_{\overline{\rho_p\rho_q}}} \tag{3.12}$$

with the difference of sign in the exponent between $\left[\bar{\bar{\alpha}}_{qp}^{+}\right]_{nm}$ and $\left[\bar{\bar{\alpha}}_{qp}^{-}\right]_{nm}$.

Then

$$g(\bar{\rho} - \bar{\rho}') = \frac{1}{4jk}\sum_{n'} RgE_{n'}\left(\bar{\rho} - \bar{\rho}_q\right)\left[\bar{\bar{\alpha}}_{q\bar{\rho}'}^{+}\right]_{n'0} \tag{3.13}$$

Then the wave from via q to via q through wall reflection for the m^{th} harmonic is $E_s^{Wqqm}(\bar{\rho})$ and

$$E_s^{Wqqm}(\bar{\rho}) = -\sum_{v=1}^{N_t}\frac{1}{4jk}\sum_{n'} RgE_{n'}\left(\bar{\rho} - \bar{\rho}_q\right)\left[\hat{n}' \cdot \nabla_t{}'\left[\bar{\bar{\alpha}}_{q\bar{\rho}'}^{+}\right]_{n'0}\Delta t_v\right]_{\bar{\rho}'=\bar{\rho}(t_v)}\left(\bar{\bar{Z}}^{-1}\bar{E}_m^q\right)_v \tag{3.14}$$

I define the $\bar{\bar{\gamma}}^{(qW)}$ matrix which has dimension $(2M+1) \times N_t$ where W stands for wall. The elements of $\bar{\bar{\gamma}}^{(qW)}$ are

$$\left[\bar{\bar{\gamma}}^{(qW)}\right]_{nv} = -\frac{1}{4jk}\left[\hat{n}' \cdot \nabla_t{}'\left[\bar{\bar{\alpha}}_{q\bar{\rho}'}^{+}\right]_{n0}\Delta t_v\right]_{\bar{\rho}'=\bar{\rho}(t_v)} \tag{3.15}$$

The $\bar{\bar{\gamma}}^{(qW)}$ matrix is of mixed dimension as it represents discretized MoM points coupled to wave harmonics, $m = 0, \pm 1, \ldots\ldots \pm M$. Then

$$E_s^{Wqqm}(\bar{\rho}) = Rg\bar{E}^t\left(\bar{\rho} - \bar{\rho}_q\right)\bar{\bar{\gamma}}^{(qW)}\bar{\bar{Z}}^{-1}\bar{E}_m^{qM} \tag{3.16}$$

where $Rg\bar{E}^t\left(\bar{\rho} - \bar{\rho}_q\right)$ is of dimension $1 \times (2M+1)$, and $\bar{E}_m^{qM}$ of dimension $N_t \times 1$.

To further put above in matrix form to account for the m index of harmonics, we let $\bar{E}_s^{Wqq}(\bar{\rho})$ be of dimension of $(2M+1) \times 1$, so that

$$\left[\bar{E}_s^{Wqq}(\bar{\rho})\right]_m = E_s^{Wqqm}(\bar{\rho}) \tag{3.17}$$

Next, I define a mixed dimension electric field $\bar{\bar{Q}}^{(Wq)}$ with dimension $N_t \times (2M+1)$. It represents coupling from harmonic to discretized point on the boundary. The elements of $\bar{\bar{Q}}^{(Wq)}$ are

$$\left[\bar{\bar{Q}}^{(Wq)}\right]_{\mu m} = \left[\bar{E}_m^{qM}\right]_\mu = kH_m^{(2)}\left(k\left|\bar{\rho}(t_\mu) - \bar{\rho}_q\right|\right)e^{-jm\phi_{\bar{\rho}(t_\mu)\bar{\rho}q}} \tag{3.18}$$

Then the scattered field from via q to via q through wall reflection, is, in matrix form,

$$\left[\bar{E}_s^{Wqq}(\bar{\rho})\right]^t = Rg\bar{E}^t\left(\bar{\rho} - \bar{\rho}_q\right)\bar{\bar{\gamma}}^{(qW)}\bar{\bar{Z}}^{-1}\bar{\bar{Q}}^{(Wq)} \tag{3.19}$$

The complete scattered field from via q, $\bar{E}_s^{qq}(\bar{\rho})$, of dimension $(2M+1)\times 1$ needs to include $\bar{E}_s^{Wqq}(\bar{\rho})$ as well as $\bar{E}(\bar{\rho}-\bar{\rho}_q)$

$$\bar{E}_s^{qq} = \bar{E}(\bar{\rho}-\bar{\rho}_q) + \bar{E}_s^{Wqq}(\bar{\rho}) \tag{3.20}$$

Next I determine the T-matrix of via q in the presence of the wall.

Let the exciting field on via q be $E_{ex}^q(\bar{\rho})$ and the scattered field be $E_s^{qq}(\bar{\rho})$

$$E_{ex}^q = Rg\bar{E}^t(\bar{\rho}-\bar{\rho}_q)\bar{w}^q \tag{3.21}$$

and

$$E_s^{qq} = \left[\bar{E}_s^{qq}(\bar{\rho})\right]^t \bar{A}^q \tag{3.22}$$

where $\bar{w}^q$ and $\bar{A}^q$, are of dimensions $(2M+1)\times 1$, and contain exciting field coefficients, $[\bar{w}^q]_m = w_m^q$ and scattered field coefficients $[\bar{A}^q]_m = A_m^q$, $m = 0, \pm 1, \ldots\ldots \pm M$.

Then the total field is,

$$E_{ex}^q(\bar{\rho}) + \bar{E}_s^{qq}(\bar{\rho}) = Rg\bar{E}^t(\bar{\rho}-\bar{\rho}_q)\bar{w}^q + \left[\bar{E}^t(\bar{\rho}-\bar{\rho}_q) + Rg\bar{E}^t(\bar{\rho}-\bar{\rho}_q)\bar{\bar{\gamma}}^{(qW)}\bar{\bar{Z}}^{-1}\bar{\bar{Q}}^{(Wq)}\right]\bar{A}^q \tag{3.23}$$

Let the via be circular and with radius a. The electric field is zero at $|\bar{\rho}-\bar{\rho}_q| = a$.

Thus

$$w_m^q J_m(ka) + A_m^q H_m^{(2)}(ka) + J_m(ka)\left[\bar{\bar{\gamma}}^{(qW)}\bar{\bar{Z}}^{-1}\bar{\bar{Q}}^{(Wq)}\bar{A}^q\right]_m = 0 \tag{3.24}$$

The form of the above equation is analogous to equation (9) of the case of circular cavity of [34].

The T-matrix coefficient is

$$T_m = -\frac{J_m(ka)}{H_m^{(2)}(ka)}; m = 0, \pm 1, \ldots\ldots, \pm M \tag{3.25}$$

The T matrix $\bar{\bar{T}}^q$, is a $(2M+1)\times(2M+1)$ diagonal matrix, with diagonal element equal T_m. Then

$$\bar{A}^q - \bar{\bar{T}}^q\bar{\bar{\gamma}}^{(qW)}\bar{\bar{Z}}^{-1}\bar{\bar{Q}}^{(Wq)}\bar{A}^q = \bar{\bar{T}}^q\bar{w}^q \tag{3.26}$$

Thus

$$\bar{A}^q = \bar{\bar{\tau}}^{(q)}\bar{w}^q \tag{3.27}$$

where $\bar{\bar{\tau}}^{(q)}$ is the T-matrix in the presence of the wall and is

$$\bar{\bar{\tau}}^{(q)} = \left[\bar{\bar{I}} - \bar{\bar{T}}^q\bar{\bar{\gamma}}^{(qW)}\bar{\bar{Z}}^{-1}\bar{\bar{Q}}^{(Wq)}\right]^{-1}\bar{\bar{T}}^q \tag{3.28}$$

The form of the equations above are analogous to equations (9) and (10) of the case of circular cavity of [34].

3.5 FOLDY-LAX MULTIPLE SCATTERING EQUATIONS

Using the scattered field coefficients $\bar{A}^q$ of the scattered field that includes wall reflection, and the $\bar{\bar{\tau}}^{(q)}$, T matrix including the wall effects, I derive Foldy-Lax multiple scattering equations in this section.

Consider multiple vias, $q = 1,2,3,\ldots.N$ (Figure 3.2 a). The derivations are as follows. The exciting field on via q has three contributions: (i) incident field from source via, (ii) incident field from source via that is reflected from the wall, and (iii) field from other vias $p \neq q$ which is the sum of the direct and the reflection from the wall.

Then the field from via p to via q is

$$\bar{E}_s^{qp} = \bar{E}\left(\bar{\rho} - \bar{\rho}_p\right) + \bar{E}_s^{Wqp}(\bar{\rho}) \tag{3.29}$$

$\bar{E}_s^{qp}$ is analogous to the previous section with the field originating from via p, reflected by the wall and then onto via q

$$\bar{E}_s^{qp} = Rg\bar{E}^t\left(\bar{\rho} - \bar{\rho}_q\right)\bar{\bar{\gamma}}^{(qW)}\bar{\bar{Z}}^{-1}\bar{\bar{Q}}^{(Wp)} \tag{3.30}$$

where $E_s^{Wqpm}(\bar{\rho})$ is via p to via q by reflection from the wall.

Then I expand $E_m\left(\bar{\rho} - \bar{\rho}_p\right)$ about q

$$\bar{E}^t\left(\bar{\rho} - \bar{\rho}_p\right) = Rg\bar{E}^t\left(\bar{\rho} - \bar{\rho}_q\right) \cdot \bar{\bar{\alpha}}_{qp}^{+} \tag{3.31}$$

Then

$$\left[E_s^{qp}\right]^t = Rg\bar{E}^t\left(\bar{\rho} - \bar{\rho}_q\right) \cdot \bar{\bar{\alpha}}_{qp}^{+} + Rg\bar{E}^t\left(\bar{\rho} - \bar{\rho}_q\right) \cdot \bar{\bar{X}}^{Wqp} \tag{3.32}$$

where

$$\bar{\bar{X}}^{Wqp} = \bar{\bar{\gamma}}^{(qW)}\bar{\bar{Z}}^{-1}\bar{\bar{Q}}^{(Wp)} \tag{3.33}$$

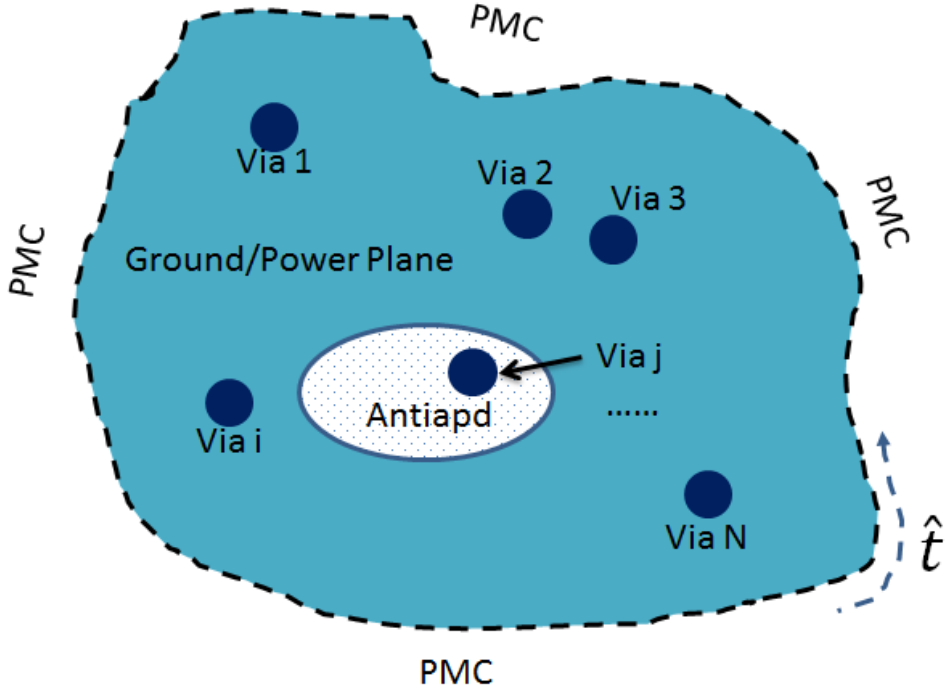

(a) Top view of N vias structures with arbitrarily shaped power/ground planes.

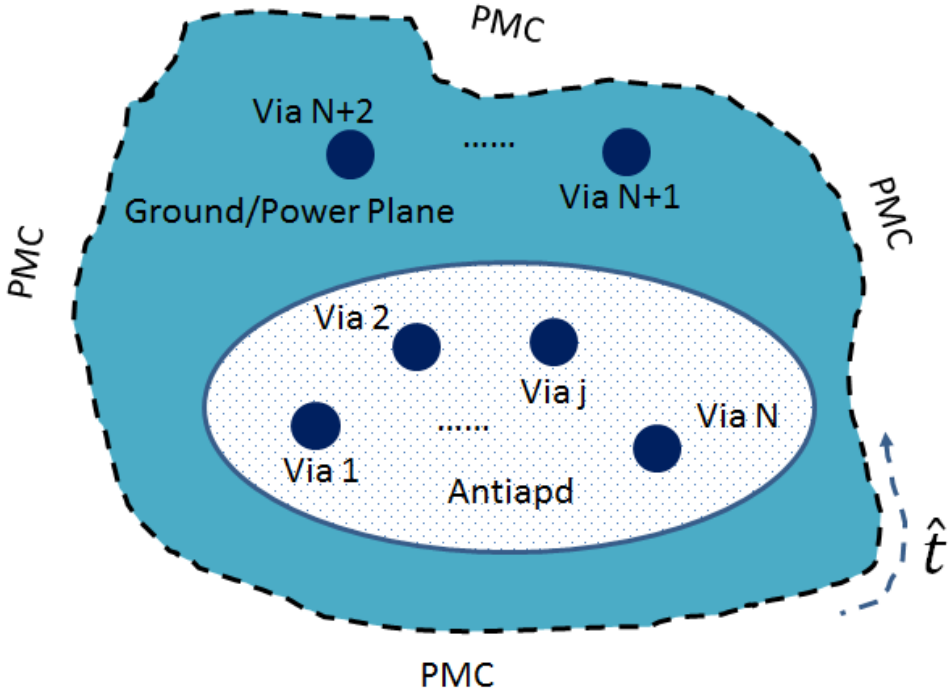

Figure 3.2 (b) Top view of N vias sharing the same antipad with arbitrarily shaped power/ground planes.

Let the incident field onto via q be $Rg\bar{\bar{E}}^t(\bar{\rho}-\bar{\rho}_q)\bar{a}^{q,inc}$, I shall derive $\bar{a}^{q,inc}$ in the next section. Then the exciting field is

$$E_{ex}^q(\bar{\rho}) = Rg\bar{\bar{E}}^t(\bar{\rho}-\bar{\rho}_q)\bar{w}^q \tag{3.34}$$

Based on Foldy-Lax equations, it is the sum of incident field and scattered field from all other vias

$$Rg\bar{\bar{E}}^t(\bar{\rho}-\bar{\rho}_q)\bar{w}^q = Rg\bar{\bar{E}}^t(\bar{\rho}-\bar{\rho}_q)\bar{a}^{q,inc} + \sum_{\substack{p=1\\p\neq q}}^{N} E_s^{qp}(\bar{\rho}) \tag{3.35}$$

Thus, substituting in, I obtain the Foldy-Lax equations

$$\bar{w}^q = \bar{a}^{q,inc} + \sum_{\substack{p=1\\p\neq q}}^{N}\left[\bar{\bar{\alpha}}_{qp}^{+} + \bar{\bar{X}}^{Wqp}\right]\bar{A}^p \tag{3.36}$$

Using the $\bar{\bar{\tau}}^{(p)}$, the T-matrix including wall effects, I have

$$\bar{w}^q = \bar{a}^{q,inc} + \sum_{\substack{p=1\\p\neq q}}^{N}\left[\bar{\bar{\alpha}}_{qp}^{+} + \bar{\bar{X}}^{Wqp}\right]\bar{\bar{\tau}}^{(p)}\bar{w}^p \tag{3.37}$$

where

$$\bar{\bar{\tau}}^{(p)} = \left[\bar{\bar{I}} - \bar{\bar{T}}^p\bar{\bar{X}}^{Wpp}\right]^{-1}\bar{\bar{T}}^p \tag{3.38}$$

3.6 Incident Field From the Source $\bar{a}^{qj,inc}$, Including Reflection From The Wall

3.6.1 *A. Single Via in An Antipad for Eccentric Case*

Suppose the source magnetic current is at the antipad of via j. The shape of the antipad can be irregular. Then, given the voltage at the via j, I solve the Laplace equation using 1D MoM for antipad j, to determine $\sigma_{sj}(\bar{\rho}')$ which is the 1D charge density on the boundary of the via S_j and the outer boundary S_{gj} of the antipad. Then the incident wave from source j can be calculated by a 1D integration over the surface of S_j and S_{gj}

$$E^{inc}(\bar{\rho}) = \frac{1}{d\varepsilon}\int_{S_j+S_{gj}} dl' g(\bar{\rho},\bar{\rho}')\sigma_{sj}(\bar{\rho}') \tag{3.39}$$

The incident field coefficients on the via q are

$$\left[\bar{a}^{qj,inc}\right]_m = a_m^{qjd} + a_m^{qjW} \tag{3.40}$$

where, a_m^{qjd} is the direct from antipad j to via q, and a_m^{qjW} is the antipad j to via q by reflection from the wall.

The expression for a_m^{qjd} is obtained by expansion of $g(\bar{\rho},\bar{\rho}')$ around via q.

The expression for a_m^{qjW} is by expansion of $g_0(\bar{\rho},\bar{\rho}')$ to find incident field on the wall from source j, and calculate reflection from the wall incident onto via q.

Then

$$a_m^{qjd} = \frac{1}{4jkd\varepsilon}\int_{S_j+S_{gj}} dl' H_m^{(2)}\left(k\left|\bar{\rho}'-\bar{\rho}_q\right|\right)e^{jm\phi_{\bar{\rho}'\bar{\rho}_q}}\sigma_{sj}(\bar{\rho}') \tag{3.41}$$

and

$$a_m^{qjW} = \sum_{n'}\left[\bar{\bar{X}}^{(qj)}\right]_{mn'}\left[\frac{1}{4jkd\varepsilon}\int_{S_j+S_{gj}} dl' J_{n'}\left(k\left|\bar{\rho}'-\bar{\rho}_j\right|\right)e^{jn'\phi_{\bar{\rho}'\bar{\rho}_j}}\sigma_{sj}(\bar{\rho}')\right] \tag{3.42}$$

The form of the equations above are analogous to equations (13) and (14) of the case of circular cavity of [35].

For the special case that the antipad is a concentric cylinder with outer radius b and inner radius a, and voltage V_j, the incident field coefficients as shown in [30], simplify to

$$a_m^{qjW} = \frac{j\pi}{2kd}\frac{V_j}{ln\left(\frac{b}{a}\right)}\left(J_0(kb)-J_0(ka)\right)\left[\bar{\bar{X}}^{(Wqj)}\right]_{m0} \tag{3.43}$$

$$a_m^{jjW} = \frac{j\pi}{2kd}\frac{V_j}{ln\left(\frac{b}{a}\right)}\left(H_0^{(2)}(kb)-H_0^{(2)}(ka)\right)\delta_{m0} \tag{3.44}$$

$$a_m^{qjd} = \frac{j\pi}{2kd}\frac{V_j}{ln\left(\frac{b}{a}\right)}\left(J_0(kb)-J_0(ka)\right)(-1)^m H_m^{(2)}\left(k\left|\bar{\rho}_q-\bar{\rho}_j\right|\right)e^{jm\phi_{\bar{\rho}_q\bar{\rho}_j}}, q\neq j \tag{3.45}$$

3.6.2 *B. Multiple Vias Sharing Same Antipad*

Consider an antipad with multiple circular vias, $q = 1,2\ldots N$ sharing the same antipad. The vias are centered at $\bar{\rho}_q$ $q = 1,2\ldots N$, (Figure 2b). The outer boundary of the antipad is S_g. Let $\bar{\rho}_g$ be a convenient center of the antipad. I solve the Laplace equation subject to the boundary conditions $\psi_L = V_j$ on S_j which is the j^{th} via's boundary, $j = 1,2,\ldots N$ and $\psi_L = 0$ on S_g. Let $S = \sum_{i=1}^{N} S_i$, the surface charge density $\sigma_{sj}(\bar{\rho}')$ obey the 1D surface integral equation

$$\oint_{S+S_g} dl' g_L(\bar{\rho},\bar{\rho}')\frac{\sigma_s(\bar{\rho}')}{\varepsilon} = \begin{cases} V_j & \bar{\rho}\ is\ on\ S_j \\ 0 & \bar{\rho}\ is\ on\ S_g \end{cases} \tag{3.46}$$

where g_L is Green's function for Laplace equation and is

$$g_L(\bar{\rho},\bar{\rho}') = -\frac{1}{2\pi} ln\sqrt{(x-x')^2+(y-y')^2} \tag{3.47}$$

After the 1D MoM equations, the $\sigma_{s_j}(\bar{\rho}')$, $j = 1,\ldots N$ and $\sigma_{s_g}(\bar{\rho}')$ on the outerboundary of the antipad are obtained. Then the incident field coefficients on via $q = 1,2\ldots N$ are

$$\left[\bar{a}^{q,inc}\right]_m = a_m^{qd} + a_m^{qW} \tag{3.48}$$

where a_m^{qd} is the direct from the surface charges in the antipad vias and outer boundary, and a_m^{qW} is due to wall reflections.

$$a_m^{qd} = \frac{1}{4jkd\varepsilon}\left(\sum_{j=1}\int_{S_j} dl' H_m^{(2)}\left(k\left|\bar{\rho}' - \bar{\rho}_q\right|\right)e^{jm\phi_{\bar{\rho}'\bar{\rho}_q}}\sigma_{sj}(\bar{\rho}') + \int_{S_g} dl' H_m^{(2)}\left(k\left|\bar{\rho}' - \bar{\rho}_q\right|\right)e^{jm\phi_{\bar{\rho}'\bar{\rho}_q}}\sigma_{sg}(\bar{\rho}')\right) \tag{3.49}$$

In the case of small antipad, according to previous paper [36], the above can be approximated by $E^{inc,d} = \frac{V_q}{d}$ on the surface of via q. Then a_m^{qd} simplifies to

$$a_m^{qd} = \delta_{m0}\frac{V_q}{kdJ_0(ka)} \tag{3.50}$$

Next consider the wall reflection term a_m^{qW}. The total wall reflection is, including fields from surface $\sigma_{sj}(\bar{\rho}'), j = 1,2..N$ and the surface charge $\sigma_{sg}(\bar{\rho}')$

$$a_m^{qW} = \frac{1}{4jkd\varepsilon}\left\{\sum_{j=1}\sum_{n'}\left[\bar{\bar{X}}^{Wqj}\right]_{mn'}\int_{S_j} dl' J_{n'}\left(k\left|\bar{\rho}' - \bar{\rho}_j\right|\right)e^{jn'\phi_{\bar{\rho}'\bar{\rho}_j}}\sigma_{sj}(\bar{\rho}') + \sum_{n'}\left[\bar{\bar{X}}^{(Wqg)}\right]_{mn'}\int_{S_g} dl' J_{n'}\left(k\left|\bar{\rho}' - \bar{\rho}_g\right|\right)e^{jn'\phi_{\bar{\rho}'\bar{\rho}_g}}\sigma_{sg}(\bar{\rho}')\right\} \tag{3.51}$$

3.7 VIA CURRENTS

After the Foldy-Lax equations are solved, $\bar{w}(q), q = 1,2\ldots N$ are obained. The total field at via q is the sum of the excited field E_{ex}^q and the scattered field E_s^q

$$E_{ex}^q(\bar{\rho}) + E_s^q(\bar{\rho}) = Rg\bar{E}^t\left(\bar{\rho} - \bar{\rho}_q\right)\bar{w}^q + \left[\bar{E}^t\left(\bar{\rho} - \bar{\rho}_q\right) + Rg\bar{E}^t\left(\bar{\rho} - \bar{\rho}_q\right)\bar{\bar{X}}^{Wqq}\right]\bar{A}^q \tag{3.52}$$

Then the magnetic field in the $\hat{\phi}$ direction can be obtained. The surface currents J_s^q is in the z direction and is calculated from the magnetic field on the surface of the via

$$J_s^q = \frac{k^2}{j\omega\mu}\left(\sum_m w_m^q J_m{}'(ka)e^{-jm\phi_{\bar{\rho}\bar{\rho}_q}} + \sum_m\left[H_m^{(2)'}(ka)A_m^q + J_m{}'(ka)\left(\bar{\bar{X}}^{Wqq}\bar{A}^q\right)_m\right]e^{-jm\phi_{\bar{\rho}\bar{\rho}_q}}\right) \tag{3.53}$$

Current I_s^q is integration over the surface of the via, so that only the $m = 0$ in the above contributes. Using also $\bar{A}^q = \bar{\bar{\tau}}^q\bar{w}^q$

$$I_s^q = a\int_0^{2\pi} d\phi_{\bar{\rho}\bar{\rho}_q} J_s^q = \frac{-j2\pi ak}{\eta}\left\{\left(H_0^{(2)\prime}(ka)\bar{\bar{\tau}}^{(q)} + J_0{}'(ka)\left(\bar{\bar{I}} + \bar{\bar{X}}^{Wqq}\bar{\bar{\tau}}^{(q)}\right)\right)\bar{w}^q\right\}_0 \tag{3.54}$$

where $\bar{\bar{I}}$ is $(2M+1)\times(2M+1)$ unit matrix and $\{\ \}_0$ represents the 0^{th} harmonic of the column vector. Note that in the above, I calculate the current of the $l = 0$ mode. The $l \geq 1$ modes are also calculated but without considering the wall effects. The total current is the sum of currents of all l. Once the currents are determined, the calculation of the scattering matrix proceed in manners as described in previous papers [4, 35, 36].

3.8 Numerical Results and Discussions

In this section I illustrate the results and make comparisons with Ansoft's HFSS version 12.

All single-ended S-parameters provided here are referenced to 50 Ω, and all mixed-mode S-parameters are referenced to 100 Ω for differential mode. In the case specifications, h stands for waveguide thickness, and t stands for the plane thickness in the specifications of both cases.

3.8.1 *A. 10 Vias Array for Each Via Going Through One Antipad Eccentrically (Single-Ended Signaling Case) in A Rectangular Cavity*

Figure 3.3 shows top view of structure about 10 vias. The figure on the right is the zoom in showing the detail of via-antipad region. Each signal via goes through one antipad and the via location is eccentric. The specifications are: $\varepsilon_r = 4.0$ (silicon dioxide), $R_{via} = 5\ mil$,$R_{antipad} = 10\ mil$, eccentric pitch $e = 2\ mil$, via pitch $p_x = 150\ mil$, $p_y = 100\ mil$, $h = 50\ mil$, $t = 1.3\ mil$, plane width $W = 500\ mil$, plane length $L = 800\ mil$. The 10 signal vias locate at $(102{,}200)\ mil$, $(252{,}200)\ mil$, $(402{,}200)\ mil$, $(552{,}200)\ mil$, $(702{,}200)\ mil$, $(102{,}300)\ mil$, $(252{,}300)\ mil$, $(402{,}300)\ mil$, $(552{,}300)\ mil$, and $(702{,}300)\ mil$.

In figure 3.4 and 3.5, I compared the insertion loss and return loss between bottom corner via and bottom center via, up to 20GHz. The simulation results obtained from the Foldy-Lax agreed well with HFSS. From the figures, we can see that the first resonance for the left bottom corner via happen at lower frequency than the bottom center via. This can be explained by the physical layout of the vias.

The resonances are due to the reflections of the multiple scattering among vias and the cavity walls. The bottom center via locates at a wider local region than the corner one, which leads to first resonance at lower frequency in frequency domain.

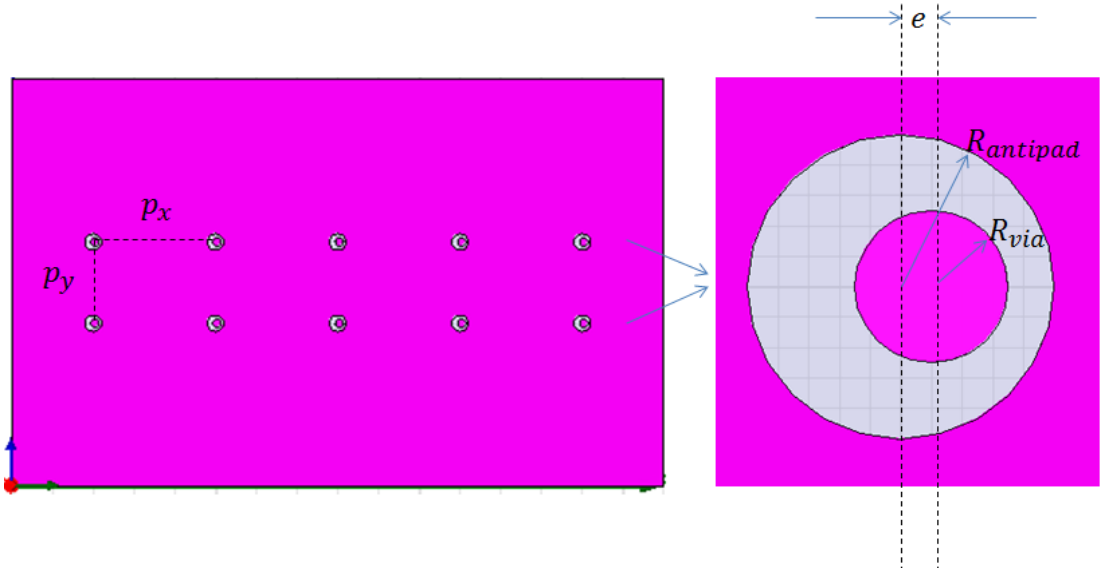

Figure 3.3. (Left) Top view of 10 eccentric vias layout for case A. (right) Zoom in for one eccentric via in anitpad.

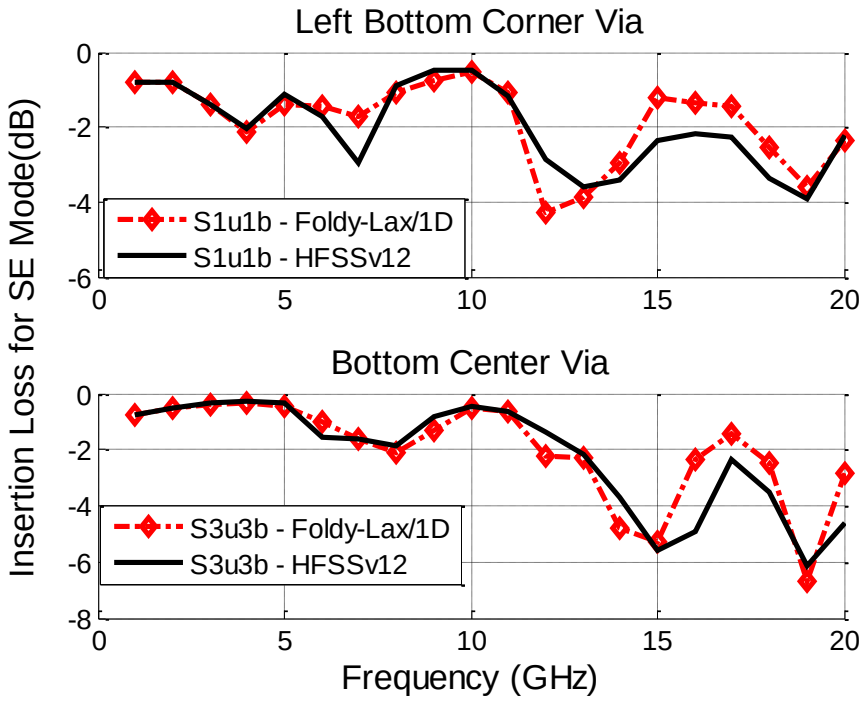

Figure 3.4. Insertion loss comparisons of left corner bottom via and center bottom via for case A.

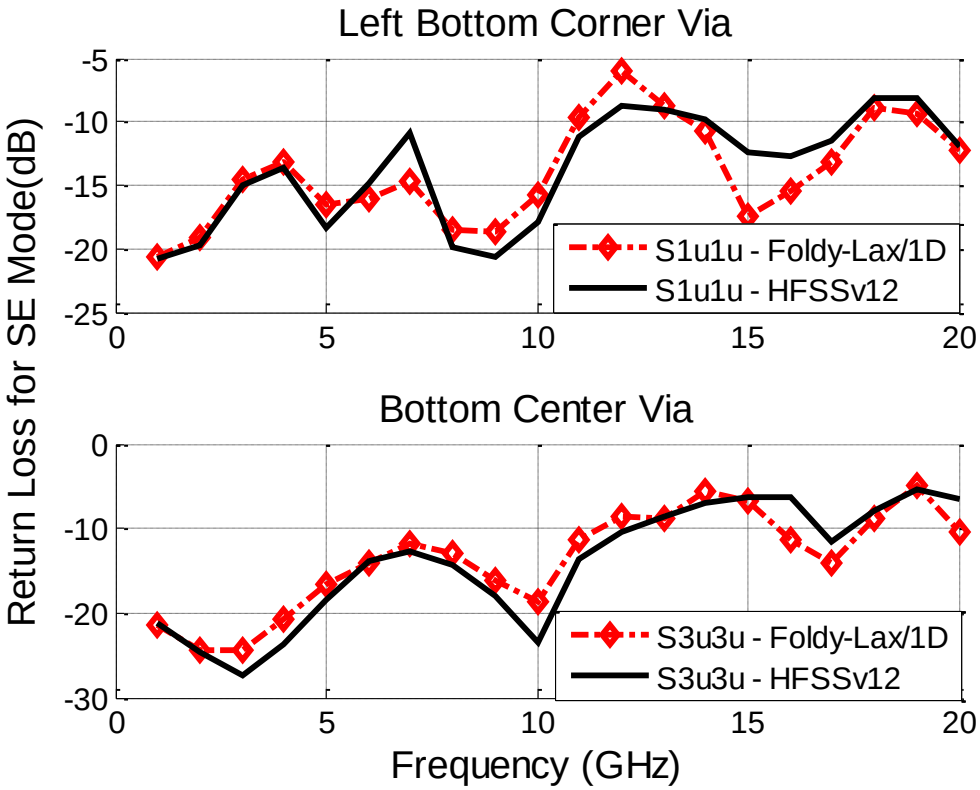

Figure 3.5. Return loss comparisons of left corner bottom via and center bottom via for case A

3.8.2 *B. 2 Vias Sharing Same Antipad (Differential Signaling Case) in A Square Cavity*

Figure 3.6 shows top view of structure about 2 vias sharing one antipad in a differential pair configuration. The differential pair of vias can be in common mode or differential mode. The specifications are: $\varepsilon_r = 4.4$, $tan\delta = 0.02$ (FR4_eproxy), $R_{via} = 15\,mil$, $R_{antipad} = 30\,mil$, $h = 50\,mil$, $t = 1.3\,mil$. The cavity is square and the length is $L = W = 500\,mil$.

In order to test the convergence of the proposed method, we let $pitch = 40\,mil$ for the one case (case B1) and $pitch = 31\,mil$ for another case (case B2). Note that in case B2, the spacing between the two vias is just $1\,mil$, as the spacing is the difference between the pitch and the sum of the radii of the two vias. For case B1, two vias are at $(200,300)\,mil$ and $(240,300)\,mil$. For case B2, two vias are at $(200,300)\,mil$ and $(231,300)\,mil$.

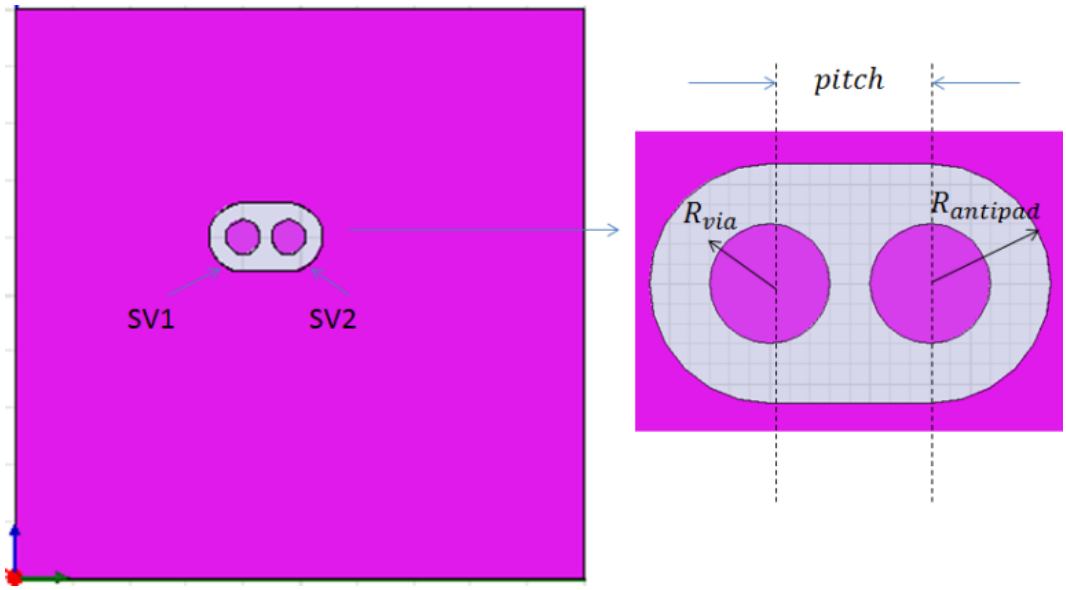

Figure 3.6. Top view of 2 vias sharing one antipad in a square cavity for case B.

Figure 3.7-3.10 show the insertion loss and return loss for both differential mode and common mode respectively for the 2 cases, up to 50GHz. The resonances are seen in both cases with the resonances of differential mode at much higher frequencies than common mode. Good agreements are in the Foldy-Lax results with HFSS simulations. One can see that the differential mode usually has less loss than the common mode for the insertion loss, due to its high immunity to the noise and high tolerance to link path discontinuities.

It is to be noted that the insertion loss for differential mode in case B1 is better than case B2. This is due to the port impedance mismatching (as we treat all mixed-mode S-parameters referenced to 100 Ω for differential mode and 25 Ω for common mode). It does not mean that the electrical performance for 2 vias farther apart is better than 2 vias closer together in the layout.

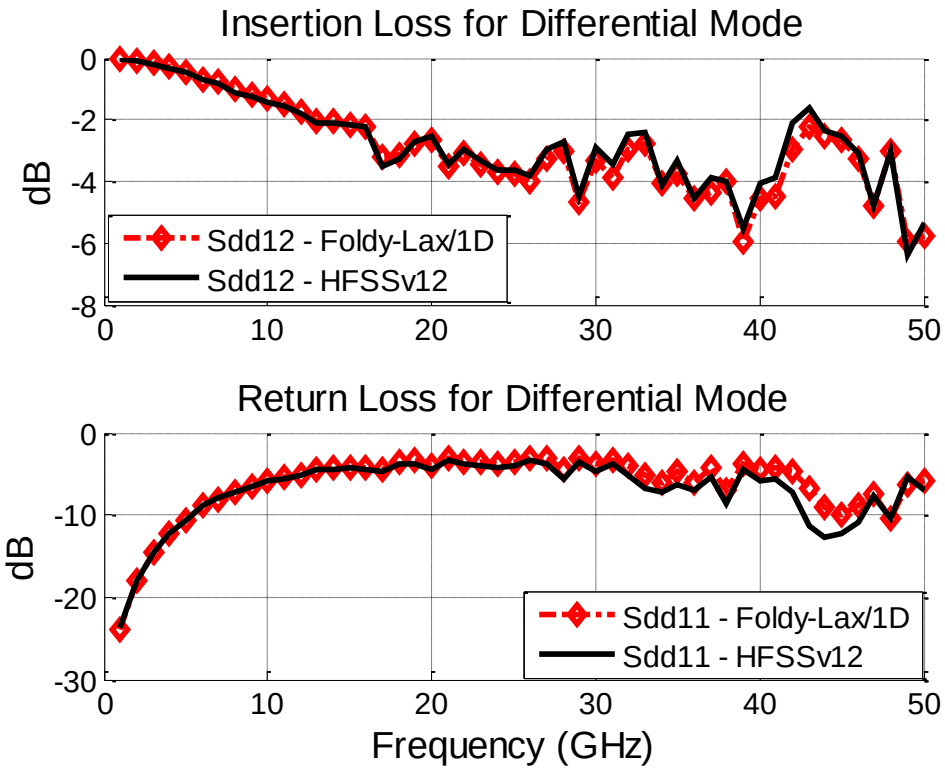

Figure 3.7. Insertion/Return loss of differential mode for case B1.

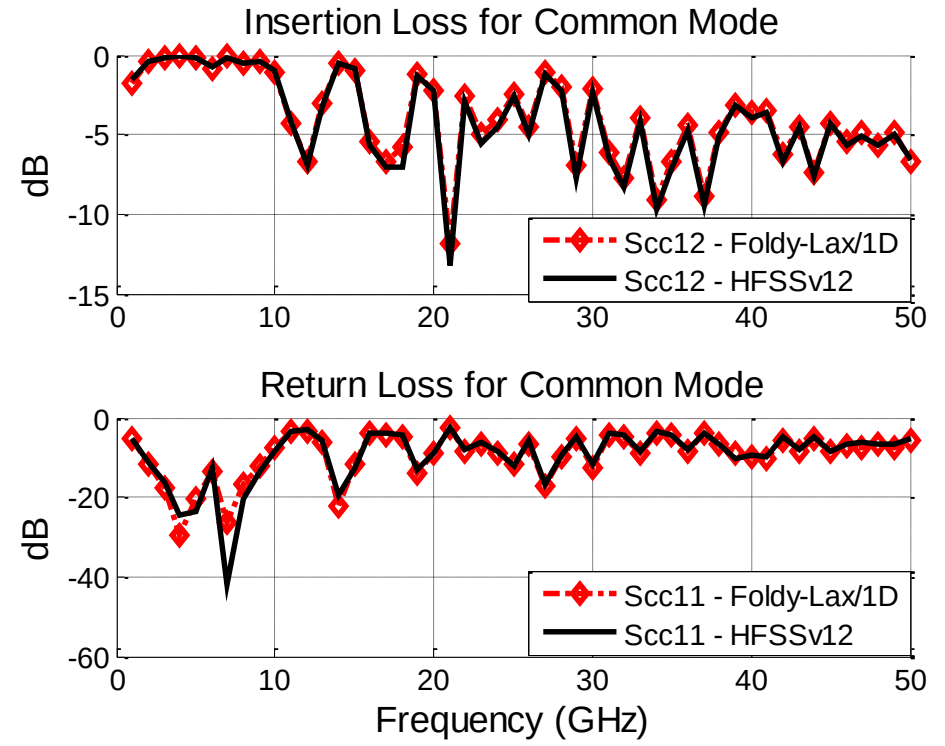

Figure 3.8. Insertion/Return loss of common mode for case B1.

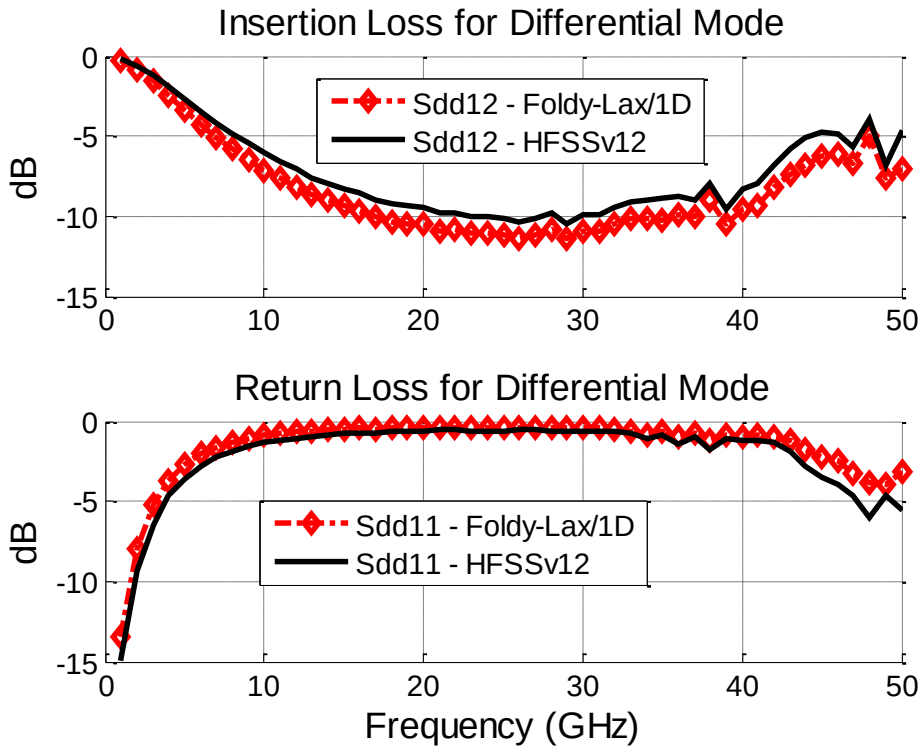

Figure 3.9. Insertion/Return loss of differential mode for case B2.

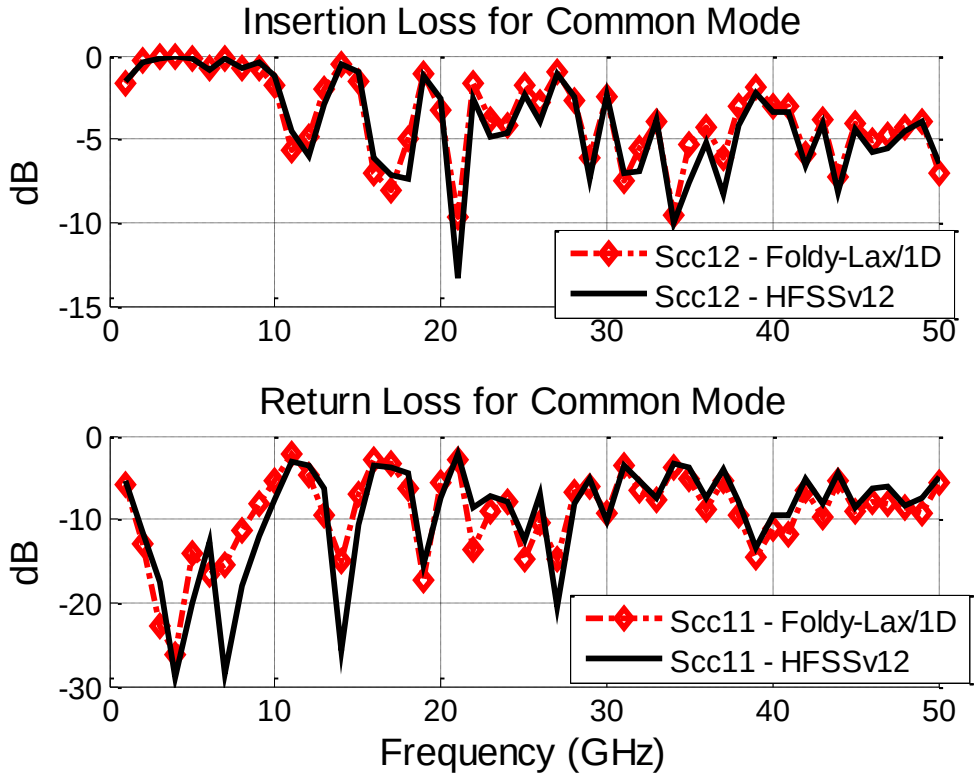

Figure 3.10. Insertion/Return loss of common mode for case B2.

3.8.3 *C. 4 Vias Sharing Same Antipad in A L-Shaped Cavity*

This case is for 4 vias sharing one antipad in a L-shaped cavity. The top view is shown in Figure 3.11. The specifications are: $R_{via} = 15\,mil$, $R_{antipad} = 60\,mil$, $W = 500\,mil$, $L_1 = 250\,mil$, $W_1 = 100\,mil$, $t = 1\,mil$, $h = 20\,mil$, $\varepsilon_r = 4.4$, $tan\delta = 0.02$, $pitch = 40\,mil$.

Figure 3.12 shows the comparisons of the insertion loss and return loss for signal via 1. Figure 3.13 shows the near-end cross talk (NEXT) between signal via 1 and via 2 (top figure), between via 1 and via3 (bottom figure). Good agreements are obtained between the results obtained from Foldy-Lax and HFSS simulations.

From the results in the figures, the resonances shown in the insertion loss, return loss and NEXT are due to the cavity resonances. One can see that such resonances effects are reduced at high frequencies, particularly for NEXT. This is due to the fact that closely placed vias provide relative lower impedance for the current return path than it provided by the cavity for signal via 1.

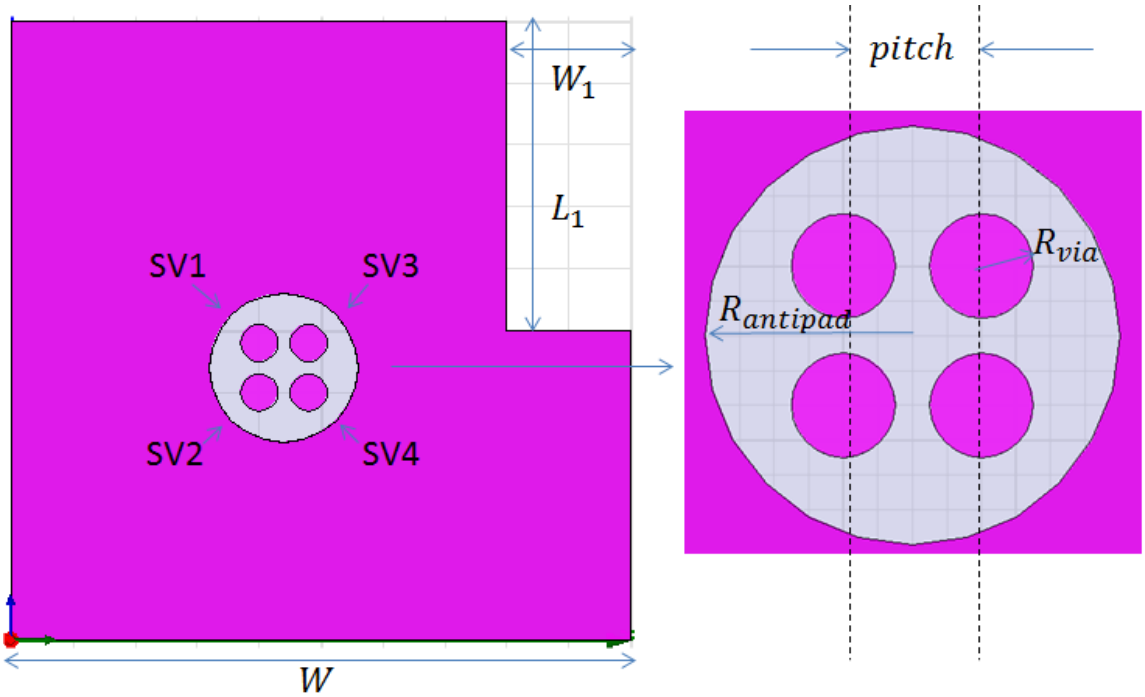

Figure 3.11. Top view of 4 vias sharing one antipad in a L-shaped cavity for case C.

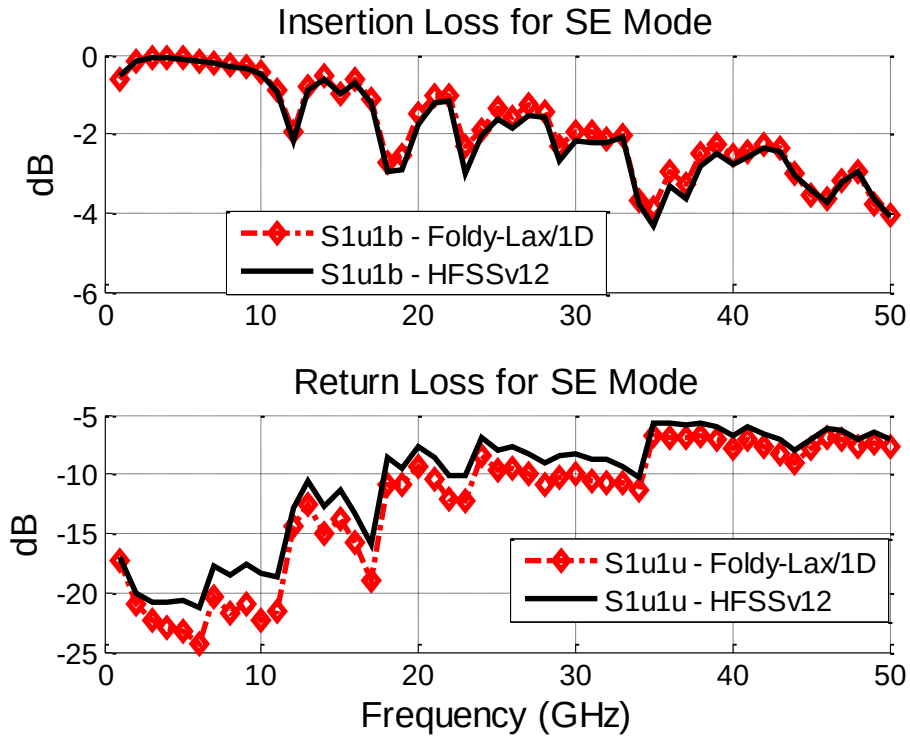

Figure 3.12. Insertion/Return loss of signal via 1 for case C.

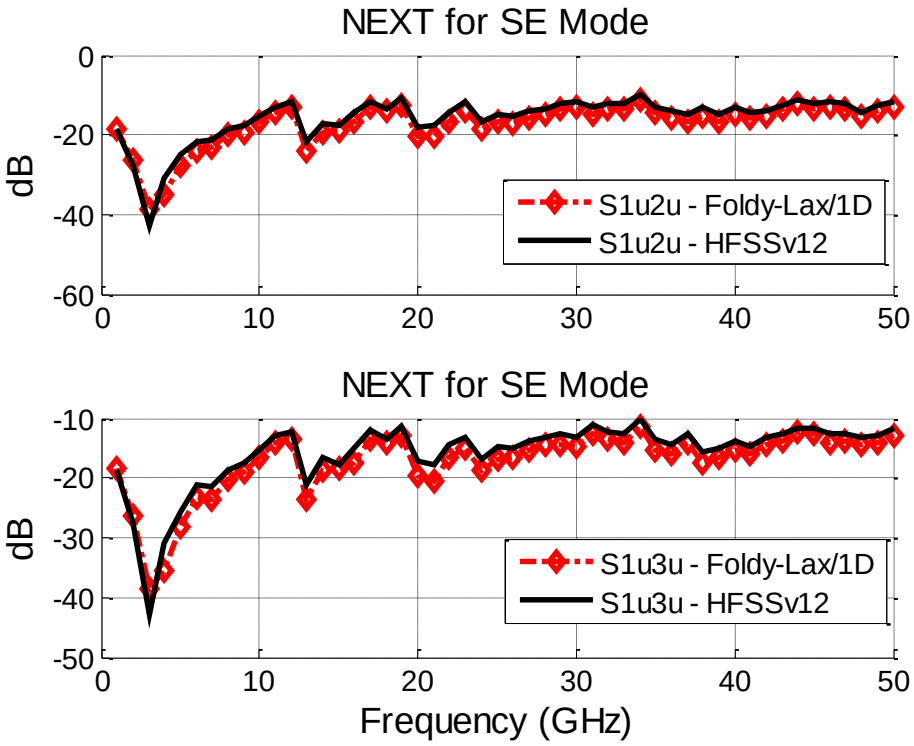

Figure 3.13. NEXT between signal via 1, via 2 and via 3 for case C.

3.8.4 *D. 36 Vias in A L-shaped Cavity Embedded with A SIW Structure*

I consider using coaxial ports as the excitation means. Fig. 3.14 shows a top view of a L-shaped cavity embedded with a SIW structure which includes 36 vias, including 2 signal vias and 34 ground vias. The frequency range is broadened up to 100GHz. In this case, $R_{via} = 5\,mil$, $R_{antipad} = 15\,mil$, $W = 500\,mil$, $L_1 = 250\,mil$, $W_1 = 150\,mil$, $t = 1\,mil$(plane thickness), $d = 50\,mil$(substrate thickness), for substrate material, $\varepsilon_r = 4.4$, $tan\delta = 0.02$, gap between vias fencing the SIW is $p = 20\,mil$.

Fig. 3.15 shows the insertion loss and return loss for signal via 1, the near end cross talk (NEXT) and far end cross talk (FEXT) between two signal vias, which stand for the leakage from signal via 1 to signal via 2 through the via gap of the SIW. In the modeling, $M = 2, L = 5$, for enough high order modes effects. From the comparisons, we can see the results of proposed method are in good agreement with the results of HFSS simulation. The average CPU times per frequency for simulation of single-ended S parameters by using Foldy-Lax method is about 20 seconds, compared with HFSS using around 200 seconds.

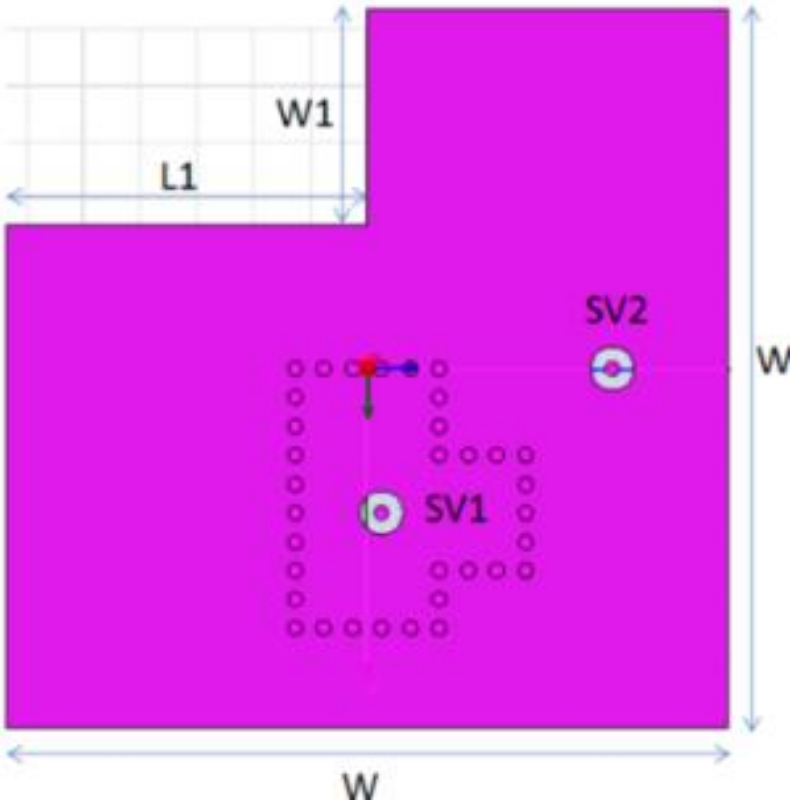

Figure 3.14. Top view of a L-shaped cavity embedded with a SIW structure.

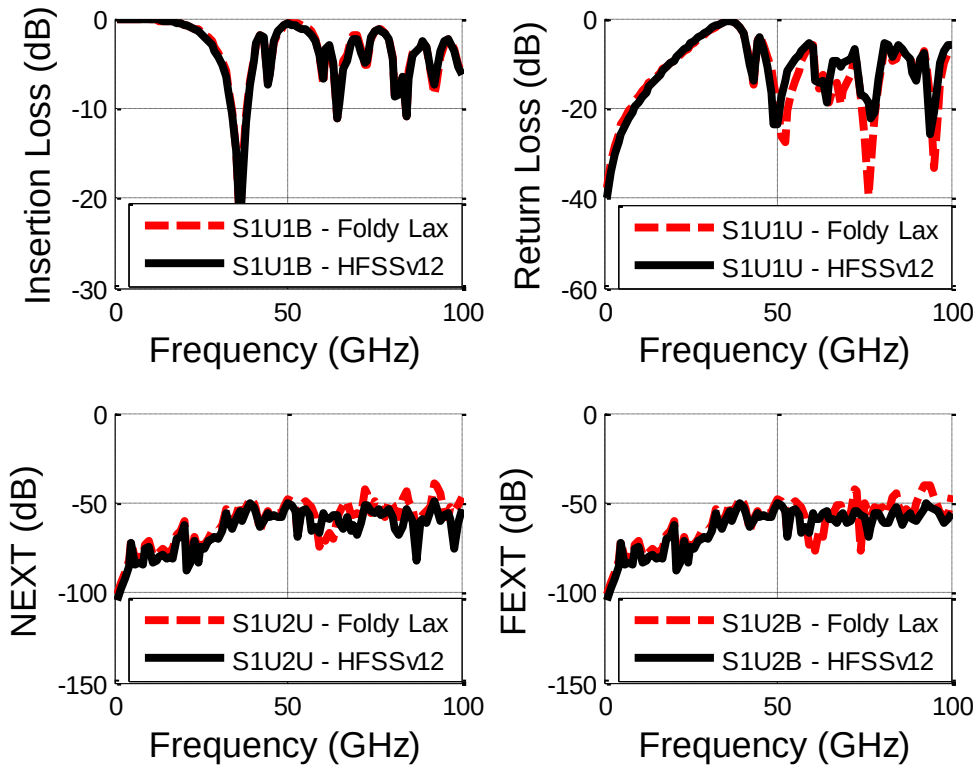

Figure 3.15. Comparisons of insertion and return loss for signal via 1, NEXT and FEXT btween signal via 1 and 2.

3.8.5 *E. 5 X 10 Dense Vias Array for Each Via Going through One Antipad*

Fig. 3.16 shows top view of structure about 5x10 dense vias geometry. Each signal via goes through one antiapd. The specifications are: $\varepsilon_r = 3.84$, $R_{via} = 7\,mil$, $R_{antipad} = 15\,mil$, $tan\delta = 0.033$, $p = 40\,mil$, $d = 30\,mil$, $t = 1\,mil$. The cavity length is $300\,mil$ in x (vertical) direction and $500\,mil$ in y (horizontal) direction. The first via which is the left top comer signal via locate at $(70,70)\,mil$. The via order increases along y (horizontal) direction first and then increases along x (vertical) direction. Port 1-50 are top ports for via 1-50 and ports 51-100 are bottom ports for via 1-50.

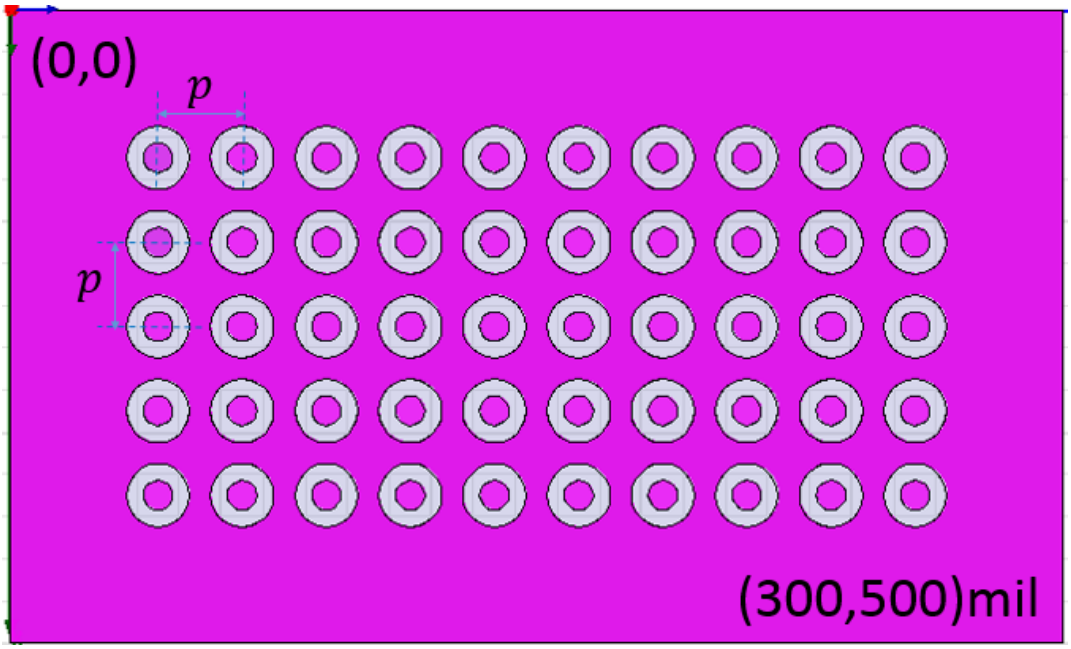

Figure 3.16. Top view of 5x8 dense via array for case E.

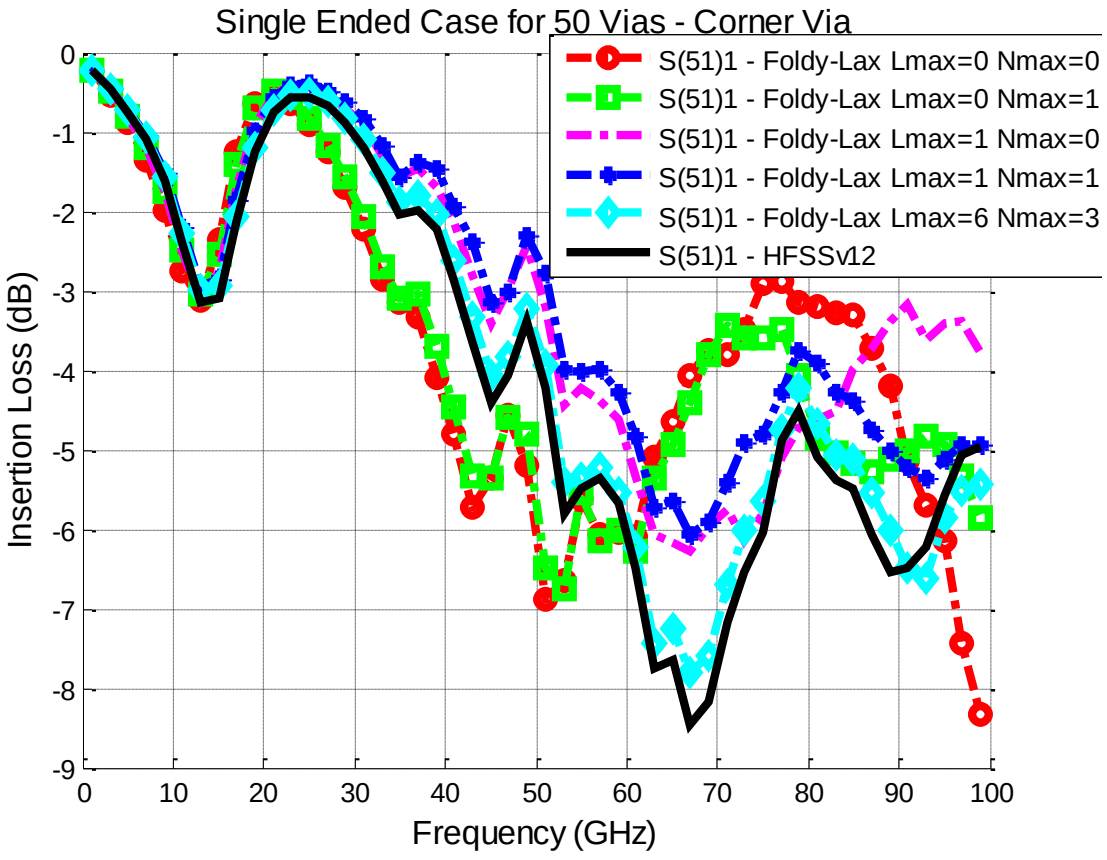

Figure 3.17. Insertion loss for corner via for case E.

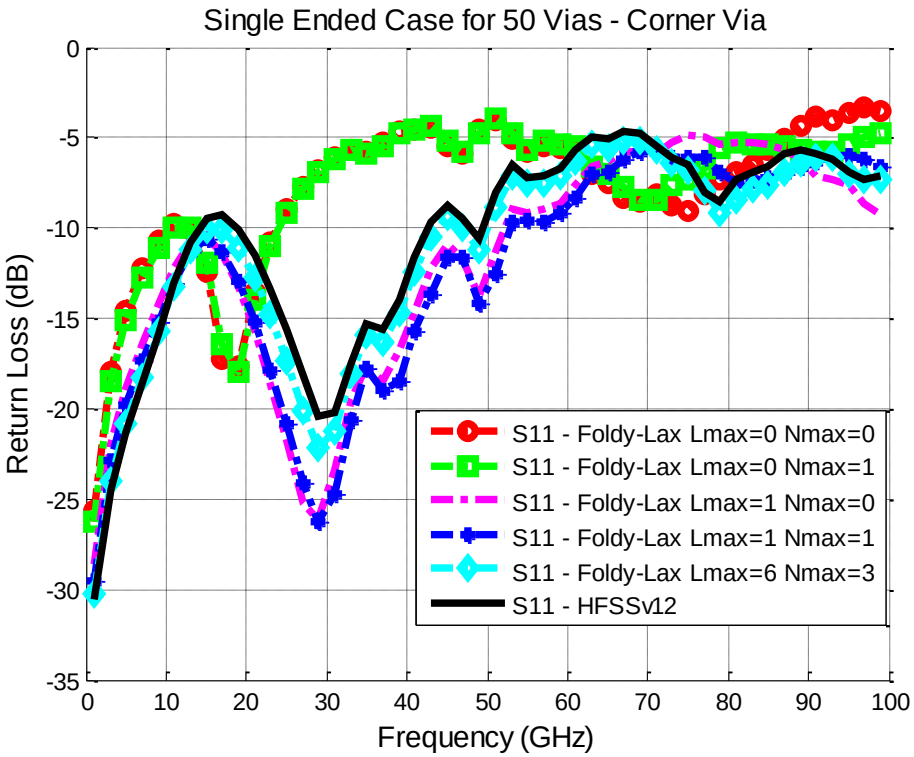

Figure 3.18. Return loss for corner via for case E.

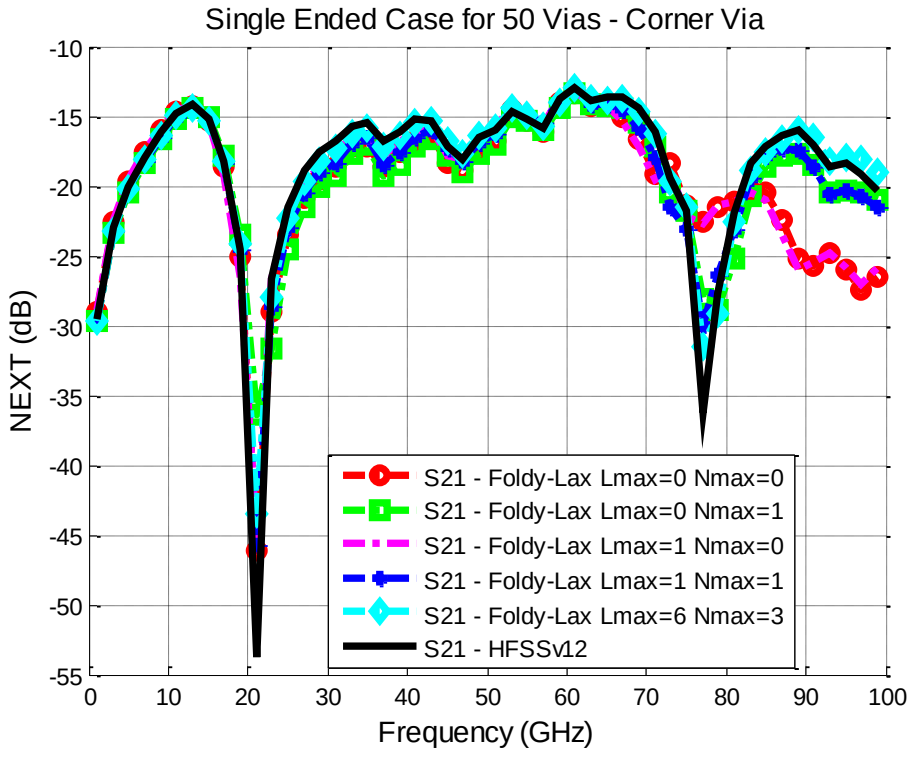

Figure 3.19. NEXT for corner via for case E.

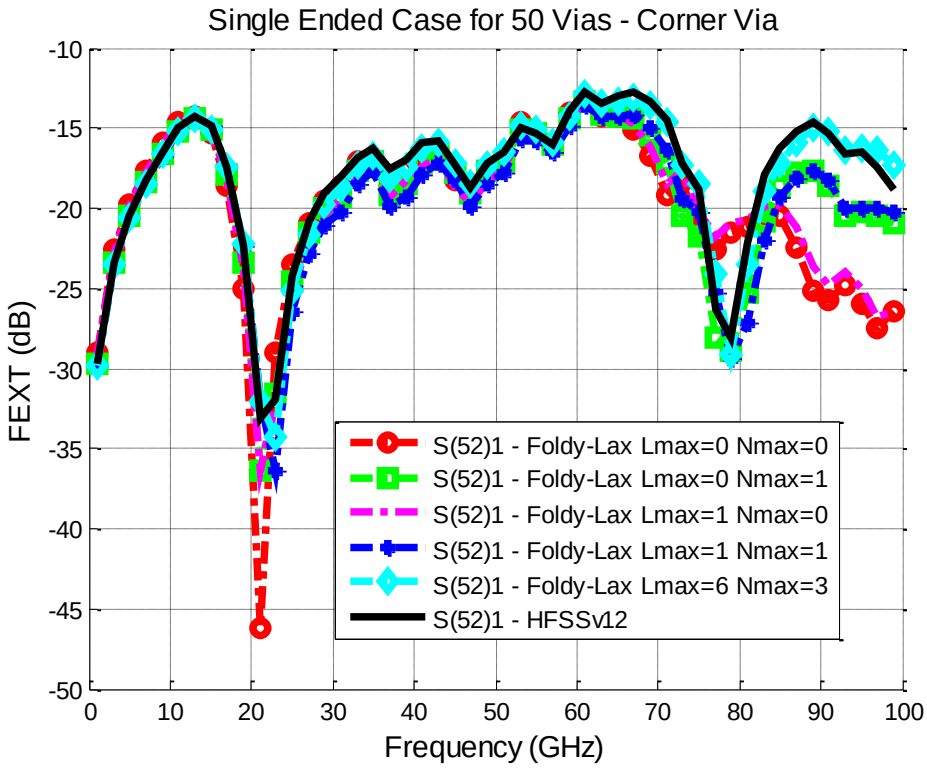

Figure 3.20. FEXT for corner via for case E.

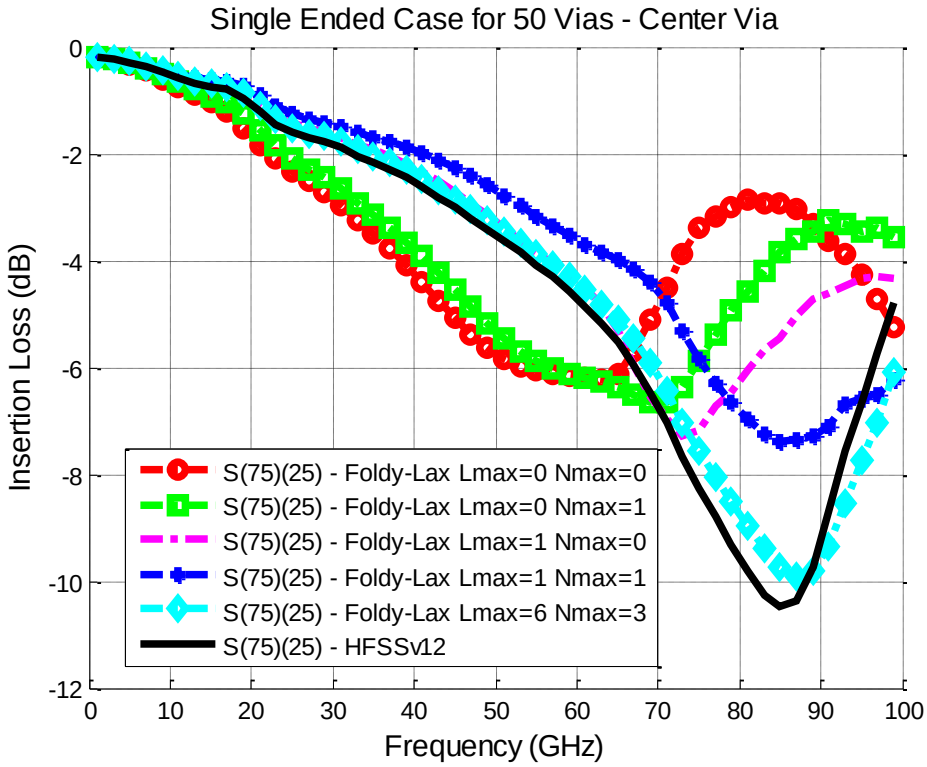

Figure 3.21. Insertion loss for center via for case E.

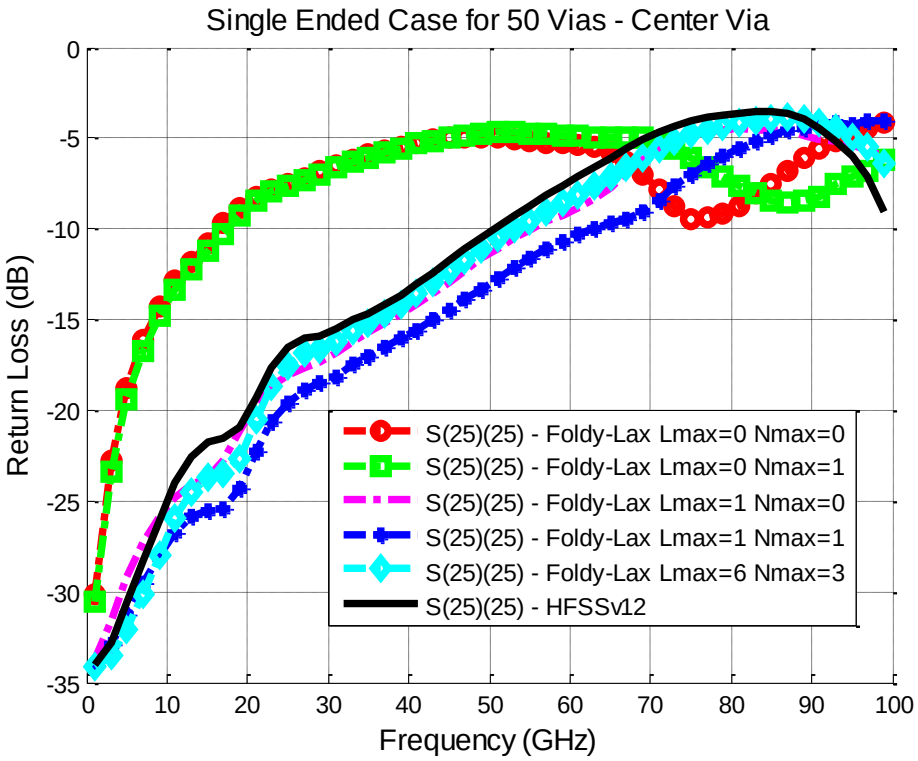

Figure 3.22. Return loss for center via for case E.

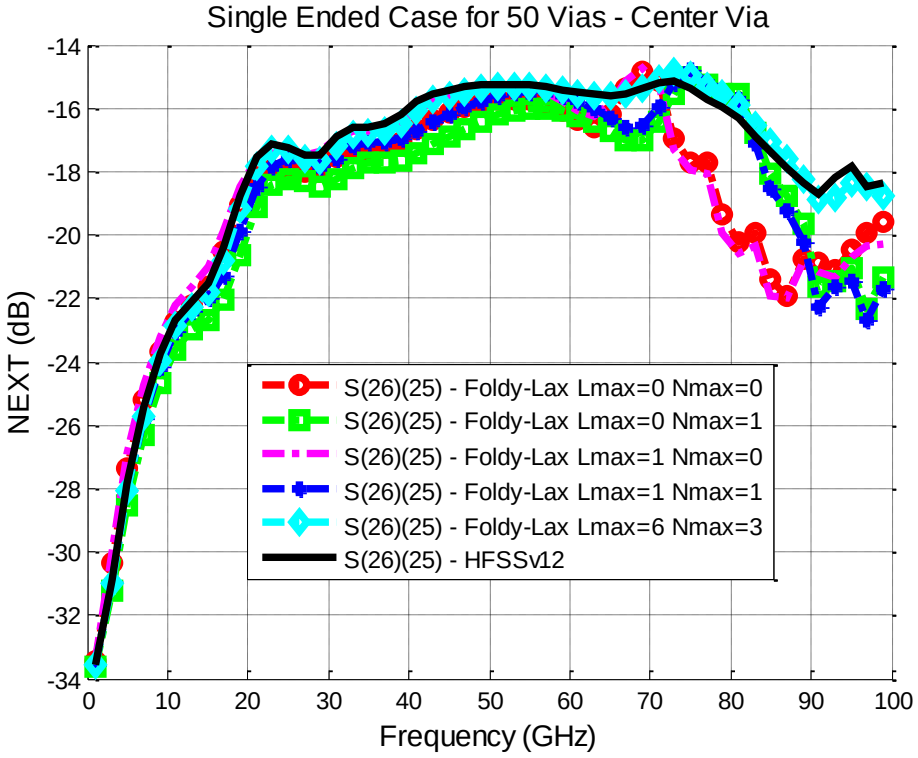

Figure 3.23. NEXT for center via for case E.

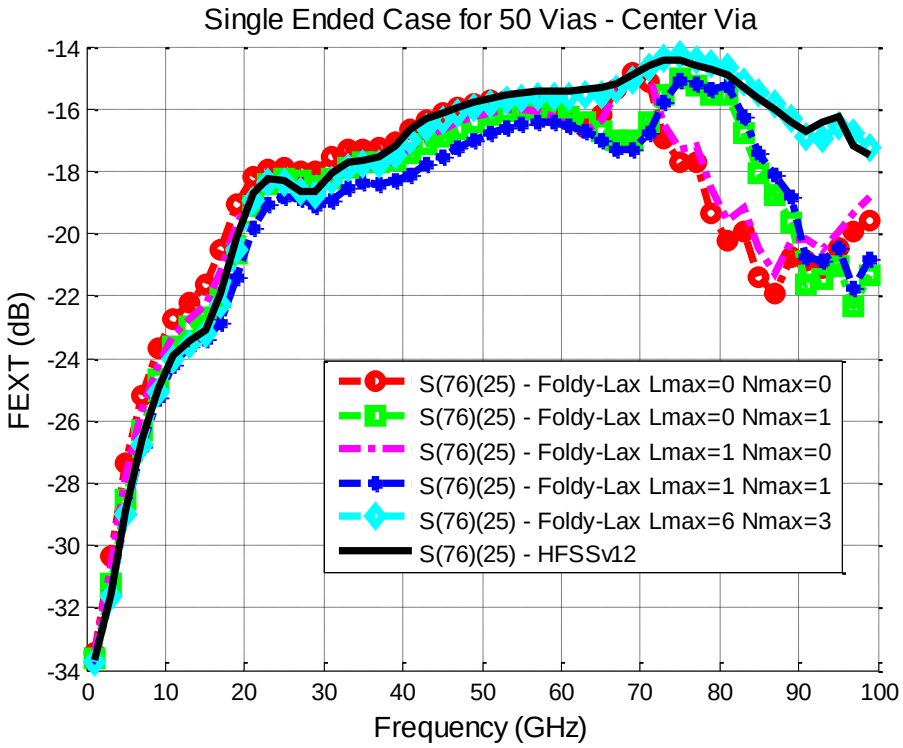

Figure 3.24. FEXT for corner via for case E.

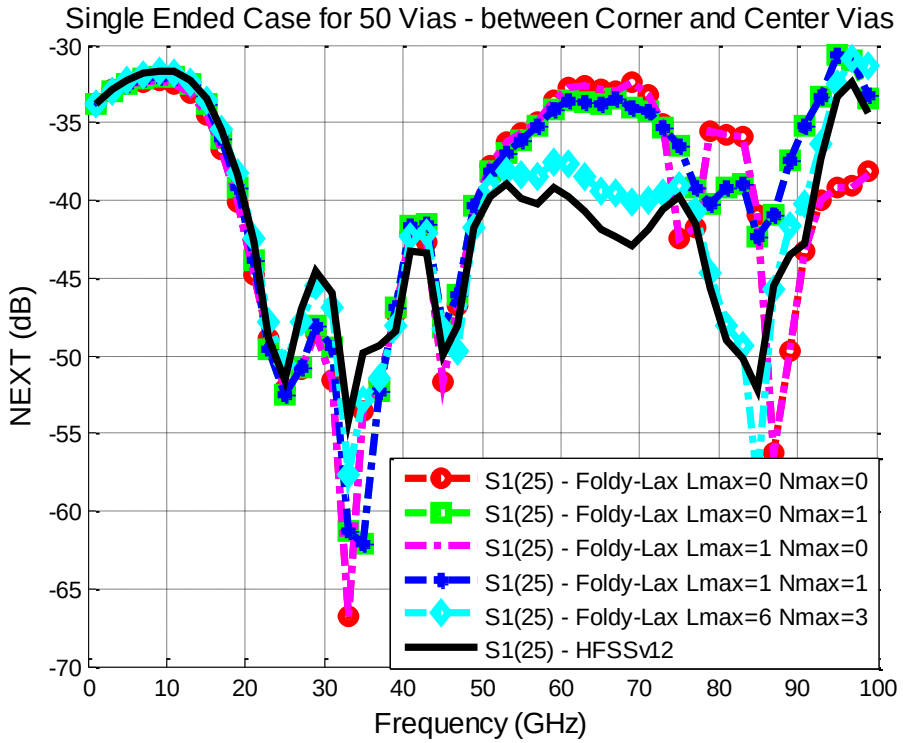

Figure 3.25. NEXT for center via for case E.

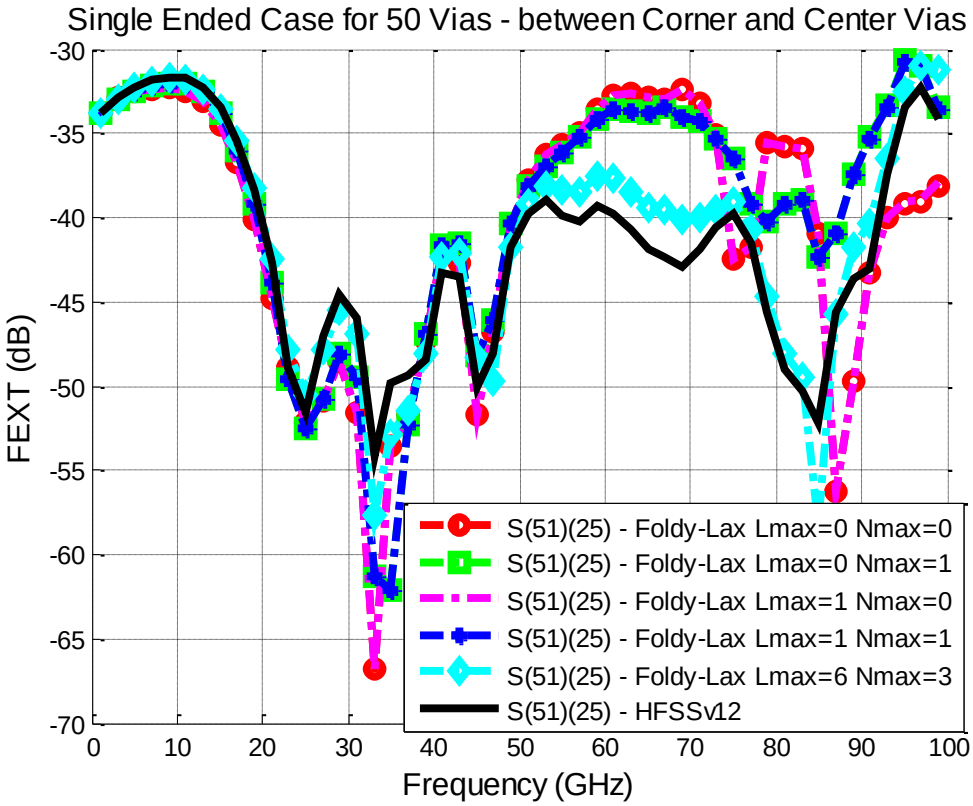

Figure 3.26. FEXT for corner via for case E.

Fig. 3.17-3.20 show the insertion loss, return loss, NEXT and FEXT for corner via which is the left top corner via. Fig. 3.21-3.24 show the insertion loss, return loss, NEXT and FEXT for center via which is the left middle center via. Fig. 3.25-3.26 show the NEXT and FEXT between the corner and center vias.

From the Fig 3.17-3.26, we can see that for dense via array in small cavity, for return loss, when the interested frequency is above 10GHz (for corner via) or 20GHz (for center via), the high order modes effects need to be included for accurate design and modeling. This is because the corner via is placed closer to the cavity side walls than the center via is. For insertion loss, high order modes effects need to be included at as low frequency as possible, as we can observe their strong contributions for the return loss. However, the higher order modes effects make weak contributions for the NEXT and FEXT, for both corner and center vias case. Their effects need to be considered when the interested frequency is above 50GHz.

3.8.6 *F. 3 X 10 Dense Vias Array for Differential Singling Pairs*

Fig. 3.27 shows top view of structure about 3x10 dense vias geometry. Each two signal via sharing same antipad. The specifications are: $\varepsilon_r = 4.4$, $R_{via} = 10\,mil$, $R_{antipad} = 20\,mil$, $tan\delta = 0.02$, $p = 35\,mil$, $p_x = p_y = 50\,mil$, $d = 50\,mil$, $t = 1\,mil$. The cavity is square with length of $350\,mil$ in both x (vertical) direction and y (horizontal) direction. The first via which is the left top comer signal via locate at $(75,75)\,mil$. The differential signaling pair order increases along y (horizontal) direction first and then increases by along x (vertical) direction. For the S parameters, u means upper port and b stands for bottom port for a via pair.

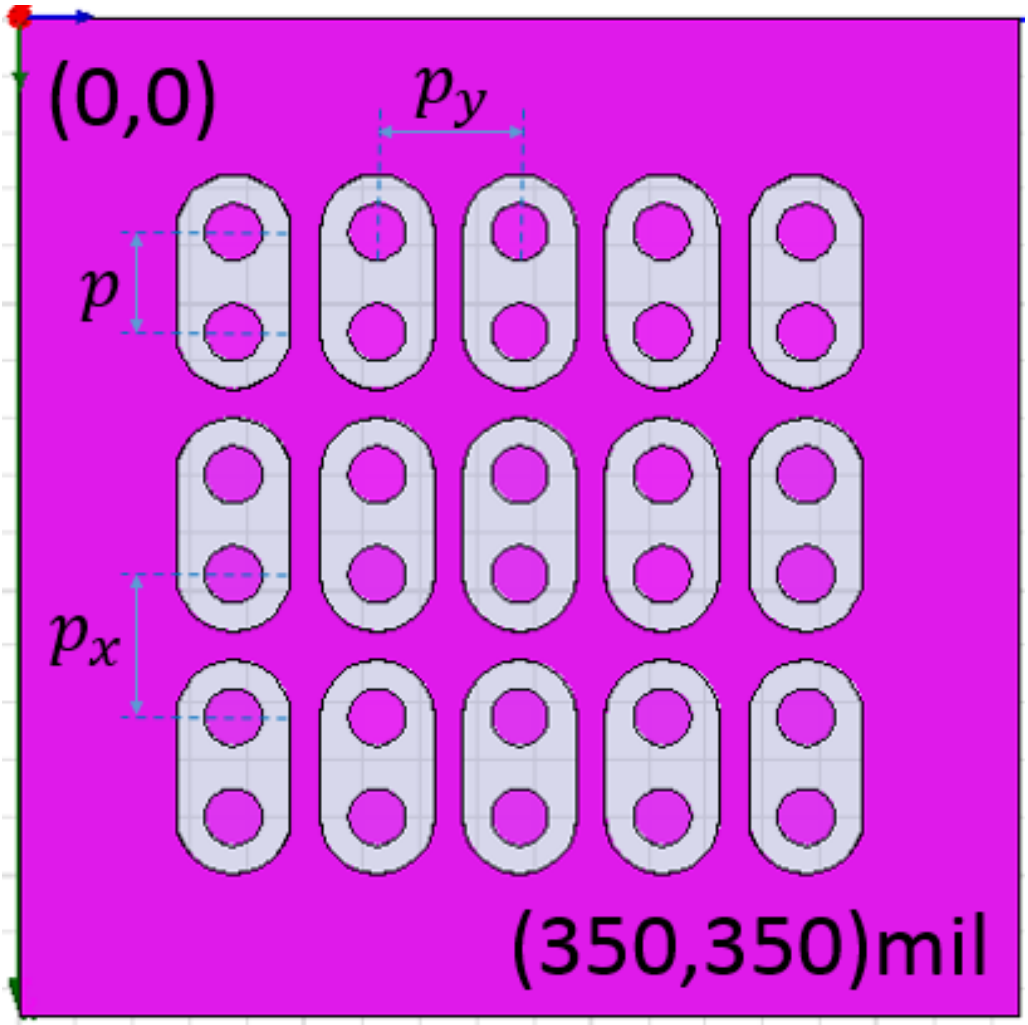

Figure 3.27. Top view of 3x10 dense via array for case F.

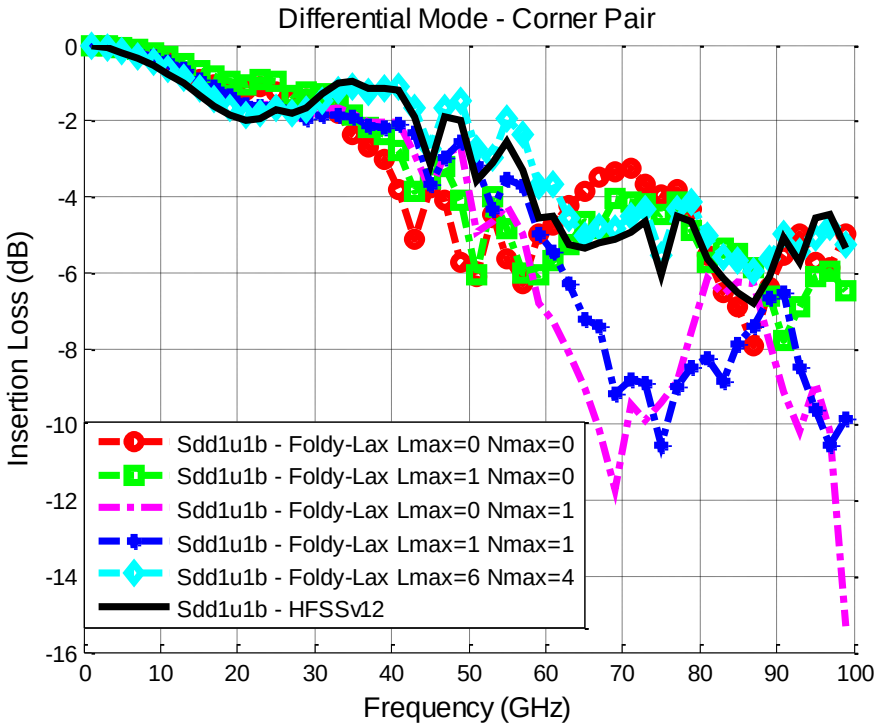

Figure 3.28. Insertion loss of differential mode for corner pair for case F.

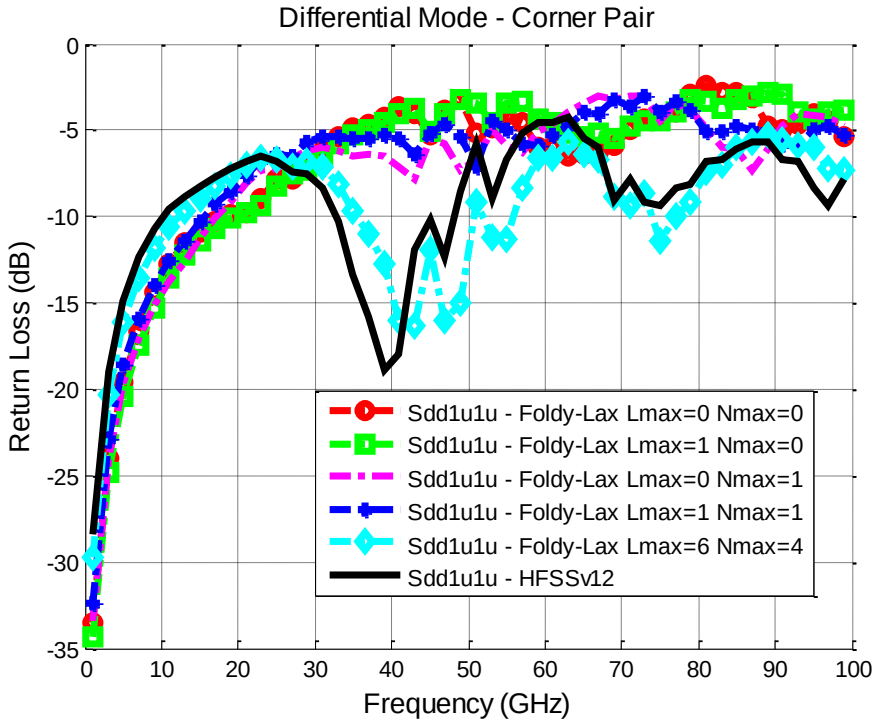

Figure 3.29. Return loss of differential mode for corner pair for case F.

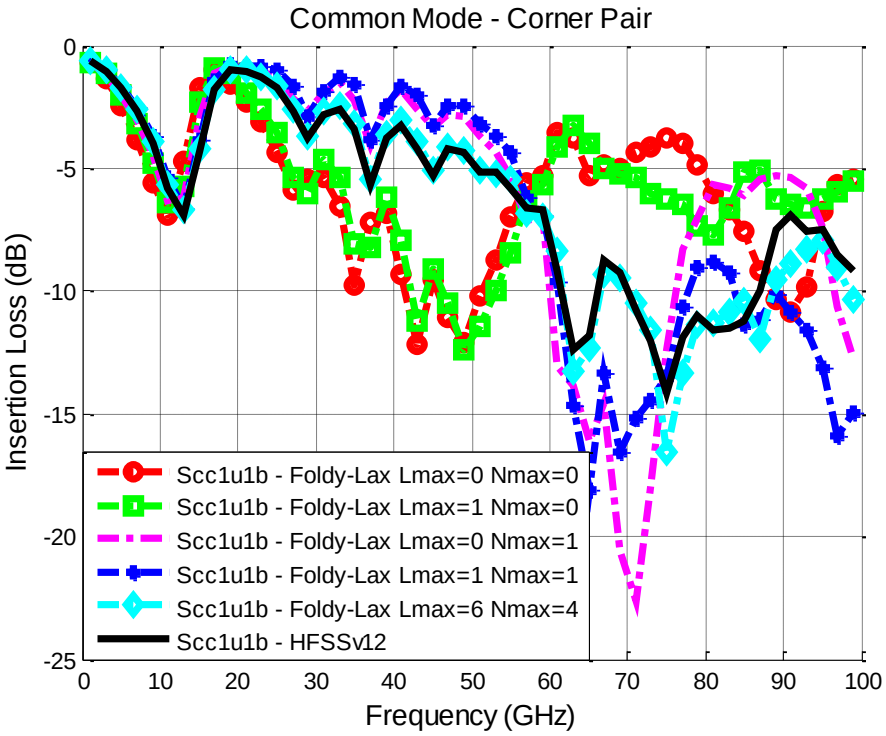

Figure 3.30. Insertion loss of common mode for corner pair for case F.

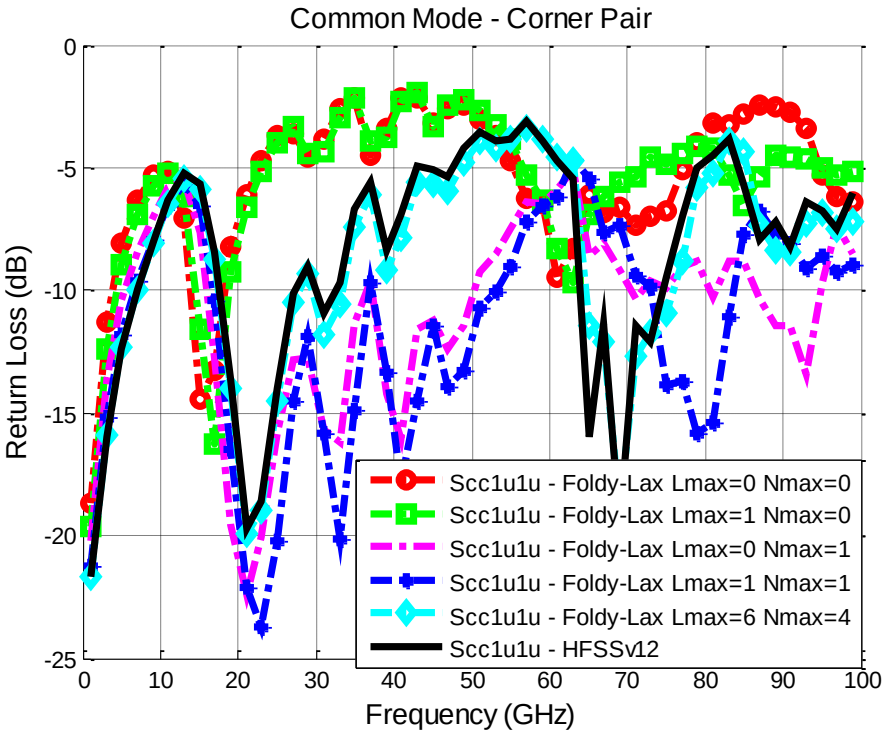

Figure 3.31. Return loss of common mode for corner pair for case F.

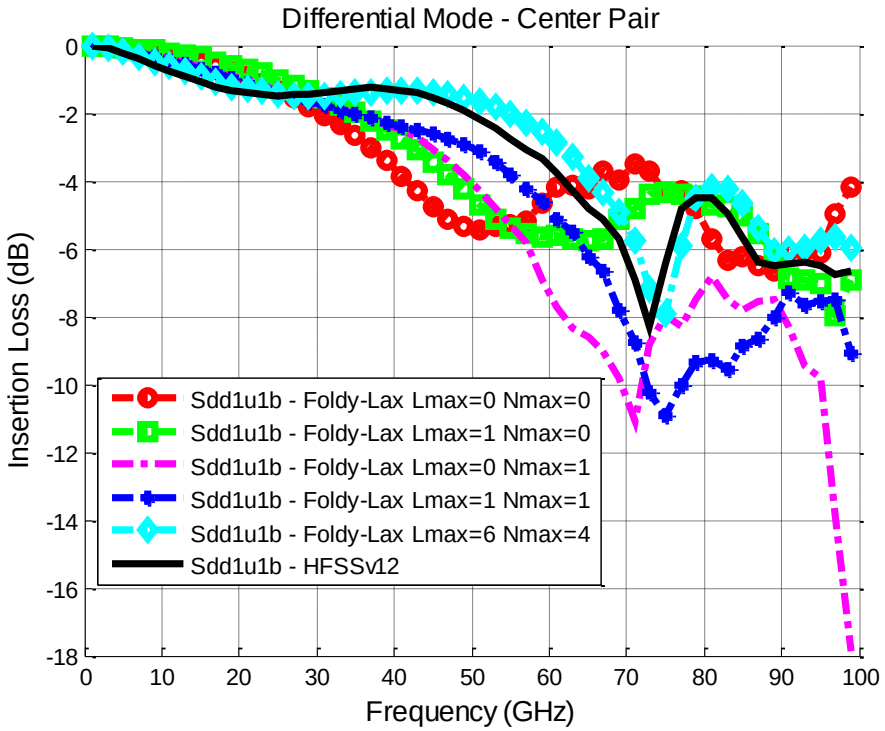

Figure 3.32. Insertion loss of differential mode for center pair for case F.

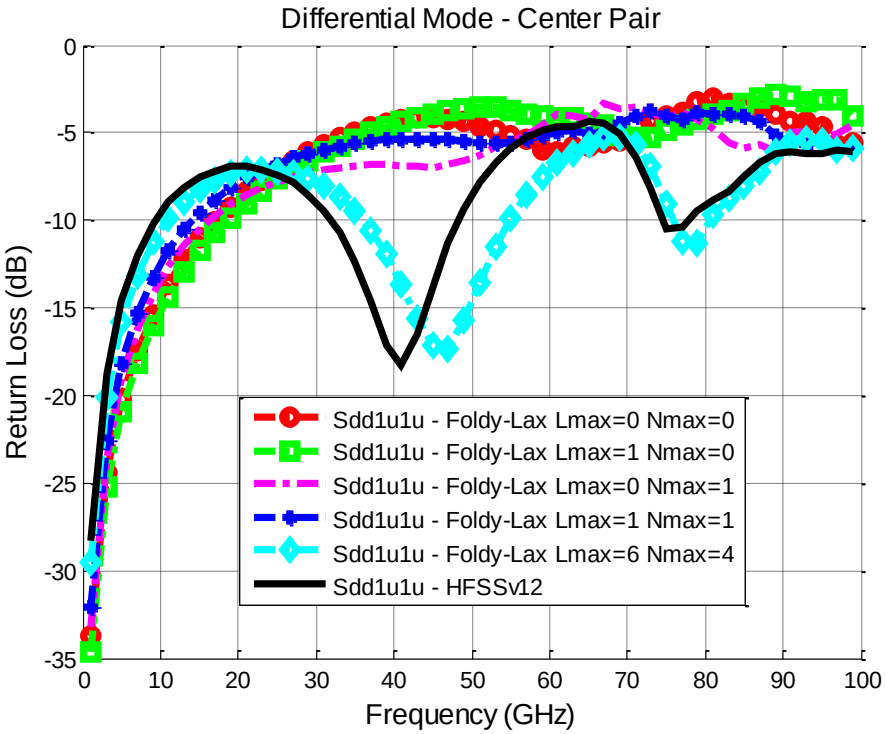

Figure 3.33. Return loss of differential mode for center pair for case F.

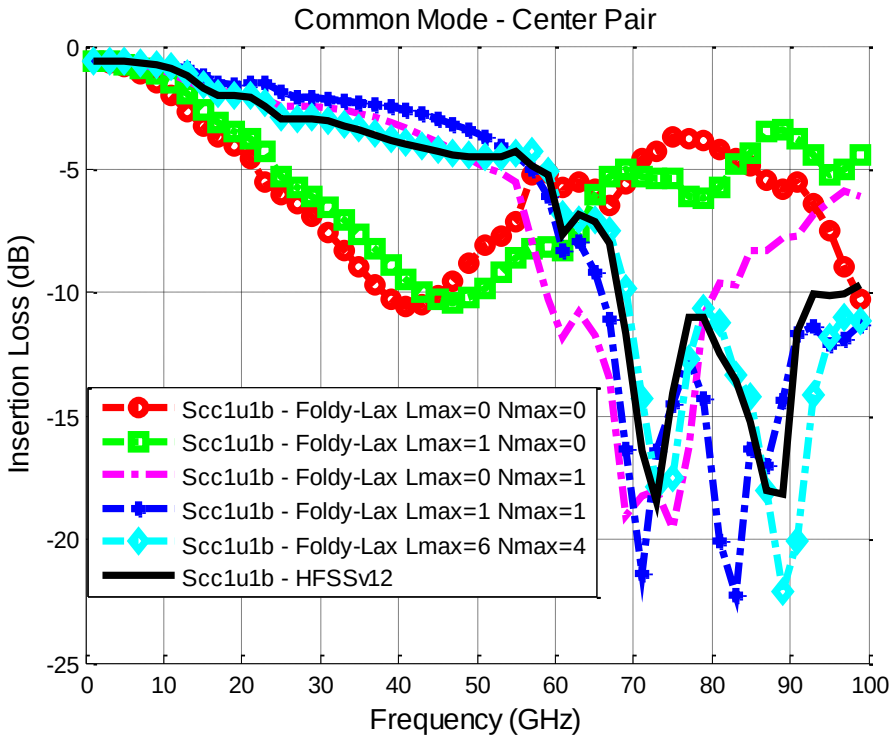

Figure 3.34. Insertion loss of common mode for center pair for case F.

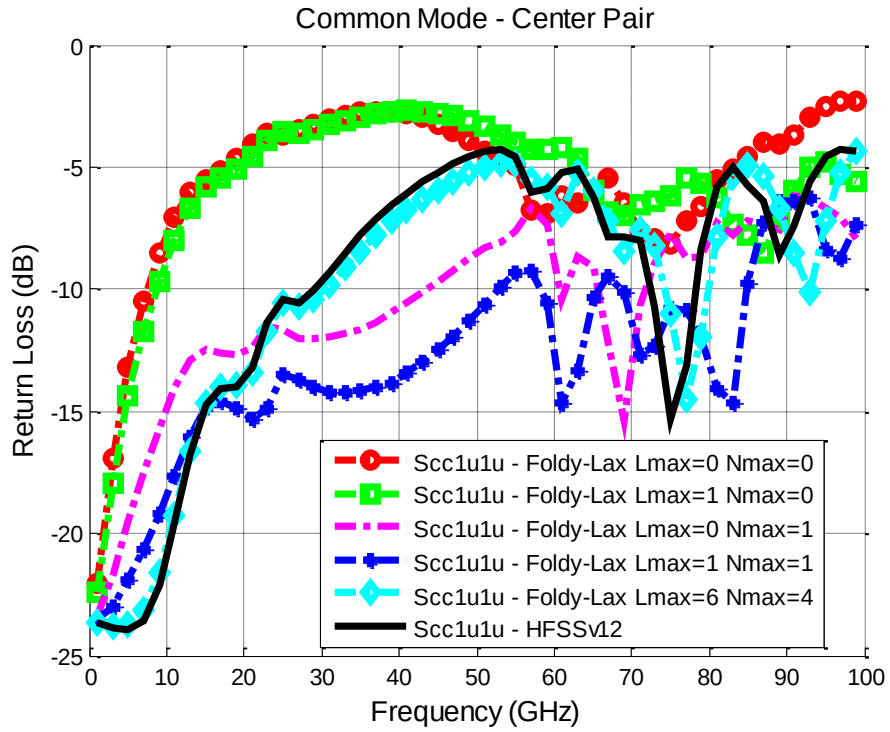

Figure 3.35. Return loss of common mode for center pair for case F.

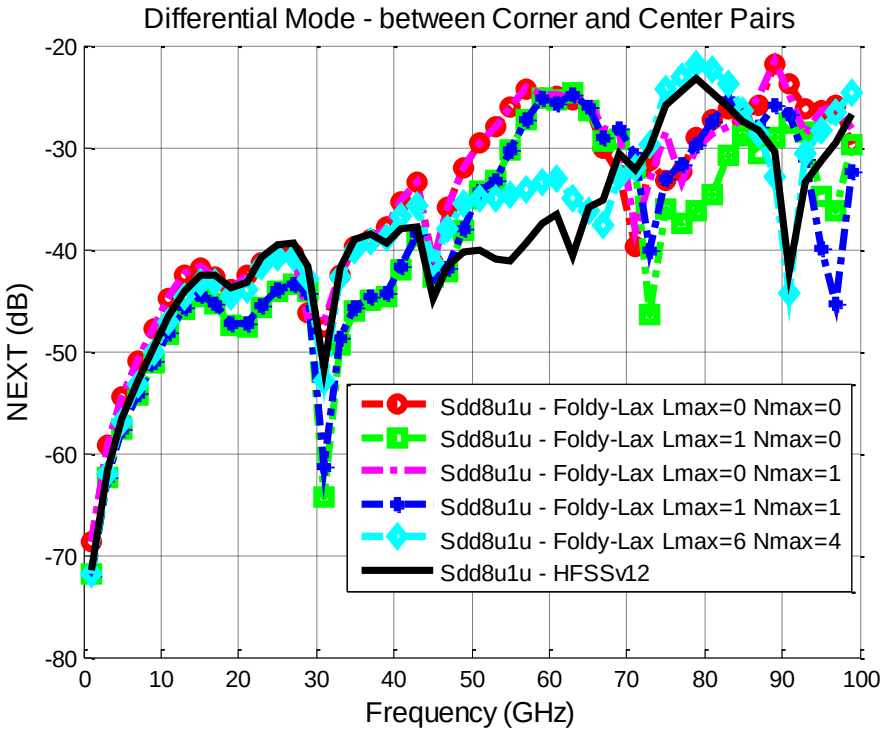

Figure 3.36. NEXT differential mode for center/corner pairs for case F.

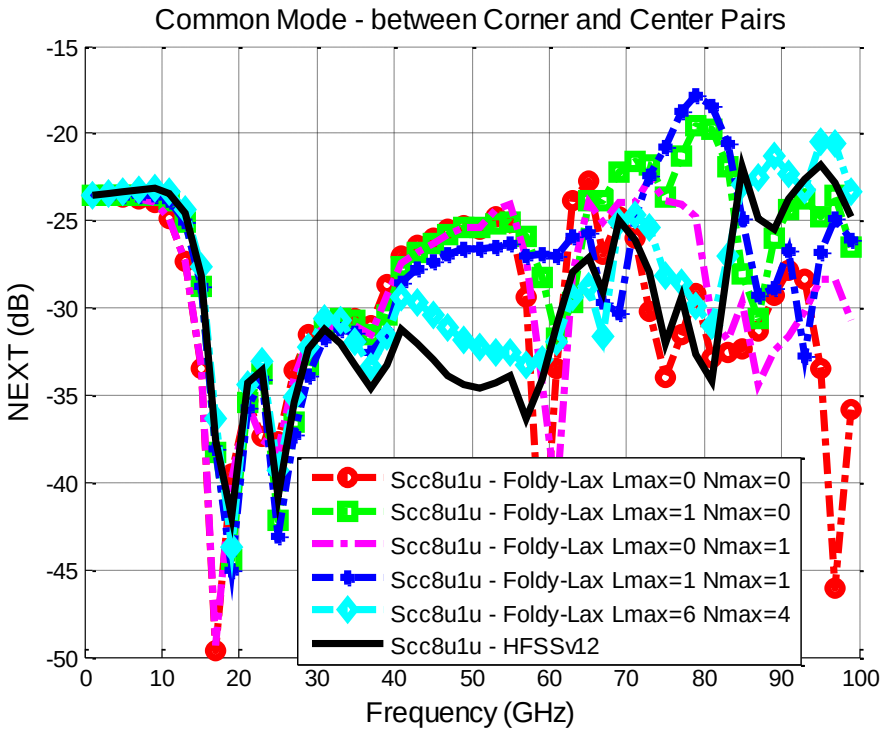

Figure 3.37. NEXT common mode for center/corner pairs for case F.

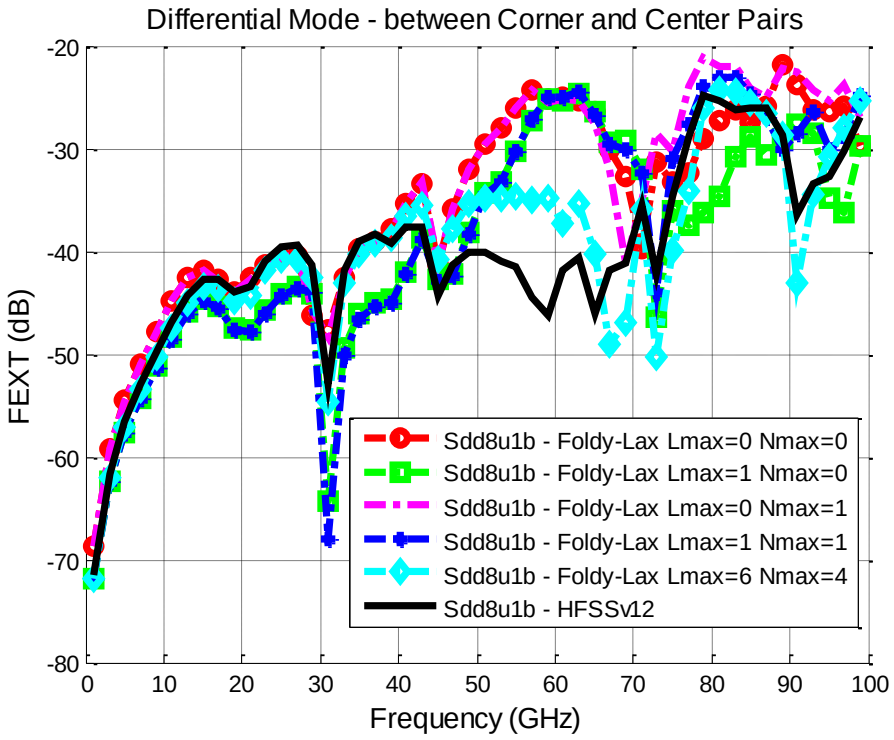

Figure 3.38. FEXT differential mode for center/corner pairs for case F.

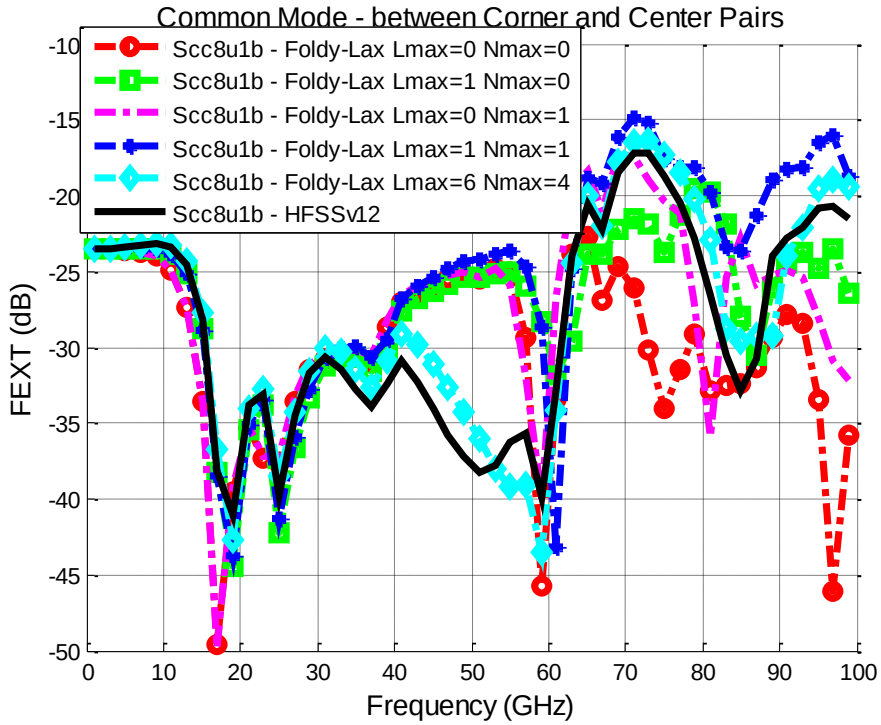

Figure 3.39. FEXT common mode for center/corner pairs for case F.

Fig. 3.28-3.31 show the insertion loss and return loss, for differential mode and common mode respectively, for corner pair which is the left top via pair. Fig. 3.32-3.35 show the insertion loss and return loss, for differential mode and common mode respectively, for center pair which is the middle pair. Fig. 3.36-3.39 show the NEXT and FEXT, for differential mode and common mode respectively, between the corner and center vias,

From the Fig 3.28-3.39, we can see that for dense via array for differential singling in small cavity, for both insertion loss and return loss, the higher order modes effects make stronger contributions for the corner pair than the center pair, for both differential mode and common mode. This is due to the physical closer locations to the cavity side walls for the corner pair than the center pair is. Also, without considering higher order modes effects may make the simulation show the resonances at lower frequency than they should be, which then limit the real design requirements.

For NEXT and FEXT between the corner pair and center pair, unlike the single through hole via case as shown in case A, the higher order mode effects show up in lower frequency as 10GHz. This means their effects are more important for the differential signaling vias than the case of single through hole via case, due to two vias sharing same antipad and strong near field coupling in high frequency.

Based on the simulations shown above, we suggest that the vias should be placed not close to the cavity side walls in order to avoid the reflections from the walls. These modes reflections may lead to resonances at undesired frequency. More vias placement also help shift the cavity modes to higher frequency.

3.9 CPU REQUIREMENT AND DISCUSSIONS

In this section, I discuss the CPU requirement and discussions between the Foldy-Lax approach and HFSS v12. The PC configurations used are: Intel(R) Core(TM)2 Duo E7300 2.66GHz processor, 3GB RAM and Windows Vista 32-bit operating system.

The Foldy-Lax approach is implemented using MATLAB. In the Foldy-Lax approach, several parameters make main contributions for the CPU resources as listed in Table 3.1. There are two MoM parts both with 1D discretization. The two parts are not coupled with each other. The first part is to solve Laplace equation, of equations (3.46) and (3.47), in the antipad to find the charge distributions on the boundaries of the vias and the antipad. The number of unknowns for

this part is denoted as N_c. Since Laplace equation is used, this part is independent of frequency and needs to be solved only once for all frequencies. With the charges distribution on boundaries of vias and antipad, I then do 1D integration to get incident field coefficients of Foldy-Lax equations for each frequency as shown in equations (3.49) and (3.51). The second MoM discretization part is for obtaining $\bar{\bar{Z}}$ of the cavity as shown in equation (3.3). I need to do the matrix filling and the matrix inversion for the cavity problem at each frequency in order to calculate $\bar{\bar{X}}^{Wqp} = \bar{\bar{\gamma}}^{(qW)}\bar{\bar{Z}}^{-1}\bar{\bar{Q}}^{(Wp)}$. The number of unknowns for this part is denoted as N_t. The boundary of the cavity is discretized using eight points per wavelength. The construction of the impedance matrix and the inverse needs to be performed for each frequency. For the Foldy-Lax equations, the highest harmonic M and highest waveguide mode L also impact the unknown's numbers. However, they are small because the vias and antipad are small. When comparing with HFSS, N_t, M and L vary with frequency and cases. The cavity boundary wall effects are only performed for $l = 0$ mode and are not included for the higher order modes which are evanescent.

In HFSS setup, for all the cases, in the adaptive solutions, the maximum number of passes is 10 and maximum delta S is 0.02. All the boundaries of the cavity walls are set as PMC boundaries. Since HFSS is based on FEM, which solve every frequency as static field after one time meshing, the total CPU time for every frequency treatment in HFSS is nearly same, as can be seen from Table 3.2, 3.4 and 3.5. Table 3.6 shows the comparisons for case E and F.

Table 3.1. Case A: Foldy-Lax Approach

Parameters	5GHz ($\lambda = 0.03$m)	20GHz ($\lambda = 0.0075$m)
MoM unknowns N_c	100	100
MoM unknowns N_t	20	72
Highest harmonic M	1	2
Highest mode L	4	5
Incident Field Integration for each l (average)	0.06 sec	0.06 sec
Matrix filling for $\bar{\bar{Z}}$ for l=0 only	0.06 sec	0.37 sec
Matrix filling for $\bar{\bar{X}}$ for each l (average)	0.12 sec	0.39 sec
Assembly and Solve Matrix of Foldy-Lax for each l (average)	0.06 sec	0.20 sec
Total CPU	1.46 sec	4.29 sec

I compare the main CPU consumption time between Foldy-Lax approach and HFSS v12 for case A in Table 3.1 and 3.2 at 5GHz and 20 GHz, and for case C in Table 3.3 and 3.4 at 5GHz and

50GHz, respectively. In Table 3.5, we compared all the cases at 5GHz and 20GHz for the two simulation methods. For the MoM setup, we use rule of 8 segments per wavelength at each operation frequency point for numerical discretization. The circumferences of the three cavities are 0.066 m, 0.0508 m and 0.0508 m. The number of unknowns N_t are shown in the tables. Note that N_c does not change with frequency. I choose an enough number for the all the frequency operations. From these tables, the proposed method is generally faster than HFSS, especially for the structure which includes more vias like case A. The proposed method can be furthermore speeded up for at least 2-3 times if programmed with C++ as the language used by HFSS, but not Matlab, based on the authors' experiences.

Table 3.2. Case A: HFSS v12

Parameters	5GHz	20GHz
Tetrahedra Number	33910	33910
Simulation Setup Time	2 sec	2 sec
Matrix Assembly Time	17 sec	17 sec
Solver MRS1	27 sec	27 sec
Total CPU	46 sec	46 sec

Table 3.3. Case C: Foldy-Lax Approach

Parameters	5GHz($\lambda = 0.028$m)	50 GHz($\lambda = 0.003$m)
MoM unknowns N_c	300	300
MoM unknowns N_t	15	144
Highest harmonic M	4	5
Highest mode L	0	1
Incident Field Integration for each l (average)	0.09 sec	0.10 sec
Matrix filling for $\bar{\bar{Z}}$ for l=0 only	0.05 sec	1.36 sec
Matrix filling for $\bar{\bar{X}}$ for each l (average)	0.05 sec	0.25 sec
Assembly and Solve Matrix of Foldy-Lax for each l (average)	0.03 sec	0.11 sec
Total CPU	0.33 sec	2.35 sec

Table 3.4. Case C: HFSS v12

Parameters	5GHz	50 GHz
Tetrahedra Number	3194	3194
Simulation Setup Time	0.2 sec	0.2 sec
Matrix Assembly Time	1.2 sec	1.2 sec
Solver MRS1	2.4 sec	2.4 sec
Total CPU	3.8 sec	3.8 sec

Table 3.5. CPU Run Time at Frequency 5Ghz and 20ghz Comparisons For Case A-C

Case	Foldy-Lax: 5GHz	Foldy-Lax: 20 GHz	HFSS v12: 5 GHz	HFSS v12: 20 GHz
A	1.46 sec	4.29 sec	46 sec	46 sec
B1	0.24 sec	0.77 sec	3.2 sec	3.2 sec
B2	0.30 sec	0.9 sec	7 sec	7 sec
C	0.33 sec	0.92 sec	3.8 sec	3.8 sec

Table 3.6. CPU Run Time per Frequency Comparisons For Case E-F

Case/Method	Foldy-Lax/1D MoM	HFSS v12
A	25 sec	720 sec
B	10 sec	196 sec

3.10 CONCLUSIONS

In this chapter, I proposed a new fast and broadband modeling method for signal/power integrity analysis for vias structures in electronic packages and printed circuit boards. The major advantage of the proposed method resides in the decomposition of the complex 3-D problem into simple mostly analytical method, at most 1D meshing and generalized T-matrix. With the generalized Foldy-Lax multiple scattering equations method, the computation resources are reduced for the complete signal/power integrity analysis of high speed vertical interconnects modeling in 3D IC, with good accuracy.

Chapter 4. MODELING TRACES IN POWER/GROUND PLANES WITH VIAS FOR LINK LEVEL SIMULATION ON MULTILAYER ELECTRONIC STRUCTURES

4.1 SUMMARY

In this chapter, geometry decomposition are proposed to efficiently solve the problem of power/ground (P/G) planes with vias and traces, for analysis of link level simulation on multilayer electronic structures. The geometry decomposition is based on the modes decoupling method and boundary value problem definitions for cavity with vias and striplines. For the modeling details, striplines structure can be solved according to multi-conductor transmission line (MTL) theory, and vias and irregular power/ground planes are treated as a whole which is solved by Foldy-Lax multiple scattering equations method, to obtain the coupling effects among vias and cavities. Then the modal effects of striplines can be recombined with the modal solution of vias and cavities effects. Different scenarios are analyzed to show that the proposed method can be applied to efficiently make link level simulations. Numerical results for the method are in good agreement with a commercial full wave numerical tool up to 40 GHz.

4.2 INTRODUCTION

In current microelectronic circuit structures, high-speed interconnects play key role for all levels of microelectronic system, including chip, packaging, and printed circuit boards (PCB), although the boundaries among these levels are more and more blurring. Due to the ever-rising clock rate and edge rate of chip-package-board systems, dimensions of interconnect structures become electrically larger as frequencies increase. The interconnects have impacts on the signal integrity (SI) and power integrity (PI) in a power distribution network (PDN). High speed interconnects are then increasingly becoming the major bottlenecks in the design of high performance electronic circuits. The passive interconnects include two main types, the first is the vertical interconnect or via, and the other is horizontal interconnect or trace. For traces, microstrip line and stripline are two main types. Inside the cavity between different layers, striplines are the most commonly used transmission-line structures in the microelectronic system because of its

advantage of radiation reduction, since the power/ground (P/G) planes that shields the signal trace. Then for a high speed interconnects system, P/G planes, vias and striplines are the three most essential elements. Therefore, the investigation of efficient modeling and simulation method, which can provide the coupling effects among all of elements, becomes important.

Different modeling methods have been developed to address the problem or parts of the whole problem [14, 15, 26, 27, 29-31, 38, 39]. For example, for horizontal interconnects or traces part, an efficient stripline model was investigated and proposed in [38], which includes the coupling effects among traces and P/G planes. For vertical interconnects or vias part, the modeling problem is complicated, since the modes effects of through hole via structures usually couple tightly with P/G planes and other vias. In [26, 27], for lumped circuit model, cavity model theory has been applied to extract parasitic captaincies and inductances due to the rectangular cavity effects with sparse vias, to model the coupling among vias and planes. Meanwhile, a rigorous electromagnetic full wave method is investigated for modeling the scattering effects of multiple vias and P/G planes for circuit model extractions [29] and full wave simulations [14, 30, 39]. It is worthwhile to note that the multiple scattering equations method used in [14, 30, 39] are actually forms of generalized Foldy-Lax equations [35-37]. In [31], a hybrid method is used to model the case of large number of vias. For the whole problem modeling strategies, extracted RLGC parameters for transmission lines and through hole vias and cavity model method are used to model vias-traces-planes for rectangular shape cavity [15, 28]. For full wave method, a combination of 2D integral equation method and 2D finite element method in [32] is used to model vias and traces in arbitrarily shaped cavity with multivias of arbitrary shapes and inhomogeneous media in substrate, up to 2GHz. In [40], a modeling method of PCB and packages was proposed through a way of extended five-port circuit model for via-stripline transition based on [39]. However, these methods have limitations for their modeling strategies. The circuit models proposed in [15, 28, 40] depend on parasitic elements very much. The parasitic elements include capacitance between via and P/G planes, the parallel plate impedance Z_{pp}, mutual capacitance and inductance among vias, transmission line model for traces, etc.. These parasitic elements are geometry dependent and must be pre-studied before being used for building up the models. For irregular geometries, e.g., for the cases of irregular cavity, eccentric vias and multiple vias sharing one antipad, complete parasitic elements are difficult to be extracted with good accuracy over a broadband frequency use [28], and the elements number can be huge if the geometry includes large number of vias and traces. The hybrid

full wave method used in [24, 32] showed examples only in relatively low frequency range (compared with 40GHz in this chapter).

In our previous work, we decomposed the via-trace transition problem as exterior problem and interior problem [4]. The microstrip line to via transition structure solved in [42] is exterior problem, and the problem of multiple scattering among vias inside the cavity or waveguide solved in [4, 19, 34-37, 42] is interior problem. For interior problem, we use a mostly analytical technique of Foldy-Lax equations to compute the full wave solution of Maxwell equations that includes multiple scattering among cylindrical vias in both infinite large waveguide [4, 19, 34, 42] and finite size cavity [35-37], with arbitrarily shaped antipad for single through hole via case and multiple vias sharing same antipad case. The methodology has good comparisons with HFSS [19, 35, 36, 42, 43] and with experiments [5]. In the recent work on the Foldy-Lax approach [36, 43], as described in chapter 2 and 3, for the case of multiple vias in antipad of arbitrary shape in infinite and finite planar waveguide, I utilize generalized T matrix that includes wall effects and 1D numerical technology [37] to model the coupling effects among vertical vias and P/G planes. I showed that the incident fields on the vias can be calculated by 1-dimensional line integrals of the surface charges on the vias and on the ground planes [36]. In this chapter, I proposed an efficient, fast and broadband full wave method to model the chip-package-board system for interior problem, which includes effects of irregular P/G planes with arbitrarily shaped antipad, multiple vias scattering and signal vias-traces transitions for multilayered electronic structures, based on the Foldy-Lax equations method. Compared with other circuit model method in [15, 24, 28, 32, 40], the proposed full wave method provides fast and broadband simulation results for general geometries. It is shown that the proposed hybrid methodology is validated by full wave commercial tool up to 40GHz. The approach shown in this paper can be considered as an extension of chapter 3, for complete link level simulation.

For the paper organization, we first discuss modes of P/G planes and stripline, and modes conversation at the location of via-stripline structure. We then discuss cavity, via, stripline boundary value problem. We show that the whole structure can be decomposed into problem for P/G planes with vias and problem for stripline structure. Then two equivalent microwave networks for two these two problems are then parallel. The parameters of problem for stripline can be extracted by using multi-conductor transmission line (MTL) theory. The parameters of problem for P/G planes with vias can be calculated by using Foldy-Lax equations method. We then

combine these two microwave parameters to calculate the parameters for the whole structure. We also use cascaded Y-parameters method to obtain the parameters of multilayer electronic structures.

In the numerical results, we show that the proposed full wave method can be applied to a wide range of complicated structures, including the eccentric via structures, differential signaling structures and dense via array structures, for the first time. Unlike all the other circuit methods in [15, 24, 28, 32, 40], for modeling of irregular geometries, no parasitic parameters need to be extracted. All the numerical discretizations and integrals are based on only one-dimensional techniques if needed, which saves many computation resources.

Also, higher order cavity modes effects are thoroughly discussed for their impacts on the modeling accuracy, for the first time. It is shown that these modes effects need to be included in high frequency (above 20GHz in this paper) simulation for the accuracy issue of via-trace modeling.

4.3 FORMULATION OF THE METHODOLOGY

4.3.1 *A. Mode Coupling between P/G Planes and Stripline at Via-Stripline Connection*

Since the structure of cavity is a close one, its modal spectrum is comprised of a infinite number of discrete modes, and they can be classified into TE modes and TM modes. As stated in chapter 2, for P/G planes with via-hole structure, only TM modes can be excited. These TM modes include the TEM mode which is the fundamental propagating mode and higher order modes. For the microstrip line, it is an open structure, its modal spectrum is comprised of a discrete number of surface waves which correspond to a finite number of propagating modes, a continuous spectrum of evanescent waves, and a continuous leaky modes due to eigenvalue field which represent radiation losses. For simplicity, we only take into account the surface-wave type modes [45]. For these surface-wave type modes, they can also be classified into TE and TM modes. As the frequency of operation is increasing, the existence of these higher order modes is undesirable and the use of the microstrip line is restricted to be below the lowest order TE_1 mode frequency f_{TE1} is [45]

$$f_{TE1} = \frac{c}{4h\sqrt{\varepsilon_r - 1}} \tag{4.1}$$

where c is the light speed in vacuum, h is the substrate thickness for the microstrip line and ε_r is the relative dielectric constant. Below this cut off frequency, the quasi-TEM mode can be assumed as the dominant propagating mode. Since a stripline sandwiched by the P/G planes can be split into two microstrip lines, its cut off frequency of TE_1 can also be estimated with (4.1).

An efficient model of stripline between P/G planes based on modal decomposition method was proposed in [38], under the assumption of quasi-TEM mode. As the frequency gets higher, the quasi-TEM assumption need to be carefully considered for the model effectiveness. For the structures investigated in this chapter, e.g., $h = 20\ mil$, $\varepsilon_r = 3.84$, then the f_{TE1} is about 87GHz. Consider the design margin, in this chapter, I make model simulation up to nearly half of the first higher order mode cutoff frequency, which is 40GHz.

For cavity structure with vias and traces, the modes of P/G planes excited by the via signal and the modes propagating on the stripline can be coupled at the via-trace transition location. We next discuss the modes coupling and their decoupling based on electromagnetic analysis.

4.3.2 *B. Boundary Value Problem Definition of P/G Planes with Vias Connecting with Stripline*

Fig. 4.1 shows the top and cross section of the considered elementary structure, comprising P/G planes and two vias connecting with a stripline. Since only TM mode for P/G planes cane be excited, then let

$$k_{zl} = \frac{l\pi}{d}; k^2 - k_{zl}^2 = k_{\rho l}^2 \tag{4.2}$$

where $l = 0,1,2\ldots..,\quad d = d_1 + d_2$ is the separation between the two plates, and k is the wavenumber. Let E_z be the electric field on the z direction, then the wave equation in the whole region is

$$\left(\nabla_t^2 + k_{\rho l}^2\right)E_z = 0 \tag{4.3}$$

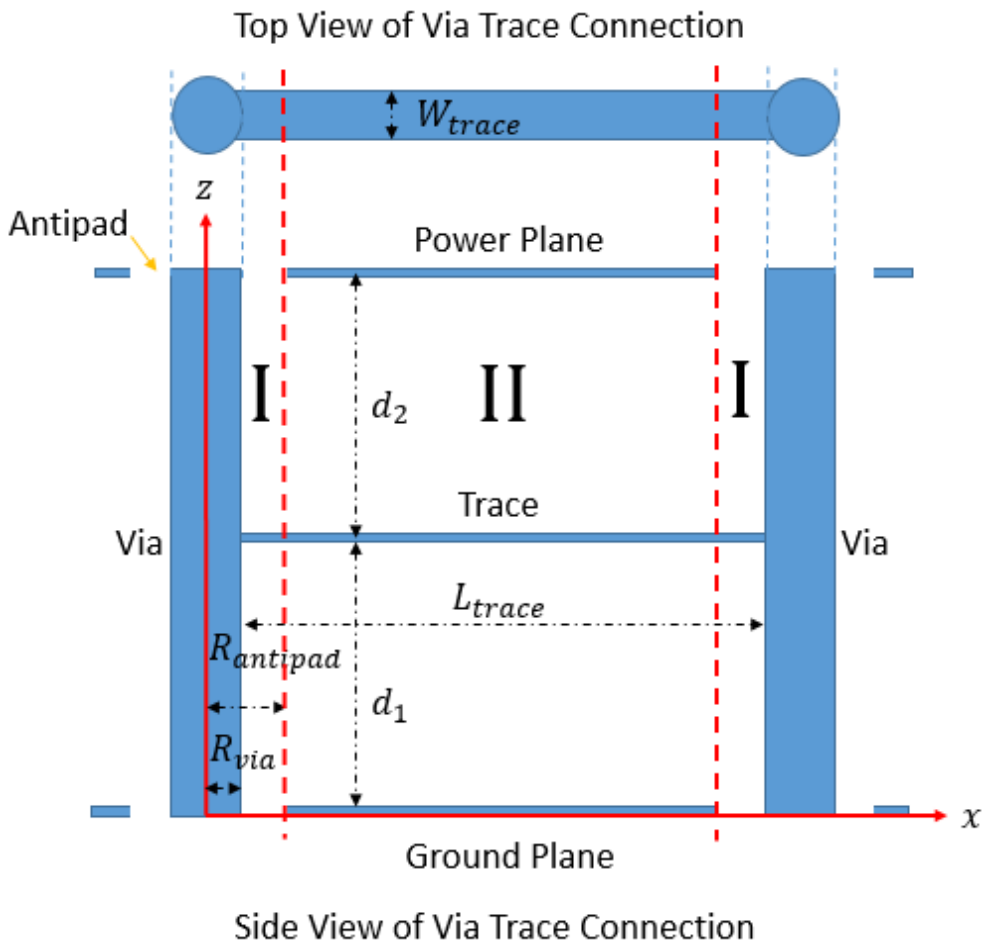

Figure 4.1. Top and side view of two vias inside a parallel waveguide connected with a trace.

Note that the trace we considered here is for zero thickness. All the conductors are PEC. As the antipad radius r_{anti} is electrically small, the via hole region can be treated as PMC, since the $E_z \approx 0$ in the antipad region. The cavity side walls can also be treated as PMC, as its thickness being electrically small. Let $\bar{E}$ be the electric field, $\hat{n}$ be the normal direction, then the boundary conditions for the problem are

$$\hat{n} \times \bar{E} = 0, at\ PEC \tag{4.4}$$

and

$$\hat{n} \times \nabla \times \bar{E} = 0, at\ PMC \tag{4.5}$$

According to the geometry of the problem, if we make approximation that we ignore the fringing field at the via-trace connection due to its being short, then the whole problem can be

decomposed into two kinds of problems, the P/G planes with vias problem which is for geometry I and the stripline problem which is for geometry II as shown in Fig. 4.2.

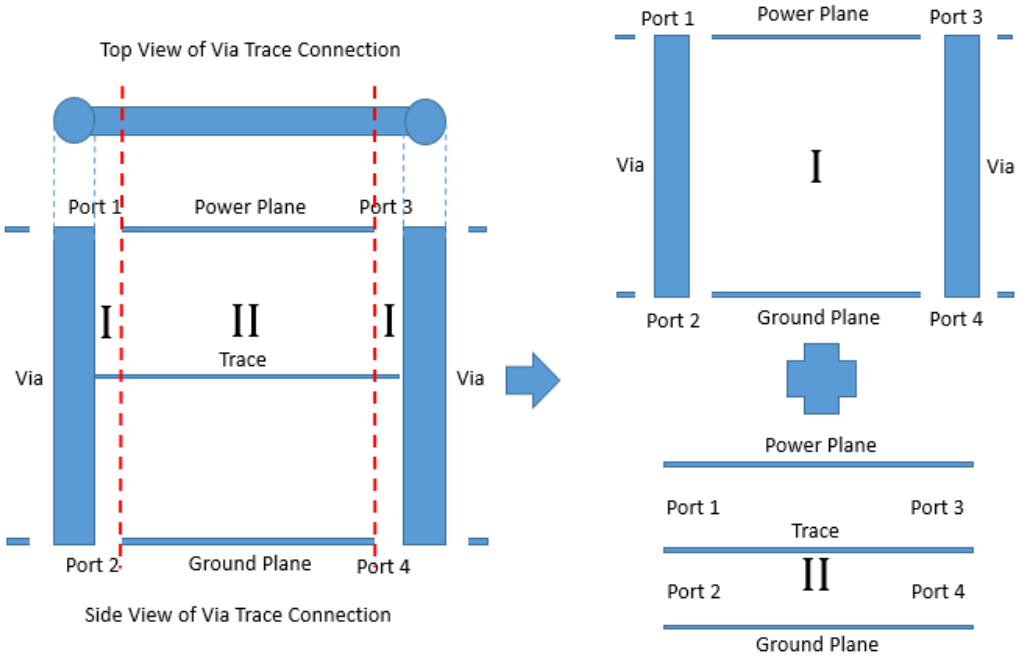

Figure 4.2. Geometry decomposition.

The problem of geometry I can be solved by the Foldy-Lax equations method as described in chapter 3, for P/G planes with multiple vias. The problem of geometry II can be solved analytically or numerically, depending on the case, for stripline solution. Hence the geometry decomposition is also the mode decomposition between P/G planes with vias and stripline.

Since both the vias and trace are referenced to the P/G planes, their equivalent microwave networks are then parallel. Let $\bar{\bar{Y}}_{P/G}$ be the admittance matrix for problem of geometry I and $\bar{\bar{Y}}_s$ be the admittance matrix for geometry II. Then, a generalized model can be formulated for one cavity and the total admittance matrix of the original problem $\bar{\bar{Y}}$ is

$$\bar{\bar{Y}} = \bar{\bar{Y}}_{P/G} + \bar{\bar{Y}}_s \tag{4.6}$$

Note that for problem shown in Fig. 4.2, both $\bar{\bar{Y}}_{P/G}$ and $\bar{\bar{Y}}_s$ are four ports network. We will then discuss how to obtain them in the next sections.

4.3.3 *C. 4-Ports Admittance Matrix $\bar{\bar{Y}}_s$ for Stripline*

We first show how to obtain admittance matrix $\bar{\bar{Y}}_s$ for geometry II for stripline problem. Usually, a transmission line including stripline is a 2 ports network, assume we can obtain the admittance matrix for stripline with 2 ports is $\bar{\bar{Y}}_{tl}$, analytically or numerically. In this section, we first show how to obtain $\bar{\bar{Y}}_{tl}$. We then show how to transfer the 2 ports parameter $\bar{\bar{Y}}_{tl}$ to 4 ports parameter $\bar{\bar{Y}}_s$ for a stripline at every via-trace location where the modes of P/G planes with vias and modes of stripline couple.

For a general transmission line, its 2 ports admittance matrix $\bar{\bar{Y}}_{tl}$ is [53]

$$\bar{\bar{Y}}_{tl} = \begin{bmatrix} \frac{1}{jZ_0 tanh(\gamma L_{trace})} & \frac{j}{Z_0 sinh(\gamma L_{trace})} \\ \frac{j}{Z_0 sinh(\gamma L_{trace})} & \frac{1}{jZ_0 tanh(\gamma L_{trace})} \end{bmatrix} \tag{4.7}$$

where Z_0 is the characteristic impedance of the transmission line, γ is complex propagation constant and L_{trace} is the length of the transmission line.

A side view of typical stripline structure is shown in Fig. 4.3, assume its width is W_{trace}, its length is L_{trace} and the length for P/G planes is $L_{P/G}$. The Z_0 of the stripline structure can be calculated analytically according to the experience formula shown in [53] or calculated by solving Laplace equation to obtain the charge distributions on the trace and the per unit length (p.u.l.) capacitance $C_{p.u.l.}$with numerical method, for example, by using the moment method [54]. The $\bar{\bar{Y}}_{tl}$ then can be obtained.

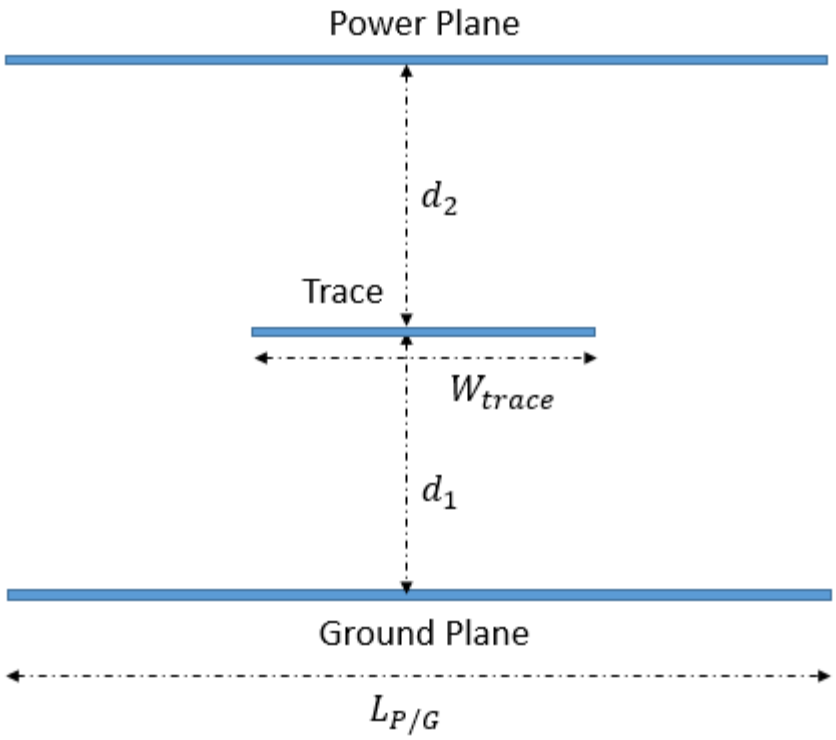

Figure 4.3. Side view of a general stripline structure.

Next, by using the skin effect approximation and modal decomposition method [38, 24, 28, 32, 40], the 4 ports admittance matrix $\bar{\bar{Y}}_s$, which is related with 2 ports admittance matrix $\bar{\bar{Y}}_{tl}$ for geometry II, can be extracted by applying MTL theory for the three conductor problem.

Note that the MTL theory applied here is under assumption of TEM mode for both parallel plate and stripline. As we stated in part A in this section, for stripline modes, the mode TE_1 for our interested geometry size is about 80GHz, which is above our interested frequency 40GHz. However, for parallel plate modes, the cutoff frequency of its lowest higher order TM mode (TM_{z01} or TM_{z10}) can be from any frequency, depending on its geometry size. Typically for a large PCB with size of 10 inch, the cutoff frequency of its first lowest higher order mode can be in the level of 100MHz. Above this cutoff frequency, the higher order modes can be excited and the MTL theory with the assumption of TEM mode is not accurate for parallel plate structure, but such assumption is still good for stripline structure. Hence we only use MTL theory to extract $\bar{\bar{Y}}_s$ for geometry II. The $\bar{\bar{Y}}_{ppTEM}$ for parallel plate structure without vias here is just auxiliary.

A general problem of geometry II are shown in Fig. 4.4. In Fig. 4.4, subscript l indicates left side, subscript r indicates right side, subscript p indicates power plane, subscript g indicates

ground plane, subscript s indicates stripline, subscript pp indicates parallel plate mode, subscript tl indicates transmission line mode. For both left and right side ports, with the ground plane as the reference plane, by using MTL theory, following transformation matrices can be used to decouple the parallel plate mode and stripline mode coupling for this problem [46]

$$\begin{bmatrix} V_{l/rp} - V_{l/rg} \\ V_{l/rs} - V_{l/rg} \end{bmatrix} = \begin{bmatrix} 1 & 0 \\ -k_i & 1 \end{bmatrix} \begin{bmatrix} V_{l/rpp} \\ V_{l/rtl} \end{bmatrix} \tag{4.8}$$

$$\begin{bmatrix} I_{l/rp} \\ I_{l/rs} \end{bmatrix} = \begin{bmatrix} 1 & k_i \\ 0 & 1 \end{bmatrix} \begin{bmatrix} I_{l/rpp} \\ I_{l/rtl} \end{bmatrix} \tag{4.9}$$

The above equations show that the current through power plane is equal to the sum of the currents from the parallel-plate mode, and those from the transmission line mode multiplied by the factor k_i [28], which is a dielectric height ratio, is

$$k_i = -\frac{d_1}{d_1 + d_2} \tag{4.10}$$

where d_1 and d_2 are the distances between the trace and bottom plane and between the top plane and the trace, respectively. Similarly, the voltage between the trace and the lower plane is equal to the voltage drop due to the transmission line mode subtract the drop between the planes due to the parallel-plate mode, multiplied also by the factor k_i.

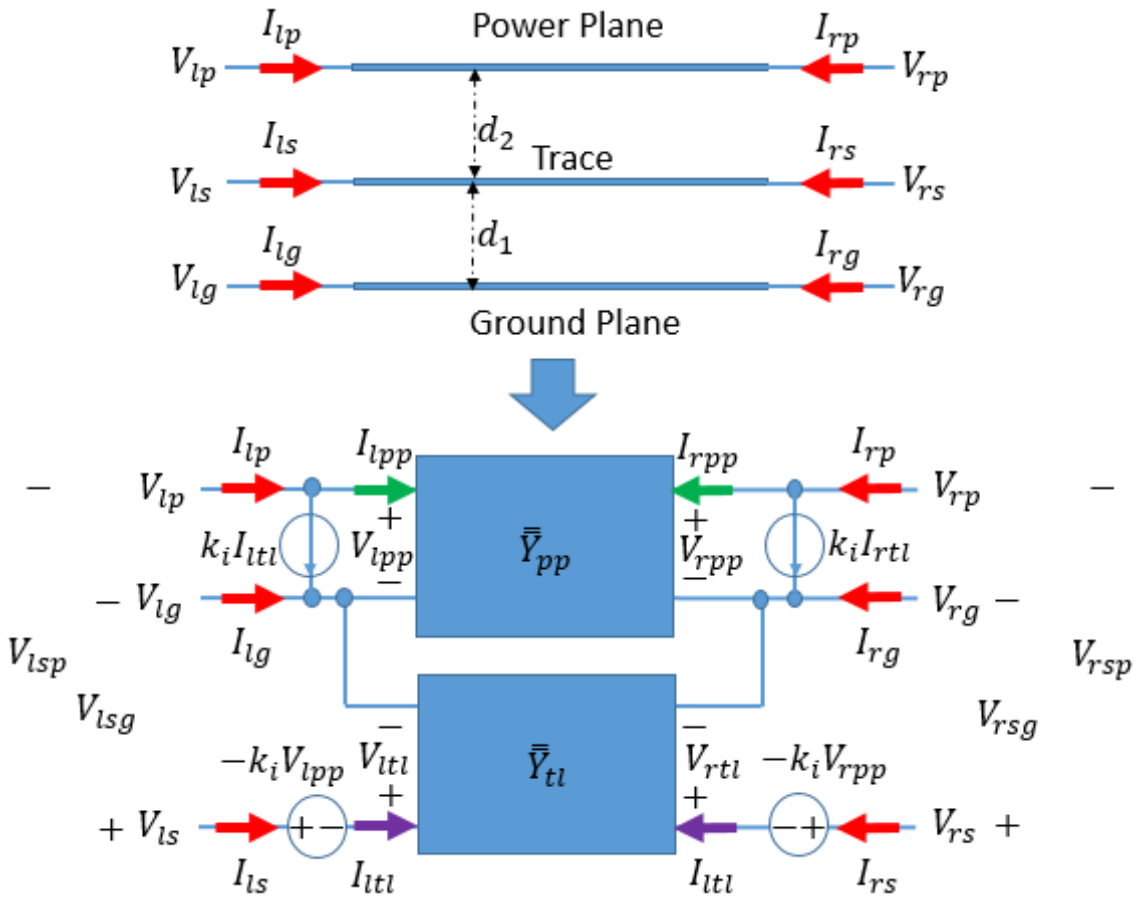

Figure 4.4. Three conductor transmission line problem and its equivalent circuit for 2 ports.

For both left and right side, define the voltages and currents of 4 ports for stripline model as $V_{l/rsg} = V_{l/rs} - V_{l/rg}$, $V_{l/rsp} = V_{l/rs} - V_{l/rp}$ and $I_{l/rs} = I_{l/rtl}$. For 4 ports striplne, both the power and ground plane should be references, then $I_{l/rs} = I_{l/rp} + I_{l/rg}$. Since we also have $I_{l/rtl} = V_{l/rtl} Y_{l/rtl}$, $I_{l/rpp} = V_{l/rpp} Y_{l/rpp}$, after some derivations, at every via-trace location where the modes of P/G planes with vias and modes of stripline couple, we can obtain [46]

$$\begin{bmatrix} \bar{I}^p \\ \bar{I}^g \end{bmatrix} = \begin{bmatrix} {k_i}^2 \bar{\bar{Y}}_{tl} + \bar{\bar{Y}}_{ppTEM} & \left(-{k_i}^2 - k_i\right)\bar{\bar{Y}}_{tl} - \bar{\bar{Y}}_{ppTEM} \\ \left(-{k_i}^2 - k_i\right)\bar{\bar{Y}}_{tl} - \bar{\bar{Y}}_{ppTEM} & \left({k_i}^2 + 2k_i + 1\right)\bar{\bar{Y}}_{tl} + \bar{\bar{Y}}_{ppTEM} \end{bmatrix} \begin{bmatrix} \bar{V}^{sp} \\ \bar{V}^{sg} \end{bmatrix} \quad (4.11)$$

where $\bar{I}^p$, $\bar{I}^g$, $\bar{V}^{sp}$ and $\bar{V}^{sg}$ are vectors include both left and right side ports, for example, $\bar{I}^p = \begin{bmatrix} I^{lp} \\ I^{rp} \end{bmatrix}$.

Eliminating parallel plate mode effects which relate with $\bar{\bar{Y}}_{pp}$, then for a "pure" 4 ports stripline model, the admittance matrix $\bar{\bar{Y}}_s$ can be extracted as

$$\bar{\bar{Y}}_s = \begin{bmatrix} {k_i}^2 \bar{\bar{Y}}_{tl} & \left(-{k_i}^2 - k_i\right)\bar{\bar{Y}}_{tl} \\ \left(-{k_i}^2 - k_i\right)\bar{\bar{Y}}_{tl} & \left({k_i}^2 + 2k_i + 1\right)\bar{\bar{Y}}_{tl} \end{bmatrix} \tag{4.12}$$

Note that the above method for 2 ports/4 ports stripline model can be used also for 2N-ports/4N ports stripline model.

4.3.4 *D. Admittance Matrix $\bar{\bar{Y}}_{P/G}$ for P/G Planes with Vias*

The admittance matrix $\bar{\bar{Y}}_{P/G}$ for problem of geometry I can be calculated with hybrid Foldy-Lax equations method and 1D MoM, as we described in chapter 3.

In this section, I briefly describe the 1D MoM for the problem of finite cavity of irregular shape. All the notations are same as shown in chapter 3.

I use the t coordinate to describe the line contour of the caivty boundary. In the MoM formulation, 1-dimensional discretization of the boundary wall is used. Let there be N_t segments. We use pulse basis functions and point matching for the t_v coordinates with $v = 1,2 \ldots N_t$ and the length of segment v is Δt_v. Then the impedance matrix $\bar{\bar{Z}}$ is of dimension $N_t \times N_t$. The impedance matrix elements are

$$Z_{\mu v} = \begin{cases} [\hat{n}' \cdot \nabla_t{}' g(\bar{\rho}, \bar{\rho}')\Delta t_v]_{\bar{\rho}' = \bar{\rho}(t_\mu), \bar{\rho}' = \bar{\rho}(t_v)} & \mu \neq v \\ \frac{1}{2} & \mu = v \end{cases} \tag{3.3}$$

for $\mu, v = 1,2 \ldots N_t$, and $g(\bar{\rho}) = \frac{1}{4j} H_0^{(2)}(k\rho)$.

Consider multiple vias, $q = 1,2,3, \ldots . N$, the Foldy-Lax equations are

$$\bar{w}^q = \bar{a}^{q,inc} + \sum_{\substack{p=1 \\ p \neq q}}^{N} \left[\bar{\bar{\alpha}}_{qp}^{+} + \bar{\bar{X}}^{Wqp}\right] \bar{A}^p \tag{3.36}$$

In general, we include harmonics of $m = 0, \pm 1, \ldots \ldots \pm M$. Harmonics of $m \neq 0$ give rise to anisotropic effects.

In the above equation, $\bar{w}^q$ and $\bar{A}^q$ are of dimemsions $(2M+1) \times 1$, and contain exciting field coefficients $[\bar{w}^q]_m = w_m^q$ and scattered field coefficients $[\bar{A}^q]_m = A_m^q$, $m = 0, \pm 1, \ldots \ldots \pm M$; $\bar{a}^{inc}$ is the incident field coefficients, $\bar{\bar{\alpha}}_{qp}^{+}$ matrix is the translation matrix for cylindrical waves and is of dimension $(2M+1) \times (2M+1)$

$$\left[\bar{\bar{\alpha}}_{qp}^{+}\right]_{nm} = H_{n-m}^{(2)}\left(k\left|\overline{\rho_p} - \overline{\rho_q}\right|\right) e^{j(n-m)\emptyset_{\overline{\rho_p \rho_q}}} \tag{3.11}$$

and

$$\bar{\bar{X}}^{Wqp} = \bar{\bar{\gamma}}^{(qW)}\bar{\bar{Z}}^{-1}\bar{\bar{Q}}^{(Wp)} \tag{3.33}$$

In equation (3.33), the $\bar{\bar{\gamma}}^{(qW)}$ matrix which has dimension $(2M+1)\times N_t$ where W stands for wall. It is of mixed dimension as it represents discretized MoM points coupled to wave harmonics, $m = 0, \pm 1, \ldots\ldots \pm M$. $\bar{\bar{Q}}^{(Wq)}$ is with dimension $N_t \times (2M+1)$. It represents coupling from harmonic to discretized point on the boundary. $\bar{\bar{Z}}^{-1}$ is the inverse of the MoM impedance matrix. Their expressions can be found in chapter 3.

Using the $\bar{\bar{\tau}}^{(p)}$, the T-matrix of single via including wall effects, we have

$$\bar{w}^q = \bar{a}^{q,inc} + \sum_{\substack{p=1 \\ p\neq q}}^{N}\left[\bar{\bar{\alpha}}^{+}_{qp} + \bar{\bar{X}}^{Wqp}\right]\bar{\bar{\tau}}^{(p)}\bar{w}^p \tag{3.37}$$

where

$$\bar{\bar{\tau}}^{(p)} = \left[\bar{\bar{I}} - \bar{\bar{T}}^p\bar{\bar{X}}^{Wpp}\right]^{-1}\bar{\bar{T}}^p \tag{3.38}$$

After the Foldy-Lax equations are solved, $\bar{w}^q, q = 1,2\ldots N$ are obained. Then the magnetic field in the $\hat{\phi}$ direction can be obtained. The surface currents J_s^q as shown in equation (3.53) is in the z direction and is calculated from the magnetic field on the surface of the via.

Once the currents are determined, the calculation of the admittance parameter matrix of multiple vias inside finite P/G planes $\bar{\bar{Y}}_{P/G}$ can be obtained as

$$\begin{bmatrix}\bar{I}^p \\ \bar{I}^g\end{bmatrix} = \bar{\bar{Y}}_{P/G}\begin{bmatrix}\bar{V}^p \\ \bar{V}^g\end{bmatrix} \tag{4.13}$$

where $\bar{I}^p$, $\bar{I}^g$, $\bar{V}^p$, $\bar{V}^g$ are current and voltage vector on power and ground apertures, and

$$\bar{\bar{Y}}_{P/G} = \begin{bmatrix}\bar{\bar{Y}}^{pp} & -\bar{\bar{Y}}^{pg} \\ -\bar{\bar{Y}}^{gp} & \bar{\bar{Y}}^{gg}\end{bmatrix} \tag{4.14}$$

Note that if the stripline is in the center of cavity, due to the reflection symmetry of the waveguide, we have the symmetry relation of the admittance matrix elements $\bar{\bar{Y}}^{pp} = \bar{\bar{Y}}^{gg}$ and $\bar{\bar{Y}}^{gp} = \bar{\bar{Y}}^{pg}$. Anyway, if the stripline is not at the middle of the cavity, the symmetry relation will be destroyed. Then the Foldy-Lax equations method need to be used twice to obtain four element matrices in $\bar{\bar{Y}}_{P/G}$.

In this chapter, we only consider $k_i = -0.5$ or centered trace case, for the modeling simplicity.

It is valuable to point out that, the $\bar{\bar{Y}}_{P/G}$ obtained from the proposed method is not $\bar{\bar{Y}}^c$ used in [15, 28] or $\bar{\bar{Y}}^a$ used in [32]. The difference between the two is that $\bar{\bar{Y}}^c$ (obtained from cavity model theory) or $\bar{\bar{Y}}^a$ (obtained from contour integral equation method) only reflects modes effects of P/G planes without vias, while $\bar{\bar{Y}}_{P/G}$ reflects modes coupling effects of P/G planes with multiple vias. In [15, 28, 32], via barrel to plane capacitance need to be extracted to express the coupling between single via and cavity, but scattering effects among vias are not considered. The proposed Foldy-Lax equations method include and integrate all the coupling and scattering effects among vias and planes. For complicated geometries, the methods in [15, 24, 28, 32, 40] can't handle cases such as irregular single through hole via, multiple vias sharing same antipad and dense via array, while the proposed method use only one-dimensional discretization and integral. I will show more simulation details in the numerical example section.

The $\bar{\bar{Y}}_{P/G}$ is not exactly same as $\bar{\bar{Y}}_{PP}$ defined in [14, 39] neither. Although both of them include scattering effects among multiple vias and planes, $\bar{\bar{Y}}_{PP}$ defined in [14, 39] does not include higher order waveguide modes effects, while $\bar{\bar{Y}}_{P/G}$ includes these effects. When the source via gets excited, parallel plate waveguide modes will be excited. In high frequency, higher order waveguide modes may not decay rapidly along the radial direction, and they do contribute to the interactions among closely spaced vias [44]. In other words, modes conversion not only occur at the transition between the signal trace and through hole via, but also through the way of wave propagation and scattering among vias from fundamental mode to some higher order modes. From simulations in section 4.4, I observe that these higher order modes effects need to be considered for the accuracy issue of modeling above 20GHz.

4.3.5 *E. Model Recombination*

We now combine (4.6), (4.11) and (4.14), then a generalized model can be formulated for one cavity and the total admittance matrix of the system is finally derived as

$$\begin{bmatrix} \bar{I}^p \\ \bar{I}^g \end{bmatrix} = \bar{\bar{Y}} \begin{bmatrix} \bar{V}^p \\ \bar{V}^g \end{bmatrix} \tag{4.15}$$

where

$$\bar{\bar{Y}} = \bar{\bar{Y}}_{P/G} + \bar{\bar{Y}}_s = \begin{bmatrix} {k_i}^2 \bar{\bar{Y}}_{tl} + \bar{\bar{Y}}^{uu} & \left(-{k_i}^2 - k_i\right)\bar{\bar{Y}}_{tl} - \bar{\bar{Y}}^{ub} \\ \left(-{k_i}^2 - k_i\right)\bar{\bar{Y}}_{tl} - \bar{\bar{Y}}^{bu} & \left({k_i}^2 + 2k_i + 1\right)\bar{\bar{Y}}_{tl}\bar{\bar{Y}}^{bb} \end{bmatrix} \tag{4.16}$$

The proposed method can be conveniently expanded to multiple vias and multiple striplines case. For vias not connected with traces, the related $\bar{\bar{Y}}_s$ is zero.

After obtaining the admittance parameter matrix, the calculation of the scattering matrix proceed in manners as described in previous papers [4, 19, 35, 36, 42].

4.3.6 *F. Model for Multilayer Electronic Structures with Different Loads*

For the multilayered structures with different types of ports, e.g., the open, shorting and load, cascaded Y parameters technique derived in [39] is used for the combination of individual network in this paper. More details for derivation and definitions of through ports and generic load ports can be found in [39, 40], I show the conclusions only for the paper self-consistent.

The admittance matrix of the i parallel plate pair $\bar{\bar{Y}}^i$ is defined as

$$\begin{bmatrix} \bar{I}_u^i \\ \bar{I}_b^i \end{bmatrix} = \begin{bmatrix} \bar{\bar{Y}}_{uu}^i & \bar{\bar{Y}}_{ub}^i \\ \bar{\bar{Y}}_{bu}^i & \bar{\bar{Y}}_{bb}^i \end{bmatrix} \begin{bmatrix} \bar{V}_u^i \\ \bar{V}_b^i \end{bmatrix} \tag{4.17}$$

Then the cascaded admittance matrix for two consecutive plate-pair networks with admittance matrices of $\bar{\bar{Y}}^i$ And $\bar{\bar{Y}}^{i+1}$ Is finally given as

$$\bar{\bar{Y}}^{i,i+1} = \begin{bmatrix} \bar{\bar{Y}}_{uu}^i - \bar{\bar{Y}}_{ub}^i \bar{\bar{Q}} \bar{\bar{Y}}_{bu}^i & -\bar{\bar{Y}}_{ub}^i \bar{\bar{Q}} \bar{\bar{Y}}_{ub}^{i+1} \\ -\bar{\bar{Y}}_{bu}^{i+1} \bar{\bar{Q}} \bar{\bar{Y}}_{bu}^i & \bar{\bar{Y}}_{bb}^{i+1} - \bar{\bar{Y}}_{bu}^{i+1} \bar{\bar{Q}} \bar{\bar{Y}}_{ub}^{i+1} \end{bmatrix} \tag{4.18}$$

where the auxiliary matrix $\bar{\bar{Q}}$ is

$$\bar{\bar{Q}} = \left[\bar{\bar{Y}}_{bb}^i + \bar{\bar{Y}}_{uu}^{i+1} \right]^{-1} \tag{4.19}$$

4.4 Numerical Results and Discussions

In this section I illustrate the results and make comparisons with Ansoft's HFSS version 12. I mainly discuss the effectiveness of the proposed method.

The proposed method are based on Foldy-Lax multiple scattering equations method. The CPU requirement and discussions between the Foldy-Lax approach and HFSS v12 has been thoroughly reported and discussed in chapter 2 and 3 or in [36, 43] section VIII. The CPU requirement of cascaded microwave Y parameters network approach has also been discussed in [40], for multilayer structures. The proposed method use much less memory requirement and CPU computation resources.

4.4.1 *A. 2 Common Vias Connected with 1 Trace in A Square Cavity for Higher Order Waveguide Modes Effects Investigation*

Figure 4.5 shows top and side view of structure about 2 vias connected with 1 trace. I test two cases for very short vertical vias and long vertical vias, to investigate the higher order waveguide modes effects. The specifications are: $R_{via} = 5\,mil$, $R_{antipad} = 15\,mil$, $W = 1200\,mil$, $t = 1\,mil$, transmission line length $L_{tl} = 600\,mil$, $h = 12\,mil$ for case A1 which is for short via and $h = 61\,mil$ for case A2 which is for long via; for substrate material, $\varepsilon_r = 3.84$, $tan\delta = 0.033$. The two signal vias locate at (200, 600) mil and (800, 600) mil.

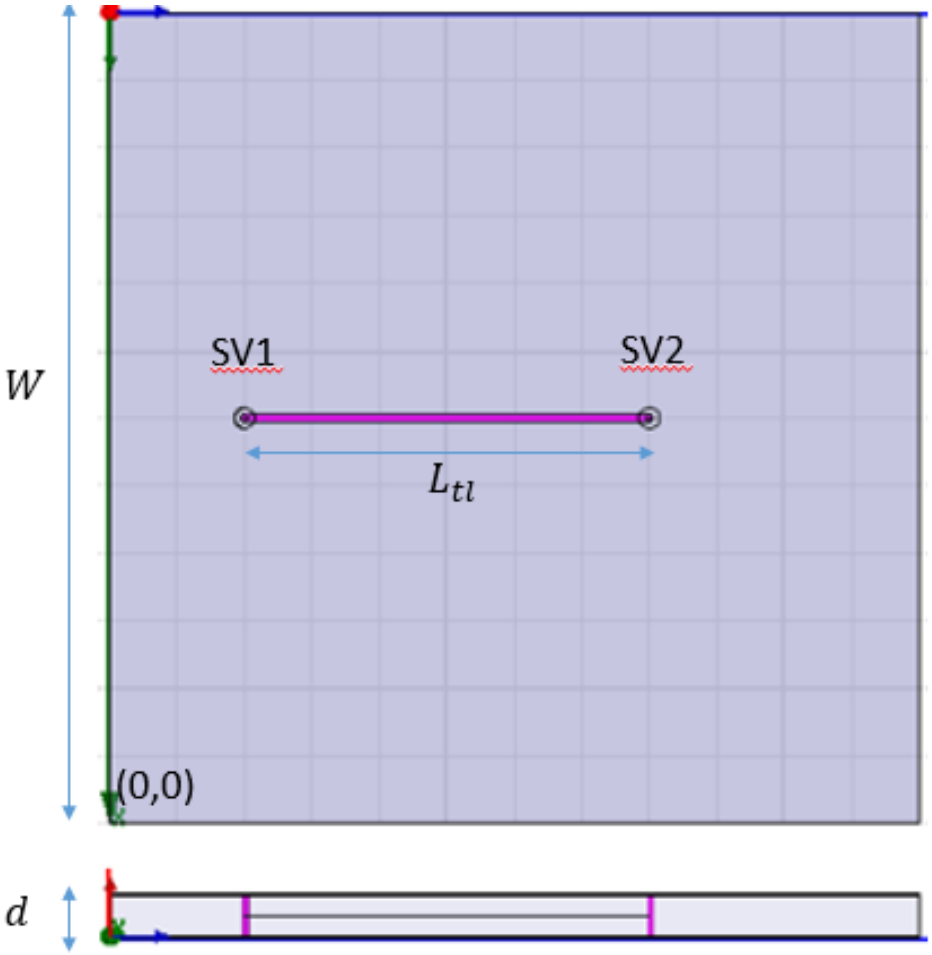

Figure 4.5. Top and side view of 2 vias connected with 1 trace in a square cavity.

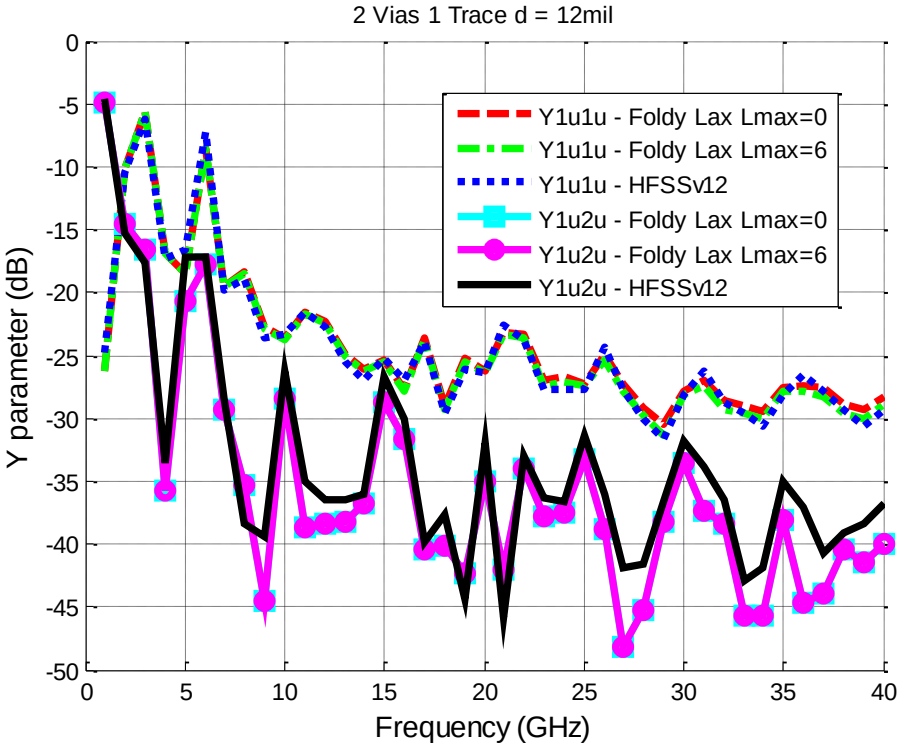

Figure 4.6. Y parameters for upper and upper ports comparisons for case A1.

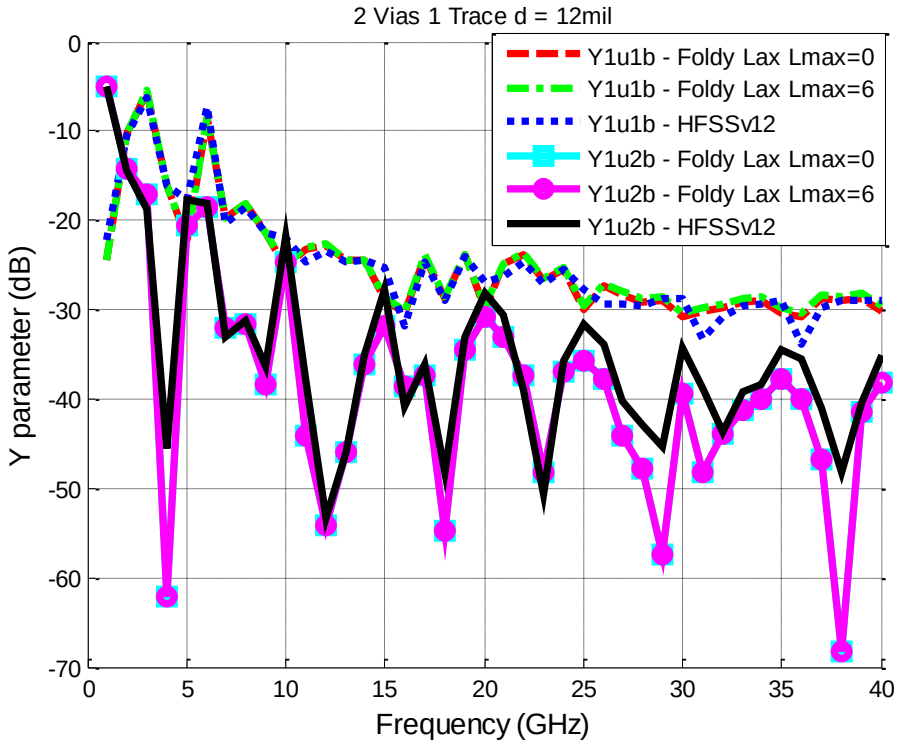

Figure 4.7. Y parameters for upper and bottom ports comparisons for case A1.

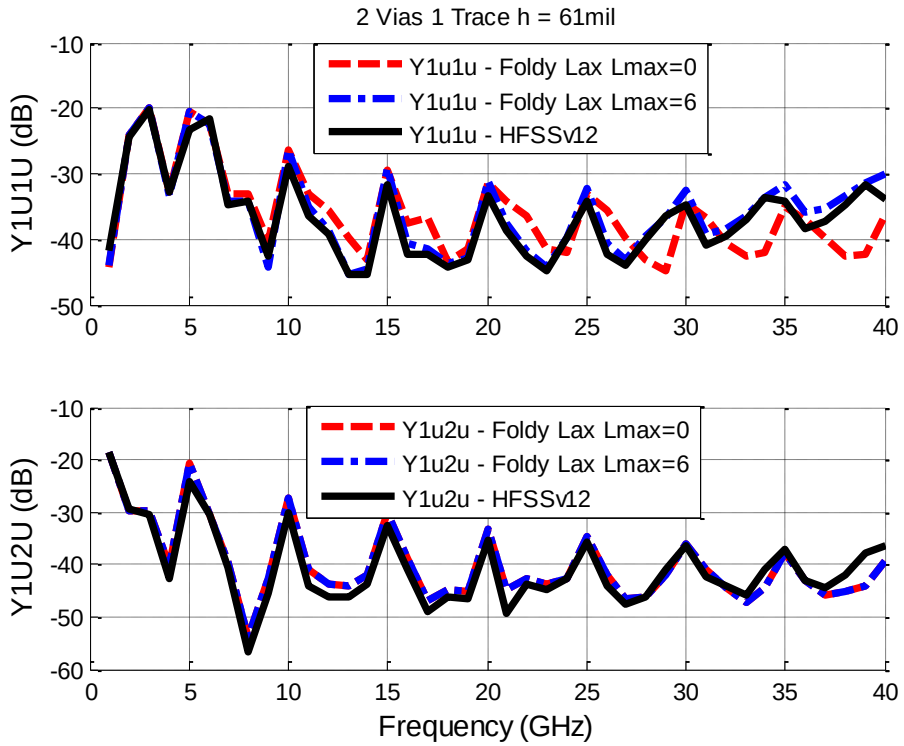

Figure 4.8. Y parameters for upper and upper ports comparisons for case A2.

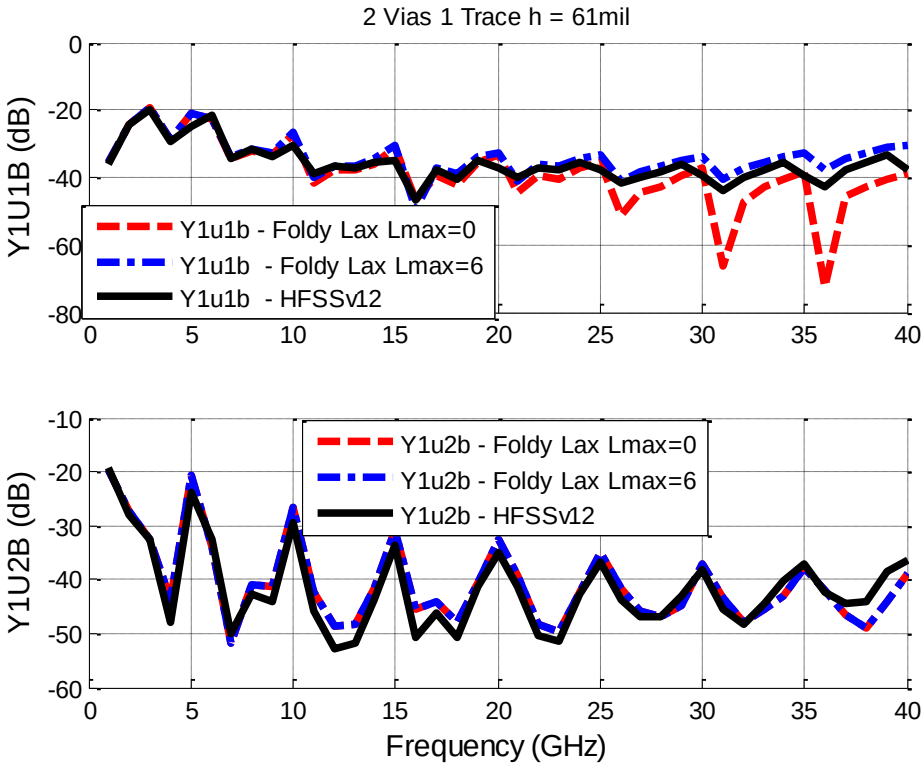

Figure 4.9. Y parameters for upper and upper ports comparisons for case A2.

As stated in section 4.3 part A, I compared the $\bar{\bar{Y}}_{P/G}$ with and without considering higher order modes effects for short and long interconnects, respectively. Figure 4.6 and 4.7 show Y parameters between upper and bottom ports comparisons for case A1, which is short via case. Figure 4.8 and 4.9 show Y parameters between upper and bottom ports comparisons for case A2, which is long via case. Good agreements can be obtained between the proposed method and HFSSv12.

As we can see, for short via case, the high order modes effects are not so important, but for long via case, in order to accurately model the self-admittance Y1u1u and through admittance Y1u1b, higher order modes effects are necessary for simulation above 20GHz. Cross-admittance Y1u2u and Y1u2b are not impacted by higher order modes effects very much, due to the transmission line length being 600 mil.

4.4.2 *B. 2 Eccentric Vias Connected with 1 Trace in A Square Cavity for Irregular Antipad Effects*

The proposed method can be conveniently expanded to modeling cases of vias with irregular antipad or eccentric vias. We show an example about eccentric via structure. Figure 4.10 shows top view of structure about 2 eccentric vias connected with 1 trace. The specifications are same as the case A2, also with the eccentric pitch $e = 2\ mil$.

Figure 4.11 shows the comparisons of S parameters about the two signal vias. We can observe that the insertion loss and return loss for signal via 1 to some degree behave like a transmission line. This is reasonable since single vertical via can be treated as a coaxial cable with virtual boundaries. The through transmission S parameters between signal via 1 and via 2 also behave as transmission line performance. The resonances shown in the curves are due to the cavity modes effects.

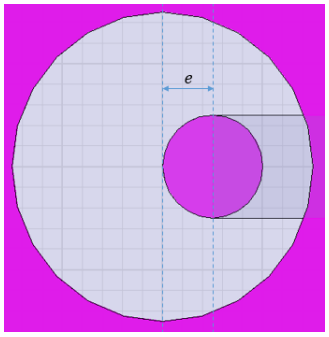

Figure 4.10. Top view for eccentric via in case B.

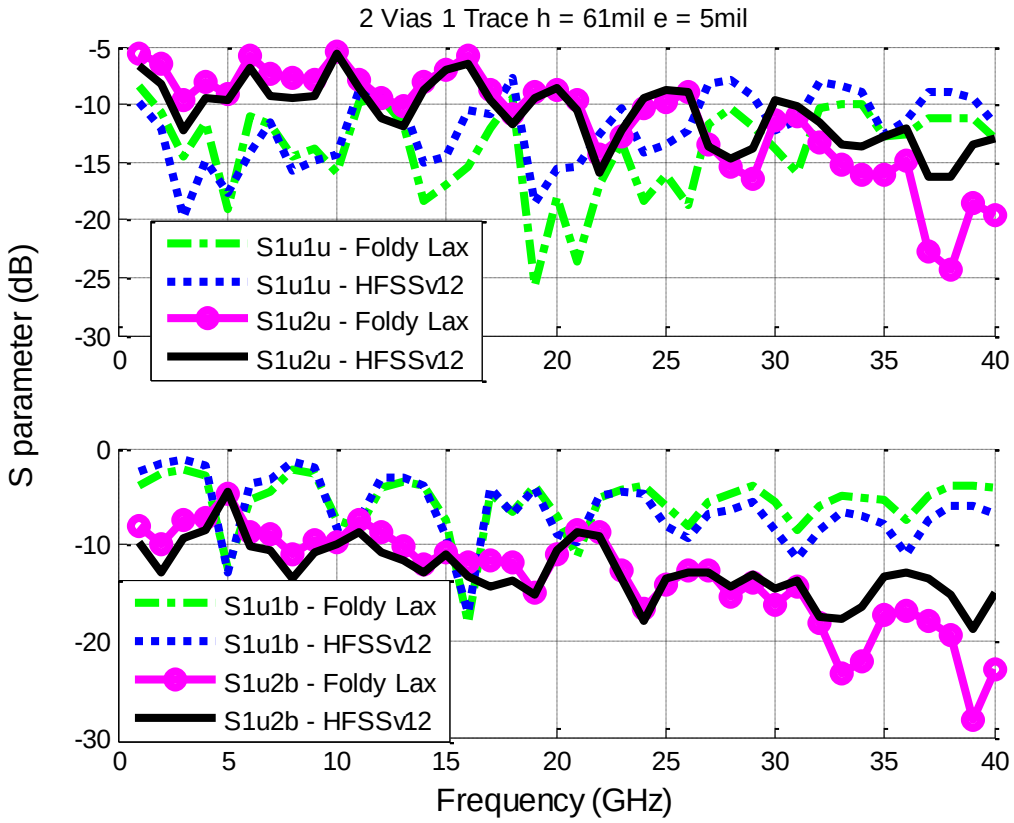

Figure 4.11. S parameters comparisons for case B.

4.4.3 *C. 2 Common Vias Connected with 1 Trace in A L-Shaped Cavity for Irregular P/G Planes Effects*

Figure 4.12 shows top view of structure about 2 vias connected with 1 trace in a L shaped cavity. The specifications are $R_{via} = 5\ mil$, $R_{antipad} = 15\ mil$,$W = 1200\ mil$, $L = 1500\ mil$, $L_1 = 200\ mil$, $W_1 = 800\ mil$, $h = 31\ mil$, $t = 1\ mil$, transmission line length $L_{tl} = 600\ mil$. The two signal vias locate at (200, 700) mil and (800, 700) mil.

Figure 4.13 shows the comparisons of S parameters about the two signal vias in the irregular P/G planes. The irregular effects in proposed method are modeled by Foldy-Lax equations method hybrid with MoM, as shown in section II part A. For the investigation of the irregular planes effects, we can compare figure 4.11 and 4.13. One then can observe that, the shapes of the insertion loss and return loss for signal via 1 are not impacted very much, since they mainly behave as a transmission line performances. But the through transmission S parameters between signal via 1

and via 2 are impacted a lot, since the cavity modes between case B and case C are very different. From the results, it can be seen that the curves for through transmission S parameters between signal via 1 and via 2 in case C are much smoother than case B.

4.4.4 *D. 48 Vias in A L-Shaped Cavity for Multiple Vias Scattering Effects*

The proposed method can accurately reflects the multiple scattering effects among vias and P/G planes, as we also stated in the section II part A. Figure 4.14 shows a top view of a L-shaped cavity embedded with a SIW structure which includes 48 vias, including 6 signal vias and 42 ground vias, in order to test the structure of dense vias array. The specifications are same as the case C, except that there are extra 4 signal vias and 42 ground vias are located in the P/G planes. The signal via 3 is locating at (900, 540) mil.

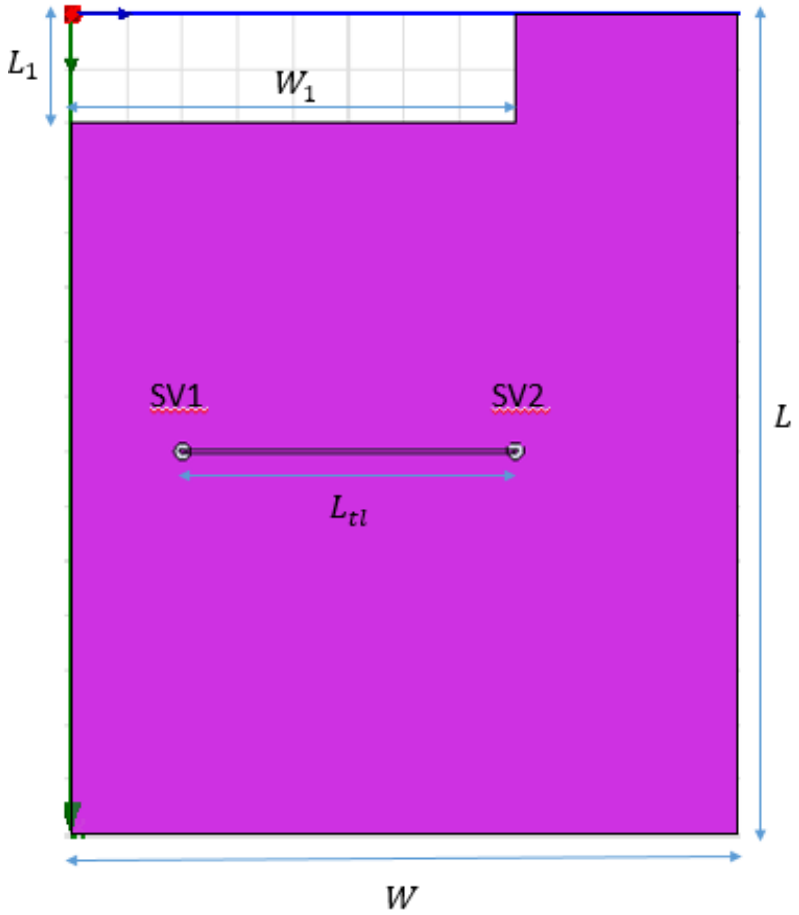

Figure 4.12. Top view for 2 vias connected with 1 trace in L shaped cavity for case C.

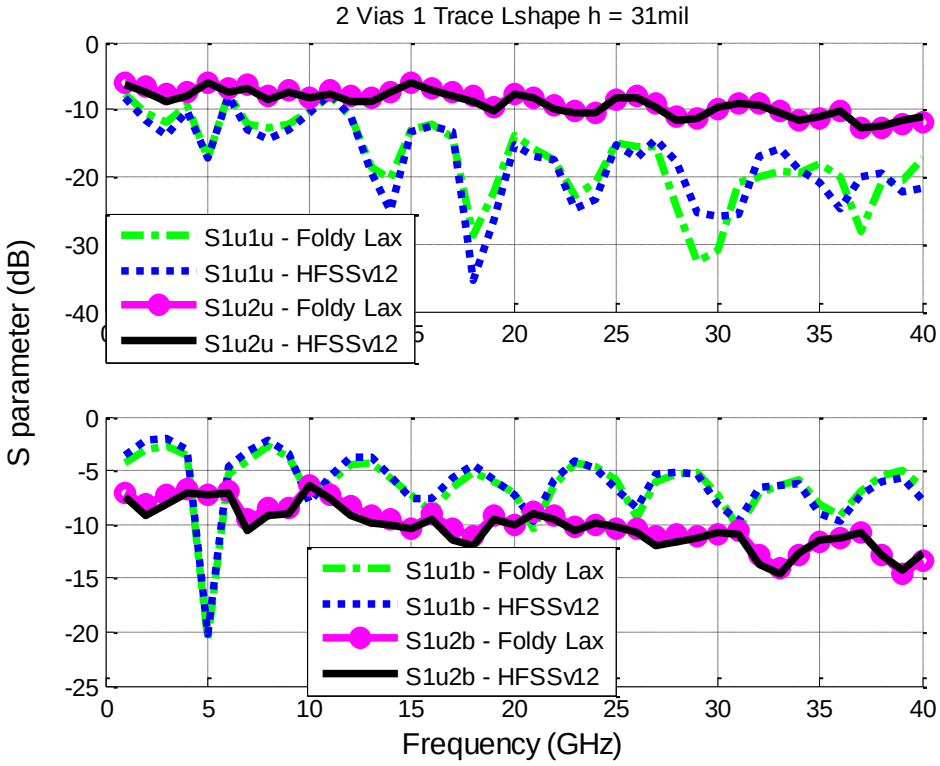

Figure 4.13. S parameters comparisons for case C.

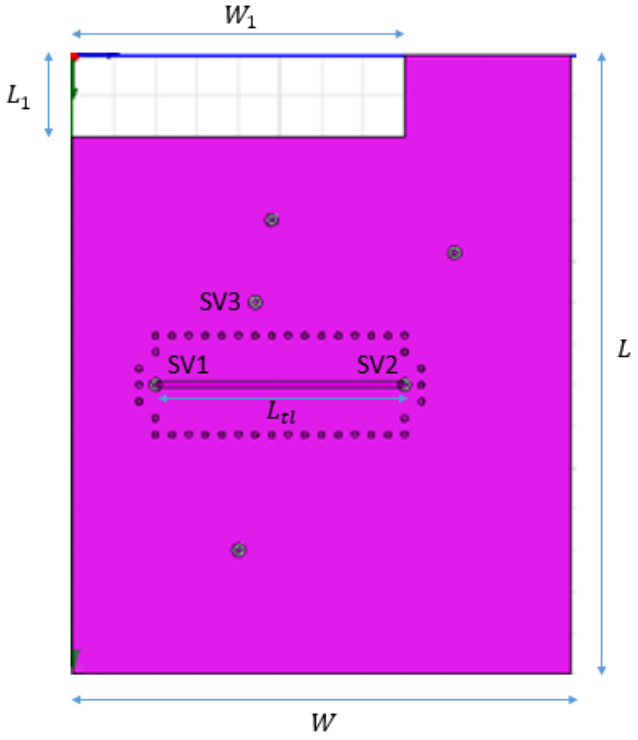

Figure 4.14. Top view of a L-shaped cavity embedded with a SIW structure for case D.

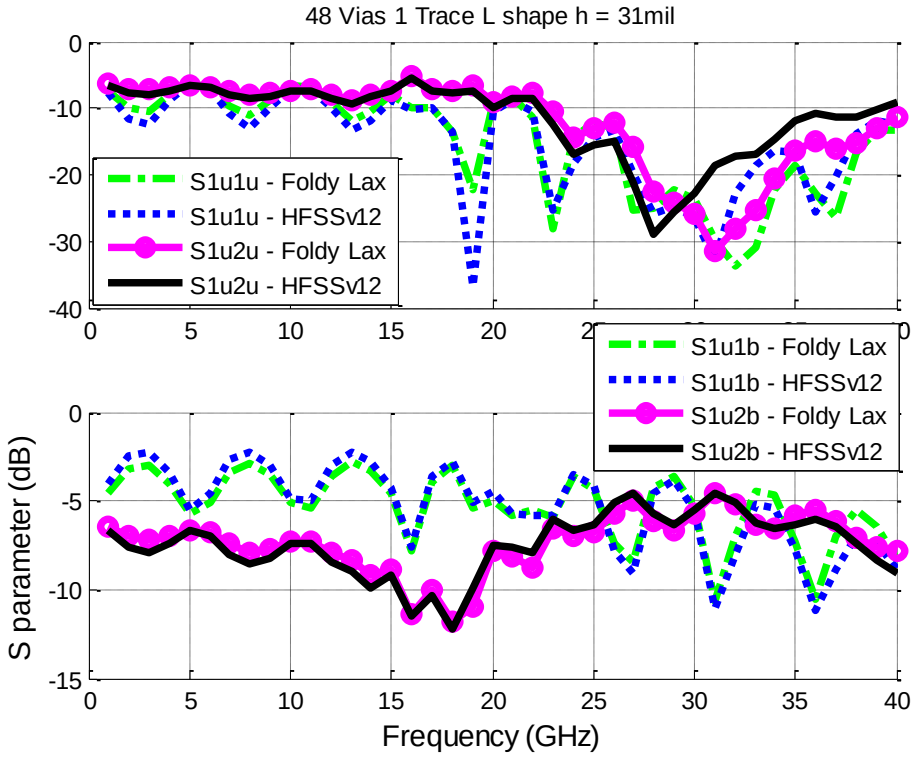

Figure 4.15. S parameters comparisons for case D.

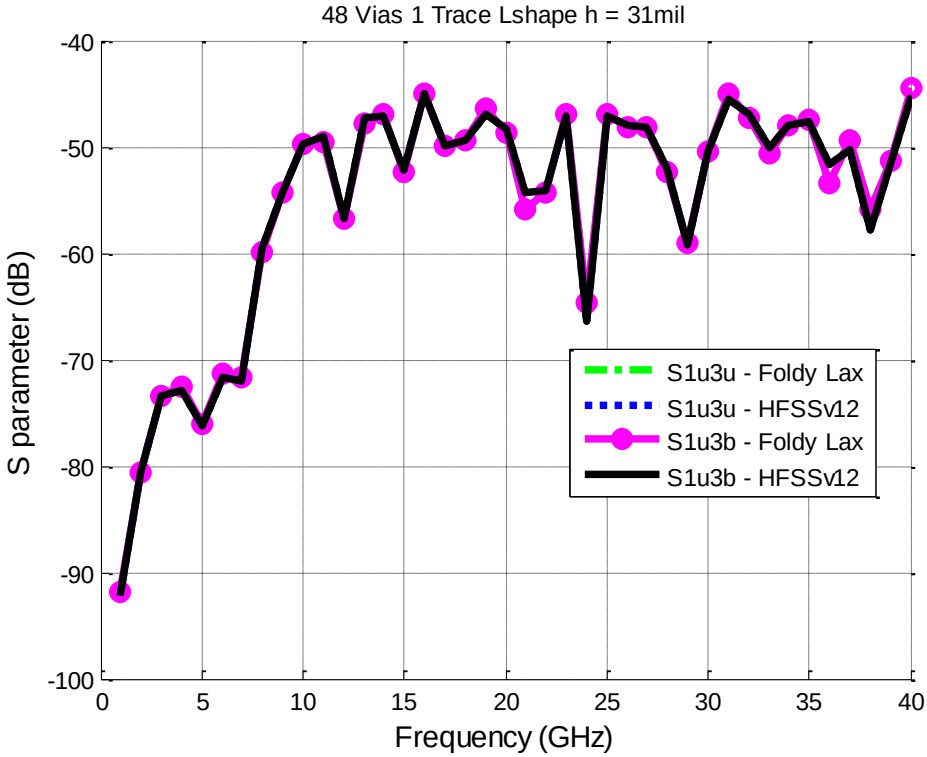

Figure 4.16. NEXT and FEXT between signal via 1 and 3 for case D.

Figure 4.15 shows the the comparisons of S parameters between signal via 1 and via 2. Figure 4.16 shows the the near end cross talk (NEXT) and far end cross talk (FEXT) between signal via 1 and via 3. From the simulation results, we can see that the insertion loss and return loss for signal via 1 and the through transmission S parameters between signal via 1 and via 2 are impacted by the embedded SIW structure. These impacts occur above 15GHz. The P/G planes effects are "hidden" by the SIW structure.

The resonances shown in the curve of through transmission S1u2u is due to the modes effects of SIW structures. There is discrepancy of the resonance between the proposed method and HFSSv12, this may be due to the neglect of the coupling among vias and trace in the proposed method. The NEXT and FEXT between signal via 1 and 3 are very small (below -40dB) and nearly same, since the via cage guard any radiation from the inside of it. But these crosstalk increase with frequency also.

4.4.5 *E. 3 Common Vias Connected with 2 Traces in 2 Layered L-Shaped Cavities for Multilayered Structures*

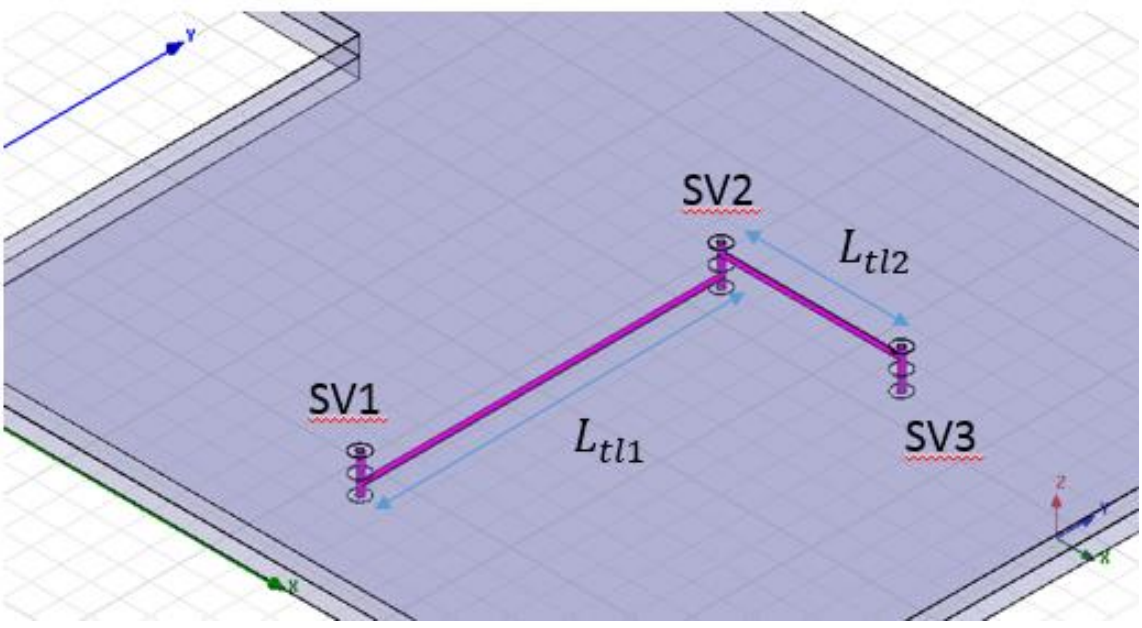

Figure 4.17. 3D view for 2 layered L shape cavities with 3 vias and 2 traces for case E.

Figure 4.17 shows 3D view for 2 layered L shape cavities with 3 vias and 2 traces. The specifications of each cavity are same as case C, except that the signal via 3 is locating at (800, 400) mil, $L_{tl1} = 600\,mil$ and $L_{tl2} = 300\,mil$.

Figure 4.18 shows the comparisons of S parameters between signal via 1 and via 3. Good agreement can be obtained up to 40GHz. We want to point that the proposed method can be conveniently expanded to model the ports with different loads, although we do not show the related case. These loads can be for open, short and decoupling capacitor. These loads can be integrated with the models in the post-processing phase [39].

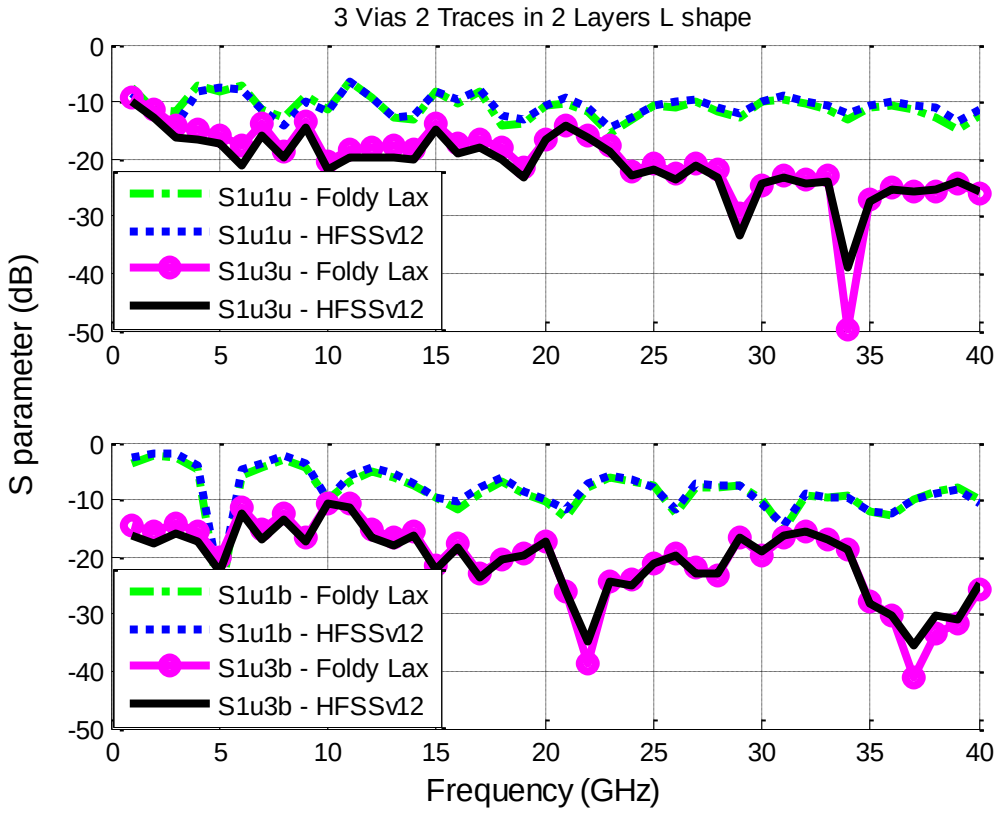

Figure 4.18. S parameters comparisons for case E.

4.4.6 *F. 2 Pairs of Differential Signaling Connected with Coupled Traces in A Rectangular Cavity*

The last case is about differential singling structures with coupled striplines. The modeling method is shown in section 4.3 part E. Note that the proposed method do not include any pre

extractions for any parasitic parameters. Figure 4.19 shows top view for 2 differential signaling pairs with coupled striplines. The differential pair of vias can be in common mode or differential mode. The specifications are: $\varepsilon_r = 4.4$, $tan\delta = 0.02$ (FR4_eproxy), $L = 2000\,mil$, $W = 1500\,mil$, $R_{via} = 15\,mil$, $R_{antipad} = 30\,mil$, $pitch = 40\,mil$, $h = 51\,mil$, $t = 1\,mil$, transmission line length $L_{tl} = 400\,mil$.

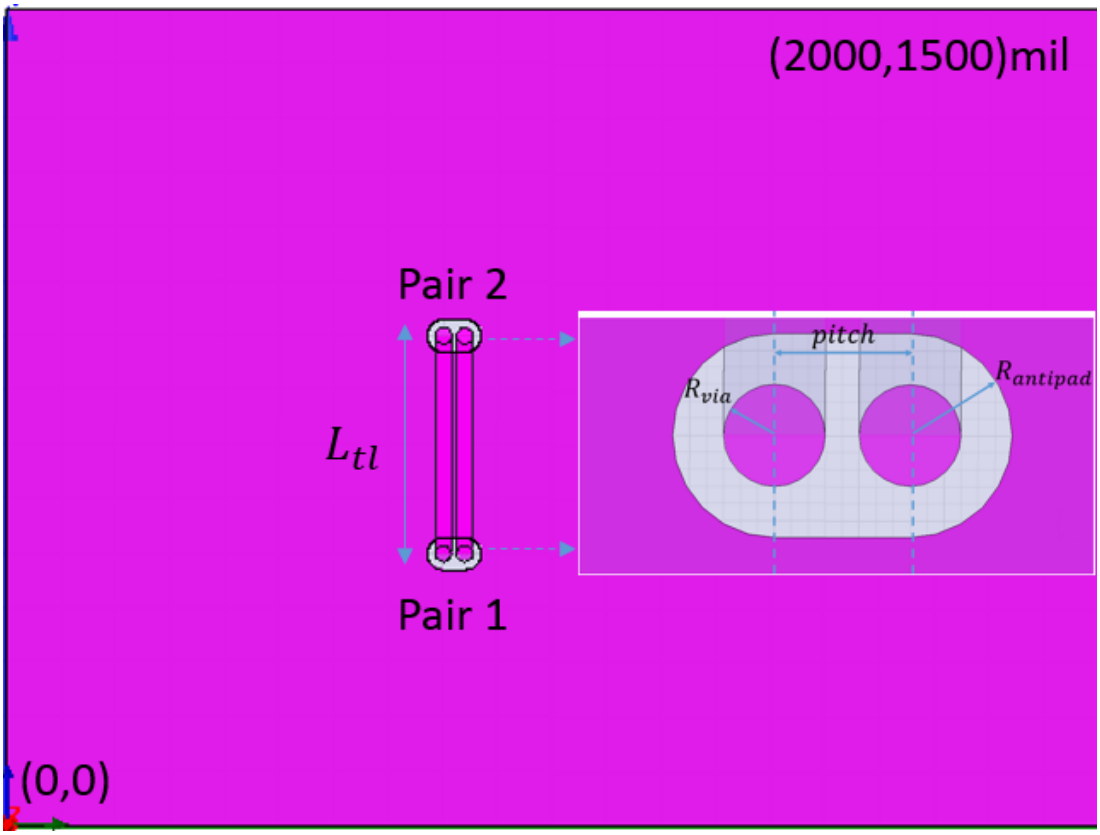

Figure 4.19. Top view for 2 differential signaling pairs with coupled striplines for case F.

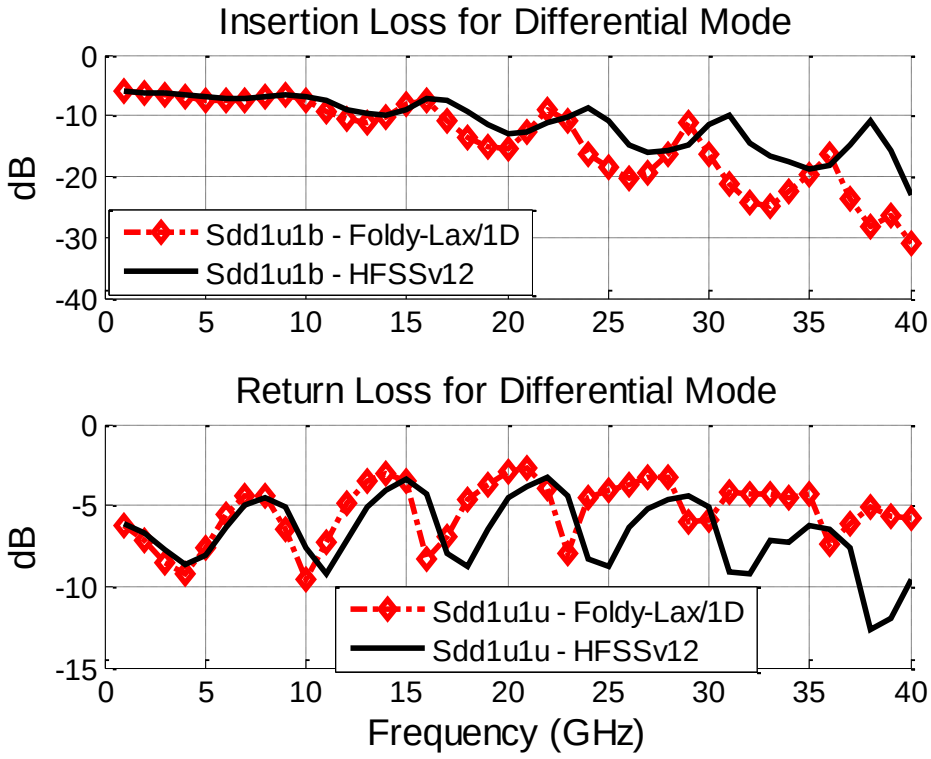

Figure 4.20. Differential mode S parameters comparisons for case F.

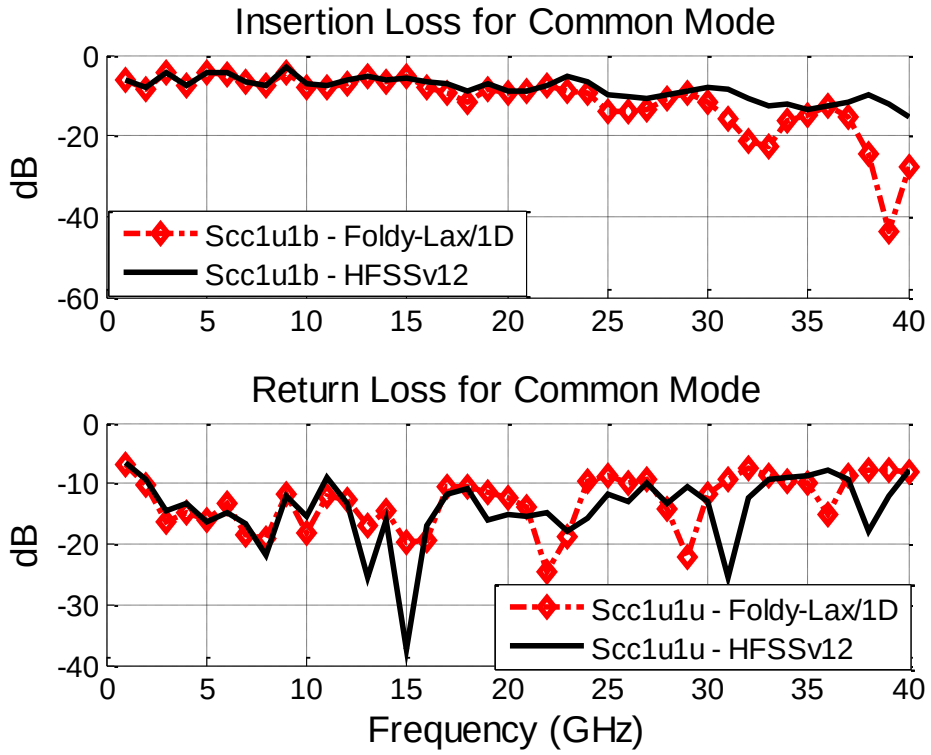

Figure 4.21. Common mode S parameters comparisons for case F.

Figure 4.20 and Figure 4.21 show the insertion loss and return loss for both differential mode and common mode respectively, also up to 40GHz. For the modeling detail, the coupled striplines model is obtained from HFSSv12. Note that the spacing between the two coupled striplines is only 10mil.

From the comparisons, I observe that the proposed method match well with the simulation results obtained from HFSSv12 below 10GHz. The model shows some discrepancies (mainly are for resonances shifts) above 10GHz. This may be due to the near filed interaction occurring between striplines and vias at the location of via-trace transitions, or higher order transmission line modes being excited. In such case, more accurate modeling methods need to be investigated for high frequency simulation.

4.5 CONCLUSIONS

In this chapter, I proposed a fast and broadband modeling method for signal/power integrity analysis for vias traces transition structures in electronic packages and printed circuit boards, for link level and channel simulations. The major advantage of the proposed method resides in the decomposition of the complex 3-D problem into simple analytical solution, 1D meshing and 2D problem if necessary. With the hybridization of generalized Foldy-Lax multiple scattering equations method and modal decomposition method, the computation resources are reduced for the complete signal/power integrity analysis of high-speed vertical and horizontal interconnects modeling in 3D IC, with good accuracy, up to 40GHz.

Chapter 5. EXTEND FOLDY-LAX EQUATION METHOD TO MODEL MIXED METAL/DIELECTRIC CYLINDERS IN PARALLEL PLATE WAVEGUIDE STRUCTURE

5.1 INTRODUCTION

In the recent antenna designs, many compact, high performance antenna are working at high millimeter-wave (mm-wave) frequencies [55-56], with a high degree of repeatability and reliability in antenna constructions. They are implemented by integrating a waveguide antenna within multilayer structures, or a new technology named as substrate integrated waveguide (SIW).

For another side, in order to make PCB and package design be more reliable from the point of view of power integrity (PI), the power deliver networks (PDN) becomes more and more complicated. A typical way to suppress the simultaneous switching noise (SSN) is to add a photonic crystal power/ground layers. The structures are also though SIW like technology. Unwanted noise then can be eliminated/significantly suppressed in the designed stopbands. The signal integrity aspect won't be impacted by doing so [57].

In this chapter, I derived a new form of Foldy-Lax equations to provide an efficient solution for modeling SIW structures, which applied scattering coefficients as unknowns, for multiple scattering among metallic and dielectric cylinders in parallel plate waveguide structure. The modeling techniques are based on rigorous electromagnetic analysis with consideration of TE/TM coupling and T matrix for dielectric cylinder in parallel plate waveguide. The modeling techniques provide fast and broadband simulation method for 3D IC and SIW based device.

5.2 T MATRIX OF DIELECTRIC CYLINDER IN PARALLEL PLATE WAVEGUIDE

I first derive the T matrix for a single dielectric cylinder in parallel plate structure. Consider a dielectric cylinder of radius a. All the notations are same as previous chapters.

5.2.1 *TM case:*

Let the exciting magnetic field of cylinder be consisting of TM modes. The parallel plates are at $z' = \frac{d}{2}$ and $z' = -\frac{d}{2}$. Then first let the exciting field is

$$\vec{H}_{ex} = \sum_{l=0}^{\infty}\sum_{n=-\infty}^{\infty}\left[w_{l,n}^{TM} Rg\vec{H}_n^{TM}\left(k_{zl}, k_{\rho l}, \vec{\rho}, z \pm z'\right)\right] \tag{5.1}$$

$w_{l,n}^{TM}$ and $w_{l,n}^{TE}$ are TM and TE exciting coefficient respectively, and note that for TM modes, $l = 0,1,2, \ldots \ldots$ For TE modes, $l = 1,2,3, \ldots \ldots$

The magnetic vector wave functions in the parallel plate waveguide are [4]

$$Rg\vec{H}_n^{TE}\left(k_{\rho l}, k_{zl}, \vec{\rho}, z\right) = \frac{e^{-jn\phi}}{\eta}\left\{-\hat{\rho}\frac{jk_{\rho l}k_{zl}}{k}J'_n\left(k_{\rho l}\rho\right)cos\left(k_{zl}(z \pm z')\right) - \hat{\phi}\frac{nk_{zl}}{k\rho}J_n\left(k_{\rho l}\rho\right)cos(k_z z) - \hat{z}\frac{k_{\rho l}^2}{k}J_n\left(k_{\rho l}\rho\right)jsin\left(k_{zl}(z \pm z')\right)\right\} \tag{5.2}$$

$$Rg\vec{H}_n^{TM}\left(k_{\rho l}, k_{zl}, \vec{\rho}, z\right) = \frac{je^{-jn\phi}}{\eta}\left\{-\hat{\rho}\frac{jn}{\rho}J_n\left(k_{\rho l}\rho\right) - \hat{\phi}k_{\rho l}J'_n\left(k_{\rho l}\rho\right)\right\}cos\left(k_{zl}(z \pm z')\right) \tag{5.3}$$

Then

$$\hat{\rho} \times Rg\vec{H}_n^{TE}\left(k_{\rho l}, k_{zl}, \vec{\rho}, z\right) = \frac{e^{-jn\phi}}{\eta}\left\{-\hat{z}\frac{nk_{zl}}{k\rho}J_n\left(k_{\rho l}\rho\right)cos\left(k_{zl}(z \pm z')\right) + \hat{\phi}\frac{k_\rho^2}{k}J_n\left(k_{\rho l}\rho\right)jsin\left(k_{zl}(z \pm z')\right)\right\} \tag{5.4}$$

$$\hat{\rho} \times Rg\vec{H}_n^{TM}\left(k_{\rho l}, k_{zl}, \vec{\rho}, z\right) = \frac{je^{-jn\phi}}{\eta}\left\{-\hat{z}k_\rho J'_n\left(k_{\rho l}\rho\right)\right\}cos\left(k_{zl}(z \pm z')\right) \tag{5.5}$$

Then the electric field is

$$\vec{E}_{ex} = \sum_{l=0}^{\infty}\sum_{n=-\infty}^{\infty}\left[w_{l,n}^{TM} Rg\vec{E}_n^{TM}\left(k_{zl}, k_{\rho l}, \vec{\rho}, z \pm z'\right)\right] \tag{5.6}$$

where the electric field wave functions are

$$Rg\vec{E}_n^{TE}(k_{\rho l}, k_{zl}, \vec{\rho}, z) = \frac{1}{j\omega\varepsilon}\nabla \times Rg\vec{H}_n^{TE}(k_{\rho l}, k_{zl}, \vec{\rho}, z)$$
$$= -e^{-jn\phi}\left\{-\hat{\rho}\frac{jn}{\rho}J_n(k_{\rho l}\rho) - \hat{\phi}k_{\rho l}J'_n(k_{\rho l}\rho)\right\}sin(k_{zl}(z \pm z')) \tag{5.7}$$

$$Rg\vec{E}_n^{TM}(k_{\rho l}, k_{zl}, \vec{\rho}, z)$$
$$= e^{-jn\phi}\left\{\hat{\rho}\frac{jk_{\rho l}k_{zl}}{k}J'_n(k_{\rho l}\rho)jsin(k_{zl}(z \pm z')) + \hat{\phi}\frac{nk_{zl}}{k\rho}J_n(k_{\rho l}\rho)jsin(k_{zl}(z \pm z')) + \hat{z}\frac{k_{\rho l}^2}{k}J_n(k_{\rho l}\rho)cos(k_{zl}(z \pm z'))\right\} \tag{5.8}$$

$$\hat{\rho} \times Rg\vec{E}_n^{TE}(k_{\rho l}, k_{zl}, \vec{\rho}, z) = e^{-jn\phi}\{\hat{z}k_{\rho l}J'_n(k_{\rho l}\rho)\}sin(k_{zl}z) \tag{5.9}$$

$$\hat{\rho} \times Rg\vec{E}_n^{TM}(k_{\rho l}, k_{zl}, \vec{\rho}, z)$$
$$= e^{-jn\phi}\left\{\hat{z}\frac{nk_{zl}}{k\rho}J_n(k_{\rho l}\rho)jsin(k_{zl}(z \pm z')) - \hat{\phi}\frac{k_{\rho l}^2}{k}J_n(k_{\rho l}\rho)cos(k_{zl}(z \pm z'))\right\} \tag{5.10}$$

Then the magnetic scattered field of the dielectric cylinder can be expressed as

$$\vec{H}_s = \sum_{l=0}^{\infty}\sum_{n=-\infty}^{\infty} w_{l,n}^{TM}\left[T_{l,n}^{TMTM}\vec{H}_n^{TM}(k_{zl}, k_{\rho l}, \vec{\rho}, z \pm z') + T_{l,n}^{TETM}\vec{H}_n^{TE}(k_{zl}, k_{\rho l}, \vec{\rho}, z \pm z')\right] \tag{5.11}$$

where $\vec{H}_n^{TM}$ is the same as $Rg\vec{H}_n^{TM}$ with Bessel function replaced by Hankel function of the second kind. In the above equations, $T_{l,n}^{TMTM}$ and $T_{l,n}^{TETM}$ are T matrix coefficients. Note that because of dielectric posts there are coupling between TE and TM modes with the coupling coefficient $T_{l,n}^{TETM}$ for $l > 0$ modes, or non TEM modes. TE modes and TM modes are decoupled for TEM mode in which case $l = 0$.

Similarly, the electric scattered field of the dielectric cylinder can be expressed as

$$\vec{E}_s = \sum_{l=0}^{\infty}\sum_{n=-\infty}^{\infty} w_{l,n}^{TM}\left[T_{l,n}^{TMTM}\vec{E}_n^{TM}(k_{zl}, k_{\rho l}, \vec{\rho}, z \pm z') + T_{l,n}^{TETM}\vec{E}_n^{TE}(k_{zl}, k_{\rho l}, \vec{\rho}, z \pm z')\right] \tag{5.12}$$

Let the dielectric cylinder be with permittivity of ε_p and permeability of μ, then let $k_p = \omega\sqrt{\mu\varepsilon_p}$, $\eta_p = \sqrt{\frac{\mu}{\varepsilon_p}}$. Note that due to the phase matching in the z direction, the k_{zl} are same for inside and outside of the dielectric cylinder.

For dielectric cylinder, the internal magnetic field vector wave functions are obtained from equations 5.2 and 5.3, which are

$$Rg\vec{H}_n^{pTE}(k_{p\rho l}, k_{zl}, \vec{\rho}, z) = \frac{e^{-jn\phi}}{\eta_p}\left\{-\hat{\rho}\frac{jk_{p\rho l}k_{zl}}{k_p}J'_n(k_{p\rho l}\rho)cos(k_{zl}(z \pm z')) - \hat{\phi}\frac{nk_{zl}}{k_p\rho}J_n(k_{p\rho l}\rho)cos(k_z z) - \hat{z}\frac{k_{p\rho l}^2}{k_p}J_n(k_{p\rho l}\rho)jsin(k_{zl}(z \pm z'))\right\} \tag{5.13}$$

$$Rg\vec{H}_n^{pTM}(k_{p\rho l}, k_{zl}, \vec{\rho}, z) = \frac{je^{-jn\phi}}{\eta_p}\left\{-\hat{\rho}\frac{jn}{\rho}J_n(k_{p\rho l}\rho) - \hat{\phi}k_{p\rho l}J'_n(k_{p\rho l}\rho)\right\}cos(k_{zl}(z \pm z')) \tag{5.14}$$

To determine the T matrix coefficients, let the internal field be

$$\vec{H}_{int} = \sum_{l=0}^{\infty}\sum_{n=-\infty}^{\infty} w_{l,n}^{TM}\left[C_{l,n}^{TMTM}Rg\vec{H}_n^{pTM}(k_{zl}, k_{p\rho l}, \vec{\rho}, z \pm z') + C_{l,n}^{TETM}Rg\vec{H}_n^{pTE}(k_{zl}, k_{p\rho l}, \vec{\rho}, z \pm z')\right] \tag{5.15}$$

Then the internal electric field is

$$\vec{E}_{int} = \sum_{l=0}^{\infty}\sum_{n=-\infty}^{\infty} w_{l,n}^{TM}\left[C_{l,n}^{TMTM}Rg\vec{E}_n^{pTM}(k_{zl}, k_{p\rho l}, \vec{\rho}, z \pm z') + C_{l,n}^{TETM}Rg\vec{E}_n^{pTE}(k_{zl}, k_{p\rho l}, \vec{\rho}, z \pm z')\right] \tag{5.16}$$

where $Rg\vec{E}_n^{pTM}$ and $Rg\vec{E}_n^{pTE}$ can be obtained from equations 5.8 and 5.9.

Now I match boundary condition for dielectric cylinder. The tangential field which includes both electric field and magnetic field are equal, hence, at surface of cylinder $\rho = a$, for each waveguide mode l, we have

$$\hat{\rho} \times (\bar{H}_s + \bar{H}_{ex}) = \hat{\rho} \times \bar{H}_{int} \tag{5.17}$$

$$\hat{\rho} \times (\bar{E}_s + \bar{E}_{ex}) = \hat{\rho} \times \bar{E}_{int} \tag{5.18}$$

From 5.17, we obtain

$$\begin{aligned}\hat{\rho}\times Rg\vec{H}_n^{TM}\left(k_{\rho l},k_{zl},\vec{\rho},z\pm z'\right)&\\ +\left[T_{l,n}^{TMTM}\hat{\rho}\times\vec{H}_n^{TM}\left(k_{\rho l},k_{zl},\vec{\rho},z\pm z'\right)+T_{l,n}^{TETM}\hat{\rho}\times\vec{H}_n^{TE}\left(k_{\rho l},k_{zl},\vec{\rho},z\pm z'\right)\right]&\\ =C_{l,n}^{TMTM}\hat{\rho}\times Rg\vec{H}_n^{pTM}\left(k_{p\rho l},k_{zl},\vec{\rho},z\pm z'\right)+C_{l,n}^{TETM}\hat{\rho}&\\ \times Rg\vec{H}_n^{pTE}\left(k_{p\rho l},k_{zl},\vec{\rho},z\pm z'\right)&\end{aligned} \tag{5.19}$$

Then

$$\begin{aligned}\frac{je^{-jn\phi}}{\eta}\left\{-\hat{z}k_{\rho l}J'_n\left(k_{\rho l}a\right)\right\}cos\left(k_{zl}(z\pm z')\right)&\\ +\left[T_{l,n}^{TMTM}\frac{je^{-jn\phi}}{\eta}\left\{-\hat{z}k_{\rho l}H_n^{(2)\prime}\left(k_{\rho l}a\right)\right\}cos\left(k_{zl}(z\pm z')\right)\right.&\\ +T_{l,n}^{TETM}\frac{e^{-jn\phi}}{\eta}\left\{-\hat{z}\frac{nk_{zl}}{ka}H_n^{(2)}\left(k_{\rho l}a\right)cos\left(k_{zl}(z\pm z')\right)\right.&\\ \left.\left.+\hat{\phi}\frac{k_{\rho l}^2}{k}H_n^{(2)}\left(k_{\rho l}a\right)jsin\left(k_{zl}(z\pm z')\right)\right\}\right]&\\ =C_{l,n}^{TMTM}\frac{je^{-jn\phi}}{\eta_p}\left\{-\hat{z}k_{p\rho l}J'_n\left(k_{p\rho l}a\right)\right\}cos\left(k_{zl}(z\pm z')\right)&\\ +C_{l,n}^{TETM}\frac{je^{-jn\phi}}{\eta_p}\left\{-\hat{z}\frac{nk_{zl}}{k_pa}J_n\left(k_{p\rho l}a\right)cos\left(k_{zl}(z\pm z')\right)\right.&\\ \left.+\hat{\phi}\frac{{k_{p\rho l}}^2}{k_p}J_n\left(k_{p\rho l}a\right)jsin\left(k_{zl}(z\pm z')\right)\right\}&\end{aligned} \tag{5.20}$$

Then, by matching $\hat{z}$ and $\hat{\phi}$ components, we obtain

$$\begin{aligned}\frac{j}{\eta}\left\{k_{\rho l}J'_n\left(k_{\rho l}a\right)\right\}+\left[T_{l,n}^{TMTM}\frac{j}{\eta}\left\{k_{\rho l}H_n^{(2)\prime}\left(k_{\rho l}a\right)\right\}+T_{l,n}^{TETM}\frac{1}{\eta}\left\{\frac{nk_{zl}}{ka}H_n^{(2)}\left(k_{\rho l}a\right)\right\}\right]&\\ =C_{l,n}^{TMTM}\frac{j}{\eta_p}\left\{k_{p\rho l}J'_n\left(k_{p\rho l}a\right)\right\}+C_{l,n}^{TETM}\frac{1}{\eta_p}\left\{\frac{nk_{zl}}{k_pa}J_n\left(k_{p\rho l}a\right)\right\}&\end{aligned} \tag{5.21}$$

$$\left[T_{l,n}^{TETM}\frac{1}{\eta}\left\{\frac{k_{\rho l}^2}{k}H_n^{(2)}\left(k_{\rho l}a\right)\right\}\right]=C_{l,n}^{TETM}\frac{1}{\eta_p}\left\{\frac{{k_{p\rho l}}^2}{k_p}J_n\left(k_{p\rho l}a\right)\right\}$$

(5.22)

From 5.18 which is tangential E continuous at the dielectric post surface $\rho = a$, we obtain

$$\hat{\rho} \times Rg\vec{E}_{l,n}^{TM}\left(k_{\rho l}, k_{zl}, \vec{\rho}, z \pm z'\right) + \left[T_{l,n}^{TMTM}\hat{\rho} \times \vec{E}_{l,n}^{TM}\left(k_{\rho l}, k_{zl}, \vec{\rho}, z \pm z'\right) + T_{l,n}^{TETM}\hat{\rho} \times \vec{E}_{l,n}^{TE}\left(k_{\rho l}, k_{zl}, \vec{\rho}, z \pm z'\right)\right] = C_{l,n}^{TMTM}\hat{\rho} \times Rg\vec{E}_{l,n}^{pTM}\left(k_{p\rho l}, k_{zl}, \vec{\rho}, z \pm z'\right) + C_{l,n}^{TETM}\hat{\rho} \times Rg\vec{E}_{n}^{pTE}\left(k_{p\rho l}, k_{zl}, \vec{\rho}, z \pm z'\right)$$

(5.23)

Then

$$e^{-jn\phi}\left\{\hat{z}\frac{nk_{zl}}{ka}J_n\left(k_{\rho l}a\right)jsin\left(k_{zl}(z \pm z')\right) - \hat{\phi}\frac{k_{\rho l}^2}{k}J_n\left(k_{\rho l}a\right)cos\left(k_{zl}(z \pm z')\right)\right\} + \left[T_{l,n}^{TMTM}e^{-jn\phi}\left\{\hat{z}\frac{nk_{zl}}{ka}H_n^{(2)}\left(k_{\rho l}a\right)jsin\left(k_{zl}(z \pm z')\right) - \hat{\phi}\frac{k_{\rho l}^2}{k}H_n^{(2)}\left(k_{\rho l}a\right)cos\left(k_{zl}(z \pm z')\right)\right\} + T_{l,n}^{TETM}e^{-jn\phi}\left\{\hat{z}k_{\rho l}H_n^{(2)\prime}\left(k_{\rho l}a\right)\right\}sin\left(k_{zl}(z \pm z')\right)\right] = C_{l,n}^{TMTM}e^{-jn\phi}\left\{\hat{z}\frac{nk_{zl}}{k_p a}J_n\left(k_{p\rho l}a\right)jsin\left(k_{zl}(z \pm z')\right) - \hat{\phi}\frac{k_{p\rho l}{}^2}{k_p}J_n\left(k_{p\rho l}a\right)cos\left(k_{zl}(z \pm z')\right)\right\} + e^{-jn\phi}\left\{\hat{z}k_{\rho l}J_n{}'\left(k_{p\rho l}a\right)\right\}sin\left(k_{zl}(z \pm z')\right)$$

(5.24)

Then by matching $\hat{z}$ and $\hat{\phi}$ components, we obtain

$$\left\{\frac{nk_{zl}}{ka}J_n\left(k_{\rho l}a\right)j\right\} + \left[T_{l,n}^{TMTM}\left\{\frac{nk_{zl}}{ka}H_n^{(2)}\left(k_{\rho l}a\right)j\right\} + T_{l,n}^{TETM}\left\{k_{\rho l}H_n^{(2)\prime}\left(k_{\rho l}a\right)\right\}\right] = C_{l,n}^{TMTM}\left\{\frac{nk_{zl}}{k_p a}J_n\left(k_{p\rho l}a\right)j\right\} + C_{l,n}^{TETM}\left\{k_{p\rho l}J_n{}'\left(k_{p\rho l}a\right)\right\}$$

(5.25)

$$\left\{\frac{k_{\rho l}^2}{k}J_n\left(k_{\rho l}a\right)\right\} + \left[T_{l,n}^{TMTM}\left\{\frac{k_{\rho l}^2}{k}H_n^{(2)}\left(k_{\rho l}a\right)\right\}\right] = C_{l,n}^{TMTM}\left\{\frac{k_{p\rho l}{}^2}{k_p}J_n\left(k_{p\rho l}a\right)\right\}$$

(5.26)

Sort them as matrix form, we have

$$\begin{bmatrix} jk\left\{k_{\rho l}H_n^{(2)\prime}(k_{\rho l}a)\right\} & \left\{\frac{nk_{zl}}{a}H_n^{(2)}(k_{\rho l}a)\right\} & -jk_p\{k_{p\rho l}J'_n(k_{p\rho l}a)\} & -\left\{\frac{nk_{zl}}{a}J_n(k_{p\rho l}a)\right\} \\ 0 & \left\{k_{\rho l}^2H_n^{(2)}(k_{\rho l}a)\right\} & 0 & -\{{k_{p\rho l}}^2J_n(k_{p\rho l}a)\} \\ \left\{\frac{nk_{zl}}{ka}H_n^{(2)}(k_{\rho l}a)j\right\} & \left\{k_{\rho l}H_n^{(2)\prime}(k_{\rho l}a)\right\} & -\left\{\frac{nk_{zl}}{k_pa}J_n(k_{p\rho l}a)j\right\} & -\{k_{p\rho l}J_n{}'(k_{p\rho l}a)\} \\ \left\{\frac{k_{\rho l}^2}{k}H_n^{(2)}(k_{\rho l}a)\right\} & 0 & -\left\{\frac{{k_{p\rho l}}^2}{k_p}J_n(k_{p\rho l}a)\right\} & 0 \end{bmatrix}$$

$$\times \begin{bmatrix} T_{l,n}^{TMTM} \\ T_{l,n}^{TETM} \\ C_{l,n}^{TMTM} \\ C_{l,n}^{TETM} \end{bmatrix} = \begin{bmatrix} -jk\{k_{\rho l}J'_n(k_{\rho l}a)\} \\ 0 \\ -\left\{\frac{nk_{zl}}{ka}J_n(k_{\rho l}a)j\right\} \\ -\left\{\frac{k_{\rho l}^2}{k}J_n(k_{\rho l}a)\right\} \end{bmatrix} \tag{5.27}$$

We can then solve the T matrix coefficients of dielectric cylinder for TM modes.

5.2.2 *TE case*

Now let the exciting field be TE modes excitation. When matching tangential magnetic and electric filed continuously at the dielectric post surface $\rho = a$, we have

$$\begin{aligned} &\hat{\rho} \times Rg\vec{H}_n^{TE}(k_{\rho l}, k_{zl}, \vec{\rho}, z \pm z') \\ &\quad + \left[T_{l,n}^{TMTE}\hat{\rho} \times \vec{H}_n^{TM}(k_{\rho l}, k_{zl}, \vec{\rho}, z \pm z') + T_{l,n}^{TETE}\hat{\rho} \times \vec{H}_n^{TE}(k_{\rho l}, k_{zl}, \vec{\rho}, z \pm z')\right] \\ &\quad = C_{l,n}^{TMTE}\hat{\rho} \times Rg\vec{H}_n^{pTM}(k_{p\rho l}, k_{zl}, \vec{\rho}, z \pm z') + C_{l,n}^{TETE}\hat{\rho} \\ &\quad \times Rg\vec{H}_n^{pTE}(k_{p\rho l}, k_{zl}, \vec{\rho}, z \pm z') \end{aligned} \tag{5.28}$$

$$\begin{aligned} &\hat{\rho} \times Rg\vec{E}_n^{TE}(k_{\rho l}, k_{zl}, \vec{\rho}, z \pm z') \\ &\quad + \left[T_{l,n}^{TMTE}\hat{\rho} \times \vec{E}_n^{TM}(k_{\rho l}, k_{zl}, \vec{\rho}, z \pm z') + T_{l,n}^{TETE}\hat{\rho} \times \vec{E}_n^{TE}(k_{\rho l}, k_{zl}, \vec{\rho}, z \pm z')\right] \\ &\quad = C_{l,n}^{TMTE}\hat{\rho} \times Rg\vec{E}_n^{pTM}(k_{p\rho l}, k_{zl}, \vec{\rho}, z \pm z') + C_{l,n}^{TETE}\hat{\rho} \\ &\quad \times Rg\vec{E}_n^{pTE}(k_{p\rho l}, k_{zl}, \vec{\rho}, z \pm z') \end{aligned} \tag{5.29}$$

Then, by matching $\hat{z}$ and $\hat{\phi}$ components, we have

$$T_{l,n}^{TETE}\frac{nk_{zl}}{ka}H_n^{(2)}(k_{\rho l}a)+T_{l,n}^{TMTE}jk_{\rho l}H_n^{(2)\prime}(k_{\rho l}a)-C_{l,n}^{TETE}\frac{nk_{zl}}{ka}J_n(k_{p\rho l}a)$$
$$-C_{l,n}^{TMTE}j\frac{k_p}{k}k_{p\rho l}J'_n(k_{p\rho l}a)=-\frac{nk_{zl}}{ka}J_n(k_{\rho l}a)$$

(5.30)

$$T_{l,n}^{TETE}k_{\rho l}^2H_n^{(2)}(k_{\rho l}a)-C_{l,n}^{TETE}{k_{p\rho l}}^2J_n(k_{p\rho l}a)=-k_{\rho l}^2J_n(k_{\rho l}a)$$

(5.31)

and

$$T_{l,n}^{TETE}k_{\rho l}H_n^{(2)\prime}(k_{\rho l}a)+T_{l,n}^{TMTE}j\frac{nk_{zl}}{ka}H_n^{(2)}(k_{\rho l}a)-C_{l,n}^{TETE}k_{p\rho l}J'_n(k_{\rho l}a)$$
$$-C_{l,n}^{TMTE}j\frac{nk_{zl}}{ka}J_n(k_{p\rho l}a)=-k_{\rho l}J'_n(k_{\rho l}a)$$

(5.32)

$$T_{l,n}^{TMTE}\frac{k_{\rho l}^2}{k}H_n^{(2)}(k_{\rho l}a)-C_{l,n}^{TMTE}\frac{{k_{p\rho l}}^2}{k_p}J_n(k_{p\rho l}a)=0$$

(5.33)

Then

$$\begin{bmatrix}\frac{nk_{zl}}{ka}H_n^{(2)}(k_{\rho l}\rho) & jk_{\rho l}H_n^{(2)\prime}(k_{\rho l}\rho) & -\frac{nk_{zl}}{ka}J_n(k_{p\rho l}\rho) & -j\frac{k_p}{k}k_{p\rho l}J'_n(k_{p\rho l}\rho)\\ k_{\rho l}^2H_n^{(2)}(k_{\rho l}\rho) & 0 & -{k_{p\rho l}}^2J_n(k_{p\rho l}\rho) & 0\\ k_{\rho l}H_n^{(2)\prime}(k_{\rho l}\rho) & j\frac{nk_{zl}}{ka}H_n^{(2)}(k_{\rho l}\rho) & -k_{p\rho l}J'_n(k_{\rho l}\rho) & -j\frac{nk_{zl}}{ka}J_n(k_{p\rho l}\rho)\\ 0 & \frac{k_{\rho l}^2}{k}H_n^{(2)}(k_{\rho l}\rho) & 0 & \frac{k_{\rho l}^{d\ 2}}{k_p}J_n(k_{p\rho l}\rho)\end{bmatrix}\times\begin{bmatrix}T_{l,n}^{TETE}\\T_{l,n}^{TMTE}\\C_{l,n}^{TETE}\\C_{l,n}^{TMTE}\end{bmatrix}$$
$$=\begin{bmatrix}-\frac{nk_{zl}}{ka}J_n(k_{\rho l}\rho)\\-\frac{nk_{zl}}{ka}J_n(k_{\rho l}\rho)\\-k_{\rho l}J'_n(k_{\rho l}\rho)\\0\end{bmatrix}$$

(5.34)

We can then solve the T matrix coefficients of dielectric cylinder for TE modes.

Note that, for $l = 0$ which is TEM mode for waveguide, only TM modes are excited, and the analytical solution for T matrix for dielectric cylinder is [34]

$$T_{0,n}^{TMTM} = -\frac{k_p J_n(ka) J_n{}'(k_p a) - k J_n{}'(ka) J_n(k_p a)}{k_p H_n^{(2)}(ka) J_n{}'(k_p a) - k H_n^{(2)\prime}(ka) J_n(k_p a)} \tag{5.35}$$

which can also be obtained from equation 5.27.

5.3 Foldy-Lax Equations for Multiple Scattering among Dielectric Cylinders in Parallel Plate Waveguide

I now derive the Foldy-Lax equations with multiple scattering among dielectric cylinders in parallel plate waveguide.

The Foldy-Lax equations state that the final exciting field of particle q is equal to the incident wave plus the scattered waves to particle q from all other particles p except q itself. For multiple scattering problem of dielectric cylinders, there are three forms of Foldy-Lax equations as shown in [34]. The first form is for listing final exciting field as unknowns, as we used in chapter 2-4. However, the Foldy-Lax equations with this form cannot be solved accurately, as the matrix is very badly conditioned for its inverse operation, as shown in chapter 2, we need to rescaled the equations and obtain accurate results. Instead of using equations for the exciting field coefficients, the scattered field coefficients and internal field coefficients can also be used for listing Foldy-Lax equations. I found that the form which uses the scattered field coefficients showed more accurate inverse operation due to its matrix having lower condition number. I adopt this form in this chapter to solve problem.

For multiple scattering problem of dielectric cylinders with TE and TM modes decoupling case, all the three forms have been shown in the [34]. In this chapter, I derive Foldy-Lax equations for mixed metal/dielectric cylinders with TE and TM modes coupling case in parallel plates waveguide structures.

I first derive form of Foldy-Lax equations that use the final exciting field coefficients as unknowns for TE/TM modes coupling case, then I derive form of Foldy-Lax equations that use the scattered field coefficients as unknowns for TE/TM modes coupling case.

Consider N cylinders between the two parallel plats centered at $\vec{\rho}_1, \vec{\rho}_2, \ldots\ldots, \vec{\rho}_N$, the cylinders can be PEC or dielectric cylinders. Within the Foldy-Lax formulation, the final exciting field on cylinder p is

$$\vec{H}_{ex}^{(p)} = \sum_{l=0}^{\infty}\sum_{n=-\infty}^{\infty}\Big[w_{l,n}^{TM(p)} Rg\vec{H}_n^{TM}\big(k_{zl}, k_{\rho l}, \vec{\rho}-\vec{\rho}_p, z\pm z'\big) + w_{l,n}^{TE(p)} Rg\vec{H}_n^{TE}\big(k_{zl}, k_{\rho l}, \vec{\rho}-\vec{\rho}_p, z\pm z'\big)\Big] \tag{5.36}$$

The final scattered field from cylinder p is

$$\begin{aligned}\vec{H}_s^{(p)} = \sum_{l=0}^{\infty}\sum_{n=-\infty}^{\infty}\Big\{&\Big[T_{l,n}^{TMTM(p)}\vec{H}_n^{TM}\big(k_{zl}, k_{\rho l}, \vec{\rho}-\vec{\rho}_p, z\pm z'\big) \\ &+ T_{l,n}^{TETM(p)}\vec{H}_n^{TE}\big(k_{zl}, k_{\rho l}, \vec{\rho}-\vec{\rho}_p, z\pm z'\big)\Big] w_{l,n}^{TM(p)} \\ &+ \Big[T_{l,n}^{TMTE(p)}\vec{H}_n^{TM}\big(k_{zl}, k_{\rho l}, \vec{\rho}-\vec{\rho}_p, z\pm z'\big) \\ &+ T_{l,n}^{TETE(p)}\vec{H}_n^{TE}\big(k_{zl}, k_{\rho l}, \vec{\rho}-\vec{\rho}_p, z\pm z'\big)\Big] w_{l,n}^{TE(p)}\Big\}\end{aligned} \tag{5.37}$$

The scattered field will be incident on cylinder q, the propagator is same as we used in chapter 2 and 3 for infinite large parallel plates waveguide, which is equation (3.11). Then the scattered field form p onto cylinder q is

$$\begin{aligned}\vec{H}_s^{(p)} = \sum_{l=0}^{\infty}\sum_{n=-\infty}^{\infty}\sum_{m=-\infty}^{\infty}\Big\{&\Big[T_{l,n}^{TMTM(p)} Rg\vec{H}_m^{TM}\big(k_{zl}, k_{\rho l}, \vec{\rho}-\vec{\rho}_q, z\pm z'\big) \\ &+ T_{l,n}^{TETM(p)} Rg\vec{H}_m^{TE}\big(k_{zl}, k_{\rho l}, \vec{\rho}-\vec{\rho}_q, z\pm z'\big)\Big] w_{l,n}^{TM(p)} \\ &+ \Big[T_{l,n}^{TMTE(p)} Rg\vec{H}_m^{TM}\big(k_{zl}, k_{\rho l}, \vec{\rho}-\vec{\rho}_q, z\pm z'\big) \\ &+ T_{l,n}^{TETE(p)} Rg\vec{H}_m^{TE}\big(k_{zl}, k_{\rho l}, \vec{\rho}-\vec{\rho}_q, z\pm z'\big)\Big] w_{l,n}^{TE(p)}\Big\}\big[\bar{\bar{\alpha}}_{qp}^{+}\big]_{nm}\end{aligned} \tag{5.38}$$

or

$$\begin{aligned}\vec{H}_s^{(p)} = \sum_{l=0}^{\infty}\sum_{n=-\infty}^{\infty}\sum_{m=-\infty}^{\infty}\Big\{&\Big[T_{l,n}^{TMTM(p)} w_{l,n}^{TM(p)} + T_{l,n}^{TMTE(p)} w_{l,n}^{TE(p)}\Big] Rg\vec{H}_m^{TM}\big(k_{zl}, k_{\rho l}, \vec{\rho}-\vec{\rho}_q, z\pm z'\big) \\ &+ \Big[T_{l,n}^{TETM(p)} w_{l,n}^{TM(p)} + T_{l,n}^{TETE(p)} w_{l,n}^{TE(p)}\Big] Rg\vec{H}_m^{TE}\big(k_{zl}, k_{\rho l}, \vec{\rho}-\vec{\rho}_q, z\pm z'\big)\Big\}\big[\bar{\bar{\alpha}}_{qp}^{+}\big]_{nm}\end{aligned}$$

(5.39)

Thus we get the Foldy-Lax multiple scattering equations by balancing every coefficient for each mode,

$$w_{l,n}^{TM(q)} = a_{l,n}^{TM(q)} + \sum_{\substack{p=1,\\ p\neq q}}^{N} \sum_{m=-\infty}^{\infty} \left[T_{l,n}^{TMTM(p)} w_{l,n}^{TM(p)} + T_{l,n}^{TMTE(p)} w_{l,n}^{TE(p)} \right] Rg\vec{H}_m^{TM}\left(k_{zl}, k_{\rho l}, \vec{\rho} - \vec{\rho}_q, z \pm z'\right) H_{n-m}^{(2)}\left(k_{\rho l}\left|\overline{\rho_p} - \overline{\rho_q}\right|\right) e^{j(n-m)\emptyset_{\overline{\rho_p \rho_q}}} \tag{5.40}$$

$$w_{l,n}^{TE(q)} = a_{l,n}^{TE(q)} + \sum_{\substack{p=1,\\ p\neq q}}^{N} \sum_{m=-\infty}^{\infty} \left[T_{l,n}^{TETM(p)} w_{l,n}^{TM(p)} + T_{l,n}^{TETE(p)} w_{l,n}^{TE(p)} \right] Rg\vec{H}_m^{TE}\left(k_{zl}, k_{\rho l}, \vec{\rho} - \vec{\rho}_q, z \pm z'\right) H_{n-m}^{(2)}\left(k_{\rho l}\left|\overline{\rho_p} - \overline{\rho_q}\right|\right) e^{j(n-m)\emptyset_{\overline{\rho_p \rho_q}}} \tag{5.41}$$

where $a_{l,n}^{TM(q)}$ and $a_{l,n}^{TE(q)}$ are the incident field coefficients for TM and TE modes on cylinder q, which will be discussed later in this chapter.

The above two equations are Foldy-Lax equations by using the final exciting field coefficients as unknowns for TE/TM modes coupling case. I then derive Foldy-Lax equations by using the scattered field coefficients as unknowns for TE/TM modes coupling case.

Let scattered field coefficients of TE and TM modes for cylinder p are $v_{l,n}^{TE(p)}$ and $v_{l,n}^{TM(p)}$, and $v_{l,n}^{TMTM(p)} = T_{l,n}^{TMTM(p)} w_{l,n}^{TM(p)}$, $v_{l,n}^{TETE(p)} = T_{l,n}^{TETE(p)} w_{l,n}^{TE(p)}$, $v_{l,n}^{TMTE(p)} = T_{l,n}^{TMTE(p)} w_{l,n}^{TE(p)}$, and $v_{l,n}^{TMTE(p)} = T_{l,n}^{TMTE(p)} w_{l,n}^{TE(p)}$. Then we can obtain

$$v_{l,n}^{TM(p)} = T_{l,n}^{TMTM(p)} w_{l,n}^{TM(p)} + T_{l,n}^{TMTE(p)} w_{l,n}^{TE(p)} = v_{l,n}^{TMTM(p)} + v_{l,n}^{TMTE(p)} \tag{5.42}$$

$$v_{l,n}^{TE(p)} = T_{l,n}^{TETM(p)} w_{l,n}^{TM(p)} + T_{l,n}^{TETE(p)} w_{l,n}^{TE(p)} = v_{l,n}^{TETM(p)} + v_{l,n}^{TETE(p)} \tag{5.43}$$

Then equations (5.40) and (5.41) become

$$w_{l,n}^{TM(q)} = a_{l,n}^{TM(q)} + \sum_{\substack{p=1,\\ p\neq q}}^{N} \sum_{m=-\infty}^{\infty} v_{l,n}^{TM(p)} Rg\vec{H}_m^{TM}\left(k_{zl}, k_{\rho l}, \vec{\rho} - \vec{\rho}_q, z \pm z'\right) H_{n-m}^{(2)}\left(k_{\rho l}\left|\overline{\rho_p} - \overline{\rho_q}\right|\right) e^{j(n-m)\emptyset_{\overline{\rho_p \rho_q}}} \tag{5.44}$$

$$w_{l,n}^{TE(q)} = a_{l,n}^{TE(q)} + \sum_{\substack{p=1,\\ p\neq q}}^{N} \sum_{m=-\infty}^{\infty} v_{l,n}^{TE(p)} Rg\vec{H}_m^{TE}\left(k_{zl}, k_{\rho l}, \vec{\rho} - \vec{\rho}_q, z \pm z'\right) H_{n-m}^{(2)}\left(k_{\rho l}\left|\overline{\rho_p} - \overline{\rho_q}\right|\right) e^{j(n-m)\emptyset_{\overline{\rho_p \rho_q}}} \tag{5.45}$$

Let (5.44) multiplies $T_{l,n}^{TMTM(q)}$ and (5.45) multiplies $T_{l,n}^{TMTE(q)}$, we get

$$v_{l,n}^{TMTM(q)} = T_{l,n}^{TMTM(q)} a_{l,n}^{TM(q)} + T_{l,n}^{TMTM(q)} \sum_{\substack{p=1,\\ p\neq q}}^{N} \sum_{m=-\infty}^{\infty} v_{l,n}^{TM(p)} Rg\vec{H}_m^{TM}\left(k_{zl}, k_{\rho l}, \vec{\rho} - \vec{\rho}_q, z \pm z'\right) H_{n-m}^{(2)}\left(k_{\rho l}\left|\overline{\rho_p} - \overline{\rho_q}\right|\right) e^{j(n-m)\emptyset_{\overline{\rho_p \rho_q}}} \tag{5.46}$$

$$v_{l,n}^{TMTE(q)} = T_{l,n}^{TMTE(q)} a_{l,n}^{TE(q)} + T_{l,n}^{TMTE(q)} \sum_{\substack{p=1,\\ p\neq q}}^{N} \sum_{m=-\infty}^{\infty} v_{l,n}^{TE(p)} Rg\vec{H}_m^{TE}\left(k_{zl}, k_{\rho l}, \vec{\rho} - \vec{\rho}_q, z \pm z'\right) H_{n-m}^{(2)}\left(k_{\rho l}\left|\overline{\rho_p} - \overline{\rho_q}\right|\right) e^{j(n-m)\emptyset_{\overline{\rho_p \rho_q}}} \tag{5.47}$$

Add (5.46) and (5.47), by using (5.42), we obtain

$$v_{l,n}^{TM(q)} = \left(T_{l,n}^{TMTM(q)} a_{l,n}^{TM(q)} + T_{l,n}^{TMTE(q)} a_{l,n}^{TE(q)}\right) + \sum_{\substack{p=1,\\ p\neq q}}^{N} \sum_{m=-\infty}^{\infty} \left[T_{l,n}^{TMTM(q)} v_{l,n}^{TM(p)} Rg\vec{H}_m^{TM}\left(k_{zl}, k_{\rho l}, \vec{\rho} - \vec{\rho}_q, z \pm z'\right) + T_{l,n}^{TMTE(q)} v_{l,n}^{TE(p)} Rg\vec{H}_m^{TE}\left(k_{zl}, k_{\rho l}, \vec{\rho} - \vec{\rho}_q, z \pm z'\right)\right] H_{n-m}^{(2)}\left(k_{\rho l}\left|\overline{\rho_p} - \overline{\rho_q}\right|\right) e^{j(n-m)\emptyset_{\overline{\rho_p \rho_q}}} \tag{5.48}$$

Similarly, we can also obtain

$$v_{l,n}^{TE(q)} = \left(T_{l,n}^{TETM(q)} a_{l,n}^{TM(q)} + T_{l,n}^{TETE(q)} a_{l,n}^{TE(q)}\right) + \sum_{\substack{p=1,\\ p\neq q}}^{N} \sum_{m=-\infty}^{\infty} \left[T_{l,n}^{TETM(q)} v_{l,n}^{TM(p)} Rg\vec{H}_m^{TM}\left(k_{zl}, k_{\rho l}, \vec{\rho} - \vec{\rho}_q, z \pm z'\right) + T_{l,n}^{TETE(q)} v_{l,n}^{TE(p)} Rg\vec{H}_m^{TE}\left(k_{zl}, k_{\rho l}, \vec{\rho} - \vec{\rho}_q, z \pm z'\right)\right] H_{n-m}^{(2)}\left(k_{\rho l}\left|\overline{\rho_p} - \overline{\rho_q}\right|\right) e^{j(n-m)\emptyset_{\overline{\rho_p \rho_q}}} \tag{5.49}$$

The above two equations are Foldy-Lax equations by using the scattered field coefficients as unknowns for TE/TM modes coupling case.

5.4 Incident Field and Post Processing

I only consider case of coaxial ports excitation in this chapter, and the ports are on antipads which only are gone through by PEC cylinders. Then the incident field coefficients $a_{l,n}^{TM(q)}$ then are same as shown in equation (2.8). Since the TE modes are not excited directly by coaxial ports excitation, then $a_{l,n}^{TE(q)} = 0$. But note that the TE modes can be excited due to TM/TE modes coupling effects for $l > 0$ waveguide modes.

Once we solve the Foldy-Lax equations, the currents for each via can be obtained as described in chapter 2 and 3.

5.5 NUMERICAL RESULTS AND SUMMARY

In this chapter, I make different SIW based structures for verifying my derivations. I first start investigation of multiple PEC vias caged SIW in parallel plate waveguide; then I add one dielectric post close to PEC signal vias, to see what is impact of the addition of the dielectric post; at last, I added two more dielectric posts (3 total) around the signal via to observe the difference among S parameters of three configurations. To verify the proposed method, I compare my modeling results obtained from Foldy-Lax equations with them from HFSS simulations, up to 50GHz.

Note that since the SIWs are caged by multiple closely spaced PEC vias, which means the boundary reflection effects of the cavity or waveguide that the SIWs are embedded in can be ignored, due to narrow gap between two close vias. Then both in the Foldy-Lax simulation and HFSS simulation, the targeted SIWs are embedded in an infinite large parallel plates.

In each configuration figure, purple color stands for PEC vias, orange color stands for air (I use vacuum in HFSS) cylinder. $\varepsilon_r = 4.4$, $\delta = 0.02$, $R_{via} = 5\,mil$, $R_{antipad} = 15\,mil$, $h = 50\,mil$, $t = 1.3\,mil$, air cylinder radius is $a = 20\,mil$.

5.5.1 *A. SIW structure with one signal via inside and without any dielectric cylinders. The first resonance happens at about 36GHz.*

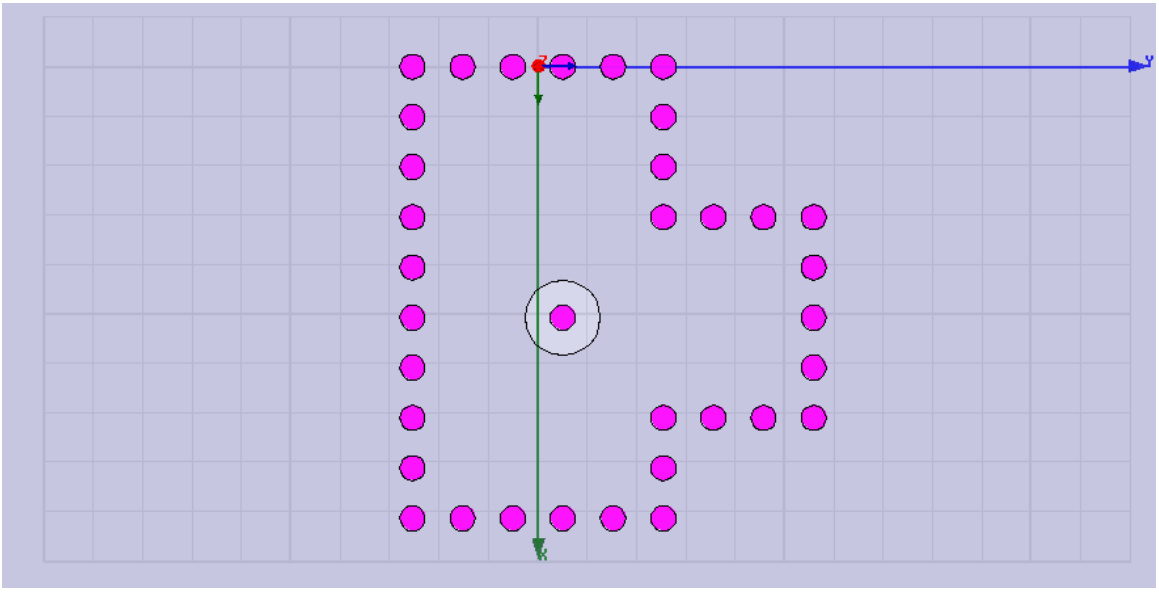

Figure 5.1. Geometry for case A

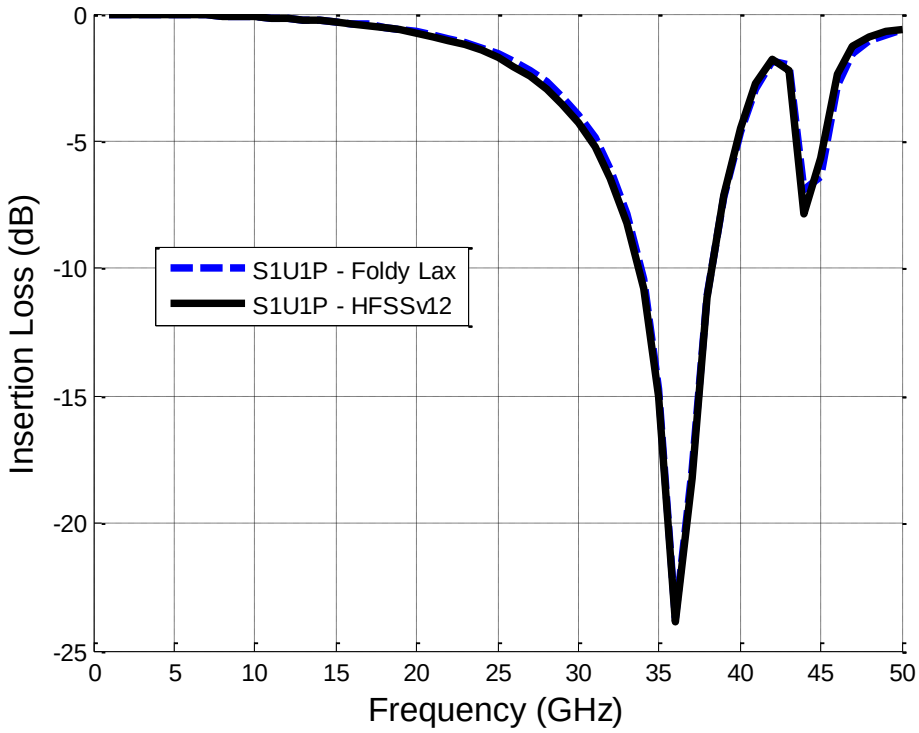

Figure 5.2. Insertion loss comparisons between Foldy-Lax and HFSS for case A.

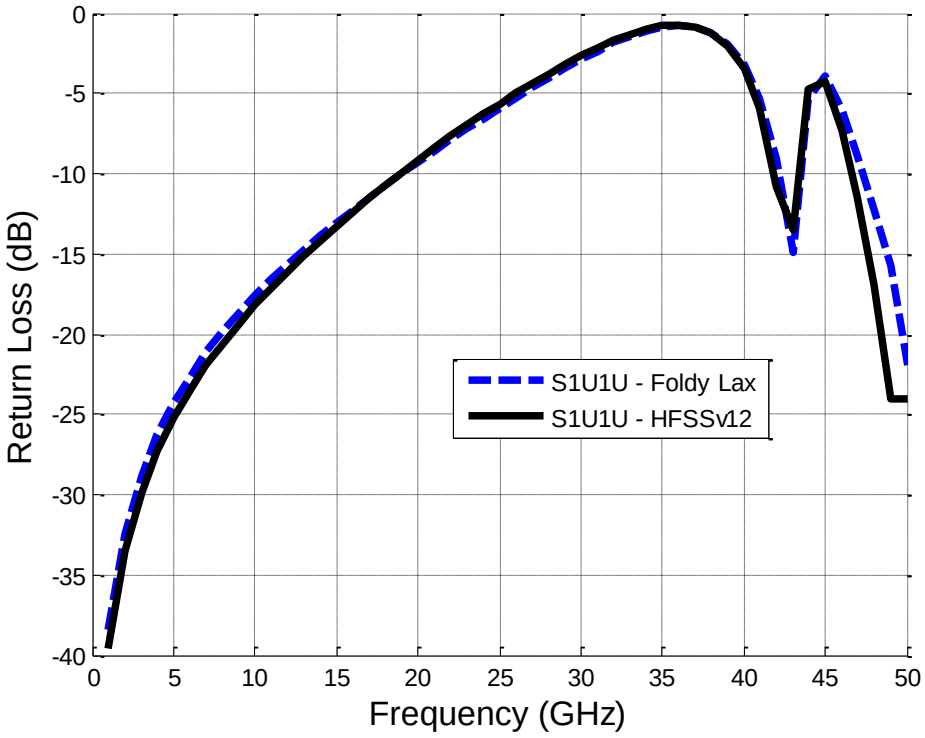

Figure 5.3. Return loss comparisons between Foldy-Lax and HFSS for case A.

5.5.2 *B. SIW structure with one signal via inside and 1 closely placed dielectric cylinder. The first resonance happens at about 37GHz.*

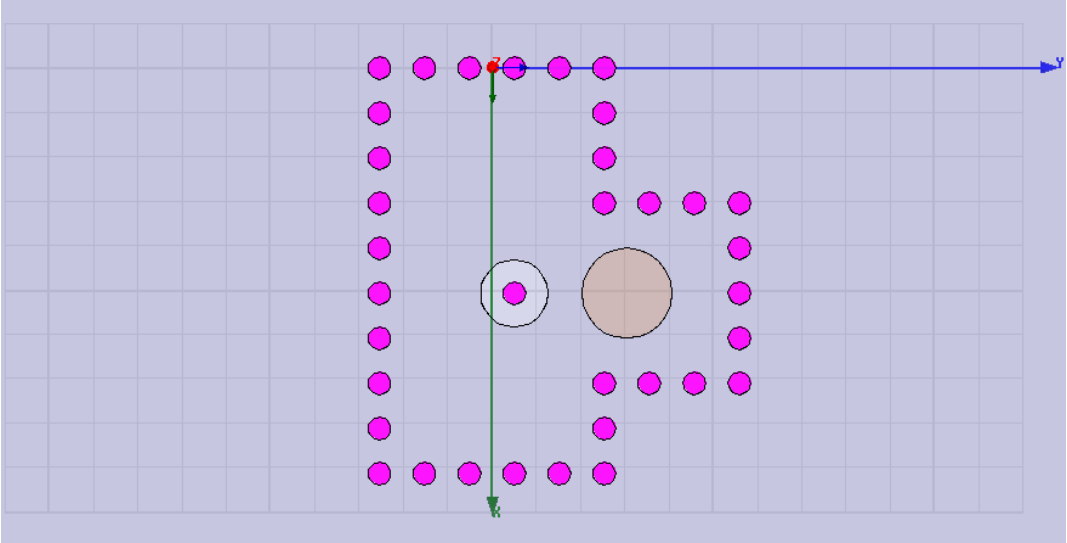

Figure 5.4. Geometry for case B

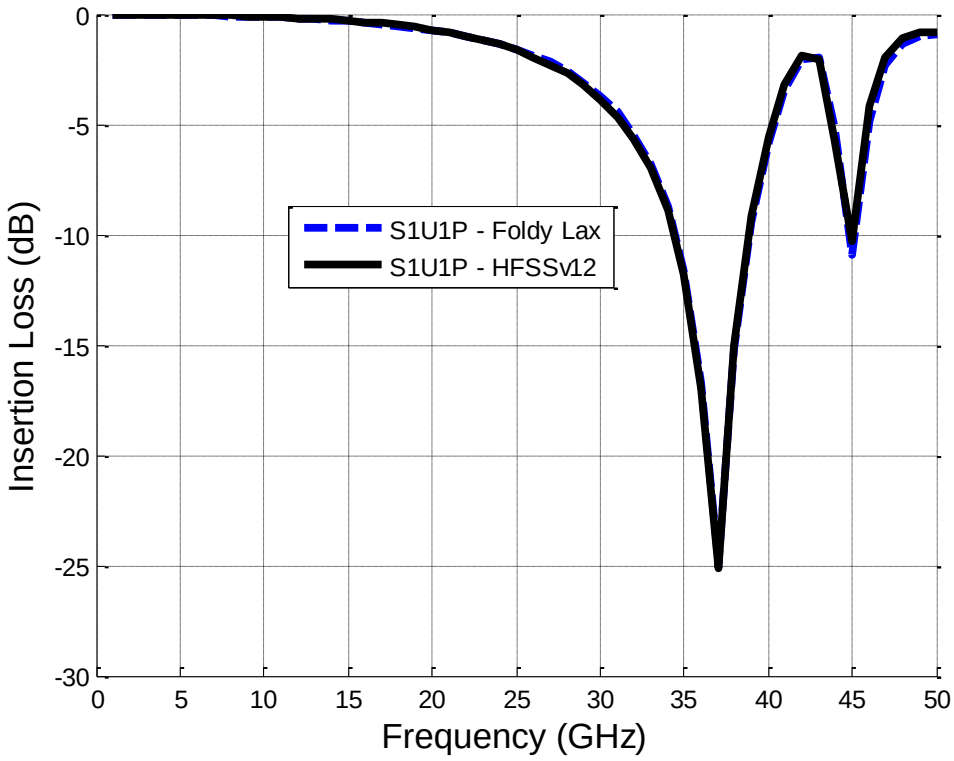

Figure 5.5. Insertion loss comparisons between Foldy-Lax and HFSS for case B.

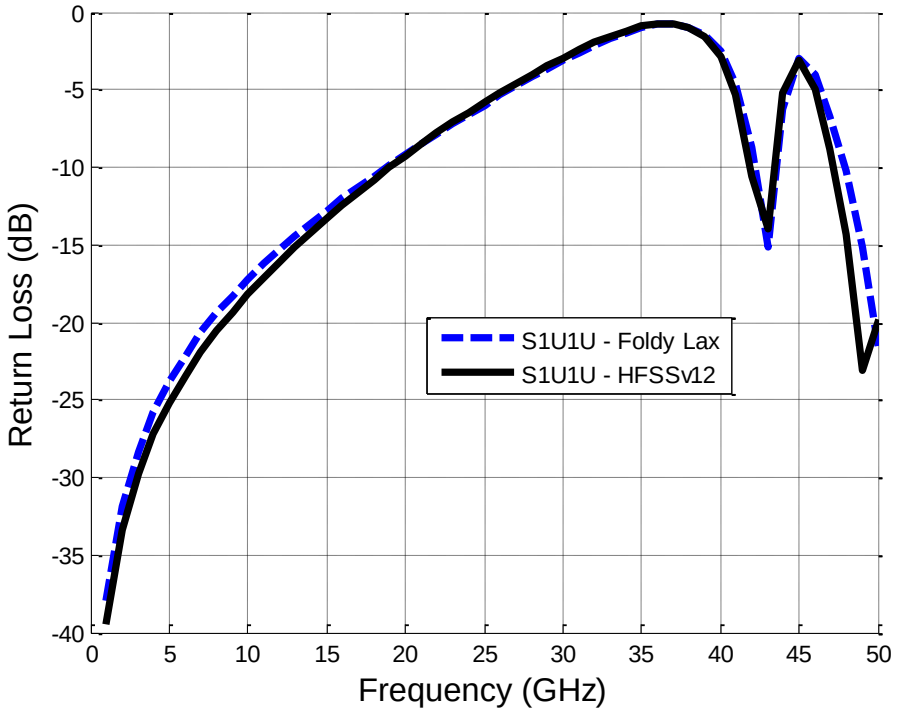

Figure 5.6. Return loss comparisons between Foldy-Lax and HFSS for case B.

5.5.3 *C. SIW structure with one signal via inside and 3 closely placed dielectric cylinders. The first resonance happened at about 41GHz.*

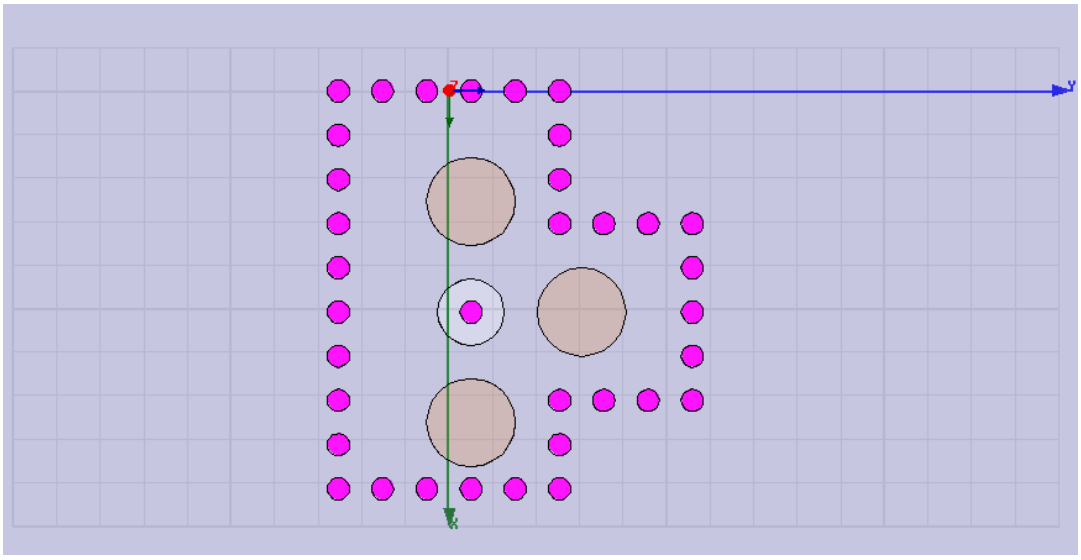

Figure 5.7. Geometry for case C.

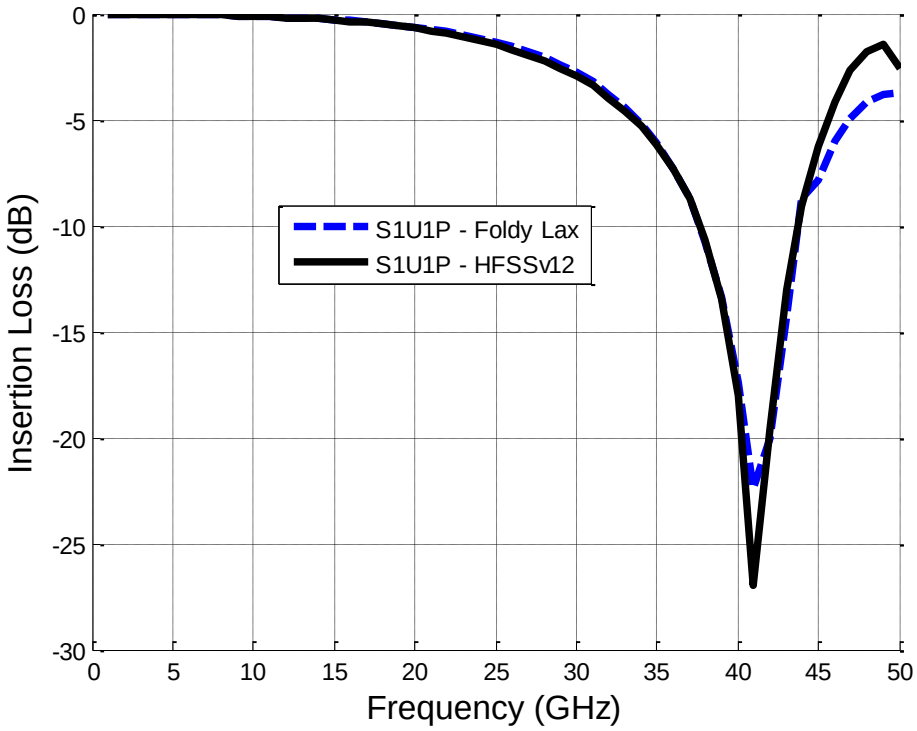

Figure 5.8. Insertion loss comparisons between Foldy-Lax and HFSS for case C.

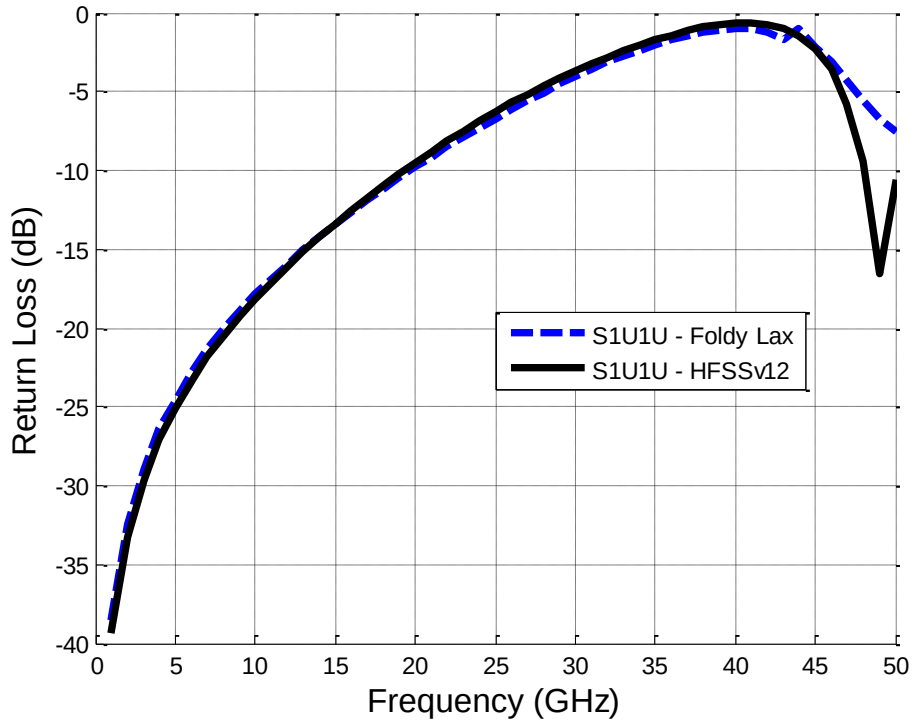

Figure 5.9. Return loss comparisons between Foldy-Lax and HFSS for case C.

From the comparisons from these benchmarks, we can observe that the results obtained from Foldy-Lax equations method match well with results from HFSS simulations up to 50GHz. Also, the resonance frequency is increasing with more and more dielectric cylinders being placed closely to signal via in SIW structures. The resonance/bandwidth of a SIW based device actually can be changed by locating different metallic and dielectric cylinders. And the proposed method provides a fast and accurate way to predict such change in pre-design phase for SIW based devices.

BIBLIOGRAPHY

[1] D.G. Kam, M.B. Ritter, T.J. Beukema, J.F. Bulzacchelli, P.K. Pepeljugoski, Y.H. Kwark, L. Shan, X. Gu, C.W. Baks, R.A. John, G. Hougham, C. Schuster, R. Rimolo-Donadio, and B. Wu, "Is 25 Gb/s on-board signaling viable?" special issue, *IEEE Trans. Advanced Packaging*, vol. 32, no. 2, pp. 328-344, May 2009.

[2] M. Bozzi, et al, "Review of substrate-integrated waveguide circuits and antennas", *IET Microw. Antennas Propag.*, vol. 5, iss. 8, pp. 909–920, 2011.

[3] Y. J. Cheng, et al, "94 GHz Substrate Integrated Monopulse Antenna Array", *IEEE Transactions on Antennas and Propagation*, vol. 60, no. 1, pp. 121-129, January 2012.

[4] L. Tsang, H. Chen, C.-C. Huang, and V. Jandhyala, "Modeling of multiple scattering among vias in planar waveguides using Foldy-Lax equations," *Microwave Optical Technol. Lett*. vol. 31, pp. 201-208, Nov. 2001.

[5] X. Gu, B. Wu, C. Baks and L. Tsang, "Fast full wave analysis of PCB via arrays with model-to-hardware correlation," *Proc. IEEE Electrical Performance of Electrical Packaging and Systems Conf., (EPEPS'09)*, Oct. 2009, pp. 175-178.

[6] B. Wu, et al, "Electromagnetic Modeling of Massively Coupled through Silicon Vias for 3-D Interconnects", *Micro. Opt. Technol. Lett*., vol.53, no.6, pp. 1204-1206, Jun. 2011.

[7] K. L. Lai, et al, "Application of multilevel UV method to analyze large microstrip patch structures", *IEEE Antennas Wireless Propagat. Lett.*, vol.4, pp. 471-474, 2005.

[8] C.-J. Ong et al, " Full-Wave Analysis of Large-Scale Interconnects Using the Multilevel UV Method With the Sparse Matrix Iterative Approach (SMIA) ", *IEEE Trans. Adv. Pkg.*, vol. 31, no. 4, pp. 818-829, Nov 2008.

[9] C. C. Huang, L. Tsang, C. H. Chan and K. H. Ding, "Multiple scattering among vias in planar waveguides using pre-conditioned SMCG method", *IEEE Transactions on Microwave Theory and Techniques*, vol. 52, no. 1, pp. 20-28, January 2004.

[10] Q. Li, et al, "Quasi-static Parameters, Low Frequency Solutions, and Full Wave Solutions of a Single Layer Via", *Microwave Opt. Technol. Lett.*, vol. 35, pp34-40, Oct. 2002.

[11] B. Wu and L. Tsang, "Signal integrity analysis of package and printed circuit board with multiple vias in substrate of layered dielectrics," IEEE Trans. Advanced Packaging., vol. 33, no. 2, pp. 510-516, May 2010.

[12] T. Okoshi, Planar Circuits for Microwaves and Lightwaves. Berlin, Germany: Springer-Verlag, 1985.

[13] G. T. Lei, R. W. Techentin, P. R. Hayes, D. J. Schwab, and B. K. Gilbert, "Wave model solution to the ground/power-plane noise problem," *IEEE Trans. Instrum. Meas.*, vol. 44, no. 2, pp. 300-303, Apr. 1995.

[14] Y. Zhang, G. Feng, and J. Fan, "A novel impedance definition of a parallel-plate pair for an intrinsic via circuit model," *IEEE Trans. Microwave Theory Tech.*, vol. 58, no. 12, pp. 3780-3789, Aug. 2010.

[15] X. Chang, B. Archambeault, M. Cocchini, F. De Paulis, V. Sivarajan, et al., “Return via connections for extending signal link path bandwidth of via transitions,” in *Proc. Int. Symp. Electromagn. Compat. Eur.*, Hamburg, Germany, pp. 1-6, Sep. 2008.

[16] L. Tsang, et al, “Methods for Modeling Interactions between Massively Coupled Multiple Vias in Multilayered Electronic Packaging Structures”, U.S. Patent 7 149 666, Dec. 12, 2006.

[17] H. Chen, Q. Li, L. Tsang, C.C. Huang and V. Jandhyala, "Analysis of large number of vias and differential signaling in multi-layered structures," *IEEE Trans. on Microw. Theory and Tech.*, vol. 51, pp818-829, Mar. 2003

[18] L. Tsang and D. Miller, “Coupling of vias in electronic packaging and printed circuit board structures with finite ground plane,” *IEEE Trans. Adv. Packag.* vol. 26, pp. 375-384. Nov. 2003

[19] C.J. Ong, D. Miller, L. Tsang, B. Wu and C.C. Huang, "Application of the Foldy-Lax multiple scattering method to the analysis of vias in ball grid arrays and interior layers of printed circuit boards," *Microw. Opt. Tech. Lett.*, vol. 49, no. 1, pp. 225-31, Jan. 2007

[20] B. Wu, and L. Tsang, “Modeling multiple vias with arbitrary shape of antipads and pads in high speed interconnect circuits,” *IEEE Microwave and Wireless Comp. Lett.*, vol. 19, pp. 12-14, Jan. 2009.

[21] B. Wu and L. Tsang, "Full-wave modeling of multiple vias using differential signaling and shared antipad in multilayered high speed vertical interconnects," *Progress In Electromagnetics Research, PIER 97*, pp. 129-139, 2009.

[22] W.C. Chew, Waves in Inhomogeneous Media, IEEE Press, 1985.

[23] B. Wu, X. Chang, L. Tsang and T. Mo, “Fast electromagnetic modeling of 3D interconnects on chip-package-board,” *Proc. Progress In Electromagnetics Research Symposium (PIERS’10)*, Cambridge, MA, July 2010.

[24] E.-P. Li, X. Wei, A. C. Cangellaris, E.-X. Liu, Y. Zhang, et al., "Progress review of electromagnetic compatibility analysis technologies for packages, printed circuit boards, and novel interconnects," *IEEE Trans. Electromagn. Compat.*, vol. 52, no. 2, pp. 248-265, May, 2010.

[25] L. Tsang, and Q. Li, "Wave scattering with UV multilevel partitioning method for volume scattering by discrete scatterers", *Microw. Opt. Tech. Lett.*, vol. 41, pp. 354-361, Jun. 2004.

[26] C. Schuster, Y. Kwark, G. Selli, and P. Muthana, ``Developing a 'physical' model for vias," *Proc. IEC DesignCon Conf.*, Santa Clara, CA USA, Feb. 6 - 9, 2006, pp.1-24.

[27] J. Kim, L. Ren, and J. Fan, “Physics-based inductance extraction for via arrays in parallel planes for power distribution network design,” *IEEE Trans. Microw. Theory Tech.*, vol. 58, no. 9, pp. 2434–2447, Sep. 2010.

[28] R. Rimolo-Donadio, X. Gu, Y. H. Kwark, M. B. Ritter, B. Archambeault, F. D. Paulis, Y. Zhang, J. Fan, H.-D. Bruns, and C. Schuster, “Physics-based via and trace models for efficient link simulation on multilayer structure up to 40 GHz,” *IEEE Trans. Microw. Theory Tech.*, vol. 57, no. 8, pp. 2072–2083, Aug. 2009.

[29] Y.-J. Zhang, J. Fan, "An intrinsic via circuit model for multiple vias in an irregular plate pair through rigorous electromagnetic analysis," *IEEE Trans. Microwave Theory and Technology*, vol. 58, no. 8, pp. 2251-2265, 2010.

[30] Y.-J. Zhang and J. Fan, "A generalized multiple scattering method for dense vias with axially-anisotropic modes in an arbitrarily-shaped plate pair," *IEEE Trans. Microw. Theory Tech.*, vol. 60, no. 7, pp. 2035–2045, Jul. 2012.

[31] S. Muller, F. Happ, X. Duan, Rimolo-Donadio, R., H. Bruns, and C. Schuster, "Complete modeling of large via constellations in multilayer printed circuit boards," *IEEE Trans. Compon. Packag. Manuf.*, vol. 3, no.3, pp. 489-499, March. 2013.

[32] X. Wei and E. Li, "Integral-equation equivalent-circuit method for modeling of noise coupling in multilayered power distribution networks," *IEEE Trans. Microw. Theory Tech.*, vol. 58, no. 3, pp. 559-565, Mar. 2010.

[33] H. Wang and J. Fan, "Modeling local via structures using innovative PEEC formulation based on cavity green's functions with wave port excitation", *IEEE Trans. Microw. Theory Tech.*, vol. 61, no. 5, pp. 1748-1757, May. 2013.

[34] L. Tsang, J. A. Kong, K. H. Ding, and C. Ao, "Scattering of electromagnetic waves: vol. 2, Numerical simulations", Wiley Interscience, New York, 2001.

[35] L. Tsang and D. Miller, "Coupling of vias in electronic packaging and printed circuit board structures with finite ground plane", *IEEE Trans. Advanced Packaging*, vol. 26, pp. 375-384, Nov. 2003.

[36] L. Tsang and X. Chang, "Modeling of vias sharing the same antipad in planar waveguide with boundary integral equation and group T matrix method," *IEEE Trans. Comp. Packag. Manuf. Technol.*, vol. 3, pp. 315–327, Feb. 2013.

[37] L. Tsang, J. A. Kong, and R. Shin, Theory of microwave remote sensing, Wiley-Interscience, New York, 1985.

[38] A. E. Engin, W. John, G. Sommer, W. Mathis, and H. Reichl, "Modeling of striplines between a power and a ground plane," *IEEE Trans.Adv. Packag.*, vol. 29, no. 3, pp. 415–426, Aug. 2006.

[39] Y.-J. Zhang, Z. Z. Oo, X. C. Wei, E.-X. Liu, J. Fan, and E.-P. Li, "Systematic microwave network analysis for multilayer printed circuit boards with vias and decoupling capacitors," *IEEE Trans. Electromagn. Compat.*, vol. 52, no. 2, pp. 401–409, Mar. 2010.

[40] Z. Z. Oo, E.-X. Liu, X. C. Wei, Y. Zhang and E.-P. Li, "Cascaded microwave network approach for power and signal integrity analysis of multilayer electronic packages," *IEEE Trans. Comp.Packag. Manuf. Technol.*, vol. 1, pp. 1428–1437, Sep. 2011.

[41] Y. Zhang, R. Rimolo-Donadio, C. Schuster, E. Li, and J. Fan, "Extraction of via-plate capacitance of an eccentric via by an integral approximation method," *IEEE Microwave and Wireless Components Letters*, vol. 19, no. 5, pp. 275-277, May 2009.

[42] C.-J. Ong, B. Wu, L. Tsang and X. Gu, "Full-wave solver for microstrip trace and through-hole via in layered media," *IEEE Trans. Advanced Packaging*, vol. 31, no. 2, pp. 292-302, May 2008.

[43] X. Chang and L. Tsang, “Fast and Broadband Modeling Method for Multiple Vias With Irregular Antipad in Arbitrarily Shaped Power/Ground Planes in 3-D IC and Packaging Based on Generalized Foldy--Lax Equations,” in press, *IEEE Trans. Comp.Packag. Manuf. Technol.*, 2014.

[44] X. Chang and L. Tsang, “A New Efficient Method for Modeling Dense Via Arrays with 1D Discretization in 2D Method of Moment and Group T Matrix”, 2012 *Electrical Performance of Electronic Packaging International Symposium*, Tempe, AZ, USA, October, 2012.

[45] E. J. Denlinger, “A frequency dependent solution for microstrip transmission lines”, *IEEE Trans. Microw. Theory Tech.*, vol. 19, no. 1, pp. 30-39, Jan. 1971.

[46] R. Rimolo-Donadio, H.-D. Brüns, and C. Schuster, “Including stripline connections into network parameter based via models for fast simulation of interconnects,” in *Proc. 20th Int. Electromagn. Compat. Symp.*, Zurich, Switzerland, Jan. 2009, pp. 345–348.

[47] C. R. Paul, “Analysis of Multiconductor Transmission Lines”. New York: Wiley, 1994, pp. 47–76, 187–245.

[48] Xiaomin Duan, Rimolo-Donadio, R., Bruns, H. and Schuster, C., “Extension of the Contour Integral Method to Anisotropic Modes on Circular Ports”, *IEEE Trans. Comp.Packag. Manuf. Technol.*, vol. 2, no. 2, pp. 321-331, 2012.

[49] B.C. Wadell, “Transmission Line Design Handbook”, Artech House, Norwood, MA, 1991.

[50] A. Ishimaru, Wave Propagation and Scattering in Random Media, vol. 1 and 2, Academic Press, New York, 1978.

[51] A. Ishimaru, Electromagnetic Wave Propagation, Radiation and Scattering, Prentice Hall 1991.

[52] B. Wu, L. Tsang and C.J. Ong, "Fast All Modes (FAM) Method Combined with NMSP for Evaluating Spatial Domain Layered Medium Green's Functions of Moderate Thickness," Microw. Opt. Tech. Lett., vol. 49, no. 12, pp. 3112-3118, Dec. 2007.

[53] David Pozar, “Microwave Engineering”, 3rd Edition, John Wiley & Sons Inc., 2005.

[54] R. F. Harrington, “Field Computation by Moment Methods”. IEEE Press, 1993.

[55] R. Gordin, et al, “Design and Modeling Methodology of Vertical Interconnects for 3DI Applications”, *IEEE Transactions on Components, Packaging and Manufacturing Technology*, vol. 1, no. 2, pp. 163-167, February 2011.

[56] Y. J. Cheng, et al, “94 GHz Substrate Integrated Monopulse Antenna Array”, *IEEE Transactions on Antennas and Propagation*, vol. 60, no. 1, pp. 121-129, January 2012.

[57] Xinxin Tian ; Yao-Jiang Zhang ; Dazhao Liu ; Liangqi Gui ;Qingxia Li ; Jun Fan, “Efficient Analysis of Power/Ground Planes Loaded with Dielectric Rods and Decoupling Capacitors by Extended Generalized Multiple Scattering Method”, *IEEE Trans.* Electromagn. Compat. Volume: 57 Issue: 1, pp. 135 - 144.

APPENDIX A

A.1 2D METHOD OF MOMENT WITH 1D DISCRETIZATION AND INTEGRATION

I also solve the entire problem using 2D MoM based on 1D discretization and 1D integration. In this Appendix, I briefly describe this alternative method. We have also compared the results of this alternative method with the Foldy-Lax/MoM1D. The two results are in excellent agreement.

A.1.1 Incident Electric Field and Surfaces Currents

Consider a distribution of magnetic surface currents $\bar{M}_s(\bar{\rho}')$ in the antipad at $z = \frac{d}{2}$. Then the z component of incident electric field $E_z^i(\bar{\rho}, z)$ of the TM mode onto the via is equal to sum of the TM_l modes, $l = 0,1,2, ...$

$$E_z^i(\bar{\rho}, z) = \sum_{l=0}^{\infty} E_{z,l}^i(\bar{\rho})\, cos\left(k_{zl}\left(z + \frac{d}{2}\right)\right) \tag{A.1.1}$$

where

$$E_{z,l}^i(\bar{\rho}) = \frac{(-1)^l}{d} f_l \iint dx'dy' \left(\frac{j}{2}\right) k_{\rho l}\, H_1^{(2)}\left(k_{\rho l}\rho_{\overline{\rho\rho'}}\right) \times \left(\hat{x}sin\phi_{\overline{\rho\rho'}} - \hat{y}cos\phi_{\overline{\rho\rho'}}\right) \cdot \bar{M}_s(\bar{\rho}') \tag{A.1.2}$$

$(\bar{\rho}, z)$ is on the surface of via, $\bar{\rho}$ is the 2-dimensional position vector in the x-y plane, $k_{\rho l} = \sqrt{k^2 - \left(\frac{l\pi}{d}\right)^2}$, $\overline{\rho\rho'}$ is the vector pointing from $\bar{\rho}'$ to $\bar{\rho}$. The weighting factors are $f_l = \frac{1}{2}$ for $l = 0$ and $f_l = 1$ for $l = 1,2, ...$

For $l = 0$ (TEM) mode, the incident field becomes

$$E_{z,0}^i(\bar{\rho}) = -\frac{1}{d}\iint dx'dy'\hat{z} \times \nabla_t{}' g_0 \cdot \hat{z} \times \nabla_t{}' \psi_L(x', y') = \frac{1}{d}\iint dx'dy' \nabla_t{}' g_0 \cdot \nabla_t{}' \psi_L \tag{A.1.3}$$

where $g_0(\bar{\rho}, \bar{\rho}') = -\frac{j}{4} H_0^{(2)}\left(k\rho_{\overline{\rho\rho'}}\right)$. Using Green's theorem and using the fact that, ψ_L obeys Laplace equation we then have

$$E_{z,0}^i(\bar{\rho}) = \frac{1}{d\varepsilon}\oint_S \, dl' g_0(\bar{\rho}, \bar{\rho}')\sigma_s(\bar{\rho}') \tag{A.1.4}$$

I use equation (A.1.4) to calculate the incident field for the case that the via surface is in the same antipad of the magnetic current source. A simplification can be made for the antipad which is much smaller than a wavelength because we solved the Laplace equation for the magnetic surface current. I further simplify the expression for $E^i_{z,0}$, $g_0(\bar{\rho},\bar{\rho}') \approx g_L(\bar{\rho},\bar{\rho}') + C$, where g_L is the Laplace Green's function and C is the constant and $C = -\frac{1}{2\pi} ln(k)$. Substituting in (A.1.4), it can be shown that the C term does not contribute, since $\oint_S dl'\sigma_s(\bar{\rho}') = 0$. Then $E^i_{z,0}(\bar{\rho}) = \frac{1}{d\varepsilon}\oint_S dl' g_L(\bar{\rho},\bar{\rho}')\sigma_s(\bar{\rho}')$ for $\bar{\rho}$ on the surface S_i.

From the surface integral equation of Laplace equation, we then have, for $\bar{\rho}$ on the surface S_i

$$E^i_{z,0}(\bar{\rho}) = \frac{V_i}{d} \tag{A.1.5}$$

where V_i is the voltage on the i^{th} via. Equation (A.1.5) is a simple result for the incident field of the TEM mode on the i^{th} via. Previously, the result was shown to be true for the case of a circular via centered at the antipad [4]. In the above derivations, we show that the simple relation is true for general situations of arbitrary shapes of vias and also for an arbitrary number of vias sharing the antipad.

For $l = 1,2,$ ... mode, similar derivations apply and lead to

$$E^i_{z,l}(\bar{\rho}) = (-1)^l \frac{2}{d\varepsilon}\oint_S dl' g_l(\bar{\rho},\bar{\rho}')\sigma_s(\bar{\rho}') \tag{A.1.6}$$

where $g_l(\bar{\rho},\bar{\rho}') = -\frac{j}{4}H_0^{(2)}\left(k_{\rho l}\rho_{\overline{\rho\rho'}}\right)$. Note that in (A.1.6), in the line integral $\oint_S dl'$, S is the summation over all line boundaries for the $\bar{\rho}'$ coordinates. This means $S = \sum_{i=1}^N S_i + S_g$, over all the vias as well as the ground plane. However, the field coordinate $\bar{\rho}$ for $E^i_{z,l}(\bar{\rho})$ is only over the via boundaries $S_{vias} = \sum_{i=1}^N S_i$.

Then, the surface current for the l mode obeys the equation

$$-\frac{j\omega\varepsilon}{k_{\rho l}^2} E^i_{z,l}(\bar{\rho}) = \oint_{S_{vias}} dl' g_l(\bar{\rho},\bar{\rho}')\, J_{sl}(\bar{\rho}') \tag{A.1.7}$$

for $\bar{\rho}$ on the surface S_q of the via q., and $l = 0,1,2$ ....

Thus the distinctions from the line integral equation of Laplace equation are that (i) the line integrals are only over the vias, and (ii) the Green's function is $g_l(\bar{\rho},\bar{\rho}') = \frac{j}{4}H_0^{(2)}\left(k_{\rho l}\rho_{\overline{\rho\rho'}}\right)$, $l = 0,1,2$ ....

After the 1D integral equations are solved, we obtain $\bar{J}_{sl}^{(q)}(\bar{\rho}')$, the surface current unknowns for the l^{th} mode on the via. Then

$$\bar{J}_s^{(q)} = \sum_l \hat{z} J_{sl}^{(q)}(\bar{\rho}) cos\left(k_{zl}\left(z+\frac{d}{2}\right)\right) \tag{A.1.8}$$

and the current on the q^{th} via is

$$\bar{I}^{(q)} = \sum_l \oint_{S_q} dl\, J_{sl}^{(q)}(\bar{\rho}) cos\left(k_{zl}\left(z+\frac{d}{2}\right)\right) \tag{A.1.9}$$

For vias in the same antipad, equation (A.1.6) and (A.1.7) have the same impedance matrices. Thus it is convenient to store the impedance matrix when we get incident field from (A.1.6) and then apply it directly to solve (A.1.7) without the need of re-calculations.

A.1.2 Group T-Matrix

The 2D MoM method has been proposed in [24]. We can also calculate the group T matrix using MoM. Let N_p be the segments number of via p after the discretization, and Δt_{j_p} be the length of segment j_p of via . After some derivations, we get the T matrix of the N_g vias as

$$\bar{\bar{\tau}}^{(N_g)} = [\bar{\bar{W}}^{(1)} \quad \bar{\bar{W}}^{(2)} \quad \dots \quad \bar{\bar{W}}^{(N_g)}] \begin{bmatrix} \bar{\bar{Z}}^{(11)} & \bar{\bar{Z}}^{(12)} & \dots & \bar{\bar{Z}}^{(1N_g)} \\ \bar{\bar{Z}}^{(21)} & \bar{\bar{Z}}^{(22)} & \dots & \bar{\bar{Z}}^{(2N_g)} \\ \dots & \dots & \dots & \dots \\ \bar{\bar{Z}}^{(N_g 1)} & \bar{\bar{Z}}^{(N_g 2)} & \dots & \bar{\bar{Z}}^{(N_g N_g)} \end{bmatrix}^{-1} \begin{bmatrix} \bar{\bar{B}}^{(1)} \\ \bar{\bar{B}}^{(2)} \\ \dots \\ \bar{\bar{B}}^{(N_g)} \end{bmatrix} \tag{A.1.10}$$

where the impedance matrix of MoM $\bar{\bar{Z}}_{i_q j_p}^{qp}$ is $N_q \times N_p$, and

$$\bar{\bar{Z}}_{i_q j_p}^{qp} = \begin{cases} \dfrac{\Delta t_{j_p}}{4j} H_0^{(2)}\left(k_{\rho l}\left|\overline{\rho_{\iota_q}} - \overline{\rho_{J_p}}\right|\right) & i_q \neq j_p \\ \dfrac{\Delta t_{j_p}}{4j}\left[1 - j\dfrac{2}{\pi} ln\left(\dfrac{\gamma k_{\rho l}}{4e}\Delta t_{j_p}\right)\right] & i_q = j_p, l = 0 \\ -\dfrac{\Delta t_{j_p}}{2\pi} ln\left(\dfrac{\gamma \alpha_{\rho l}}{4e}\Delta t_{j_p}\right) & i_q = j_p, l \neq 0 \end{cases} \tag{A.1.11}$$

where $\alpha_{\rho l} = \sqrt{\left(\frac{l\pi}{d}\right)^2 - k^2}$, and $\gamma = 1.78107$.

In (A.1.11), $\bar{\bar{W}}^{(q)}$ is a $(2N_{max}+1) \times N_q$ matrix, and N_q is the segments number of via q after the discretization, and Δt_{i_q} is the length of segment i_q of via q. Then

$$\bar{\bar{W}}_{ni_q}^{(q)} = \frac{j}{4}\Delta t_{i_q} J_n\left(k_{\rho l}\left|\overline{\rho_{i_q}} - \bar{O}_g\right|\right) e^{jn\emptyset_{\overline{\rho_{i_q}}}}$$
$$n = -N_{max}, \dots, 0, \dots, N_{max}, i_q = 1,2, \dots, N_q$$

(A.1.12)

$\bar{\bar{B}}^{(q)}$ is $N_p \times (2N_{max} + 1)$ matrix, and

$$\bar{\bar{B}}_{j_p m}^{(p)} = J_m\left(k_{\rho l}\left|\overline{\rho_{j_p}} - \bar{O}_g\right|\right) e^{-jm\emptyset_{\overline{\rho_{j_p}}}}$$
$$m = -N_{max}, \dots, 0, \dots, N_{max}, j_p = 1,2, \dots, N_p$$

(A.1.13)

Good agreements are obtained when comparing the group T matrix calculated from Foldy-Lax multiple scattering equation and from 2D MoM.

A.2 $\boldsymbol{\tau}$ Matrix and Foldy Lax Multiple Scattering Equations in the Presence of the Cavity Wall

I show simplified derivations, using operator formalism, of the τ matrix and Foldy-Lax multiple scattering equations in the presence of cavity wall.

Consider a single via scatterer in an infinite waveguide. Let U be the scattering potential, and G_0 be the Green's function for infinite waveguide. The Green's function for the single via scatterer, G_s, obeys the Lippman Schwinger equation [37]

$$G_s = G_0 + G_0 U G_s \tag{A2.1}$$

The T matrix of the via for infinite power/ground plane is T such that $TG_0 = UG_s$. The Lippman Schwinger equation for the T matrix is [37]

$$T = U + UG_0T = (1 - UG_0)^{-1}U \tag{A2.2}$$

The T matrix is assumed to be known for a single via.

Next I derive the T matrix in the presence of the wall. For the case of finite ground plane, the Green's function, G_{00},is the sum of G_0 and G_W

$$G_{00} = G_0 + G_W \tag{A2.3}$$

where G_W is Green's function corresponding to the reflection from the wall.

The Green's function for a single via G_s in finite ground plane then obeys the Lippman Schwinger equation with G_{00}

$$G_s = G_{00} + G_{00} U G_s \tag{A2.4}$$

If we define the τ matrix to be

$$UG_s = \tau G_{00} \tag{A2.5}$$

then

$$\tau = U + UG_{00}\tau \tag{A2.6}$$

Substitute in G_{00}, and rearranging terms gives

$$\tau = (1 - UG_0)^{-1}(U + UG_W\tau) = T + TG_W\tau \tag{A2.7}$$

Hence

$$\tau = (1 - TG_W)^{-1}T \tag{A2.8}$$

Thus τ is the T matrix in the presence of the wall with the reflection included. In matrix notations, equation (3.28) corresponds to the operator equation of (A2.8).

For N vias in finite power/ground plane, let U_j be the scattering potential of the j^{th} via, $j = 1,2, \ldots \ldots, N$. Then

$$\tau_j = U_j + U_j G_{00} \tau_j \tag{A2.9}$$

is the T matrix of via j , , $j = 1,2, \ldots \ldots, N$, in the presence of the wall. The Green's function G for the entire problem of multiple vias in finite ground/power plane, is

$$G = G_{00} + \sum_{j=1}^{N} G_{00} U_j G \tag{A2.10}$$

Let G_j be the exciting Green's function of via j, such that

$$G_j = G_{00} + \sum_{l \neq j}^{N} G_{00} U_l G \tag{A2.11}$$

Then

$$G = G_j + G_{00} U_j G \tag{A2.12}$$

It follows from (A2.12) and (A2.9) that

$$U_j G = \left(1 - U_j G_{00}\right)^{-1} U_j G_j = \tau_j G_j \tag{A2.13}$$

Substituting (A2.13) in (A2.10) gives the Foldy-Lax equation for the exciting Green's function

$$G_j = G_{00} + \sum_{l \neq j}^{N} G_{00} \tau_l G_l \tag{A2.14}$$

The total Green's function is

$$G = G_{00} + \sum_{j=1}^{N} G_{00} \tau_j G_j \tag{A2.15}$$

For the electric field, let E_j^{ext} be the exciting field of the j^{th} via. Then the Foldy-Lax equation for the exciting field is

$$E_j^{ext} = E_{inc} + \sum_{l \neq j}^{N} G_{00} \tau_l E_l^{ext} \tag{A2.16}$$

and the total field E is

$$E = E_{inc} + \sum_{j=1}^{N} G_{00} \tau_j E_j^{ext} \tag{A2.17}$$

where the incident field E_{inc} is the sum of direct, E^d, from the source and reflection E^W of the direct from the wall. Thus $E_{inc} = E^d + E^W$. In matrix form, equation (3.37) corresponds to (A2.16).

VITA

I received the B.S. and M.S. degrees from Jilin University, Changchun, China, in 2003 and 2007, respectively, all for Electrical Engineering. I am currently a graduate student of PhD program with Electrical Engineering department in University of Washington, Seattle, WA, since September 2009. My current research interests include signal integrity/power integrity modeling and analysis for 3-D integrated circuit interconnects and packaging system, electromagnetic theory, microwave engineering, computational electromagnetics, metamaterials, and quantum electronics. I was elected as one of awarded nominees of Outstanding Teaching Assistant with the Electrical Engineering Department, University of Washington, in 2011, 2012, and 2013 respectively.

My selected publications are shown below:

[1] L. Tsang and X. Chang, "Modeling of vias sharing the same antipad in planar waveguide with boundary integral equation and group T matrix method," *IEEE Trans. Comp. Packag. Manuf. Technol.*, vol. 3, pp. 315–327, Feb. 2013.

[2] X. Chang and L. Tsang, "Fast and Broadband Modeling Method for Multiple Vias With Irregular Antipad in Arbitrarily Shaped Power/Ground Planes in 3-D IC and Packaging Based on Generalized Foldy--Lax Equations," *IEEE Trans. Comp. Packag. Manuf. Technol.*, vol. 4, pp. 685-696, April, 2014.

[3] X. Chang etc, "Application of Foldy-Lax equations for modeling scattering effects of irregular power/ground planes, multiple vias and traces for link level simulation on multilayer electronic structures", to be submitted.